Optical Approaches to Characterising Engineered Nanoparticles for Size and Shape in Aquatic Systems

Samuel R Thompson

PhD

University of York

Physics

March 2017

Abstract

Engineered nanoparticles are increasingly being used in a wide range of commercial products including paints, personal care products, textiles, and coatings. As a result, increasingly large quantities of engineered nanoparticles are being released into the environment via a range of different pathways. While there are a wide selection of available tools capable of making measurements of engineered nanoparticles in the environment, these all have their own unique drawbacks. In this thesis, a range of optical techniques for the measurement of engineered nanoparticles are critically assessed. One of these, nanoparticle tracking analysis, was selected for further investigation. This investigation commenced with a conventional nanoparticle fate and behaviour study using an existing commercial solution in order to get a better understanding of the capabilities of currently available systems. One of the primary issues identified was the inability of available commercial equipment to operate effectively at concentrations as low as those predicted for the natural environment. Following this, further development of the nanoparticle tracking analysis paradigm resulted in the twin capabilities of shape determination directly from light-scattering data (which has never been successfully achieved before) and an improvement in low-concentration performance by three orders of magnitude. Finally, a simple nanoparticle aggregation study from the literature was repeated, this time at concentrations leveraging the new, lower-concentration capability. The profoundly different outcome from running this experiment at environmentally relevant conditions – that aggregation proceeded at a sufficiently reduced rate that the nanoparticles were effectively stabilised – demonstrates the importance of this development: at environmentally relevant concentrations nanoparticles behave in very different ways compared to the current standard of lab-based studies at artificially high concentrations. Using this newly-developed low-concentration approach it is possible to cheaply and quickly work at these concentrations.

Contents

List of Tables

List of Figures

Acknowledgements

I would like to acknowledge my two supervisors, Professor Jun Yuan and Professor Alistair B A Boxall for their invaluable guidance and support.

This work would not have been possible without the dedicated support of all the support staff in both the Physics and Environment departments, including Rebecca Sutton, Deborah Sharpe, Dave Hay, Neil Johnson, Andrew Vick, Mark Laughton, and Dave Coulthard.

I'd also like to thank my wife, Hannah, for many cups of tea, and for ongoing support despite long hours spent behind a keyboard.

Further thanks are owed to a great many people from York Community Church, and in particular the Red Herrings, who have helped me see the positive side and keep plugging away.

Finally, much thanks is due to David Fergusson and the Analytical Chemistry Trust Fund, who alongside the Natural Environment Research Council have generously provided the funding for this work.

Declaration

I declare that this thesis is a presentation of original work and I am the sole author, except where noted explicitly below. This work has not previously been presented for an award at this, or any other, University. All sources are acknowledged as References.

Appendix E contains a review for which I was the principal author; this was published in SETAC Globe in 2016, and was co-authored with Patrick Bauerlein (KWR Watercycle Research, Netherlands), Lars Michael Skjolding (Denmark Technical University), and Ralf Kaegi (Swiss Federal Institute of Aquatic Science and Technology).

TEM images of two of the nanoparticle samples (30nm citrate-capped and 30nm PEG-capped) were obtained by Gnanavel Thirunavukkarasu. All the TEM images of the 'Au750' sample which appear in this thesis were obtained by Jun Yuan.

The contents of Chapters 2, 5, 3, and 4 have been written up as research papers for publication, and are awaiting submission.

Some of the work contained within this thesis has been presented at the following conferences:

SETAC Barcelona 2015 Platform presentation. Results concerning the reversibility of nanoparticle aggregation (Chapter 2).

MMC:EMAG Manchester 2015 Poster. Preliminary results concerning the optical determination of nanoparticle shape (Chapter 5).

EAP Fareham 2016 Platform presentation. Full results concerning the optical determination of nanoparticle shape (Chapter 5).

SETAC Nantes 2016 Platform presentation. Full results concerning the optical measurement of nanoparticles at low concentrations (Chapter 3). Optical shape detection was also discussed.

Nanoalloys Birmingham 2016 Poster. Full results concerning the optical determination of nanoparticle shape (Chapter 5).

Chapter 1

Introduction

1.1 Thesis structure

This thesis is structured as follows:

Chapter 1 contains a general overview of nanoparticles and nanoparticle suspensions, and summarises much of the more important work which has thus far been completed in the field. This is followed by a more detailed exposition on the behaviour and measurement of nanoparticles in the context of environmental study. It culminates in a comparison of some of the more important measurement methods, examining their strengths and weaknesses. These are used to justify the choice of nanoparticle tracking analysis (NTA) for further investigation.

Chapter 2 contains a pilot study using NTA for an environmental study in order to further assess the advantages and shortcomings of current NTA offerings in order to better justify the later developments to the NTA instrumentation and use. This study also turns up some important results in its own right, and these are discussed.

Chapter 3 takes the largest shortcoming identified in NTA (the ability to take measurements at environmentally relevant concentrations) and works to mitigate this by describing a bespoke development of the NTA concept which is capable of taking measurements at concentrations improved by approximately three orders of magnitude compared to currently available commercial implementations. This bespoke equipment is validated against the relevant guidelines from ISO17025 to ensure it is operating in a scientifically useful (precise, robust, and reproducible) manner.

Chapter 4 leverages the development of the NTA concept described in Chapter 3 to perform an experiment which would previously have been infeasible. Nanoparticle aggregation kinetics are tracked in real-time at concentrations nearly three orders of magnitude lower than would previously have been possible, and this is used to verify that nanoparticle aggregation kinetics scale with concentration; many previous results which were obtained from lab-based studies at unrealistically high nanoparticle concentrations have yielded results which are of little or no relevance for environmental study.

Chapter 5 addresses another of the shortcomings of NTA which were identified in Chapter 1. In this chapter, the issue of analysis of nanoparticles for shape is tackled, and a novel method of optical analysis was used which allowed the inference of nanoparticle shape directly from the scattering data, while previously this type of analysis was limited to electron-microscopy.

Finally, Chapter 6 draws all the results together and emphasises the importance of these results in the context of the current state of human knowledge and understanding of nanoparticles in the environment, while proposing some additional developments to the work.

The software that was developed to accompany and enable this work is included digitally.

1.2 Context

1.2.1 What is a nanoparticle?

According to a 2011 EU paper on the subject [1], a nanoparticle is: ‘a natural, incidental or manufactured material containing particles, in an unbound state or as an aggregate or as an agglomerate and where, for 50 % or more of the particles in the number size distribution, one or more external dimensions is in the size range 1 nm – 100 nm.’ This definition is very broad, and includes a wide range of naturally-occurring substances, including zinc sulphide nanoparticles produced as waste by many bacteria [2], a great many biological substances (including the iron storage protein eukaryotic ferritin [3], exosomes [4], and cholesterol-carrying lipoproteins [5]), and many naturally-occurring minerals [6].

Engineered or manufactured nanoparticles are those which have been manufactured by humans to fulfil a particular purpose. While humans have used engineered nanomaterials and engineered nanoparticles for millennia [7–9], it is only more recently that we have recognised them as such. Indeed, some of the earliest references to these materials as ‘engineered’ are from some of the earliest environmental studies [10, 11], which were some of the first to make the distinction between naturally-occurring and man-made engineered nanoparticles. This distinction is important, particularly given the context that engineered particles of a substance have been shown to be capable of exhibiting distinct behaviour when compated with apparently identical naturally-occurring particles [12].

Engineered nanoparticles are becoming increasingly ubiquitous in 21st century life and are used in a range of products from deodorants, socks, suncream, bandages and fuels to cutting-edge medical treatments [13–21], they are a new high-tech selling point for many products. For an up-to-date picture, please consult the database of nanoparticle-containing products maintained at `http://www.nanotechproject.org/inventories/`. While this proliferation of products may be good news for many industries that have developed to service demand for ever more salubrious make-up and sleeping bags, there is very little in the way of specific regulation regarding nanoparticle manufacture, use, or disposal [22, 23]. Concerns have therefore been raised about the possibility that these particles could have negative effects upon the health of both ecosystems and humans [24].

1.2.1.1 Nanoparticle structure and coating

At their most simplistic, nanoparticles are small quantities of a single element or crystalline compound. These may be either polycrystalline [25] or single crystals [26, 27]. However, there are many more complex forms a nanoparticle may take. For example, when there is more than a single component in a nanoparticle there are a multitude of ways they can couple. A selection of some of the better-understood examples is shown in Figure 1.1 [28].

Many commercially available particles come with ‘capping agents’ adsorbed onto the surfaces of the particles, the chief aim of which is usually to prevent the particles from aggregating [29, 30]. These usually work in one of two ways: either by increasing the surface charge on the particles in order that the coulomb force repels them and decreases the energy of collisions to reduce the probability of adhesion and aggregation [31], or by affecting the entropy of the particle surfaces such that entropy is maximised when the particles are well dispersed, and entropy is lowered when particles are attached to each other [137]. This is known as steric repulsion [32].

The coating materials are very important when considering the fate, behaviour, and ecotoxicology of engineered nanoparticles [33]. This is because, provided the coating remains intact, the majority of the behaviour and interactions of the particle is determined by the coating rather than the composition of the core material [34]. This is the same principle that has piques scientific interest in core-shell nanoparticles like those shown in Figure 1.1 – for particles of something expensive like platinum, a platinum-coated particle could be an equally-effective and significantly cheaper option [35].

1.2.2 Nanoparticles in the environment

There are many ways that these particles may be released into the environment. For example, nanoparticle-containing toothpaste will typically be disposed of using a domestic washbasin – these particles will travel through the sewage treatment process and eventually be released into a natural water system with the effluent [36]. Similarly, nanoparticles added to fuel will be released into the air with the exhaust; this will either remain aerosolised in the air, or settle

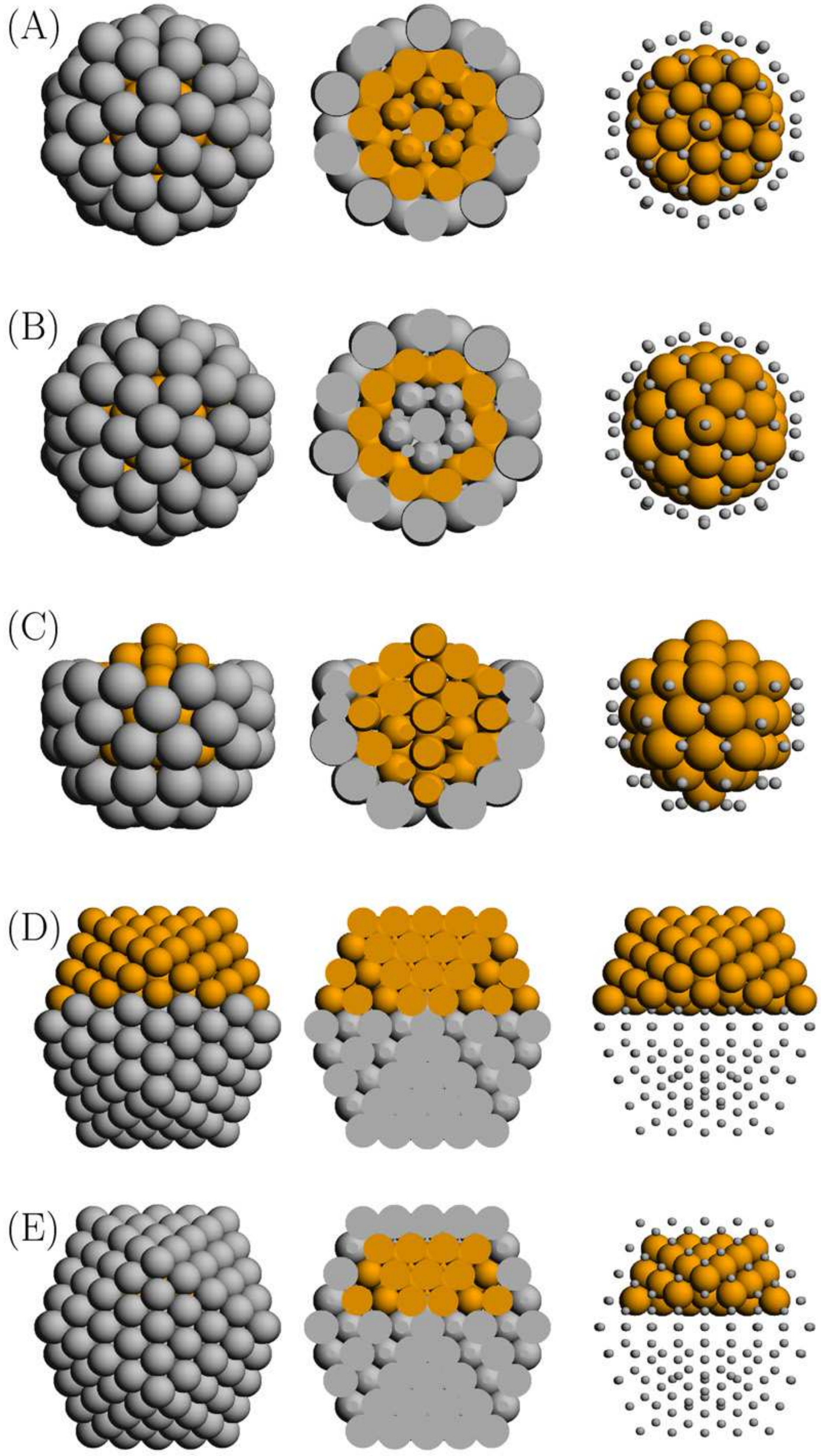

Figure 1.1: Diagram illustrating some of the many ways 2-element nanoparticle may form. A: Core-shell structure; B: Multishell; C: Ball-and-cup; D: Janus; E: Quasi-Janus. Diagram reproduced from [28].

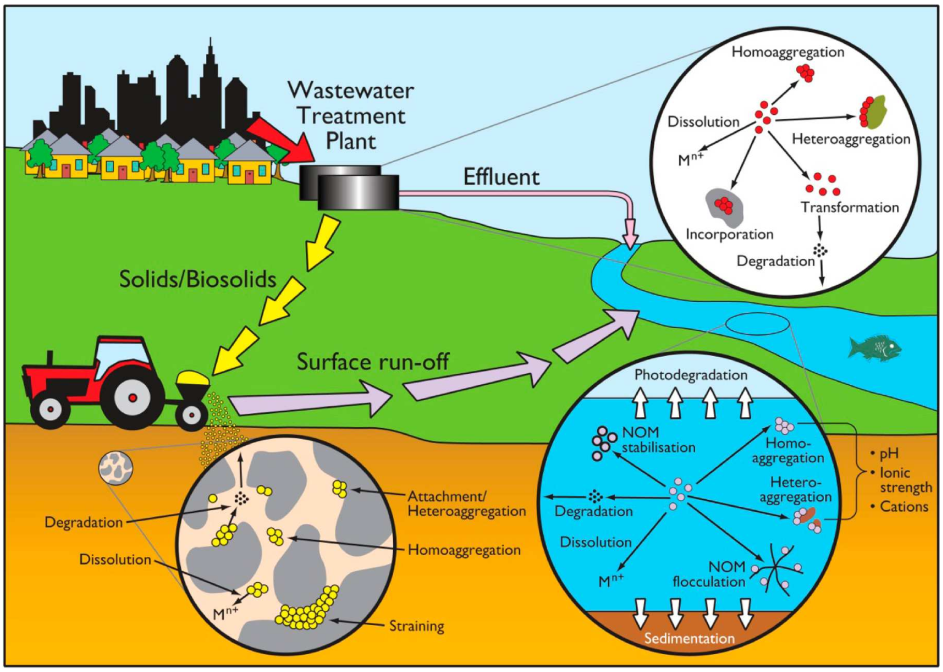

Figure 1.2: Diagram illustrating some of the processes and possible eventual fates for engineered nanoparticles which have been released into the environment. Reproduced from [36].

out upon road surfaces, to be carried into natural water systems next time it rains [37–40] This is illustrated in Figure 1.2. Estimates of nanoparticle concentrations in the environment have been made, suggesting concentrations of certain particles could be as high as 30 μg/L [41, 42]

A major concern is how these particles affect the ecosystems into which they are released, both during normal use and at their end-of-life disposal. Before these questions of ecological and wider environmental impact can be answered, the behaviour and eventual fate of these particles needs to be well understood [15]. A diagram illustrating a few of the types of behaviour which need to be considered for environmental study are summarised in Figure 1.2.

Engineered nanoparticles (ENPs) are a class of emerging pollutant [43] whose fate and behaviour in the natural envionment is very poorly understood. One of the processes that ENPs are known to undergo in natural environments is the aggregation of primary particles to form larger masses [36]. These aggregates tend to have lower activity levels compared to the primary particles due to factors such as the reduced surface area [44].

Gold is a good example of the possible hazards posed by ENPs. In bulk form it is extremely chemically stable [45] and virtually unregulated. In bulk form, this makes sense – if a large quantity of bulk gold were to be deposited or disposed of in a river, it would stay there. It would not readily transform into anything harmful, it would not poison anything – at worst it could produce shading effects [46, 47] which aren't specific to its chemical properties. However, nanometer-sized gold behaves completely differently. It can form 5-fold crystals [48, 49] which have significant levels of strain at the surfaces, generating resonances at energies that allow it to become strongly catalytically active [50]. At even smaller sizes, gold particles actually cease to be electrically conductive at all – it has an insulating transition at about 2 nm [51]. Clearly, a material such as this requires more robust regulation than is currently in place.

1.2.2.1 Risk assessment and regulation

As has hopefully been made clear, there are some significant potential environmental risks posed by the continued use of engineered nanoparticles. This points to a clear need for a well-reasoned and rigorous approach to regulation, and environmental regulations require robust and scientifically-literate risk assessments [52, 53].

In order to carry out a meaningful environmental risk assessment, there are several steps which need to be taken. Firstly, there must be at least one pathway for the potential toxicant from the product or process for which it is used into the environment. Once such a pathway has been proposed, it then needs to be established that the potential toxicant does actually follow that pathway and is present in the environment. In the case of nanoparticles, this has been covered thoroughly; research has covered environmental emission of nanoparticles from textiles [54], personal care products [55, 56], fuel additives [38], and generic incineration of nanoparticle-containing materials [57] as just a few examples.

Once it has been established that there is a viable pathway for the potential toxicants into the environment, these potential toxicants need to be shown to have toxic effect upon organisms at the concentrations and in the forms in which they are found in the environment, or a form into which they could transform. This latter condition may be illustrated using the well-known example of mercury toxicity [58, 59]. While methyl mercury is highly bioavailable [60, 61] and bioaccumulative [62, 63], ethyl mercury (usually in the form of thimerosal, commonly used to stabilise vaccinations) is not generally considered to be a significant toxicant [64].

Assuming it has been established that a substance has a pathway into the environment, and that there are organisms in the environment which are sensitive to the toxicant, it is then necessary to understand the effects, if any, which may be caused in those organisms by this toxicant at the modelled/measured concentrations, and thence to the wider ecosystem [65]. Only once all these steps are satisfied can a meaningful estimate of risk be determined and therefore a meaningful regulatory regime be imposed [66].

Current sticking-points for the regulation of nanoparticles are centred around three main issues. These are the ability to measure nanoparticles in the environment [67], an understanding of exactly how various different nanoparticles behave in the environment (under environmentally relevant conditions) [14], and how environmentally-relevant doses of engineered nanoparticles affect organisms and ecosystems [68].

While it is increasingly widely accepted that many of the engineered nanoparticles which are seeing widespread use currently pose little risk on their own [69, 70], efforts to characterise fate, behaviour, and risk from these particles have demonstrated that currently-available analytical techniques fall short of the efficacy required for effective risk assessment and realistic environmental measurement, as will be made clear in the following sections. While this may not be a significant issue here and now, it is clear that as ever more types of nanoparticle and nanoparticle-based products are developed and sold, eventually some of these will be genuinely highly toxic, and it would be greatly advantageous for there to already be effective and sufficient analytic techniques in place to deal with and mitigate this threat.

1.2.2.2 Early studies

While nanoparticles have been used by humans for millenia [7–9], it is only in the past few decades that they have been intentionally used, and used in large quantities [71]. However, most of these nanoparticles have not been considered from an environmental toxicology or eco-toxicological perspective until more recently; some of the earliest peer-reviewed acknowledgements of the possible risks of ENPs in the environment weren't published until 2003 [10, 11], though their mammalian toxicology had been investigated more than ten years previously in 1992 [72]. This relatively large delay was principally due to the fact that in most jurisdictions these new nanoparticle-containing products were (and remain) largely unregulated – the ENPs used in these products are familiar and well-understood chemicals in bulk quantities – substances like silver, zinc oxide, and titanium dioxide are commonly used [54, 73].

Many of these early studies cited in this section involved suspending high concentrations (up to about 1 g/L [74]) of ENPs in water before exposing organisms to them [75, 76]. At very high concentrations like these, ENPs of almost any composition and morphology can have serious toxic effects – they can coat biological surfaces and effectively 'smother' organisms [77]. This is quite apart from some of the other toxic effect mechanisms which can operate at lower particle concentrations, including cytotoxicity and genotoxicity [78, 79], endocrine disruption [80, 81], and reproductive impairment [33, 82].

Studies into the behaviour of ENPs have historically tended to focus upon their homoaggregation (aggregation of a species of particle with other members of its own species) and sedimentation behaviour, and the earliest studies were more concerned about the consequences of these processes for nano-enabled medicines than the environmental perspective [83–85]. While these can be useful for understanding the behaviour of small aspects of ENP behaviour in isolation, they do not usually produce results which have direct relevance for understanding and predicting the behaviour of ENPs in the environment [86].

1.2.2.3 More recent progress

More recently, the study of nanotoxicology has become less of a scattergun exercise and far more methodical and rigorous. While previous studies may have focussed upon the specific effects of a specific nanoparticle upon a specific organism under specific conditions, now more general, useful, and widely-applicable results are pursued. Machine-learning has become a hot topic in the study of 'big data', and this has been brought to bear upon nanotoxicological studies [87]. The ability to sequence genomes quickly and inexpensively has led to more rigorous study of genotoxicity [88]. Related systems biology in the form of genomics, metabolomics, proteomics, and transcriptomics are allowing much higher-throughput screening for genetic and epigenetic changes induced by the tested stressors [20, 89–92]. This is hugely important for the measurement of nanotoxicity because it permits the detection and measurement of effects which are not manifested in ways picked up by traditional endpoint toxicology studies, in which a limited number of endpoints are monitored and observed for toxicologically-induced changes.

Behavioural studies have started to investigate a wider range of processes, including heteroaggregation (aggregation of nanoparticles of one species with nanoparticles of another species) and the more general interactions with the chemistry and biology of the natural environment [93]. In general it has been found that in systems which contain a population of ENPs among a wider population of naturally-occurring particles, the dominant aggregation process is in fact heteroaggregation of natural organic nanoparticles and ENPs [94, 95].

These behavioural studies also feed into fate modelling and experimentation – once the behaviour of any given particles in a given environmental scenario is known then is is possible to determine what their eventual fate is, and on what timescales the particles will progress to their eventual fate. Some important environmental fate studies include the conclusive demonstration that local water chemistry can have a profound effect upon whether particles will remain suspended or sediment out [96] and recognition that in soils, soil composition is just as important as nanoparticle composition and coating [97]. While it has long been recognised that sewage sludge is an important final resting place for a range of pollutants [98, 99], sewage treatment plants have generally not been designed for removal of nanoparticles, so assessment of removal efficiencies in treatment plants is also important [100].

A further recently-reported complication is the suggestion that under certain environmentally-relevant conditions, metal ions could be reduced to form nanoparticles while in the natural environment [101]. This adds an additional layer of complexity to the tracing of apparently engineered nanoparticles detected in the environment to their source, an area in which there appears to have been no progress made in the peer-reviewed literature.

1.3 Nanoparticle behaviour

In order to understand the eventual fate of engineered nanoparticles in the environment, it is necessary to understand and quantify their intermediate behaviour. The main behavioural processes which engineered nanoparticles have been shown to undergo are sedimentation [102], dissolution [103], and aggregation [104].

1.3.1 Sedimentation

Sedimentation is a process which usually only plays a minor role in the fate and behaviour of nanoparticles which fit within the EU definition (which typically do not fit within the EU definition of a nanoparticle [1], owing to being larger than 100 nm), as it is a process which has an increasing influence on suspensions of larger particles or aggregates of smaller particles which have grown to the degree that they are no longer stable in suspension. Sedimentation is largely independent of the composition of the nanoparticles [102], though heavier nanoparticles have been shown to sediment faster than lighter particles [105]. It has also been shown that sedimentation rates can be affected by the means by which the nanoparticles were initially suspended, suggesting that more evenly-dispersed nanoparticles (such as those which have been ultrasonically dispersed) will sediment less than those which have been less adequately dispersed (for example using a vortex dispersion technique) [106]. Sedimentation is important when considering the environmental effects, fate, and behaviour, because it can be a means of partitioning particles to the sediment phase in aquatic systems [107, 108] where they may become less bioavailable. In in-vitro toxicology assays it can also be important because the location of the sample in a vial becomes important – a biofilm on the bottom of a vial may receive a different effective dose when compared to an identical biofilm which is vertically mounted [105].

Colloids are stable suspensions of particles or molecules which do not exhibit sedimentation at all [109]. Colloids are usually accepted to be formed of particles no larger than 1 μm in diameter, as particles larger than this are usually accepted to be insufficiently stable to remain in suspension indefinitely [110].

There is a significant body of research investigating techniques to prevent sedimentation, some of which revolve around the modification of the suspending medium, using guar gum for example [111], while others indirectly influence the sedimentation rate by retarding the aggregation rate, resulting in a slower formation of larger aggregates and thereby reducing the effective sedimentation rate [112]. Yet other approaches involve examining the quality of the suspension and optimising suspension techniques to prevent sedimentation [106].

Sedimentation rates have been used as a means of estimating the sizes of nanoparticles, based upon the principle that under accelerated sedimentation (centrifuge) conditions, larger particles will sediment faster [113–117]. However, this technique doesn't appear to have gained traction and isn't commonly used in the literature.

1.3.2 Dissolution

Dissolution is important for the study of nanoparticles in the environment for several reasons [118]. Firstly, it can allow a nanoparticle to release its content slowly over time, which could cause either an increase in toxicity (when the particle's constituent parts are more toxic or bioavailable in solution than in suspension [68]), or a decrease in observed toxicity (because the release is over a longer period of time, the effective dose would be lower than that from an equivalent quantity of ions being directly released). This can be a serious complication when attempting to conduct an environmental impact assessment [15]. Secondly, the solubility of nanoparticles can have a direct effect upon their usefulness or useful life. An example of this is the use of silver nanoparticles in textiles; if the particles are too readily soluble, then they won't survive ordinary textile laundering processes [119]. Finally, dissolution can occur during the extraction and measurement process, and in order to ensure that measurements of soluble particles are representative of the particles initially present in the sample, additional care must be exercised [120]. Understanding the mechanisms of nanoparticle solubility also is impactful in other fields, for example, the development of nano-enabled drug-delivery approaches [121]. There is some interest in the development of systems capable of electrochemically measuring dissolution rates of nanoparticles is suspension [122].

As far as was possible, all the nanoparticles used in the work presented in this thesis were made from gold (which is insoluble in water), in order to avoid having to deal with the issue of dissolution.

1.3.3 Aggregation

Aggregation is the third of the three dominant physical processes undergone by engineered nanoparticles in the environment [104]. A brief introduction to aggregation has already been given in Section 1.2.2.3.

Aggregation is, as has already been alluded to, important for the study of the fate and behaviour of engineered nanoparticles for several reasons. Firstly, aggregation can increase the sedimentation rate of particles as they aggregate and become less stable in suspension [112].

Aggregation can also have an important effect upon the bioavailability of the particles – a larger particle may be less bioavailable, while an engineered particle which has heteroaggregated with a natural nanoparticle may actually become more bioavailable [36,123]. Finally, there EU definition of a nanoparticle should be considered in the context of aggregation. While the EU definition [1] considers particles purely on their primary size (so even a large aggregate should be seen as a collection of smaller constituent particles), it is not easily possible to measure a particle and state definitively whether it is a primary particle or an aggregate – only TEM is well-placed to interrogate aggregate structure and determine this. While in some highly-controlled laboratory-based circumstances it may be obvious which particles are aggregates and which are primary particles, in general this is not true. This is a crucially important point, for reasons which will be covered in Chapter 2.

It is commonly assumed that the process of aggregation is not reversible except in special cases where particles have been explicitly designed to disaggregate. Examples of the disaggregation of ENPs include intentional disaggregation for the formation of metallic thin-films, [277] particles which have aggregated exceedingly fast into unstable fractal forms with high surface energy or when influenced by biological processes such as aptamer binding [278], when encapsulated in synthetic dendrimer [279], or in the presence of high organic matter concentrations [280]. Once aggregated particles have been released into the environment it is often tacitly assumed that they will remain in their aggregated state. For example, the effect of pH upon nanoparticle aggregation has been investigated before, but only in terms of the effect upon unaggregated particles and not in terms of the effect upon existing aggregates that have formed under different environmental conditions. This has repercussions for current exposure models [41], which at present only include nanoparticle aggregation as an irreversible process [115]. This need for more research into the reversibility of nanoparticle aggregation in environmentally relevant circumstances has been acknowledged in the literature [281].

1.3.3.1 DLVO Theory

Except where otherwise noted, all the material in this section on Derjaguin-Landau-Verwey-Overbeek (DLVO) theory has been drawn from some standard texts, available in the following references: [110,124–126]. More detail is given in Appendix B, though is unnecessary to understand the contents of this thesis.

Derjaguin-Landau-Verwey-Overbeek (DLVO) theory [127,128] is one of the foundational theories of the behaviour of suspensions of particles in dilute electrolytes, and is commonly used to provide an estimate of the aggregation behaviour of nanoparticles in aqueous suspensions. The first principles of DLVO theory were laid down in the 1940s and 1950s, building upon the work of Schulze, Hardy, and Smoluchowski. Schulze and Hardy determined that the critical coagulation concentration was related to the inverse sixth power of the charge of the counter-ion [129, 130]. Notably, Hardy showed in the same paper that different ions with the same charge may also have an effect upon aggregation kinetics. This becomes relevant in Chapter 2. This is commonly referred to at the 'Schulze-Hardy Rule'. Smoluchowski's contribution to the understanding of aggregation kinetics and DLVO theory was the derivation of an integrodifferential description of the particle size distribution in an aggregating system [131]. However, direct application of 'Smoluchowski's Law' requires the derivation of a 'kernel' for the aggregation type (for example: diffusion-limited, reaction-limited; these are discussed further in the following section), a non-trivial task. For this reason, Smoluchowski's law isn't used directly in this thesis.

The main premise of DLVO theory is that in a regime for which the van der Waals attraction is greater than the coulomb repulsion between particles, the net rate of aggregation will be positive. At the 'tipping point' where the attraction is equal to the repulsion, the particles will completely fail to 'see' each other, and won't interact, and when the repulsive forces are greater than the attractive ones, the particles will interact, but will remain dispersed. Thence the theory predicts that there will exist a definite point at which the repulsive force generated by the surface charge on particles (the source of the coulomb repulsion) is equal to the van der Waals attraction, one side of which the rate of aggregation is effectively zero, and the other side of which the rate of aggregation will increase with the increase in the difference between the forces. An additional level of DLVO theory includes the description of an 'electric double layer' (EDL; also sometimes referred to as the 'diffuse double layer'). This is formed of counter-ions from the solution which have an opposite charge to the particle surface. To a certain extent, this cloud of counter-ions can have the effect of shielding the coulomb repulsion from the surfaces of the particles, thereby decreasing the total repulsion. The resulting potential is illustrated in Figure 1.3.

There exists a simplified version of the theory, which is only true for $\psi < \frac{50}{z'}\mathrm{mV}$, where ψ is the surface potential of the particles, and z' is the valency of the ion with the greatest charge. This simplified version is stated in Equation (1.1)

$$\frac{x_i A}{D_e \psi^2} = \mathrm{const} \tag{1.1}$$

where x_i is the reciprocal of the thickness of the ionic atmosphere of the particles, A is the van der Waals constant and D_e is the dielectric constant.

However, this is a rarely useful equation; the conditions necessary are seldom fulfilled for

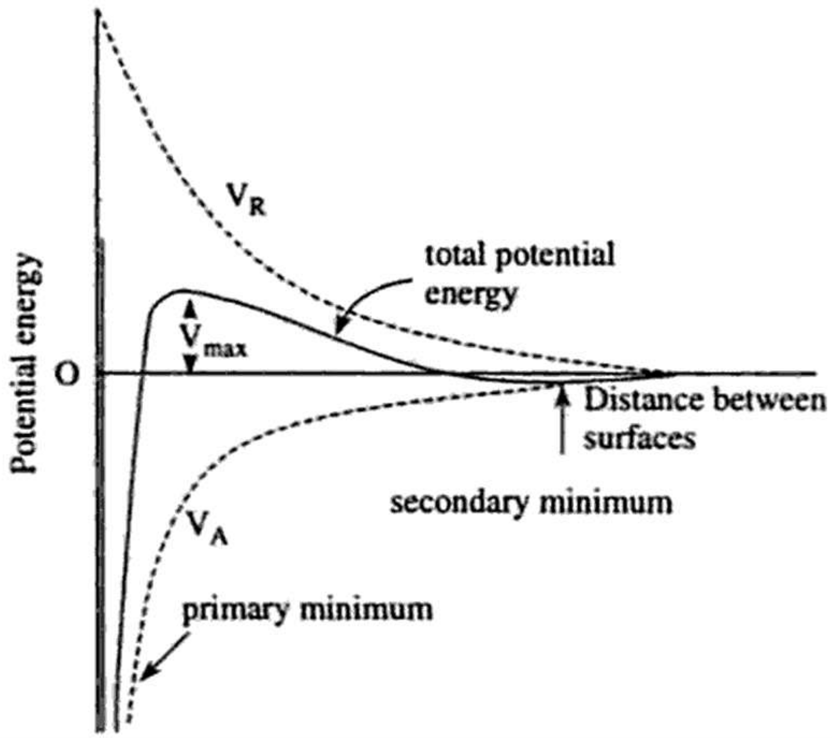

Figure 1.3: Graph showing the shape of the potential given by DLVO theory. The graph clearly shows the attractive van der Waals potential V_A and the repulsive electrostatic potential V_R combining to give a net potential. The primary minimum is the energy minimum which occurs when particles are aggregated. Changes in chemical context may in certain circumstances lower this energy barrier sufficiently that shear forces or even spontaneous diffusion could cause the particles to disaggregate. The secondary minimum is a stable distance at which it is energetically favourable for particles to remain, though it is not always present for every combination of particles and electrolytes. In systems in which a secondary minimum is present, it can render it energetically favourable for particles to form weak associations with each other in a process called ‘flocculation’, as distinct from ‘aggregation’. Flocculation can lead to aggregation further down the line. The potential which must be overcome in order for aggregation to occur is marked as V_{max}. This image is reproduced from [132]

a real-world scenario. A more rigorous and widely applicable equation is given by Equation (1.2)

$$m_r = \frac{1}{\gamma n_{\text{dom}}} \cong C_d f_d(\beta) \frac{Ae^6 z_1^6}{D_e^3 (k_B T)^5} \tag{1.2}$$

where A is the van der Waals constant, e is the electronic charge, γ is the concentration of the electrolyte in mol.cm^{-3}, n_{dom} is the number of dominating ions in one molecule, D is the dielectric constant, k_B is the Boltzmann constant, β is the ratio of the valency of the auxilliary ion z_2 to the dominating ion z_1, C_d is a constant, and $f_d(\beta)$ is a function of the 'asymmetry of the electrolyte' such that $f_d(1) = 1$, and $f_d(\beta) \approx 1$. m_r is the reciprocal concentration of the dominating ion in the solution. The 'dominating', or 'potential-determining' ions are those which have the greatest effect upon the surface potential of the nanoparticles, which in dilute aqueous solutions is are usually H$^+$ and OH$^-$ ions [133]. Auxiliary ions are those which create the electrical double layer (EDL) around the surfaces of the particles, and can typically include all the ions in solution of opposing charge to the dominating ions.

However, the derivation of these equations relies upon a number of key assumptions. Firstly, it assumes that the energy barrier between particles remains constant regardless of whether it is a single particle or a large aggregate. This is a reasonable assumption for larger particles for which the ionic atmosphere is small compared to the radius of the particle, but for smaller particles this is not necessarily the case.

Another important assumption made is the neglect of Brownian motion. This is important because should a particle be moving under the influence of Brownian motion, it will possess kinetic energy. This will effectively decrease the energy barrier between particles, in theory making it easier for them to aggregate. However, the effect can be shown via the Stokes-Einstein relation [134, 135]

$$D = \frac{k_B T}{6\pi\eta r_h} \tag{1.3}$$

to scale with r_h^2 such that the larger particles find their energy barriers decreased by significantly more than smaller particles, suggesting that aggregation may occur in more of a cascade-like exponential manner – the further it has proceeded, the greater its propensity to continue. This is because the Stokes-Einstein equation scales as $\frac{1}{r_h}$, meaning larger particles will diffuse more slowly, kinetic energy scales with mass, and mass scales as r^3, leaving the second-power relationship. The variables are as follows: D is diffusivity, k_B is the Boltzmann constant, T is the absolute temperature, η is the viscosity of the fluid, and r_h is the sphere-equivalent hydrodynamic radius. This r_h^2 dependence comes from the fact that the diffusion coefficient is actually an expression of the area a particle will diffuse through per unit time. Converting this to a mean linear velocity But this comparison relies on a few assumptions of its own.

Firstly, that the Stokes-Einstein relation is a good approximation in these circumstances, and secondly and most importantly, that the hydrodynamic radius in the Stokes-Einstein relation may be used interchangeably with the radius of curvature of a sphere-equivalent particle. Additional theoretical work would be required to determine whether this is a relevant effect in these circumstances.

The third major assumption that DLVO theory appears to rely upon is the approximation of the interaction of spherical particles. The theory itself is derived for a pair of infinite flat plates separated by a uniform layer of electrolyte, and this effect is mapped onto a pair of spherical particles using Equation (1.4)

$$N_d = G_d \int_H^\infty R\left(h\right) \mathrm{d}h \tag{1.4}$$

where $R\left(h\right)$ is the repulsion per unit area of parallel plates separated by h, H is the smallest seperation of the curved surfaces, N_d is the repulsive force of the curved surfaces, and G_d is a factor that relates the shape and spatial orientation of the particles to the electric field curvature, and in DLVO theory is assumed to be described by $G_d = \pi r_h$. This is an approximation that only holds for large r_h, such that $x_i r_h \gg 1$ and $\frac{r_h}{H} \gg 1$, where x_i is the reciprocal of the thickness of the ionic atmosphere. Additional calculation would be required to determine precisely what corrections are required to this assumption to extend it for smaller values of r_h.

Furthermore, it is pointed out by Grasso et al [136] that DLVO theory also fails to account for effects like hydrogen bonding and steric interactions, both of which are highly relevant for the analysis of aggregating nanoparticle systems. There are also certain known systems which DLVO theory completely fails to describe the behaviour of [137]

To conclude, DLVO theory requires a large number of variables, has many shortcomings (including an inability to describe certain systems directly[1]), and cannot describe the actual mechanism of attachment (for example, some aggregates can be observed under TEM to have sintered together, while others remain loosely bound [138]).

1.3.3.2 Aggregate structures

Aggregation rates principally have two limiting factors 'diffusion' and 'reaction'. When one or other of them is limiting the rate of aggregation, the process is referred to as 'diffusion-limited aggregation' [139] or 'reaction-limited aggregation' [140]. Diffusion-limited aggregation is the fast limit of aggregation, where the attachment efficiency is 1. This means that every

---

[1] Though various additions – 'extended DLVO' – theories have been developed to attempt to include additional capability to classical DLVO theory.

single collision between particles results in an aggregation event, and the rate of aggregation is completely controlled by the collision rate or diffusion rate of the particles – the larger their diffusion coefficients, the more frequently they will collide [141]. Reaction-limited aggregation is the slow limit of aggregation [142], where the attachment efficiency approaches zero. This means that the majority of collision events do not result in aggregation [143].

Aggregation rates may be estimated from a combination of the attachment efficiency and the 'single collector contact efficiency'. The single collector contact efficiency is effectively the rate of impact of particles with a surface of unit area (the 'single collector'). Once it is known at what rate collisions between particles occur and what the probability of adhesion on contact (the attachment efficiency) is, then it is trivial to take the product and calculate the number of successful aggregation events per unit time, or the aggregation rate. Aggregation rates are usually only given as the rate of primary particle-primary particle aggregation, as aggregation rates for larger compound particles is strongly dependent upon the structure of the aggregates being formed. However, here a more complex model is considered, because for the calculation of the mass of particles constituting an aggregate, some knowledge of the density or porosity of the aggregates is necessary.

It has been shown that for diffusion-limited aggregation, the fractal dimension of an aggregate is approximately 1.7, while for a more compact and slowly created reaction-limited case, a fractal dimension D_f approaching 2.3 is more typical (Figure 1.4) [144]. Thereby, a zero-order approximation to the fractal dimension of an unknown aggregate which is known to be neither diffusion- or reaction-limited is about 2. Equation (1.5)

$$n_{\text{col}} = \left(\frac{r_h}{r_0}\right)^{D_f} \tag{1.5}$$

where n_{col} is the mean number of particles in an aggregate, and hence the number of successful collisions per particle that need to have occurred, r_h is the aggregate hydrodynamic radius, and r_0 is the radius of the primary particles prior to aggregation, allows the number of particles in an aggregate to be estimated.

The number of collisions that did occur during the same period may be calculated using the mean free path, in Eqn (1.6)

$$\lambda_f = \frac{1}{\sqrt{2}n_p\sigma} \tag{1.6}$$

for particles whose velocities follow a Maxwell distribution[2], where λ_f is the mean free path in metres, n_p is the particle concentration, and σ is the collision cross-section. The collision cross-section is the cross-sectional area that one particle's centre must traverse in order to

---

[2] The statistical distribution which describes the motion of dilute particles in thermal equilibrium [145].

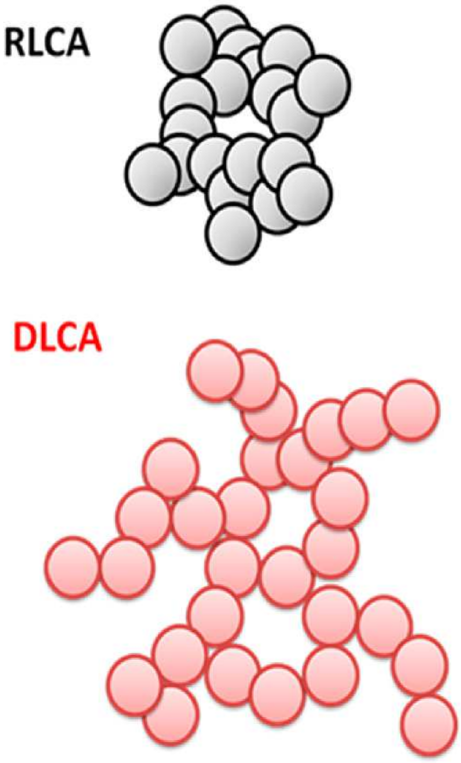

Figure 1.4: Diagram showing the difference in structure between structures which typically arises from diffusion-limited aggregation (labelled DLCA), and reaction-limited aggregation (Labelled RLCA). Figure reproduced from [144].

collide with another particle.

When combined with a mean linear velocity from Equation (1.7) [146]

$$\bar{v} = \sqrt{\frac{2k_BT}{6\pi\eta r}} \tag{1.7}$$

it can yield a mean rate of collisions per particle in the sample suspension. Hence, for a given size of aggregate over a given time interval, it is possible to compare the rate of collisions that occur to the rate of collisions that need to be successful in order to achieve the requisite aggregate size for a given fractal dimension. This process is summarised in Eqn (1.8)

$$\alpha_e = \frac{\left(\frac{r_h}{r_0}\right)^D}{\left(4n_pt_{\text{tot}}\sqrt{\frac{2k_BT\pi r_h^3}{3\eta}}\right)} \tag{1.8}$$

where t_{tot} is the duration for which aggregation has been allowed to occur, η is the viscosity of the matrix, T is the temperature at which aggregation occurred, k_B is the Boltzmann Constant, α_e is the attachment efficiency and all other variables are as previously defined.

If TEM images could be used to confirm that the relationship between fractal dimension and aggregation mode is sufficiently strong, it would be possible to map the attachment efficiency directly onto a fractal dimension. Should the relationship work, this new fractal dimension could be fed back into the equation to generate a higher-order estimate for the fractal dimension of the aggregate. This would be trivial to iterate over until the change in fractal dimension between iterations is small compared to the error margin associated with the correlation of attachment efficiency and fractal dimension.

An alternative means of calculating the attachment efficiency is to consider the rate of loss of primary particles rather than the rate of formation of the largest aggregates at the end. This has the benefit of allowing the collision rate to decrease as a function of time as the number of particles decreases, but doesn't fully allow for the increase in the collision cross-section as particles grow. Using this approach, a comparable means of calculating the attachment efficiency may be derived, though this would have to wait for future work.

A challenge presented by the measuremet of aggregation is the capability of a given measurement technique to detect aggregated dimers – it is mathematically obvious that an increase in hydrodynamic diameter of ≈28 % occurs as a result of a single aggregation of two spherical particles (Table 1.1). However, even populations of nominally homogenous particles contain a distribution of particle sizes; there will be a variation of typically ±20 % for smaller particles. Consequently, should 2 nominally 10 nm particles, whose actual diameter happened to be 8 nm, aggregate, then the mean hydrodynamic diameter of the aggregate would be 10.24 nm, significantly smaller than the largest expected particles in the original sample. For larger particles, the variance will be smaller as a fraction of particle size, and so the overlap between the size of a possible small aggregate and the size of a possible large particle contunies up to a particle size variation of just over ±10 %. However, even in this case the two peaks would be sufficiently close that it would require not inconsiderable statistical analysis to differentiate the two peaks. Factoring in the broadening of distributions inherent in the NTA technique [147], it is entirely possible that even particles exhibiting a variation in diameter of ±5% could become indistinguishable from their dimers.

Number of Particles	Mean Relative Sphere-Equivalent Hydrodynamic Diameter
1	1
2	1.28
3	1.50
4	1.66
5	1.79

Table 1.1: Mean relative hydrodynamic diameter of all possible aggregation shapes for a given number of particles. This assumes that all possible n-particle shapes occur with equal frequency. The precise method by which this was estimated is given in Appendix A

1.3.4 Light scattering

The interaction of light with small particles (a term which will be used generically for particles whose size is small compared to the wavelength of visible light) is well understood, and can be explained by several theories of increasing complexity. Those relevant to the light-scattering experiments described later are described below.

1.3.4.1 Rayleigh scattering

Rayleigh scattering is a sub diffraction-limit optical phenomenon that has been known about for many years [148], and exploited for many applications, including nanoparticle measurement [149]; weather radar [150]; paint [151], glass [8], and ceramic pigmentation [152].

Rayleigh scattering is one of the most basic descriptions of the scattering of light by small particles, though it is perfectly adequate for many applications when the conditions outlined later in this section are met. In general, it is a good description of the light-scattering behaviour of particles for which the radius is significantly smaller than the wavelength of illumination. The exact cut-off for the validity of the approach is still a disputed matter, with various estimates ranging from $\frac{2r}{\lambda} \leqslant 0.05$ [153] to $n_a k_0 r \ll 1$ [154], where n_a is the relative refractive index, k_0 is the wavenumber of the illumination, λ is the corresponding wavelength, and r is the radius of the particle . For larger particles (or shorter wavelengths) then Mie scattering is more accurate (see Section 1.3.4.2).

A basic mathematical description of Rayleigh scattering is given in Equation (1.9)

$$I = I_0 \frac{16\pi^4 r^6}{R^2 \lambda^4} \left(\frac{m^2 - 1}{m^2 + 2} \right)^2 \sin^2(\phi) \tag{1.9}$$

where $m = \frac{n_{a2}}{n_{a_1}}$; n_{a_1} is the refractive index of the particles and n_{a_2} is the refractive index of the suspending medium. ϕ is the scattering angle, I is the scattered intensity, and I_0 is the incident intensity. R is the distance from which the observation was made (i.e. the scattered light follows the standard $\frac{1}{R^2}$ falloff with distance), and r is the radius of the particles.

Thus it can be seen that the scattering efficiency is strongly dependent upon the radius of the scatterer, scaling as r^6. This is important when considering optical measurement techniques, as will be outlined later. It can also be seen that there is a strong inverse dependence $\left(\frac{1}{\lambda^4}\right)$ upon illuminating wavelength – shorter wavelengths will result in far more efficient scattering. This will also be used later.

Of significant importance for Chapter 5 is the origin of this theory. While a full derivation is not given here (one is available in [155]), it relies upon the assumption that the scatterers are significantly smaller than the wavelength of electromagnetic radiation illuminating them. Then, as the wave propagates past them, the scatterers experience an oscillating electric field which is of approximately constant magnitude across the entire scatterer. The effect of this upon the electrons in the scatterer is to periodically accelerate them back and forth in step with the oscillations of the electric field. This acceleration of the charged particles itself emits radiation of a frequency corresponding to the frequency of oscillation, and therefore to the frequency of the illuminating radiation. The efficiency with which this scattering mechanism works depends upon the number of electrons in the scatterer which may be influenced by the oscillating field, and the degree to which these electrons are free to move (how easily polarisable the particle is). These two quantities are captured by the use of the refractive index in the Rayleigh equation.

One more important thing to note is the $\sin^2(\phi)$ term. This dictates that scattering efficiency will be maximal perpendicular to the direction of illumination. Again, this aspect of the Rayleigh scattering phenomenon will be used later.

A full derivation of this is given in one of Rayleigh's original papers [155], and considerable further discourse on the matter by Kerker [153].

1.3.4.2 Mie Scattering

Mie scattering is another commonly-used description of the light-scattering behaviour of spherical particles of arbitrary sizes, including those described by the Rayleigh approximation. Mie scattering is considerably more mathematically complex, and so only some key results are quoted here. For these purposes, the scattering efficiency Q is one of the most important results. This is given in Equation (1.10)

$$Q = \left(\frac{2\pi}{k_{\text{medium}}^2}\right) \sum_{n=1}^{\infty} (2n+1) \Re\left(a_n + b_n\right) \tag{1.10}$$

where

$$a_n = \frac{\mu m^2 j_n\left(m x_m\right)\left[x_m k_n\left(x_m\right)\right]' - \mu_1 j_n\left(x_m\right)\left[m x_m j_n\left(m x_m\right)\right]'}{\mu m^2 j_n\left(m x_m\right)\left[x_m h_n^{(1)}\left(x_m\right)\right]' - \mu_1 h_n^{(1)}\left(x_m\right)\left[m x_m j_n\left(m x_m\right)\right]'} \tag{1.11}$$

$$b_n = \frac{\mu_1 j_n\left(m x_m\right)\left[x_m j_n\left(x_m\right)\right]' - \mu j_n\left(x_m\right)\left[m x_m j_n\left(m x_m\right)\right]'}{\mu_1 j_n\left(m x_m\right)\left[x_m h_n^{(1)}\left(x_m\right)\right]' - \mu h_n^{(1)}\left[m x j_n\left(m x\right)\right]'} \tag{1.12}$$

$$k_{\text{medium}} = \frac{2\pi n_{\text{medium}}}{\lambda_0} \tag{1.13}$$

The j_n are the spherical Bessel functions of the first kind, h_n are the spherical Hankel functions, m is the relative refractive index, $x_m = k_{\text{medium}} r_p$, and μ and μ_1 are the permeabilities of the particle and the suspending medium respectively. Primes denote derivatives with respect to x_m. These results may be found in publications by Cox and van de Hulst [154,156].

In contrast to the Rayleigh approximation, the dependency of the scattering efficiency on the illuminating wavelength and the particle size in Mie scattering is not explicit, and is in fact dependent upon the value of the n^{th} Bessel function and the n^{th} Hankel function. Another significant difference between the predictions of Rayleigh and Mie scattering is that the Rayleigh approximation always predicts that scattering is maximal perpendicular to the illumination. However, Mie scattering predicts that as the size of the scatterer increases, the angle of maximal scattering will tend towards the forward direction. This is important when attempting to capture light scattered by scatterers within certain size ranges – the smallest scatterers will scatter most strongly perpendicularly, so may be effectively excluded by capturing light from a slightly larger angle.

When the results of the Mie solution are compared with the results given by the Rayleigh approximation, it turns out that even significantly beyond the accepted region of applicability for the Rayleigh approximation, the Rayleigh approximation can give a very useful estimate of the scattering behaviour in a far more mathematically elegant way – in order to calculate a Mie scattering efficiency[3], it is necessary to make use of a computer to calculate the convergence of the infinite summation, while calculating a Rayleigh scattering efficiency is a single quick calculation which may be accomplished analytically. This will be demonstrated in Chapter 5.

1.4 Measurement of nanoparticles

A key consideration when conducting any investigation into nanoparticles, whether in the laboratory or in the wider environment, is the nano-metrology of the particles. There are a variety of different metrology techniques available, a brief introduction to some of the most important and widely-used of these is given below.

1.4.1 Electron microscopy

Electron microscopy in its various forms is usually considered to be the gold standard for measurement of ENPs because it allows accurate and reproducible direct measurements of the physical sizes of particles [157], while competing techniques only indirectly infer the size. Some of the most salient considerations pertaining to the use of electron microscopy are recounted below.

---

[3] 'Scattering efficiency' is defined as the fraction of incident light of a given frequency which is scattered, often at a particular angle.

1.4.1.1 Scanning Electron Microscopy

Scanning electron microscopy is a frequently-used approach [29], and has the key advantage that relatively large sample volumes can be processed quickly. In SEM imaging, an electron probe scans across the surface of the sample, and the electrons which are scattered are recorded and used to generate an image. Two different types of scattered electrons are typically generated: 'backscattered' electrons, which scatter off the surface of the sample, and 'secondary electrons' which are dislodged from the surface by the incident electrons (Figure 1.5). Typical resolution for modern SEM systems can be down to about 1nm in ideal conditions [158], though many systems still in frequent use are much older models with corresponsingly lower resolution. Two uses/developments of SEM are of particular note for the purposes of measuring ENPs in an environmentally relevant context. Atmospheric SEM, in which the sample itself is held at a low vacuum while differential pumping techniques maintain other parts of the microscope at appropriately higher vacuum, allows particles to be directly imaged in liquid suspensions [159]. This technique is reported to only permit detection of relatively large particles [160]. Other competing implementations of this include the use of sealed sample-filled capsules with silicon nitride windows to permit the electrons through. The trade-off is that these images tend to be less sharp than those captured using more conventional SEM approaches [161]. Single-particle tracking of liquid-suspended ENPs in real-time using SEM has been achieved, though this has only been shown to be possible in non-volatile ionic liquids, and is therefore not directly applicable to environmental measurement [162].

SEM can also be used together with electron spectroscopy techniques to probe for the presence of certain elements. Coupled with the relatively large samples which can be analysed, this allows for screening of natural material for the presence of build-ups of materials commonly used in ENPs. Images at this resolution are typically not suitable for analysing the size and shape of the particles, but are only indirectly capable of inferring the presence of ENPs – other possible causes for small masses of these materials must be neglected [163].

1.4.1.2 Transmission Electron Microscopy

Transmission electron microscopy is typically capable of achieving very much better spatial resolution than SEM; typical new microscopes have a spatial resolution of down to 0.1 nm or better [164]. While SEM depends upon the scanning of an electron probe across a sample, TEM instead uses a wider beam which illuminates the entire sample. STEM instead uses a scanning probe similar to SEM, which is slower but carries many of the advantages of SEM over to TEM [165]. The higher resolution of TEM allows it to be used for far more accurate

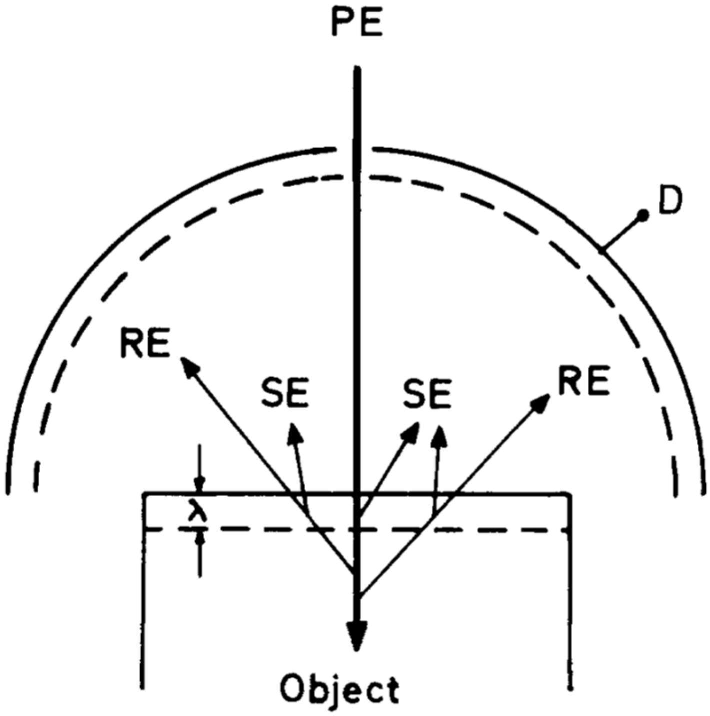

Figure 1.5: Diagram showing scanning electron microscope function. PE denotes primary (incident) electrons, RE denotes the 'reflected' (backscattered) electrons, and SE denotes the secondary electrons. Diagram taken from [157].

determination of shapes and sizes of nanoparticles. A camera placed behind the sample records the transmitted electrons. Because contrast in TEM images requires electrons to be deflected from the beam, under normal circumstances it is only suitable for the measurement of objects made from heavier elements (phase-contrast [166] notwithstanding, though phase contrast imaging techniques are not used in this thesis).

Owing to the high spatial resolution, TEM is the de-facto standard for measuring ENP sizes and shapes [161]. In common with SEM, there have been several important innovations which are relevant for environmental study of ENPs. One of the most significant is the development of liquid-cell TEM. This is usually done using a pair of silicon nitride plates with the sample sandwiched between them, though this can have a deleterious effect upon the resolution [167–169].

Another important innovation is environmental TEM. This is very similar to environmental SEM, and shares many of the benefits and drawbacks. One of the major differences is the need for a much higher vacuum in a TEM column than is usually present in an SEM. This is accounted for by the use of additional apertures between the sample area and the vacuum-sensitive parts of the TEM and the adoption of a very effective series of pumping stages [170, 171].

1.4.2 Single-particle ICP-MS, and associated hyphenated techniques

Single-particle inductively-coupled mass-spectrometry (spICP-MS) is a development of the ICP-MS concept to allow for detection and classification of single ENPs) [172]. This technique is very widely-used for environmental ENP measurements [103, 173, 174]. Ordinarily, ICP-MS uses an inductively-coupled plasma flare as an ionisation stage for a mass spectrometer (MS). The MS stage can then scan through a range of mass-to-charge ratios and produce a picture of the entire contents of the sample [175].

In single-particle operation, the ICP-MS setup is a little different – the MS is typically set to only detect a single mass-to-charge ratio which corresponds to the expected composition of the ENPs to be analysed [176]. The dwell time on the system is shortened as much as is practical for the MS without raising the noise sufficiently to obscure or obfuscate the signals relating to ENPs, and the input sample is diluted sufficiently that there is a low probability of several ENPs travelling through the system simultaneously [117]. With careful tuning, this should enable the individual particles to be detected as short peaks in the appropriate mass-to-charge ratio over time. The exact sizes of these peaks may be used to determine the approximate size of these particles [177]. For gold or silver ENPs, spICP-MS is reported to be reliable down to particle sizes of 15 nm [178]. Because the standard system only considers a single isotope at a time, it is largely impervious to interference from natural nanoparticles. This does mean, however, that it cannot directly yield useful information about heteroaggregation and heteroaggregates. Aggregation is discussed in more detail in Section 1.3.3.

There are many further additions to this system which can enable more in depth analysis, analysis of samples with different characteristics – less homogenous samples for example – by the addition of further stages. These are often referred to as 'hyphenated techniques', because while none of the technology is necessarily new, the particular combination of techniques may well be novel. For example, an sp-ICP-MS setup may sometimes include aysmmetric flow field flow fractionation (AF_4) equipment to 'preprocess' the particles to select for particular size fractions. AF_4 is based on the principle that small particles experience less drag than larger particles; thereby a vessel with a flow gradient may be used to draw the larger particles away from the smaller particles [95, 179–181]. Another example is the inclusion of tandem MS units (spICP-MS/MS). The use of tandem MS units allows for much better detection of trace elements due to far better rejection of contaminants with similar mass:charge ratios [182].

Finally, a key recent development is the use of time-of-flight apparatus. This optimisation overcomes the specific limitation that usually sp-ICP-MS is only capable of measuring a single element at a time, leveraging the capabilities of ICP-TOFMS [183–185]. Time-of-flight capability can allow for more than one element or isotope to be measured simultaneously [186], allowing composition or isotopic ratios to be obtained [176]. Praetorius et al [176] have used spICP-TOFMS recently to determine isotopic ratios of lanthanide nanoparticles, allowing naturally-occurring particles to be differentiated from engineered anthropogenic particles.

Many other hyphenated techniques are available, and some have applications to measurement of ENPs in the environment [187,188]. There is no reason why many of these hyphenated techniques may not be used in conjunction with other techniques described herein, though such integration is uncommon. One example is the coupling of AF_4 to a multi-angle light-scattering system [189].

As an associated hyphenated technique, hydrodynamic chromatography (HDC) is of particular note. A development of the familiar concept of chromatography, rather than achieving separation based upon relative solubility in the mobile and stationary phases the separation is based upon the hydrodynamic diameters of the particles. The principle was first reported in 1967 when Haller [190] successfully separated viruses on a porous glass plate by hydrodynamic size. This was further developed into a more generic method for the sizing of suspended colloidal particles by Small [191] in 1974. While early implementations were large pieces of equipment (Figure 1.6), some more recent implementations of the HDC paradigm have successfully miniaturised the equipment by replacing the column with cappilaries [192] to the point that such apparatus may now be fitted to a microfluidic chip [193,194].

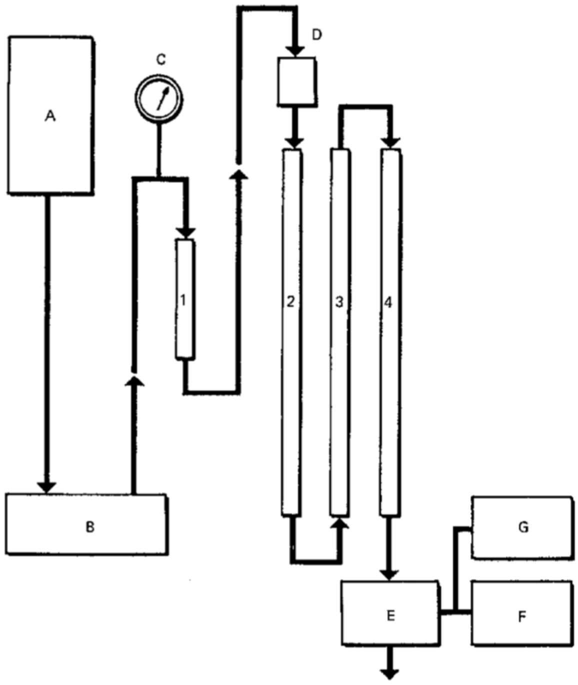

Figure 1.6: Diagram of typical hydrodynamic chromatography equipment. Labels are as follows: A – reservoir, B – pump, C – pressure gauge, D – sample injection valve, E – detector, F – recorder, G – computer. Diagram reproduced from [191].

In hydrodynamic chromatography, the analogue of the 'stationary phase' is a bed usually made from a collection of solid non-soluble beads. The 'mobile phase' is a liquid, frequently water, though other solvents may also be used [191]. As the mobile phase and sample are pumped through the stationary phase, those particles with larger hydrodynamic radii will experience greater drag and will therefore be drawn through the column faster than those particles with smaller radii and therefore lower drag coefficients. The gaps between the beads behave like a network of capillaries, such that the voids contain very high flow rate gradients are formed. In this way, the principle of operation is very similar to AF_4 [195].

HDC has been used for many different studies, including investigation of the fate of nanosilver in sewage sludge [187,188], characterisation of gold nanoparticle mixtures [196], analysis of polymer latexes [197], and various other macromolecules [198].

1.4.3 Dynamic light scattering

Dynamic light scattering (DLS) [146], sometimes also referred to as photon correlation spectroscopy (PCS), uses coherent (usually laser) illumination of the sample. Electrophoretic light scattering (ELS) is a derivative technique which uses an electric field to measure the zeta-potential (effective surface charge) of the particles at the same time as the size measurement [199–201]. The basic experimental setup (Figure 1.7) is fundamentally similar to many other light-scattering implementations, and consists of a polarised monochromatic light-source, a sample cell, and a photo-detector or photocell. In more archaic configurations, the photocell would be replaced with an autocorrelator.

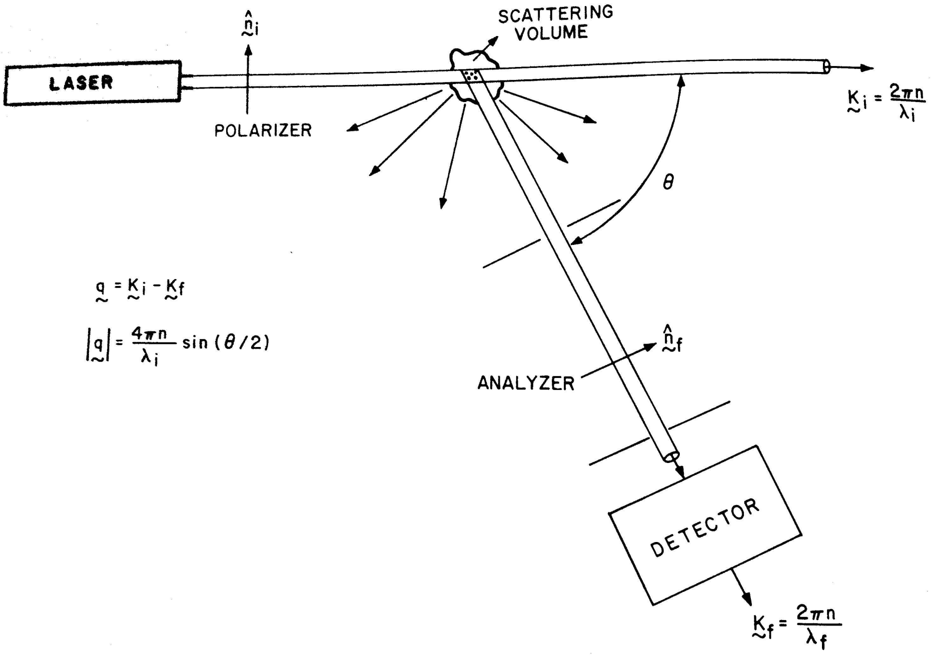

Figure 1.7: Diagram of typical multi-angle DLS experimental configuration. Diagram reproduced from [146].

The technique depends upon the measurement of the rate of intensity fluctuation of scattered light. This fluctuation is digitally recorded, and then the autocorrelation of the signal is taken. A graph showing an example of this time-dependent fluctuation is given in Figure 1.8.

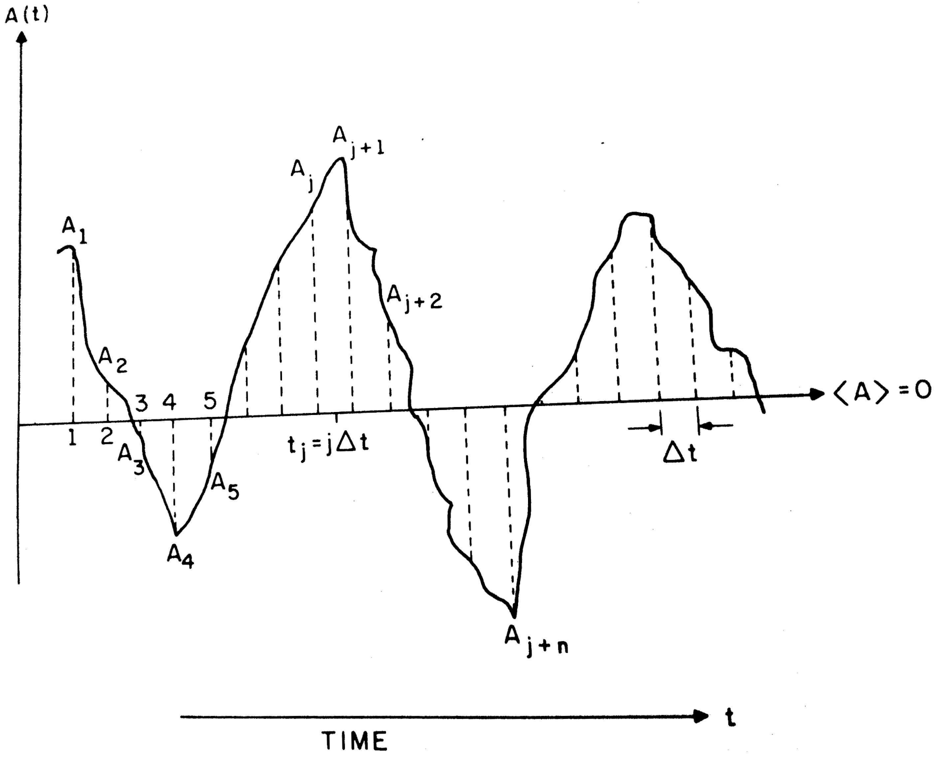

Figure 1.8: Exemplar plot showing the fluctuation in intensity of scattered light recorded for DLS measurement, of the type which could be obtained using the apparatus shown in Figure 1.7. Image reproduced from [202].

Autocorrelation is a technique in signal processing which examines the similarity between different regions in a pair of functions. Autocorrelation is a special case of cross-correlation. The mathematical definition of a cross-correlation of two functions, $f(t)$ and $g(t)$, is given in Equation (1.14) [203]

$$(f \star g)(\tau) = \int_{-\infty}^{\infty} f^*(t)\, g(t-\tau)\, \mathrm{d}t \tag{1.14}$$

$f^*(t)$ is the complex conjugate of $f(t)$, and τ is commonly referred to as the 'lag'. This form of the equation is strictly for use on continuous functions; for the discrete time-quantised functions recorded from DLS experiments it is necessary to consider the integral as a summation over all measured values of t.

Autocorrelation is the special case in which $f(t) = g(t)$. Then at time $t = 0$, the autocorrelation will be maximal – $f(t)$ correlates with itself perfectly and has no lag ($\tau = 0$). However, as we continue to evaluate the autocorrelation function for $t \neq 0$, τ may adjusted such that $0 \leqslant \tau \leqslant t$. In this way, the autocorrelation function is effectively correlating every datapoint between $f(0)$ and $f(\tau)$ with $f(t)$. As t increases, the autocorrelation should decay as the configuration of particles scattering light changes due to the random motion of the particles. The rate at which the configuration of particles changes is related to the rate at which they diffuse via Brownian motion, and therefore the hydrodynamic size of the particles. Thereby, the rate of decay in the calculated autocorrelation function is directly related to the sphere-equivalent hydrodynamic diameter of the measured particles.

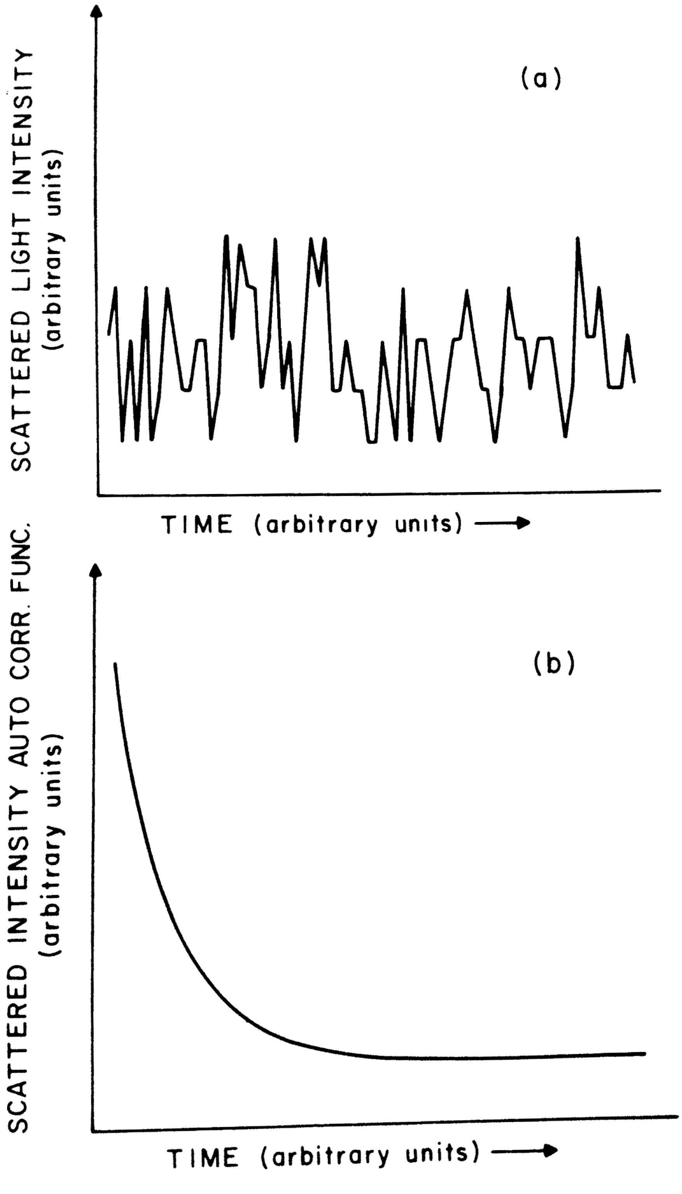

Figure 1.9: Plot showing a) an exemplar time-dependent intensity fluctuation of the type shown in Figure 1.8, and b) the autocorrelation of this fluctuation, showing the decay of autocorrelation with time. Figure reproduced from [146].

Each differently-sized particle in a sample will be diffusing at a different rate, and will therefore be contributing a term to the decay. Thus the decay can be expressed as given in Equation (1.15)

$$I\left(t\right) = \sum_i a_i \exp\left[\frac{-t}{\tau_i}\right] \tag{1.15}$$

where the a_i are the relative abundances of the populations of particles and the τ_i are the characteristic times associated with those populations which have been derived from the autorrelation series [146]. In this case, characteristic times are proportional to the inverse of the diffusion rate.

In the case that the sample being analysed is monodisperse, then there will be a single characteristic time which it is simple to extract by fitting an exponential to the decay function. However, in polydisperse suspensions, each particle or population of identical particles will be contributing an exponential term to this sum, assuming there are i different populations. Each of these decays has a characteristic time, τ_i, and these times are directly related to the diffusion rate, which in turn is related to the sphere-equivalent hydrodynamic diameter of the particles.

Obviously, it is challenging to analytically separate a sum of exponential decays. It is possible to do this numerically, provided the characteristic times of the different exponentials are sufficiently different, and that the relative magnitudes of the a_i are such that no single decay dominates. This analysis may be accomplished using the CONTIN algorithm developed by Stephen Provencher in Fortran, though an open-source Matlab version is now also available. [204–207]. Each characteristic time returned by the algorithm may then be fed into the calculation of the sphere-equivalent hydrodynamic diameters of the particles.

One problem with DLS that should be easy to appreciate is that it is incapable of differentiating between intensity fluctuations caused by the changing of particle configurations and the intensity fluctuations caused by the rotating of aspherical particles. Thence, should a sample of aspherical particles be measured, the additional fluctuations will either be interpreted by the algorithm as evidence of an additional population of particles with a different hydrodynamic diameter, or just as a single population but with a grossly skewed and unrepresentative hydrodynamic diameter. Some modern systems include the ability to correct for this if the aspect ratio of the particles is input into the system, though this does somewhat defeat the object of making measurements of unknown samples.

Another limitation of DLS is that larger particles will scatter light significantly more efficiently than smaller particles, as is shown in Section 1.3.4.1. Using the Rayleigh approximation, it has been shown that the scattering efficiency of a small particle scales as the 6th power of the radius, i.e. a particle of 20 nm diameter would appear to be 64 times as bright as a particle of 10 nm. This makes it very easy for larger particles to completely mask any signal being generated by smaller particles in the same sample – this masking is commonly referred to in the literature as ‘poisoning’. Some commercial DLS systems add the capability to take data at a range of scattering angles though cheaper commercial solutions will tend to rely upon a fixed angle of $\frac{\pi}{2}$. This variable-angle capability can help in the remediation of the problem of poisoning by large particles [208,209].

DLS also requires the use of samples sufficiently dilute that no multiple scattering occurs – allowing multiple scattering increases the rate at which configurations appear to change because there are intrinsically many more n-particle configurations possible than there are 1-particle configurations. The technique has been extended to account for this in a more recent approach which has been dubbed ‘diffusing-wave spectroscopy’ (DWS) [210].

These things make DLS a very useful technique for rapid low-cost characterisation of ENPs which are known to be monodisperse and spherical. However, for the majority of size-measurement situations associated with the study of ENPs in the natural environment, it is an ill-suited technique due to its poor performace faced with polydisperse or non-spherical particles. This is not to say it isn’t widely used for this purpose [211–213].

DLS has been used in a range of nanoparticle behaviour studies, mainly involving measuring aggregation behaviour of nanoparticles [93,212,214], though more recently it appears to be being eclipsed in the peer-reviewed literature by some of the other techniques described here.

1.4.4 Differential dynamic microscopy

Differential dynamic microscopy (DDM) is closely related to DLS, in that it shares the use of the time-dependent variation in intensity of scattered light to determine the particle size. However, the two key differences are that DDM uses white-light illumination as opposed the the laser illumination of DLS, and DDM uses a high-speed camera[4] camera rather than a photodiode for data acquisition. This allows DDM to examine the light scattered at a range of scattering vectors, which is roughly equivalent to running a multi-angle DLS experiment but measuring several angles simultaneously [215]. DDM can function regardless of whether the objects being imaged are sufficiently large as to be independently-resolvable using an optical microscope [216,217].

More rigorously, DDM considers the differences between an initial frame and each subsequent frame. Thereby it builds up a stack of difference images, $|\text{frame}_2 - \text{frame}_1|$, $|\text{frame}_3 - \text{frame}_1|$... $|\text{frame}_n - \text{frame}_1|$. This may be repeated many times using different starting frames. These difference images are referred to as $D\left(x, y; \Delta t\right)$. We then define $\sigma^2\left(\Delta t\right)$ as the sum of the squares of all the pixels as shown in Equation (1.16).

$$\sigma^2\left(\Delta t\right) = \int \left|D\left(x, y; \Delta t\right)\right|^2 \mathrm{d}x\mathrm{d}y \tag{1.16}$$

If σ^2 is plotted as a function of Δt, it should increase from a small value to eventually

---

[4] The precise speed required depends upon the size of the particles being imaged – smaller particles diffuse faster and therefore require a faster camera.

plateau at a higher value. This represents an increase in difference from the initial frame to the point that any additional changes in a frame cause no discernible increase in difference. This is very useful for demonstrating that there is some information in the video file which may be extracted, but is not directly useful for extracting it.

By Parseval's theorem, which states that energy is conserved by a Fourier transform, it is possible to re-cast σ^2. This is shown in Equation (1.17)

$$\sigma^2\left(\Delta t\right) = \int \left|F_D\left(U_x, U_y; \Delta t\right)\right|^2 \mathrm{d}U_x \mathrm{d}U_y \tag{1.17}$$

given that F_D is the Fourier transform of D, and U_x and U_y are the co-ordinate axes in Fourier space.

Because on a sufficiently large length scale, the images captured are isotropic (or nearly so), it is then possible to calculate the 1-dimensional power spectrum[5] $\left|F_D\left(u; \Delta t\right)\right|^2$ given that $u = \sqrt{U_x^2 + U_y^2}$.

Using the substitution $q = 2\pi u$, a family of curves may then be plotted of $\left|F_D\left(q, \Delta t\right)\right|^2$ as a function of Δt, a different curve for each q. This is illustrated in Figure 1.10. Each of these curves will have two regions; the first is an exponential growth, and the second is a plateau at a particular value of $\left|F_D\left(q, \Delta t\right)\right|^2$. This exponential growth corresponds again to the decay in correlation between adjacent frames, but now it is possible to look at the decay of Fourier modes corresponding to particular scattering vectors.

It is of note that q may also be rewritten as a scattering vector, in the form

$$q = 2\pi \frac{\sin\left(\theta\right)}{\lambda_0} \tag{1.18}$$

where $k_0 = \frac{2\pi}{\lambda_0}$ and λ_0 is the wavelength of light.

Each mode decays with time as $\exp\left[\frac{-\Delta t}{\tau(q)}\right]$, with a characteristic time $\tau\left(q\right) = \frac{1}{D_m q^2}$, where D_m is the mass diffusion coefficient. Thereby we arrive at the relationship given in Equation (1.19).

$$\left|F_D\left(q; \Delta t\right)\right|^2 = A\left(q\right)\left[1 - \exp\left(\frac{-\Delta t}{\tau\left(q\right)}\right)\right] + B\left(q\right) \tag{1.19}$$

$B\left(q\right)$ is a theoretically constant term related to the power spectrum noise from the hardware. For a given value of q, $A\left(q\right)$ and $B\left(q\right)$ may be treated as fitting parameters, allowing the characteristic time $\tau\left(q\right)$ to be determined. It is then possible to work backwards and determine the diffusion coefficient corresponding to a given characteristic time, and

---

[5] The 1-dimensional power spectrum is the breakdown of the quantity of energy accounted for as a function of frequency, e.g. showing that at 1 Hz there are n W being transmitted, while at 2 Hz there may be $\frac{n}{2}$ W.

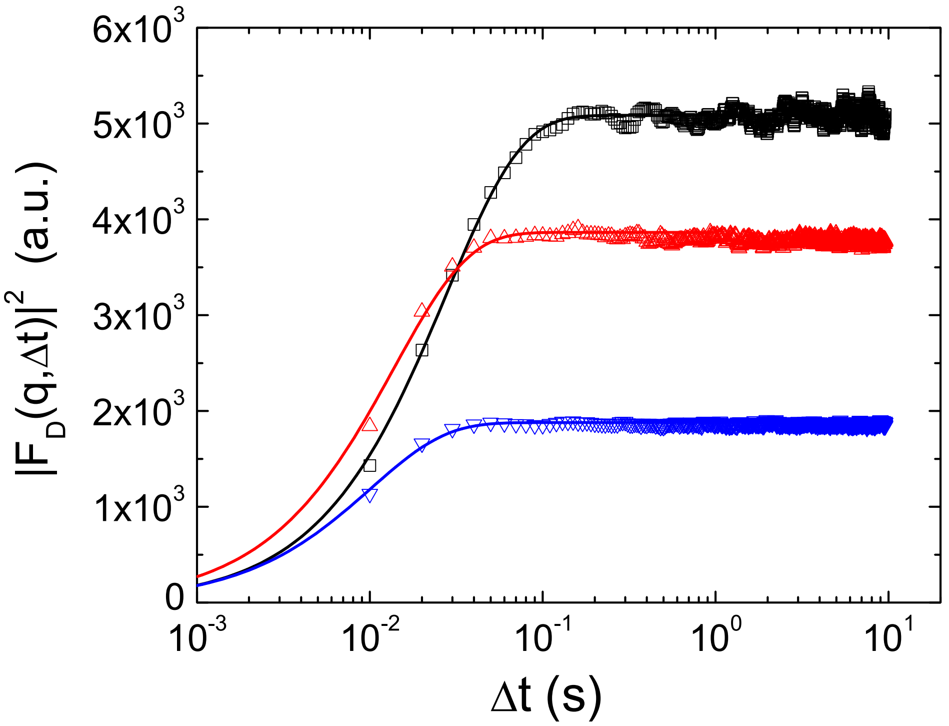

Figure 1.10: Plot showing $|F_D(q, \Delta t)|^2$ as a function of Δt for three different particle sizes. Note the differing rates of decay to differing values of $|F_D(q, \Delta t)|^2$ for differently-sized particles. Image reproduced from [216].

then with basic knowledge of the viscosity and temperature of the sample it is possible to calculate an approximate hydrodynamic diameter for the particles scattering at a particular wave-vector.

The information presented in this section, in addition to further details can be found in references [216–219].

The technique has been used for biological fluoresence analysis [220, 221], measuring motility of micro-organisms [215, 222, 223], investigation of the optical properties of janus particles [224], and the analysis of nanoparticle and protein dynamics [219, 225].

1.4.5 Nanoparticle tracking analysis

1.4.5.1 Principles of nanoparticle tracking analysis

Nanoparticle tracking analysis (NTA) is a third distinct use of light scattering to measure nanoparticles [149]. While DLS and DDM are ensemble techniques which gather data on a large number of particles simultaneously without being able to extract the effect of a single particle upon the result, NTA is a single-particle technique. NTA uses laser illumination and an ordinary microscope, allowing a video camera to be used to track the light scattered by individual particles (Figure 1.11). For a system with known magnification and pixel pitch, it is then possible to extract the diffusion coefficient and hence the hydrodynamic diameter of particles on a single-particle basis [149] using the Stokes-Einstein relation

$$D = \frac{k_B T}{6\pi\eta r_h} \tag{1.20}$$

where D is diffusion coefficient, k_B is the Boltzmann constant, T is the absolute temperature, η is the viscosity of the fluid, and r_h is the sphere-equivalent hydrodynamic radius. Clearly, this is excellent for the measurement of particles in the highly polydisperse samples which cause ensemble techniques the most difficulty.

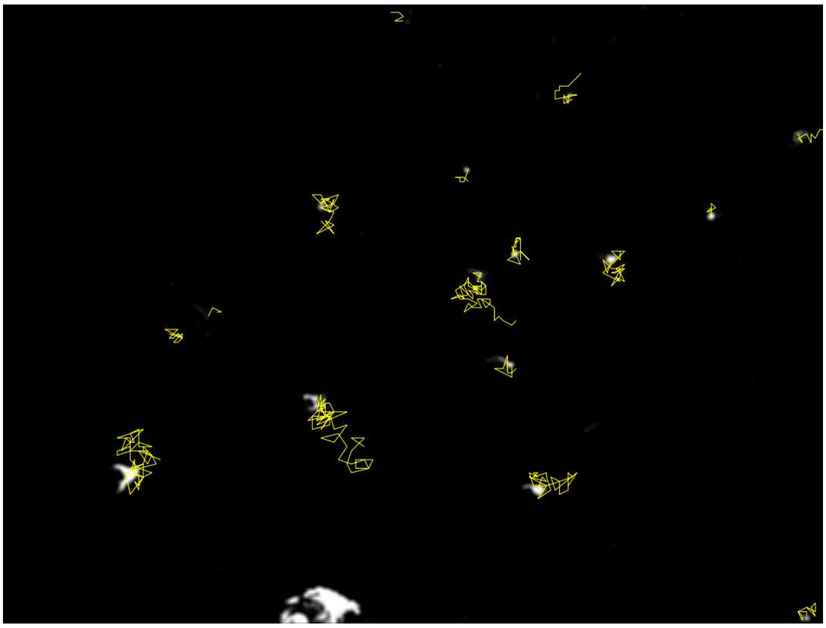

Figure 1.11: Illustration containing a frame of NTA image showing individual particles overlaid with their tracks. The image has been doctored to show several features of typical NTA operation: 1) Some particles are tracked for many frames, while others are only tracked for a small number 2) Sometimes objects that may correspond to noise in the system may be tracked for very short durations, and 3) Large artefacts (like the one shown centre-bottom) can frequently be interpreted by analysis software as more than one particle and therefore should not be tracked.

The basic apparatus necessary for taking NTA measurements is shown in Figure 1.12, though this neglects all the ancillary optics for beam delivery and imaging. The finer technical details of NTA apparatus are covered in greater detail in Chapter 3, along with a description of modifications which may be made to significantly improve the performance over currently available commercial systems.

This single-particle nature of the measurement means that there is very little poisoning effect from large, highly-scattering particles, and renders it far simpler to calculate a size distribution as opposed to a mean size. In the same vein, it is also possible to use NTA to determine the relative abundances of differently-sized particles with ease, as there is no inherent weighting in the system towards particles of one size or another [227].

NTA is also capable of making very limited differentiation between particles of differing

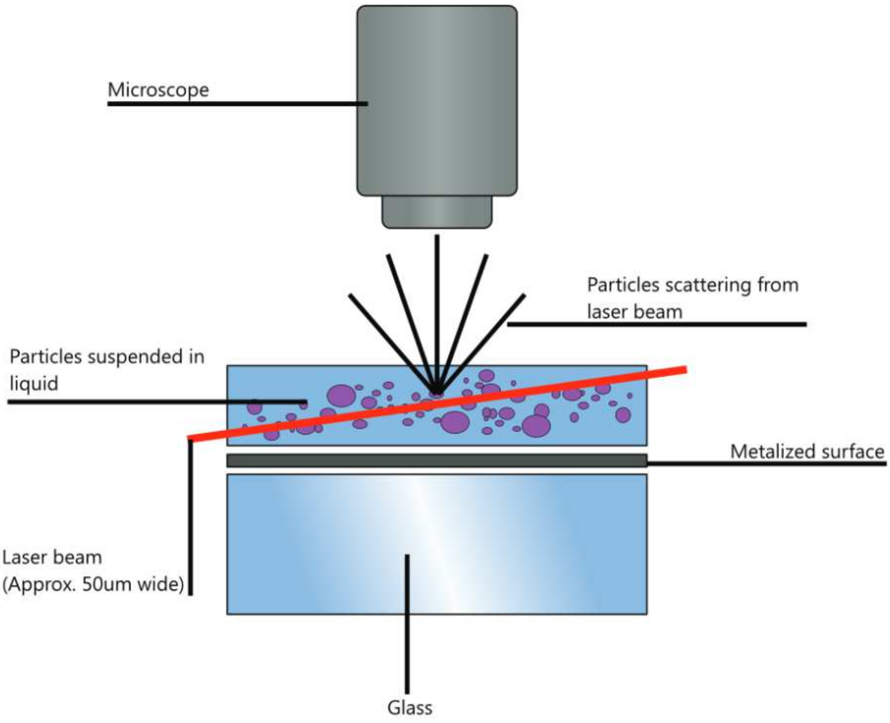

Figure 1.12: Basic schematic of a commercial piece of NTA apparatus. The glass with a metallised surface is unnecessary in general, but for this particular implementation it is technically essential. Image reproduced from [226].

composition by considering the ratio of the intensity of light scattered by a particle to the inferred hydrodynamic radius [67, 228]. The big disadvantage of this is that many particles will scatter the incident radiation in an extremely similar manner, indeed the difference in scattering power is linked more to the refractive index of the core material than it is to any possible surface effects of the particles. This makes it possible to differentiate easily between particles of latex and gold for example, but not between silver and gold [228]. Differentiation by composition using NTA is further hindered by the fact that it is challenging to obtain completely regular and even illumination across the entire field of view, meaning that two identical particles in different areas of the field of view of an NTA instrument may have very different intensities on the camera.

Crucially for regulatory purposes, NTA is the only commercial technique which is capable of measuring the number concentration of particles directly, by counting the number of particles measured in a known volume – TEM requires extrapolation from the approximate volume of sample deposited onto the TEM grid and assumptions about the distribution of particles on the grid, DLS and DDM can only roughly estimate relative abundance of different particle sizes, and spICP-MS cannot differentiate between multiple particles should more than one pass through the ICP stage simultaneously. This is of great importance, because the EU definition of a nanoparticle places the emphasis upon the number concentration of particles (particles per millilitre) rather than upon the more conventional analytical chemistry measure of mass concentration [1].

1.4.5.2 Limitations of current nanoparticle tracking analysis implementations

1.4.5.2.1 Reproducibility

NTA isn't always portrayed as the most reproducible method of analysing nanoparticles, indeed of the methods compared, Anderson et al [229] found that NTA gave the greatest variation in measured particle size distribution. These authors do concede, however, that it was a significantly faster method than either of the others tested; NTA measurements were reported to take $\leqslant$5 minutes, while allowing for sample preparation time neither of the other techniques assessed could be completed through to analysis in under 3 hours. Furthermore, it is admitted that the method for which the least variation was found was highly subjective, i.e. one researcher could remain internally consistent with the results, but the repeatability became considerably worse than that of the NTA when multiple researchers were involved with taking the measurements.

1.4.5.2.2 Large and small particles

At large particle sizes, NTA can be seen to either suffer from a greatly increased detection limit (and therefore cease to detect particles), or ascribe wildly fluctuating radii to those which it detects. This is because, as shown in Section 1.3.4.1, the intensity of scattered light is proportional to the 6th power of particle diameter [230], and so for a given input power from the illuminating laser, there will come a point when the light scattered by the particles is too much for the digital CCD and it will overload. This overloading is, as observed by Holland [231], the cause of what he refers to as a 'tracking error'. A tracking error occurs when the algorithm that detects and defines the co-ordinates of the centre of a particle cannot find anything to latch onto i.e. when the particle is a uniform collection of overloaded pixels reporting maximum luminance values, it is very hard to define a particular point within this area of maximal intensity by which to describe the particle's location. This can cause the particle-tracking algorithms to start picking different centre-points from frame to frame on an apparently arbitrary basis, which can give the impression that the particle is moving with considerably higher speed than in fact it is, and thence the deduced hydrodynamic radius will be badly skewed and inaccurate. Unfortunately, the exact centroid localisation algorithm utilised by the Nanosight NTA software is proprietary, and therefore not possible to interrogate directly.

While the Nanosight NTA appears to be accurate to both ends of its measurement range [228] it struggles to stretch to both ends of its range simultaneously (i.e. a single polydisperse sample containing both particles of $\approx$100 nm and particles of $\approx$1 μm) [232] who find that when using a mixture of 100 nm and 1 μm particles, the inclusion of the 1 μm particles causes a drop of the particle count for the 100 nm particles of $\approx$35 %. This because with a 6th power dependence of scattered intensity on particle size, the intensity of light being scattered by the larger particles will be $\approx 10^{12}$ times greater than that from the smaller particles. In order to achieve a great enough intensity of radiation to reliably track the smaller particles from frame to frame, the gain settings on the CCD would have to be turned up sufficiently high that any useful information would easily be blanked out by the relatively huge luminance off the larger particles. Similarly, should the gain of the CCD be reduced sufficiently to image the larger particles efficiently, the signature of the smaller particles would be completely lost. It is entirely possible that some pre-processing techniques like AF_4 could be used to precondition the sample.

In a similar vein, it has been reported that while in the middle of the NTA operating range it is relatively accurate, towards the ends, and in particular the lower end of its stated operating range, the accuracy drops off significantly [67]. It was found the NTA was returning values of over 100 % larger than either the nominal value of the samples, or the values measured using other means. The authors suggest that some of this may be down to the fact that NTA measures the hydrodynamic radius, and the only other assessed techniques which do the same are DLS, DDM, and HDC. This hypothesis is supported by the fact that DLS was also making significant overestimates of the size, though not to quite the same extent that NTA was.

It is suggested by Filipe et al [232] that when really small particles (i.e. particles below the detection limit of the equipment[6]) are present in a sample, the fact that they aren't directly detectable doesn't mean they have no effect on the result of a measurement. Just because they are failing to scatter light of sufficient intensity that it can be measured and tracked directly is not to say that they are completely failing to scatter light. In sufficient number, particles below the detection limit scattering light will slightly brighten the background of the recorded images, potentially masking small (but otherwise normally detectable) particles. As far as either the peer-reviewed literature or the Nanosight documentation goes, there is no mention of any statistical or computational method by which this is combated.

A possible solution to this has been described by Gallego-Urrea et al [234] suggesting

---

[6] The quoted detection limit of the Nanosight NTA is 10 nm for highly-scattering materials like gold and silver, and 'larger' for less highly-scattering materials. Detection limit for particle size is primarily determined by the scattering efficiency of the particles and particle size, though other contaminants in the sample can also have a negative effect upon the detection limit by increasing the background light levels, particularly if they fluoresce [233].

that it may be possible to 'compress' the dynamic range of captured video in order to simultaneously brighten the darker areas of the image and darken the brighter areas, making it more easily possible to simultaneously measure both larger and smaller particles. While artificially brightening the darkest areas will have a similar effect, it additionally runs the risk of amplifying any background noise sufficiently that the software picks up random speckles as particles, and thereby generates 'phantom' particles that don't really exist. The authors don't appear to quantify the effect of such digital processing, so this may be an area for future research.

1.4.5.2.3 Particle shape

It has been stated [235] that the variations in the brightness ('twinkle') of any given particle during the duration of its path across the field of view is a result of irregularities in the shape of the particle. According to Malloy and Carr [149] and Carr et al [228], one of the key assumptions of NTA is the spherical nature of the particles. However, Carr et all state explicitly that this variation in intensity cannot be used to derive any information concerning the shapes of the particles being measured.

According to Carr et al [228] and Schwyzer et al [236], when an asymmetric particle is measured, the number returned by the NTA software is a 'sphere equivalent' hydrodynamic radius. Since Rayleigh scattering efficiency is proportional to the 6th power of radius, a heavily asymmetric particle (such as Schwyzer's carbon nanotubes), will display a tremendous variation in scattered intensity, and thence will appear to fluctuate, or 'twinkle'. It is possible that this effect could be used to make broad estimates about the degree to which a particle is oblate or prolate by looking at the proportion of the time that the particle is 'bright' and 'dim', and the intensity ratio of bright:dim. It may be possible to increase the quality of this shape information further by introducing a second laser of different wavelength, perpendicular to the first. In this way, two different signals about the same particle at the same time, both varying in brightness dependent upon the area presented to them, could allow far improved shape determination.

1.4.5.2.4 Particle track length

As a result of the limited period for which NTA will track a particle, there is an inherent uncertainty in the values measured for particles. The larger number of steps it is possible to track a particle for, the more accurately one may infer its size. Estimates of the number of steps for which a single particle may typically be tracked using the Nanosight implementation vary from 5 [231] to 10 [237]. This results in particles being both under- and over-sized by the software, and a spurious broadening of the size distribution peak [238]. Saveyn et al [238] describe a statistical correction to account for this broadening and reshape the distribution to more closely resemble the true particle distribution. It is important to note that the statistical correction is not in itself infallible, and is no substitute for acquisition of good data.

1.4.5.3 Applications of nanoparticle tracking analysis

NTA has been leveraged for a great many different applications (see below), but is especially well suited for use in the characterisation of risk from ENPs in the environment – its greatest strength over many competing techniques is arguably its ability to determine the form of occurrence of ENPs in aqueous suspensions, and therefore characterise the exposure inflicted upon organisms in the environment.

The pre-eminent commercial implementation of the NTA concept is the Nanosight (Nanosight, Salisbury, UK), which has been used in a vast range of fields which require analysis of nano-sized objects between about 10 nm and 1 μm including graphene membranes [239], particle-porous medium interactions [240], microplastic/nanoplastic decomposition [241], identification and measurement of cellular vesicles [242], catalyst development [21], aggregation studies [243,244], drug development [245], and biological protein dynamics [246], not to mention nanotoxicology and environmental nanoscience [16, 54, 247–250] among others [54, 251, 252].

More specifically, in terms of environmental studies, NTA has been used to investigate the degradation of micro- and nano-plastics [241] and the effects of this [252], aquatic fate and behaviour testing of nanoparticles of CeO_2 [16] and Bi_2O_3 particles [253], measurement of particles for ecotoxicology testing [247], and the relevance of these laboratory-based nanoparticle studies to the real environment for regulatory ecotoxicology purposes [254]. A comprehensive list of several hundred relevant papers is available in [233] on pages 1-11.

Some of the techniques considered here are compared in a lot more detail in the following section.

1.4.6 Comparison of techniques

Clearly, each of the techniques considered here in detail have their own unique advantages and disadvantages. This section summarises the differences between some of available the techniques.

A quantitative comparison of a wide range of techniques is given by MacCuspie et al [67]. There are several important things to be drawn from this comparison. Firstly, the TEM values are in most cases the closest to the nominal values. This is no surprise; indeed, the TEM value is likely to be a truer representation of the actual size of the particles than the nominal value, as TEM is a direct measurement of the physical sizes of the particles. A second key point is that for the NTA measurements, the modal particle size is in all cases a far better representation of both the TEM and nominal sizes than the mean particle size. This is particularly important in Chapter 3, and will be referred to again later. A third notable point is that both DLS and NTA were reported to have over-estimated the particle sizes in the smaller (10-20nm) particles but are much closer to the nominal and TEM values for the larger (40-100 nm) particles. Unfortunately, MacCuspie et al don't detail the exact concentrations of particles they used for each of the individual measurements summarised in this table, so it is impossible to interpret the results in the light of these.

Given the techniques reviewed in Sections 1.4 and 1.4.1, Table 1.2 was compiled. This table emphasises that all the reviewed techniques have their own niches in which they are superior to other reviewed techniques in some way. Likewise, all the reviewed techniques have foibles which prevent them from being of significant use in other circumstances.

Figure 1.13 contains a brief visual comparison of some of the more important nanoparticle metrology techniques in terms of the sizes and concentrations of nanoparticles they're capable of detecting and measuring. The scales on the axes are completely arbitrary and approximate; the figure is only intended as a visual aid. Relative concentrations and resolutions are taken from the relevant sections in this chapter. As this figure makes obvious, spICP-MS is currently the only technique capable of making measurements of nanoparticles at the lowest concentrations; in this case, the far left end of the 'nanoparticle density' axis denotes environmentally relevant concentrations.

Given the information summarised here, it was decided to attempt to extend the capabilities of NTA; several motivations were used to justify this decision. Firstly, both NTA and DLS utilise relatively simple and inexpensive equipment which may be assembled from off-the-shelf commodity equipment. Hence, the technical expertise necessary to construct a custom-designed set of measurement apparatus is confined to the fields of optical systems design and implementation and computational data analysis. For comparison, consider that building a spICP-MS rig from scratch requires advanced knowledge of gas flow systems, plasma physics, vacuum systems, mass spectrometry, and detector science, to name but a few.

Another key reason to attempt to extend the NTA concept is the unique ability to track individual particles, with minimal influence of the observation upon the particle's behaviour, over relatively long periods and through relatively large volumes (when compared to the volumes particles may be tracked in fluid-cell TEM, for example). Fundamentally, this ability to obtain time-resolved data on single particles is unique to NTA, and it would be of tremendous impact to be able to make such measurements in real environmentally relevant

Measurement technique	Advantages	Disadvantages
TEM	·Very well-recognised technique ·Measures physical size directly ·Can measure shape, not just some abstract 'size' ·Can do some compositional analysis using EELS etc	·Slow, cannot be readily carried out on liquids ·Measurement process can affect the sample ·Requires expensive specialist equipment ·Not at all portable ·Not at all suitable for measuring particles at low (environmentally relevant) concentrations
DLS	·Well-recognised technique with wide commercial support ·Very short data acquisition times possible ·Compact equipment which is relatively portable ·Relatively low cost of measurement apparatus	·Poor ability to distinguish polydisperse samples ·Cannot measure non-spherical particles accurately ·No compositional ability
spICP-MS	·Capable of making measurements of particles at very low concentrations ·Can measure composition simultaneously to size ·Widely-used and well-accepted technique	·Requires complex and expensive equipment ·Not at all portable for use in the field ·Single-particle statistics are not very good; requires many particles to build up accurate picture
NTA	·Measures individual particles and can produce good per-particle statistics ·Short data acquisition and analysis times ·Relatively compact equipment which could be made to portable ·Copes well with polydisperse samples ·Can distinguish particles of differing composition by refractive index	·Only works at relatively high particle concentrations (above environmentally relevant levels) ·Cannot measure the shape of particles ·No means of analysing composition of particles

Table 1.2: Table comparing some of the more widely-used nanoparticle analysis techniques on their advantages and disadvantages for environmental study. The list of advantages and disadvantages is not exhaustive, and is only intended to cover some of the more salient points regarding environmental study. All data summarises results cited earlier in this thesis.

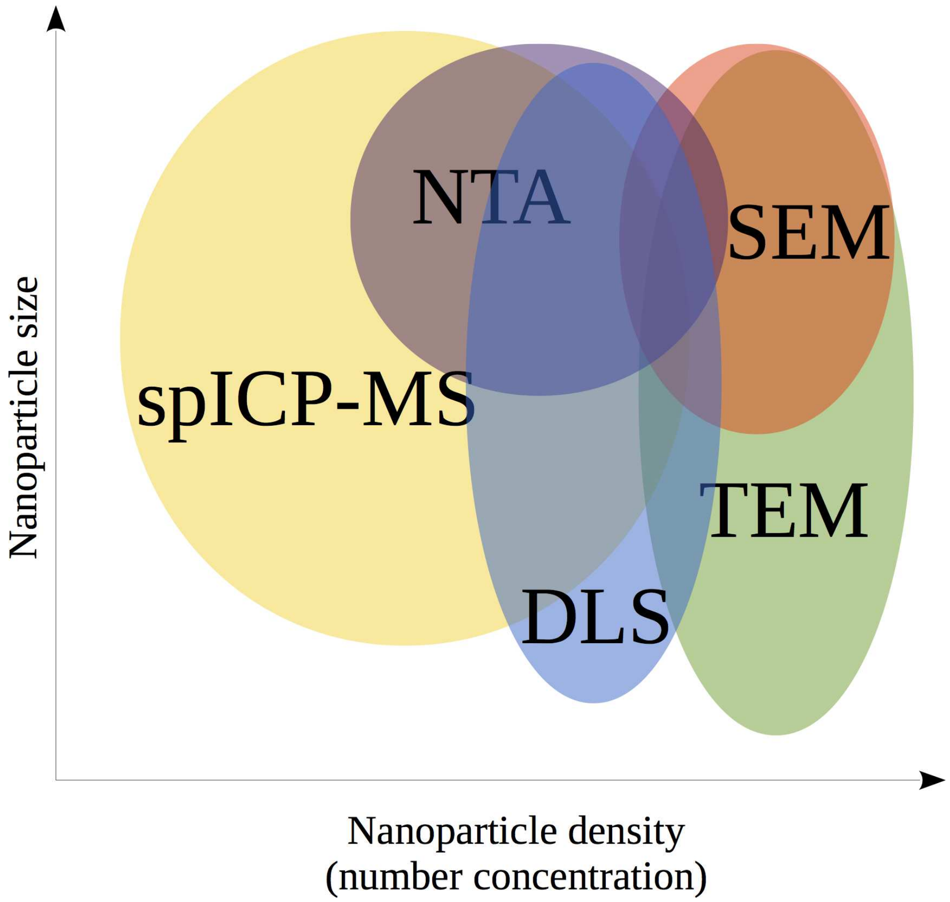

Figure 1.13: Figure showing a subset of the more popular nanoparticle measurement techniques and their current regions of usefulness in terms of particle sizes and particle densities (number concentrations). Many less-used techniques have been omitted for clarity.

samples (or even in real environmental samples).

Finally, having determined the operational parameters of NTA, it is apparent that many of the perceived limitations of NTA as a technique are more accurately limitations of the Nanosight commercial implementation of the NTA concept, and that there are no technical reasons a bespoke NTA device could not be designed and produced (still using commodity hardware) capable of significantly outperforming current commercial solutions in certain regards.

With this in mind, some environmentally-orientated nanoparticle fate and behaviour studies were run using the current commercial offering in order to confirm that the predominant issues as reported in the literature are indeed the predominant issues with the Nanosight platform in the context of environmental nanoparticle research. This is described and presented in Chapter 2 .

1.5 Important unanswered questions

The first requirement in order to effectively regulate the use of a particular material in a particular state is a robust and efficient means of classifying that material in that state [52].

While nanoparticles can be measured robustly by use of an electron microscope, this is not at all efficient in terms of either operator time or financial burden – in order to get statistically significant results it is necessary to manually count and measure a large number of particles [255], even after a complex sample-preperation procedure has been carried out. This comes on top of the financial burden associated with operating and maintaining an up-to-date TEM. Furthermore, TEM samples cannot ordinarily be aqueous – and hence the morphology of suspended particles may be effected by the sample preperation procedure [159]. Clearly, for effective regulation of nanoparticles, additional classification techniques are necessary.

1.5.1 Particle morphology

1.5.1.1 Single-Particle Shape

The shape of single nanoparticles is a very important consideration. Conventional optical measurement techniques only allow for measurement of a mean sphere-equivalent hydrodynamic diameter. While for a spherical particle this may be a useful measure, it is significantly less so for a nano-rod or nano-disc. A nano-rod of diameter 2 nm and length 100 nm would exhibit a geometric mean diameter of ≈35 nm (and therefore a sphere-equivalent mean hydrodynamic diameter slightly larger). Such a rod may be capable of penetrating a biological membrane that a 35 nm sphere would not [256] – while the two particles may have a similar diffusivity, their toxicological effects on certain species may differ significantly. A more recent example is the discovery that ENPs with high-aspect-ratio rod-like and wire-like structures can interact with tissues via the pathogenic fibre paradigm [257–261]. This paradigm is best-known as the pathogenic pathway associated with the irritation of the lungs, formation of granulomæ, and ultimate tumour growth resulting from asbestos exposure [262, 263]. Hence, for regulatory purposes it is important to be able to differentiate between the two cases.

Similarly, a nano-disc of similar semi-axes would exhibit a geometric mean diameter of ≈70 nm, and yet the adsorbative properties of a disc to certain biological (and non-biological) surfaces is significantly greater. While this may not enhance the direct toxicity, it can allow for significantly increased coating, possibly leading to photosynthetic impairment, respiratory impairment, or a range of unspecified surface-related negative effects to a much greater degree than the sphereical equivalent [46]. They have also been shown to be useful for scattering light within high concentrations of algae in bioreactors, allowing algae in the centre of the reactor to receive sufficient light [264]. However, this raises questions about whether high environmental concentrations of such discs could abet the algal blooms which are becoming an increasing problem in natural water systems when coupled with nitrogenous agricultural run-off [265]. In a similar vein, it has also been demonstrated that mammalian cells will preferentially internalise nanodiscs over nanorods [266].

It has been shown that the rates of sedimentation and diffusion of nanoparticles can have a significant effect upon the exposure and uptake of ENPs by natural organisms [267]. It is also known that the shape of nanoparticles can greatly influence the surface charge density and distributions [268] and the diffusion and sedimentation dynamics of nanoparticle suspensions and colloids [269] – this is one possible explanation for some of the differences in uptake rates between different shapes of particle. Should it be possible to take quick and accurate optical (possibly NTA-based) measurements of the shape of suspended nanoparticles, then it would permit the characterisation and prediction of exposure and uptake more accurately than current models are capable.

The effect of nanoparticle shape upon their diffusion and sedimentation dynamics is also important for the fabrication of particles of different shapes; the effect has been exploited for the selection and separation of differently-shaped particles at the fabrication stage [270, 271]. Being able to confirm the correct functioning of such fabrication systems in near real-time using an optical technique could give significant time and financial savings over the current TEM-based approaches to quality control for the production of non-spherical nanoparticles.

Therefore it would be of great significance for both regulatory and commercial applications if NTA could be developed such that the shape of single particles is measurable simultaneously to mean diameter. Possible approaches to this problem are discussed later in Chapter 5.

1.5.1.2 Aggregate structure

The structure of aggregates is another important piece of nanoparticle morphology. In general, aggregates that come together fast and have an attachment efficiency approaching unity (i.e. diffusion-limited aggregation, which is discussed in Section 1.3.3.2), will have a lower fractal dimension [144]. The fractal dimension is a quantity closely related to spatial dimension, and is useful for describing the properties of fractal- and fractal-like structures [272]; nanoparticle aggregates are one such class of fractal-like structures [273]. In this context, it is useful to visualise the fractal dimension as a coefficient describing the porosity of the particle – larger fractal indices indicate more dense and interconnected (or 'complex') aggregates [274]. This means particles with a lower fractal dimension have a more open structure and potentially a larger surface area. Toxicologically, this is important – a more open structure not only means a higher surface area, but it also allows greater solvent circulation within [275]. Consequently, particularly for nanoparticles susceptible to dissolution, this means that the toxic effects could be exacerbated compared to an aggregate of similar size and higher density.

Using comparison to TEM images, it should be possible to calibrate calculated attachment efficiencies (which may be calculated from scattering data over time, or estimated from physical and chemical parameters – both are discussed later in Sections 1.3.3.2 and 2.2.4) and particle concentrations to fractal dimension of the average resulting aggregate, and thereby develop a means for the prediction and indirect measurement of aggregate structure for non-soluble particles from light-scattering measurements.

1.5.1.3 Aggregate stability

It is widely tacitly assumed for toxicological purposes that once two nanoparticles have adhered to each other, they will remain as a single entity indefinitely [36]. Hence if a suspension of 10 nm particles, known to have significant toxic effects upon a given species at 10 nm, but not at >30 nm, were to be allowed to aggregate to 40 nm before release into the aquatic environment, this would be generally considered to be 'safe' because the risk of the 10 nm particles becoming available once more would be deemed negligible. This assumption has not been tested under environmentally relevant conditions however, and simulation of this is decidedly non-trivial. The best (and prevailing) theory currently used to mathematically describe nanoparticulate suspensions is Derjaguin-Landau-Verwey-Overbeek (DLVO) theory [127, 128]. DLVO theory is discussed in greater depth in Section 1.3.3.1.

1.5.2 Detection limits

Current NTA apparatus has a very limited range of particle concentrations it is capable of measuring – the Nanosight instrument has a useful analysis range of between 10^8 and 10^{10} particles/mL, though different versions of the Nanosight manual contradict each other on this point – one old version even suggests that it can successfully measure ENPs at 10^5 particles/mL, though this is untrue and has been removed from more recent editions. This doesn't compare very favourably to the predicted environmental concentrations (PECs) from various studies, which tend to estimate that even considering current exponential increases in nanoparticulate waste, concentrations several years down the road are unlikely to rise above about 10^5 particles/mL [36, 71, 100, 276]. Several possible ways of circumventing this issue are suggested and discussed later.

1.5.3 Particle composition

The composition of nanoparticles is equally as important in an environmental context as many of their other properties. For example, 30 nm gold ENPs may be innocuous enough in a given system, but 30 nm silver ENPs may be severely toxic to a particular organism. Similarly, naturally occurring nanoparticles, usually organic in nature, should not be considered when assessing anthropogenic nanopollution. While current techniques allow simple differentiation between species of radically differing polarisability and refractive index based on the ratio of calculated size and mean intensity of scattered light (for example, it is trivial to differentiate between populations of latex and gold, but not between gold and silver) [67, 228], it is not possible to robustly declare that an arbitrary sample of unknown composition contains any specific material. Again, for regulatory toxicological and pollution-monitoring purposes, it is very important that the composition of the nanoparticles in a sample is known, and it is significantly more beneficial if everything can be accomplished with a single piece of equipment.

1.6 Conclusion

There is a well-established community currently developing approaches for the assessment of the impact of nanopartices on individual organisms and upon ecosystems and the environment as a whole. Over the previous two decades, the science of nanotoxicology has matured from being at best a haphazard collection of largely irrelevant results into a well-regarded field of scientific endeavour with a high degree of importance to further human technological development.

There has already been a significant amount of work in the field of ENP measurement for environmental study, and this has resulted in the development of new techniques including single-particle optical tracking analysis and a broad range of single-particle hyphenated techniques. While each of these tools has its own speciality and advantages in different situations, there are still some measurement scenarios which are universally problematic. This provides scope for development of existing and novel tools to alleviate some of the related challenges.

Chapter 2

Assessment of NTA performance and reversibility of nanoparticle aggregation

In this Chapter, the Nanosight commercial NTA system is used to investigate the reversibility of the aggregation processes undergone by engineered nanoparticles in the natural environment in a selection of different environmentally-relevant conditions. This chapter is also used to give a better idea of some of the limitations of the Nanosight NTA system for application to environmental study.

2.1 Introduction

In order to verify some of the outcomes from the review of current literature, a study using the current commercially available Nanosight NTA platform was carried out. Other than the specific aims of the specific study (outlined below), it was hoped to corroborate the speculation that inability to measure particles at low concentrations and inability to infer anything about the shapes of particles and particle aggregates were one of the major drawbacks preventing NTA from being more broadly applicable to environmental nanoparticle studies.

Considering electrostatically stabilised particles, the surface charges will interact with any electrolytes in the suspension via DLVO theory [127, 128] as described in Section 1.3.3.1. These suggest that as the pH of the suspension changes, so should the surface charges. This has been experimentally confirmed [36, 282]. If an aggregate were to form at one pH, and then the pH changed in a way that increased the surface charges, it is entirely possible that this could lead to a reverse in aggregation as the aggregates become energetically unfavourable. If this is the case, it is reasonable to hypothesise that this could occur given environmentally relevant variations in water pH. This type of behaviour has already been observed in ENPs, whereby alkaline conditions were used to break up an aggregate [279]. However, this result was not environmentally relevant – the conditions described in this paper were designed to mimic the internal fluids of a human rather than those which may be found in the natural environment.

Other natural parameters that could conceivably affect the rate of aggregation include two key processes: application of shear forces (from water flow and agitation due to phenomena such as waterfalls) and freeze-thaw cycling. Firstly, it was thought that there are a great many means by which shear forces may be generated in natural water systems, from ocean tides and waves through to smaller waterfalls and eddies. These all exert some amount of shear force, and this could cause a destabilisation of nanoparticle aggregates. Clearly, the variation in the magnitude of this force over time is of some importance – while a mountain stream with many waterfalls and a steeply inclined riverbed may descend hundreds of metres in a few hours or less, wide meandering rivers may take several days or more to make the same descent.

Finally, freezing is an important process, both in the natural environment and in the laboratory [283–285]. In the natural environment, most freezing processes are slow, and result in large ice crystals, while in the laboratory, samples may be frozen slowly in a -18°C freezer or plunge-frozen in liquid nitrogen at 77 K [286]. When a sample is frozen slowly, the larger ice crystals that form could lead to an expansion inside particle aggregates, forcing them apart. Similarly, the smaller crystal structures formed by plunge-freezing could have this effect but to a lesser extent. It is known that certain combinations of complex organic molecules can stabilise nanoparticles through freeze-thaw cycles [287], but little research has been published beyond this.

The aims of this study were to verify whether or not any of the environmentally relevant conditions considered above could cause the reverse of ENP aggregation, and if so, to what degree. Secondly, the study aimed to either verify or refute the proposed shortcomings of the NTA approach for carrying out environmental nanoparticle studies. Finally, because the effect of freezing upon nanoparticle suspensions in an environmental context hasn't been investigated before in any way, the study aimed to determine the effects (if any) of freeze-thaw cycling upon nanoparticle suspensions.

2.2 Methodology/materials and methods

2.2.1 Selection of particles

All the nanoparticles used in the study were made from gold. This was in order that any effects due to dissolution could be ignored, and because gold is highly-scattering and therefore has a low detection limit for NTA analysis. It is documented [249] that much or all of the physical behaviour of ENPs is down to their surface coating, so the results are equally valid for other nanoparticle cores capable of being coated with the same agents. All particles were nominally 30 nm. This size was chosen as it is within most of the competing definitions of a nanoparticle, and is a size that is simply and accurately measured using currently available nanoparticle tracking analysis (NTA) equipment.

Three surface coatings were investigated. Firstly citrate-coated particles were chosen as negatively charged particles at pH 7 in water. Citrate-coated particles are some of the more readily available commercial particles, so it is therefore likely that they will be used more frequently than particles using more obscure or niche coatings. Neutrally coated (sterically stabilised) particles are represented by a polyethylene glycol (PEG) coated sample, and the positively-charged candidate of choice was amide-functionalised PEG (PEG-NH_2). Neither of the latter two coatings are as readily available as citrate. The citrate- and PEG- capped particles were obtained from Sigma Aldrich (Gillingham, Dorset), while the PEG-NH_2 particles were sourced from NanoCS (Elmhurst, New York).

All particles were dispersed in deionised water at concentrations of approximately 10^9 particles/mL so as to be comfortably within the concentration range of the NTA apparatus being used. The Nanosight NTA is reported to give accurate measurements of nanoparticle size and relative concentration at concentrations between 10^8 and 2.5×10^9 particles/mL [288], a figure which the authors suggest could be principally limited by the cleanliness and quality of the diluting media. The measurement of particles is discussed in Section 2.2.4.

2.2.2 Pre-study aggregation of nanoparticles

In order to study the reversibility of aggregation, all samples had to be in a uniform aggregated state prior to the testing of various conditions. This was achieved by increasing the ionic strength of the electrolyte with the addition of NaCl, a well-documented means of achieving such an end [137, 212, 289, 290] which has the benefit of having no effect upon any of the test parameters. The ionic strength of each sample was brought up to 0.2 M, and the samples were left for 72 h to aggregate. This concentration was selected because it has been shown to lead to aggregates that are neither very porous and loosely bound (with a low fractal dimension) nor very tightly-packed and very well-bound with a high fractal dimension (and therefore be highly unlikely to disaggregate in any circumstances) [144].

All samples were aggregated in the 72 h immediately prior to test conditions being applied. This avoided the problem of sample degradation or further aggregation between studies, particularly given that sample preservation techniques were among those under test.

2.2.3 Selection and implementation of conditions

The range of pH values tested was taken from the regional variation in natural waters found in the region of Yorkshire, UK [291], and the range from pH 3 through to pH 10 was used. Nanoparticles were therefore tested at the extremes of this range, at pH 3 and at pH 10, and were subjected to these conditions for 24 hours. Controls for all test conditions were used to control for the increase in ionic strength caused by the addition of NaOH and HCl, in which the ionic strength of the control was equalised with the ionic strength of the test sample by the addition of further NaCl. Acidic conditions were imposed by the use of HCl, and alkaline conditions were obtained using NaOH except where otherwise noted. All added solutions were screened to ensure they did not contain any nanoparticulate contamination.

Natural shear forces were simulated using a rotary shaking table, running at 2Hz, orbital radius 9.85 mm for 20 h. For a sample of 8 mL (as was typical during the study), this exerted sufficient acceleration over time to give a total energy exertion of 94 J per sample; approximately equivalent to the change in gravitational potential energy of a similar quantity of water flowing from an elevation of 500 m to sea-level. All test samples were accompanied by non-shaken controls.

As previously mentioned, two different freezing paradigms were selected. For one set of samples, a domestic -18°C deep freeze was used to simulate slower natural freezing processes. Samples were left in overnight to ensure that the entire sample had frozen completely. Plunge-freezing was carried out in liquid nitrogen. Less than a minute was required to freeze each sample completely, so they could be defrosted immediately for measurement. Non-frozen controls weren't used, since it is reasonable to assume that while the samples are in a frozen state, no aggregation or disagregation processes are able to take place. Frozen controls were used to verify that the phials didn't release nanoparticles during freeze-thaw cycling.

All samples were duplicated, and where the initial results suggested it was necessary, were repeated up to 5 times to guarantee reproducibility.

2.2.4 Characterisation of particles

All particles samples were characterised using TEM (JEOL 2011, JEOL, Japan) upon receipt from the suppliers, prior to the commencepent of the study. All subsequent characterisation of particles was carried out using a Nanosight LM-14 NTA instrument (Nanosight, Salisbury). All measurements using the Nanosight were repeated at least three times, and all measurements were at least 90 s long. Where appropriate, due to lower particle concentrations, more repeat measurements and longer recording times were used. When using NTA, the mean particle sizes were always used rather than the modal sizes – significant aggregation can occur without removing sufficient number of the original primary particles for the mode to change. This may be seen more clearly in Section 2.3, where Figure 2.2a shows that in common with all measured cases, despite significant aggregation having obviously taken place, the mode remained in approximately the same location throughout.

Measurements of each particle sample were made before the aggregation stage (at the commencement of the study), after the aggregation stage (just before the implementation of the stressors, 72 h after the commencement of the study), and immediately after the test period (usually 96 h after the commencement of the study, except for the frozen samples. For some of the frozen samples, further measurements were taken an additional 4 h after defrosting. pH measurements were taken of every sample at the same time as the NTA measurements.

As well as looking at the size distribution of nanoparticles, the mass balance was also examined. It is important to be sure that the change in a nanoparticle size distribution measured in the suspension is representative of all the nanoparticles in the initial sample, i.e. that there has been minimal sedimentation. It has been documented that the porosity of a nanoparticle aggregate is dependent upon the rate of aggregation [144]. While it is not possible to account for the varying rate of aggregation due to the different treatments used, the majority of the aggregation occurred during the highly-controlled pre-study aggregation phase. Using the data shared by [292], it is possible to estimate that with the concentration of NaCl used and the resulting aggregation rate, the nanoparticle aggregates formed have a mean fractal dimension of 2. It is then a simple case of using the equation $m_p = \frac{1}{3}\rho\pi r^{D_f}$ to determine the mass m_p, where ρ is the density of the nanoparticle material, r is the diameter returned by the nanosight, and D_f is the fractal dimension of the nanoparticle aggregate [293]. Given these assumptions about the state of the aggregates, and the additional assumptions that the primary particles are solid and that the number concentrations given by the Nanosight are accurate, it is possible to calculate the approximate mass of particles before and after aggregation. It was found that in all cases apart from those involving freezing that the mass concentration calculated using the tools described in Section 1.3.3.2 that there was a slightly larger mass in suspension at the end of the test aggregation compared to the mass present at the beginning. This slight increase suggests that no sedimentation occurred; because a larger particle will scatter light more efficiently than a small one, a large particle may be detected in dimmer parts of the beam profile in which smaller particles would not produce a sufficiently strong signal. In the cases of every freezing test, the mass balance suggested that a significant fraction of the particles in the sample had sedimented out.

It is important to realise that the primary (unaggregated) particles should not have this equation applied to them – they are solid spheres! Therefore, before the mass balance was calculated, the original (unaggregated) size distribution was subtracted and treated as solid spheres.

2.3 Results

All three nanoparticle types were characterised using TEM. Representative images of the three different particles used are shown in Figure 2.1. The Au-PEG-NH_2 particles were found to be (40±10) nm, the Au-PEG particles were (35±15) nm, and the Au-citrate particles were (29.8±0.2) nm. It is unsurprising that the particles which are most widely-available and widely-used are both the closest to their nominal size and have the smallest variance in size.

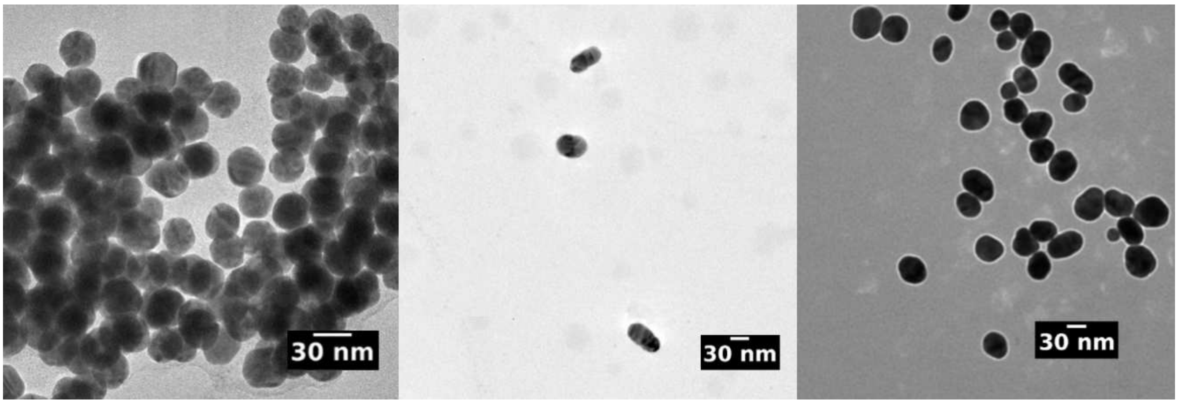

Figure 2.1: Representative TEM images of the three ENP types used in this study, L-R citrate-coated (negative surface charge), PEG coated (neutral surface charge), and PEG-NH_2 (positive surface charge).

It was found that for all aggregates subjected to acidic conditions, aggregation continued at either a similar or higher rate than the control samples (Figure 2.3). A graph showing the typical progression of this aggregation throughout the experimental process is shown in Figure 2.2a. The PEG-NH_2-coated (+ve charged) particles behaved the same in alkaline conditions, while the PEG- and citrate-coated particles exhibited different behaviour. The PEG-coated particles exhibited a decrease in aggregation relative to the control, but this was probably only due to a stabilisation, not a reverse in aggregation because the particle size still increased during the test period, albeit slower than the increase in particle sizes seen in the control samples. The citrate particles appeared to react the same, suggesting that the alkaline environment stabilised the suspension. However, in several individual samples, an actual reverse in the aggregation process – a decrease in mean particle size – was seen, suggesting that there is some kind of dynamic equilibrium or steady-state going on in this circumstance (Figure 2.3). The reverse in this case is shown very clearly in Figure 2.2b. Complete results are given in Table 2.1.

In order to verify whether this effect was caused by interaction with the NaOH specifically (for example, due to the Na reacting with the capping agent), or simply the change in pH, the alkaline treatment of the citrate-capped particles was repeated again using NH_4OH instead of NaOH to determine whether the cation was causing the effect. These experiments demonstrated that the alkalinity definitely had a strong stabilising effect upon the suspension, but in this case none of the samples exhibited any resuspension. However, the experimental error was large as a proportion of the measured values; it is therefore possible that some resuspension still occurred but was not detected.

The particles which had been shaken all exhibited an increase of aggregation rate compared to their respective controls.

All samples subjected to freezing treatment aggregated significantly compared to measurements taken immediately prior to freezing (2-way ANOVA, $p<0.05$). All samples were measured as soon as they had been defrosted sufficiently to be injected into the NTA apparatus – any change of aggregation state therefore had to occur during either the freezing or thawing processes. In addition to the general significant increase in the rate of aggregation, it was found that for all particles apart from the PEG-coated examples, this increased aggregation was much greater for the slowly-frozen particles which had been frozen at -18°C.

Subsequent measurements were taken using the Nanosight at an additional 4 hours after defrosting to investigate any longer-timescale effects of the freeze-thaw process. In none of these measurements were sufficient nanoparticles seen for the Nanosight to be able to make a measurement, this suggests the aggregation process had been accelerated by the freeze-thaw process to the degree that only a small number of large aggregates remained in the system.

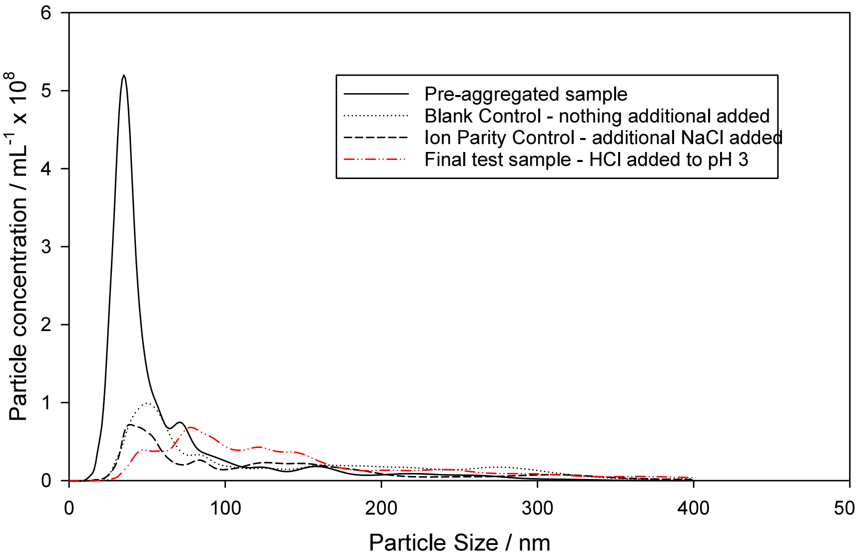

(a) Representative aggregation curve showing the NTA measurements of citrate particles after initial aggregation in NaCl and then after HCl treatment at pH 3. The ion-parity and non-ion-parity controls are also shown. This set of curves is typical of most of the conditions tested.

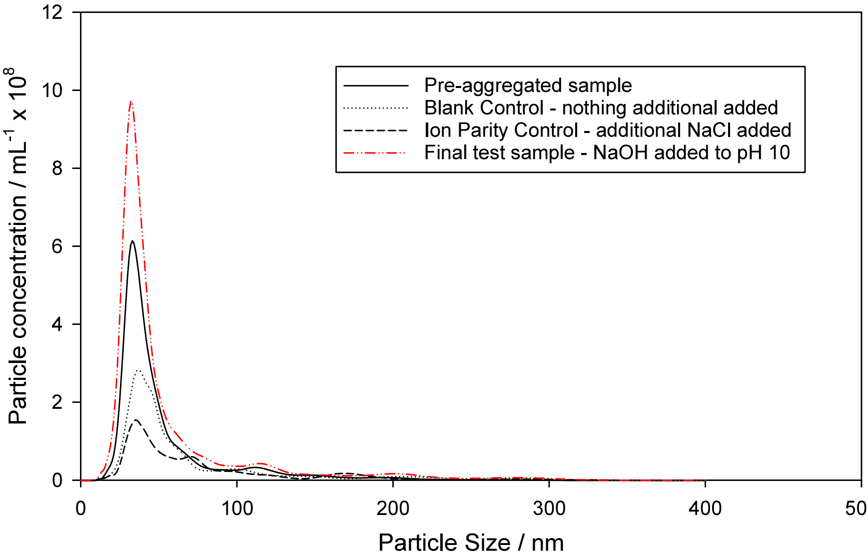

(b) Aggregation curve showing the NTA measurements of citrate particles after initial aggregation in NaCl and then after NaOH treatment at pH 10. The ion-parity and non-ion-parity controls are also shown. It can be seen that the post-alkaline treatment sample has exhibited clear disaggregation.

Figure 2.2: Two exemplar curves showing 2.2a a sample which exhibited an increase in aggregation as a result of the treatment, and 2.2b a sample in which the treatment caused a reverse in aggregation. Each curve was generated by averaging five repeat measurements. Error bars are omitted for clarity, though all errors associated with these measurements are given in Table 2.1 and in Figure 2.3. Similar graphs were obtained for all particles in all conditions.

	Initial pH	Final pH	Initial Mean Size (nm)	Control Mean Size (nm)	Final Mean Size (nm)	% size change relative to initial measurement	Adjusted % change relative to control
Acid Amide	3.10±0.1	3.13±0.1	84.5 ± 11.9	118.5 ± 21.8	168.4 ± 19	+99 %	+42 %
Acid Citrate	2.62±0.1	2.85±0.1	69.2 ± 61.3	137.0 ± 54.7	160.0 ± 75.6	+131 %	+17 %
Acid PEG	2.94±0.1	3.05±0.1	71.8 ± 6.7	82.9 ± 8.7	219.4 ± 5.9	+206 %	+165 %*
Alkali Amide	9.95±0.1	9.41±0.1	72.4 ± 5.9	110.4 ± 18.6	186.7 ± 25.1	+158 %	+69 %
NaOH Citrate	10.04±0.1	8.33±0.1	77.9 ± 19	136.3 ± 31.5	103.4 ± 23.4	+33 %	-24.2 %*
NH_4OH Citrate	9.70±0.1	8.53±0.1	77.2±49.8	139.5±91.6	120.9±65.5	+57 %	-15 %
Alkali PEG	10.05±0.1	9.14±0.1	63.9 ± 3.4	104.0 ± 16.2	80.5 ± 5.1	+26 %	-22.6 %
Amide Shake	6.51±0.1	6.70±0.1	97.3 ± 18.1	136.8 ± 20.7	222.3 ± 15.9	+128 %	+63 %*
Citrate Shake	6.17±0.1	6.46±0.1	57.8 ± 3.1	114.3 ± 14.6	188.9 ± 11.1	+227 %	+65.3 %*
PEG Shake	6.25±0.1	6.54±0.1	73.3 ± 5.7	87.1 ± 8.4	187.1 ± 2.5	+155 %	+114.8 %*
N_2 Amide	6.49±0.1	6.16±0.1	63.4 ± 4.4	- -	101.3 ± 5.8	+60 %*	- -
N_2 Citrate	6.59±0.1	6.54±0.1	125.1 ± 7.7	- -	156.3 ± 7.7	+25 %*	- -
N_2 PEG	6.90±0.1	6.72±0.1	65.0 ± 3.2	- -	88.6 ± 7.7	+36 %*	- -
Freezer Amide	6.56±0.1	7.02±0.1	72.4 ± 5.9	- -	154.2 ± 21.3	+113 %*	- -
Freezer Citrate	6.96±0.1	6.99±0.1	60.4 ± 1.7	- -	99.9 ± 6.1	+65 %*	- -
Freezer PEG	7.76±0.1	5.67±0.1	74.0 ± 3.9	- -	92.9 ± 5.4	+25 %*	- -

Table 2.1: Table showing an overview of all the results from the study. All results marked with * are significant at the $p<0.05$ level. There are no measurements given for the control mean size or the adjusted size change for the frozen samples because the frozen samples didn't have non-frozen counterparts. All frozen samples saw significantly significant aggregation, as did all shaken samples. One acid-treated sample saw significantly increased aggregation, while one alkaline-treated sample saw significant disaggregation.

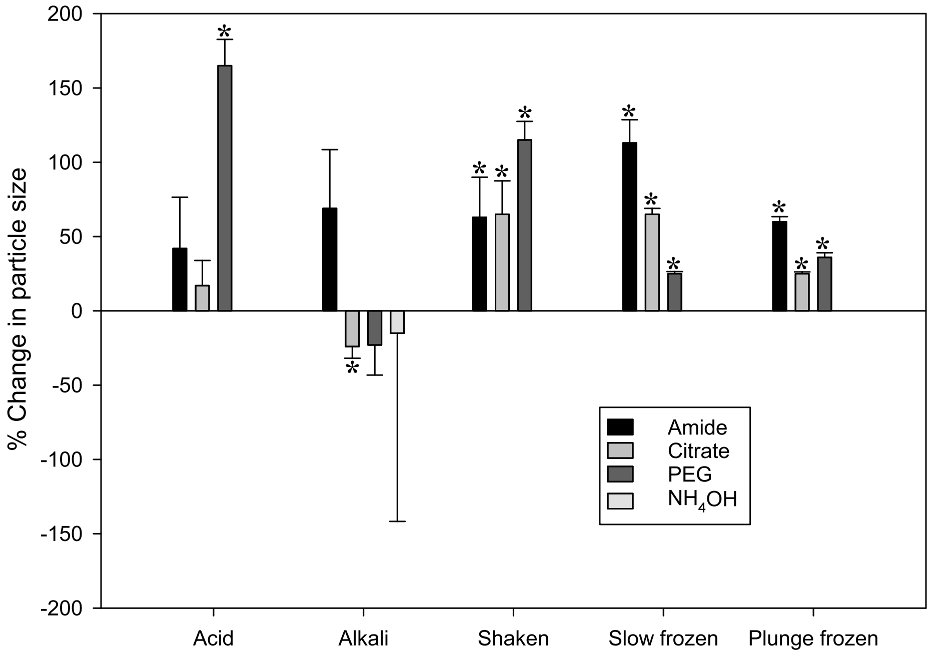

Figure 2.3: Plot of % change in mean particle diameter relative to controls in all conditions and with all particles. Error bars show standard deviations. Bars marked with * represent changes in mean particle size which are statistically significant at the $p<0.05$ level.

2.4 Discussion

2.4.1 General discussion

All the experiments conducted used nanoparticles at a concentration of $\approx 10^9$ particles/mL, which is approximately three orders of magnitude greater than the reported predicted environmental concentrations (PECs) for engineered nanoparticles [276, 294]. While there is some value in showing what may happen to a population of engineered nanoparticles under certain combinations of conditions at the artificially high concentrations which were tested, it is not necessarily possible to sensibly extrapolate and claim that in the natural environment at environmentally relevant concentrations will behave in exactly the same way. Thereby the major limitation of this work is that it's only really applicable to circumstances in which similarly high concentrations of nanoparticles are used. Examples of such situations include laboratory-based acute toxicity studies [295, 296], many studies which are carried out in microcosms [297, 298], mesocosms [299, 300] and nanocosms [301]. They are also relevant beyond environmental nanoscience – there are many other fields including nanopharmacology and materials science which increasingly make use of nanosuspensions and freezing for which these results may have important implications [302–306] .

2.4.2 pH Results

The majority of these results back up the common assumption that nanoparticle aggregation is a one-way process. However, in the case of alkaline treatment of citrate and PEG capped particles, a reverse in aggregation relative to the control was observed. In the case of the PEG-capped particles, this was only a reverse in aggregation relative to the control rather than an absolute reverse in aggregation. This corresponds to a stabilisation of the particles.

In the case of the citrate-capped particles, this was again apparently a stabilisation rather than a reversal of the aggregation process when all the samples were considered together. However, this does hide the fact that some of the individual samples did show a reverse in aggregation – a greater number of primary nanoparticles and a smaller mean particle size were observed after treatment. An example of a sample exhibiting this behaviour is given in Figure 2.2b. In samples for which this behaviour was seen, the resuspension of particles corresponded to an increase in number concentration of primary particles of up to approximately 60 % compared with the number concentration present in the pre-aggregated samples. This suggests not only that nanoparticle aggregation at environmentally relevant rates is a reversible process, but also that in certain environmentally-relevant conditions it can be a dynamic process in which aggregates are continuously forming and breaking apart until more stable configurations are formed.

In order to determine whether the reverse in aggregation was a more general phenomenon or just restricted to a specific interaction between the citrate capping and the NaOH, the same tests were repeated using NH_4OH as an alternative alkaline solution. For reasons that aren't entirely clear, these data exhibited high variability and while most samples exhibited at least a stabilisation effect, the variability was far too great to draw any concrete conclusions from. The scale of this variability is shown in Figure 2.3.

These studies were all carried out in deionised water with added NaCl. This is not representative of the more complex chemical environment in natural surface waters, and it is inevitable that real-world nanoparticle behaviour will be slightly different due to the presence of a range of other electrolytes, the presence of dissolved organic carbon and other organic macromolecules, and a range of biological and physical processes which were not modelled. While it is beyond the scope of this work to examine the extension of the experiments to natural waters, this would be a very interesting continuation.

2.4.3 Shaking results

In all cases, the shaken samples exhibited a statistically significant increase in aggregation compared to the controls. This is easily understood in terms of the number of collisions between particles, and the energy of each collision. In order for two particles to successfully adhere, they must approach each other with sufficient energy to overcome the repulsive forces (in this case either electrostatic or steric) (see Section 1.3.3.1). If the sample is being shaken, that means that the average particle will have greater kinetic energy. This translates into a greater mean velocity, shorter mean-free-path (and therefore more frequent collisions), and greater average collision energy. A possible extension of this work would be to investigate the link between additional energy added to the system and change in rate of aggregation. For example, would the same amount of energy, deposited in the sample at twice the rate for half the time have a comparable effect.

2.4.4 Freezing results

The most significant aspect of the nanoparticle freezing experimental results is that there was a dramatic increase in aggregation rate. This suggests that freezing, however it is carried out, may not be the optimum solution for storing nanoparticle and nanoparticle-containing suspensions and samples.

However, as demonstrated by the complete absence of suspended nanoparticles after a further 4 hours had elapsed, these aggregation processes are incredibly fast. All the aggregation reflected in the results shown here must have occurred during either the freezing or thawing processes. Given the high rate of post-thaw aggregation, it is likely that the capping material has been largely removed from the ENPs by the freeze-thaw cycle. The mechanism for this would be that the difference in thermal expansion coefficients between the particle, the capping agent, and the water caused the capping agent to become detached. The flash-frozen N_2 samples froze in a matter of a few seconds while the more slowly-frozen samples had a few hours in which to freeze. Similarly, the flash-frozen samples appeared to form a more polycrystalline solid (opaque white in appearance) which thawed in approximately 5 minutes, while the slowly-frozen samples formed a more solid block of ice (transparent in appearance) which took in the region of 20 minutes to defrost.

Interestingly, only the flash-frozen samples which contained nanoparticles formed such an opaque polycrystalline structure. The deionised water controls formed a far more transparent structure which took a lot longer to thaw. The difference in structure is almost certainly down to the fact that the nanoparticles provided a great number of nucleation sites, but the change in thawing rate suggests a change in latent heat of fusion as well. In the context of some research in the freeze-drying of nano-suspensions for the manufacture of nano-enabled pharmaceuticals [307, 308] this is particularly interesting. Abdelwahed et al [307] suggest that there are several distinct steps in the crystallisation of a nano-suspension in water, the first of which produces pure water ice, and the second of which produces an amorphous solid which can incorporate the nanoparticles. However, they do not state the critical concentration at which the formation of pure ice ceases and formation of amorphous ice commences. It is entirely possible that the concentration of nanoparticles in the samples was sufficiently high that the pure ice stage was completely bypassed. If this were the case, it is hard to see why the amorphous structure was only seen in the flash-frozen samples and not their more slowly-frozen counterparts.

Finally, it is worth highlighting that the PEG-NH_2-capped nanoparticles, which have the largest and most complex capping agent, exhibited the greatest degree of aggregation, while the PEG and citrate-capped particles aggregated slower. This is possibly down to an effective increase in diameter caused by the larger capping agent; this would increase the collision cross-section and therefore increase the aggregation rate for an identical attachment efficiency. Similarly, ‘bridging flocculation’ (in which the nanoparticles are bridged by large polymer molecules) is reported to work more efficiently with larger polymers [309]. If the freezing process has done something towards detatching the polymers from the surfaces of the particles, then this effect may explain the differences in aggregation rates. It is well documented that in the natural environment a nanoparticle will acquire a bio-corona which can have a profound effect upon behaviour, frequently having a stabilising effect [310] by modifying the surface chemistry; as has already been stated, the majority of the behaviour of a nanoparticle is determined by their surface chemistry. Bio-coronæ tend to be composed of a variety of differently-sized molecules; whether this has any effect upon nanoparticle stability under freeze-thaw cycling would be of great interest from a sample preservation perspective.

2.5 Conclusions

There are a few important conclusions which can be drawn from this work. Firstly, the assumption that natural aggregation processes of engineered nanoparticles are one-way processes has been shown to hold true in the majority of cases, though in a minority of simulated natural conditions it was found that the aggregation was able to be reversed. Thereby it has been demonstrated that the previously-reported disaggregation of ENPs in alkaline conditions can be replicated using environmentally relevant parameters. This should feed into future environmental fate models, and will therefore have a direct impact upon environmental risk assessment applications – it will be necessary to take account of the fact that primary (unaggregated) nanoparticles may be released from aggregates in locations remote from the site of the initial emission of nanoparticles to the environment of the site of initial aggregate formation. This will require the inclusion of water chemistry 'downstream' (either literally, in the case of a river, or metaphorically in the case of oceanic bodies of water) of emission in modelling exercises and risk assessments.

Secondly, the usefulness of freezing as an approach to sample preservation and storage for later analysis of ENPs has been called into question. While there are few viable alternatives, it has been shown that the freeze-thaw process has a detrimental effect upon the stability of all tested nanoparticle suspensions, and any measurements taken after a sample has been defrosted does not necessarily bear any relation to the contents of the sample prior to freezing. This effect was almost independent of choice of freezing process. It would be of great interest to verify whether the same effect is seen for nanoparticles in biological samples.

Finally, it has been shown that resuspension of engineered nanoparticles may readily be detected and quantified using an NTA-based methodology. However, one major limitation to this work is the concentrations at which it was carried out. While the results are directly applicable for many other fields, they are of limited value for environmental study (except in the most extreme cases of nano-pollution) owing to having been carried out at concentrations approximately three orders of magnitude higher than those predicted in the natural environment. The concentrations used were dictated by the limits of detection of the commercial NTA equipment used. This inadequacy, while shared with many contemporary pieces of environmentally-focused nanoparticle research, could be remedied by the use of a nanoparticle measurement apparatus capable of making measurements at environmentally relevant concentrations. While this could be achieved by switching to an alternative measurement technique, as reasoned in Chapter 1, it was decided to further develop the NTA technique to enable these measurements to be taken optically at lower concentrations. The methodology and results of this are presented in Chapter 3.

Chapter 3

Adaptation of NTA for low-concentration operation, and verification of modifications using ISO guidelines

In this chapter, the design, development, and testing of a new NTA apparatus is described which addresses some of the concerns identified in the preceding two chapters.

3.1 Introduction

The methodology and results presented in this chapter are directly motivated by some of the shortcomings identified in Chapters 1 and 2 regarding the ability of NTA to make measurements of nanoparticle suspensions in which the particles are present in environmentally relevant conditions.

Optical techniques like dynamic light scattering (DLS) and nanoparticle tracking analysis (NTA) [149, 311] are able to analyse samples very rapidly (when compared with TEM approaches) by observing, either directly or indirectly, the Brownian motion of the nanoparticles in a solution. However, existing optical-based methods are only capable of measuring particles at concentrations above $\approx 10^8$ particles/mL [312].

An NTA-based approach was selected for this further development after identifying the limiting factors preventing current implementations from being effective at lower concentrations. Here is introduced and evaluated an NTA-based approach for ENPs capable of functioning at concentrations down to $\approx 5\times 10^5$ particles/mL – an improvement of 3 orders of magnitude compared to existing commercially available NTA instruments.

While such single-particle radii will carry a large degree of uncertainty, when a sufficiently large number of particles are tracked the method can be used to build up a good estimate of the size distribution of particles in the sample. Currently, the only commercially available NTA system is the Nanosight (Nanosight, Salisbury) which is described in full in [149]. This instrument is specified to perform well at concentrations of the order 10^8 particles/mL and above.

3.2 Materials and Methods

3.2.1 A bespoke NTA system

A completely open NTA system was developed and is shown diagrammatically in Figure 3.1 and as a 3-dimensional render in Figure 3.2. The system was built using almost exclusively off-the-shelf components with the aim of making it as quick, cheap, and easy to replicate as possible. A description of the system components and how they differed from the current commercially available system is provided below.

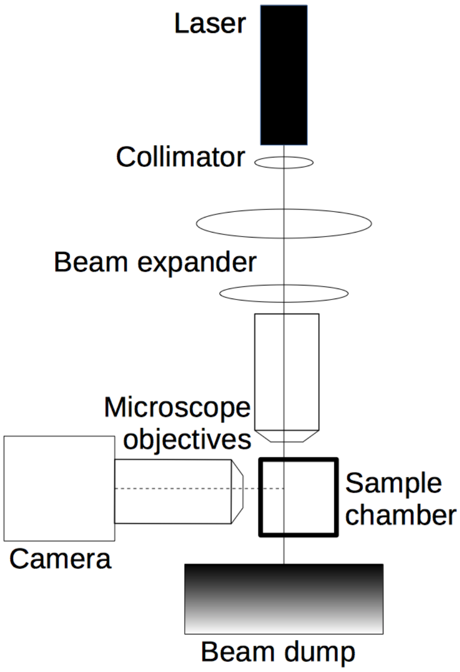

Figure 3.1: Diagram of the described apparatus. The solid vertical line denotes the optical path of the illumination beam, and the dotted line indicates the optical path of the scattered light.

Significant development work was undertaken to develop satisfactory solutions to various problems inherent in current commercial implementations of the NTA paradigm. Firstly, the (viewing) microscope objective was chosen to give as large a field of view as possible. In the first case, a 20× infinity corrected plan achromatic lens was used to give a very large field

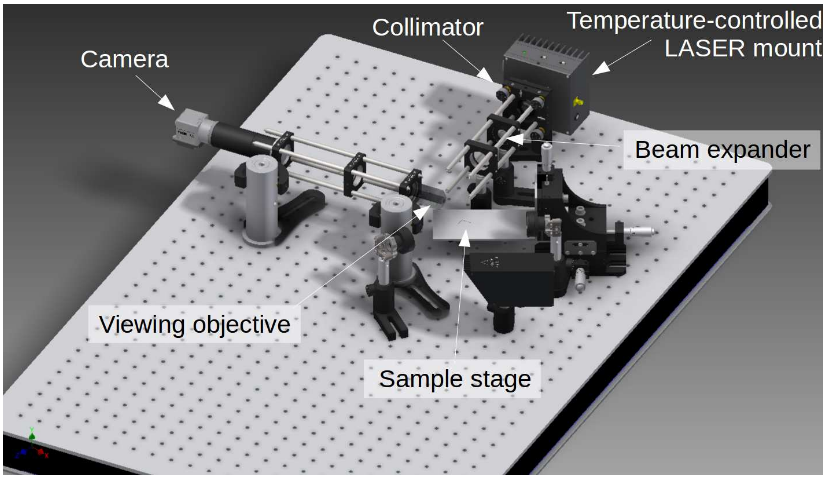

Figure 3.2: 3-dimensional render of the equipment shown in Figure 3.1.

of view. However, while some Brownian motion was detectable using this lens, the effective pixel size was too large to accurately estimate the diffusion coefficient for individual particles using this lens. Consequently, the microscope objective comprises of a 50× long working distance objective (Edmund Optics 50× EO M Plan Apochromat Long Working Distance Infinity Corrected) which has a working distance of 13.0 mm. This gives a field of view (FoV) $\approx$ 16,000 μm^2, approximately twice that of the Nanosight system. The long working distance was required in order that the lens be capable of focusing through the $\approx$0.7 mm thick wall of the sample chamber and so that a sufficient depth of fluid is between the inside of the chamber and the laser beam so that the laser doesn't illuminate and scatter off the wall; 13 mm is the working distance of the best commercially available option identified. This wasn't an issue with the lower magnification lens – less powerful lenses tend to have longer working distances anyway. This is illustrated in Figure 3.3. In common with the commercial Nanosight NTA system, a viewing angle of approximately 90° from the angle of illumination was used.

Because a much larger area is capable of being imaged, a more powerful laser was necessary to suffciently illuminate the larger volume. Here, a 400 mW 404 nm semiconductor laser diode (Thorlabs LP404P400M) was used. The shorter wavelength was chosen in order to allow the laser to couple more efficiently with smaller particles [313, 314]. Following initial trials, it was found that an additional solid-state peltier-based cooling system with a passively-cooled heatsink was necessary to hold the laser at a sufficiently constant temperature that particle tracking was realistically possible over time-scales of more than a few seconds.

Beam delivery was via an aspheric collimation lens, a basic condenser setup, and finally a 20× infinity-corrected microscope lens. Initially, when only using a 20× viewing objective, the use of a second microscope objective was unnecessary, but in order to maximally illuminate the smaller FoV afforded by the 50× viewing objective, the additional condensing objective was necessary. Experiments were also made using variable slit apertures to reduce the level of out-of-focus background, but this was found to yield no appreciable gain in image quality for a significant amount of additional alignment complication.

The larger FoV necessitated a high resolution camera in order to detect the small movement of the diffusing particles. Here an IDS UI-3240CP-C (Thorlabs, Cambridge) camera with pixel pitch of 5.3 μm was employed, leading to each pixel representing 105 nm of translation. The new camera also enabled a much higher frame-rate – up to 60 frames per second (fps) for a full FoV capture, or up to 229 fps for limited regions of interest. This high framerate could allow for further optimisation to measure smaller particles which diffuse more quickly. The camera was also fitted with a global shutter in order that particles travelling in different directions at the same velocity were not measured differently. This could occur because a rolling (non-global) shutter measures a single line at a time – a particle moving vertically would in one direction be measured earlier with each passing 'frame', and in the other direction would be measured later – an issue that is avoided by using a global shutter. The smaller pixel size on the higher-resolution camera further necessitated the use of a more powerful laser. The sample chamber comprised a 2.5 mL plastic spectrophotometry cuvette (Thermo Fisher, Winsford). One of the benefits of using such a large sample chamber in combination with such a powerful laser is that the laser is sufficiently powerful to excite convection. This convection rapidly achieves a constant rate in the region of 25 μm/s, weakly dependent upon the particle size, particle concentration, and sample volume, and can thereafter be used as a means of circulating the sample and allowing a greater proportion of the particles in the sample chamber to pass by the FoV than would otherwise be the case. Testing of the system showed that even with $<$100 μL of sample in the chamber, this convection was still present. This means that even when only a relatively small volume of sample is available, the benefits of the convection are still present.

Data for all analyses were recorded straight into a computer running Debian GNU/Linux and Matlab R2015b using a custom-written c++ framegrabber compiled as a matlab executables (MEx) function, allowing a single Matlab-based GUI to be used for both data capture and analysis. A sample was measured by recording 60 seconds of uncompressed video at a resolution of 1280×1024 pixels at 60 fps, 8 bits per colour channel. Because the camera was a colour model, only the blue channel was recorded, because for particles of the sizes measured this was the only channel containing any useful information. Each of these recordings was repeated a total of 5 times.

Analysis of these video stacks was also performed using Matlab. A derivative of the Matlab implementation of the Mosaic particle tracking package [315] was used as a starting

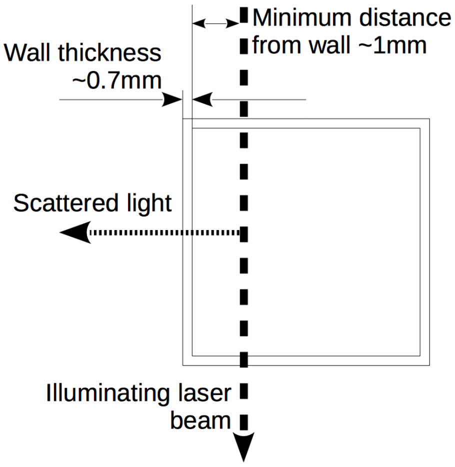

Figure 3.3: Diagram showing the sample chamber in plan view. This demonstrates the need for a viewing objective with a long focal length. The dashed vertical line denotes the optical path of the illumination beam, and the dotted line indicates the optical path of the scattered light.

point. The Mosaic package contains a number of scripts for iterative localisation and intensity determination of centroids to sub-pixel resolution, trajectory linking, and basic visualisation, parts of which are capable of taking advantage of modern multi-threaded processing hardware. Further code was written to allow for real-time visual feedback on changes to detection parameters and thresholds and demonstrate their effect, making analysis configuration as user-friendly as possible. This source code is provided as digital supplementary material, and instructions for the installation and use of this code is given in Appendix F. More detailed in instructions for the modification of the more complex parts of the code are given in Appendix G. A screenshot of the main window of the NTA software is shown in Figure 3.4.

3.2.1.1 Pre-processing of images

The analysis software includes several tools for the pre-processing of video images to eliminate noise and improve the ability of the Mosaic particle tracker to track the particles. The simplest of these is the implementation of some basic compression and thresholding to allow all pixels of intensity below a fixed level to be set to black, before all non-black pixels are re-scaled to cover the entire 8-bit gamut of the video codec. This can result in a much cleaner background with fewer stray local maxima which may be interpreted as particles. This is an implementation of the compression algorithm suggested by Gallego-Urrea et al [316] for the enhancement of NTA image contrast.

This does, however, come with a caveat – this approach can cause some of the local maxima which correspond to particles to become split in two, owing to some slightly darker pixels having been zeroed – this can lead to pairs of ‘particles’ being detected rather than just a single centroid. This is remedied by the inclusion of a variable gaussian blur which can

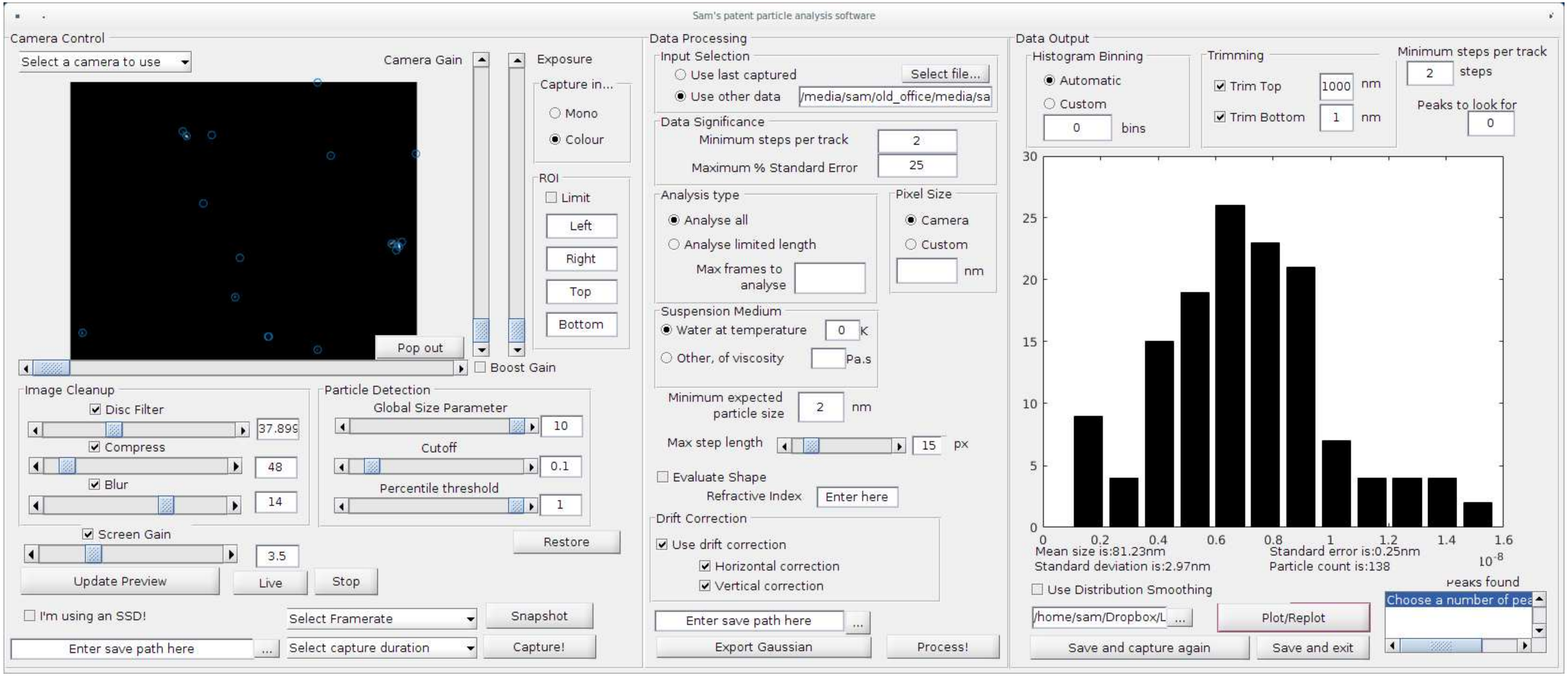

Capture in...
○ Mono
● Colour

ROI
☐ Limit
Left
Right
Top
Bottom

☐ Boost Gain

☑ Disc Filter 37.899
☑ Compress 48
☑ Blur 14
☑ Screen Gain 3.5

Global Size Parameter 10
Cutoff 0.1
Percentile threshold 1

☐ I'm using an SSD!
Enter save path here ...

○ Use last captured
● Use other data /media/sam/old_office/media/sa

Minimum steps per track 2
Maximum % Standard Error 25

● Analyse all
○ Analyse limited length
Max frames to analyse

● Camera
○ Custom nm

● Water at temperature 0 K
○ Other, of viscosity Pa.s

Minimum expected particle size 2 nm
Max step length 15 px

☐ Evaluate Shape
Refractive Index Enter here

☑ Use drift correction
☑ Horizontal correction
☑ Vertical correction

Enter save path here ...

● Automatic
○ Custom
0 bins

☑ Trim Top 1000 nm
☑ Trim Bottom 1 nm

Minimum steps per track
2 steps
Peaks to look for
0

Mean size is:81.23nm
Standard deviation is:2.97nm
Standard error is:0.25nm
Particle count is:138

☐ Use Distribution Smoothing
/home/sam/Dropbox/L ...

Figure 3.4: Screenshot of the custom-written NTA software used for capturing and processing the video data. It is split into three sections: video capture, video analysis, and data visualisation and output.

compensate for this effect. The use of gaussian blur can also correct for the influence of ‘hot’ pixels (pixels which are stuck ‘on’, and for speckle noise from other sources. Indeed, this is the same approach used by the Nanosight NTA software.

A more innovative approach to reducing the background which was also implemented in the software was the use of a ‘disc filter’. This effectively looks for circular objects (as the point-spread functions of particles should be), and darkens everything else, thus increasing the contrast between the particles and the background. It is possible to vary the size of the disc used to allow for differently-sized point-spread functions.

3.2.1.2 Analysis parameters

Most of the analysis parameters are completely self-explanatory (effective size of pixels, minimum number of steps to track a particle for etc), but a few warrant further explanation. Firstly, the ‘global size parameter’ gives the size of the ‘particle neighbourhood’. This parameter fulfils a dual function. If the software detects a centroid which is larger than this parameter (in pixels), then it will neglect to track it. Equally, if two detected centroids are found within this radius of each other, they are treated as a single particle. This has the positive effect that particles with rings around them (as slightly out-of-focus particles tend to) won’t be treated as several particles, and equally that particles crossing behind each other will not be accidentally swapped with each other upon crossing – they will just be neglected.

The ‘cutoff’ parameter gives the minimum likelihood of a detected centroid being a particle necessary in order to be tracked. This likelihood is calculated based upon the size of the local maximum, and the contrast between the local maximum and the background. The setting of this parameter is most effectively carried out using the available visual feedback to set the tracker to detect only particles which behave like particles when scrubbing through the video.

Also worthy of mention are the options for drift correction, minimum expected particle size, and data significance, which are all closely related. The drift correction allows for the suspending liquid to be in motion, either by intentional flow-through pumping, designed-in convection, or unwelcome/incidental convection. The drift correction option enables a drift-correction algorithm which calculates the time-dependent group velocity of detected particles and generates an apparent mean flow vector across the FoV. This frame-by-frame mean flow vector is then subtracted from the single-particle trajectories, thus deconvoluting the particle’s Brownian diffusion from the substrate motion. The minimum expected particle size option will throw away the data from any tracked particle with a diffusion coefficient sufficiently large that it would correspond to a particle smaller than this limit. This is important, because a large amount of background noise is generated by the tracking of random noise on the camera sensor which appears to jump around a lot. While a lot of this is removed by various algorithms already described, some still remains and needs to be removed. Similarly, the data significance option is used to set a maximum standard error permissible in the estimate of the diffusion coefficient for a single particle – particles with a standard error larger than the value of this parameter are assumed to be tracked noise or the result of the tracker jumping between two different particles, and are thus thrown away as bad data.

3.2.2 Evaluation of the system performance

ISO standard ISO17025 [317] contains a range of guidelines for the confirmation and calibration of different analytical methods. These guidelines allow analytical confirmations produced by one laboratory to be trusted by other laboratories. The approaches used in the guidelines were therefore employed to evaluate the new NTA system in terms of performance characteristics such as reproducibility, sensitivity and selectivity. The evaluation work was done using gold nanoparticles which were chosen because of their high refractive index (and therefore strong scattering), and because they are highly stable and not prone to dissolution or chemical interaction. Gold nanospheres of nominal sizes 30 nm and 100 nm (Sigma Aldrich, UK) were prepared in deionised water at 5 different nominal particle number concentrations: 10^9 mL^{-1}, 10^8 mL^{-1}, 5×10^6 mL^{-1}, 5×10^5 mL^{-1} and 10^4 mL^{-1}. For comparative purposes, the stock solutions of spheres were characterised by transmission electron microscopy (TEM) (JEOL 2011/JEOL 2200FS) and also run using a Nanosight LM14 instrument (Nanosight, Salisbury), equipped with a 532 nm 80 mW laser. Three Nanosight videos per sample were recorded; these videos were analysed using the supplied NTA3.2 software. The 30 nm particles were stabilised using a citrate coating, while the 100 nm particles were stabilised using phosphate-buffered saline (PBS). A description of the different evaluation steps is provided below.

3.2.2.1 Fundamental reproducibility

All samples were measured a minimum of 9 times (as suggested by the ISO guidelines). In order to ensure that the occasional failed measurement didn't cause the experiment to fail to meet this guideline, every sample was measured a minimum of 15 times at three different concentrations spanning the expected useful range of the instrument. Ten measurements per sample were also made at s beyond the expected detection limits in order to determine whether the effects of either small traces of nanoparticles or high concentrations are distinguishable from other causes for bad/failed measurements/noise.

3.2.2.2 Temporal stability

Analytical instrumentation may be adversely affected by local environmental factors. It is important that the instrumentation is robust to such interference, and will give the value for the same measurement regardless of possible temporally local interferences. To assess this, every measurement was repeated on different days of the week. Ideally, different spatial locations would also be tested, but this was impractical to verify.

3.2.2.3 Resistance to interference

It is crucial that any analytical technique has quantified limits of interfering contaminants that can impede, skew, or otherwise degrade the quality, reproducibility, and validity of the measurement. In the case of measuring engineered nanoparticles in natural waters, the principle source of interference is the presence of natural nanoparticles and organic matter. To assess interference from humic acids, an environmentally relevant concentration of humic acid (5mg/L) [249] was spiked into the 30 nm samples at all concentrations, and into DI water. These samples were than analysed. If separate populations of particles were visible representing the 30 nm ENPs and the HA, this was interpreted to mean that the methodology was immune to relevant levels of interference. If it was impossible to distinguish the two populations, or only a single population was detected at an incorrect size, then this was interpreted to mean that interference from the HA had prevented a successful measurement from being taken.

3.2.3 Analysis of video data

Data processing was done on the YARCC (York Advanced Research Computing Cluster), a small computing cluster based upon SGE (Sun Grid Engine). This allowed analysis to take place over a single weekend, rather than the month or more that would be required even on a more powerful personal workstation. An exemplar video frame is shown in Figure 3.5.

3.2.4 Visualisation and representation of results

When tracking a large number of particles over a number of frames, each particle will contribute an estimate of the mean particle size to the overall distribution. However, those particles which have been tracked for a larger number of frames should yield a more authoritative estimate. Brownian motion will always result in a certain variance of track lengths, but an unusually large variance could suggest that there has been a jump from tracking one particle of one size to another particle of a different size, meaning that the mean particle size this

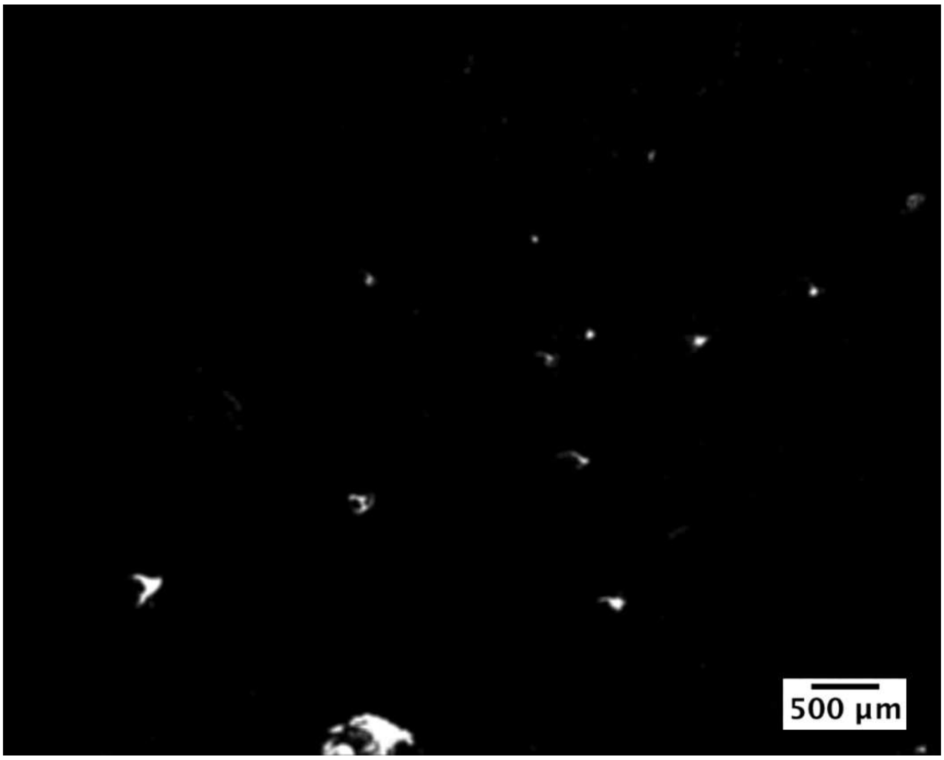

Figure 3.5: Representative frame of video, in this case taken from some 30 nm ENPs.

track contributes to the overall distribution is not necessarily representative of any of the particles present. Both of these effects can be minimalised by taking into account the variance in the contribution of each particle to the overall distribution. Rather than contributing a single count to a single bar of a histogram, each nanoparticle contributes a gaussian with unitary area (corresponding to a single particle), centered on the average estimate of the particle's size, but also with a corresponding variance. This is a simple means of incorporating an approximation to the uncertainty inherent in each single-particle measurement into the final measured output. This means each particle has still made an equal contribution to the area of the histogram and to the mean particle size, but the contributions of particles which are more likely to be truly representative of the particles in the sample give a larger weight to the localisation of particle size peaks. All the plots shown in this chapter have been treated this way.

3.3 Results and Discussion

3.3.1 TEM and Nanosight Characterisation

Representative TEM images of both ENP samples are shown in Figure 3.6. Nanosight-based NTA data is summarised in Table 3.1. Across the Nanosight videos, 4,213 particles in the 100 nm sample were tracked, along with 7,235 particles in the 30 nm sample. Usually, TEM analysis will give a similar or slightly smaller value for the particle size compared to that

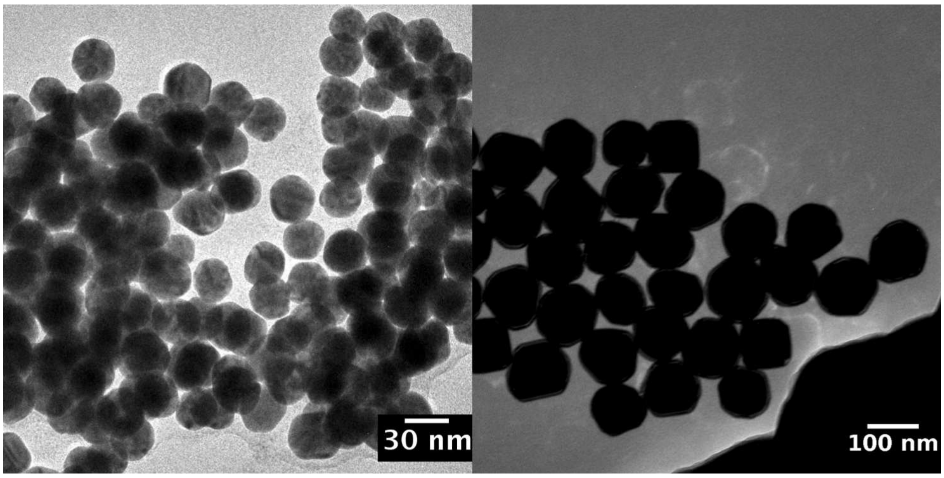

Figure 3.6: Representative TEM images of 30 nm (left) and 100 nm (right) ENPs used in this study.

measured using NTA because the physical size measured using TEM is slightly smaller than the hydrodynamic size measured by NTA. However, for the nominally 100 nm particles, the TEM measurement is significantly larger than the NTA measurement. This is possibly due to slight oblacity of the particles – so they lie flat on the TEM grid and expose their largest cross-section, while the NTA measurement is an average of all the axes of the ENP.

	30 nm ENPs	100 nm ENPs
Mean Size (Nanosight)	(62.9±1.9) nm	(89.6±13.0) nm
Mean size (TEM)	(29.8±2.6) nm	(106.2±13.1) nm
Modal Size (Nanosight)	(57.1±0.5) nm	(86.1±19.1) nm

Table 3.1: Summary of Nanosight and TEM characterisation analysis of both nanoparticle samples used.

3.3.2 Sensitivity

Representative plots for 30 nm and 100 nm particles are shown in Figure 3.7 and full results for all particles in all conditions are tabulated in Table 3.2. A complete set of plots for all measurements (including error bars) are attached in Appendix C.

In all cases the ENPs had their sizes accurately identified at concentrations of 5×10^5 mL^{-1}. A representative size distribution at this concentration is shown in Figure 3.8. Similar plots are provided for all ENPs at all concentrations at all measurement points in the supporting information. While at the lower concentration of 10^4 mL^{-1} the ENPs were occasionally accurately identified, however this was not reproducible either with time nor between different samples.

At high concentration, no samples were reproducibly measurable at 10^9 mL^{-1}. That is, while some measurements did indeed yield accurate sizes, this was not replicated between repeat measurements, and the majority of measurements failed to produce accurate size values.

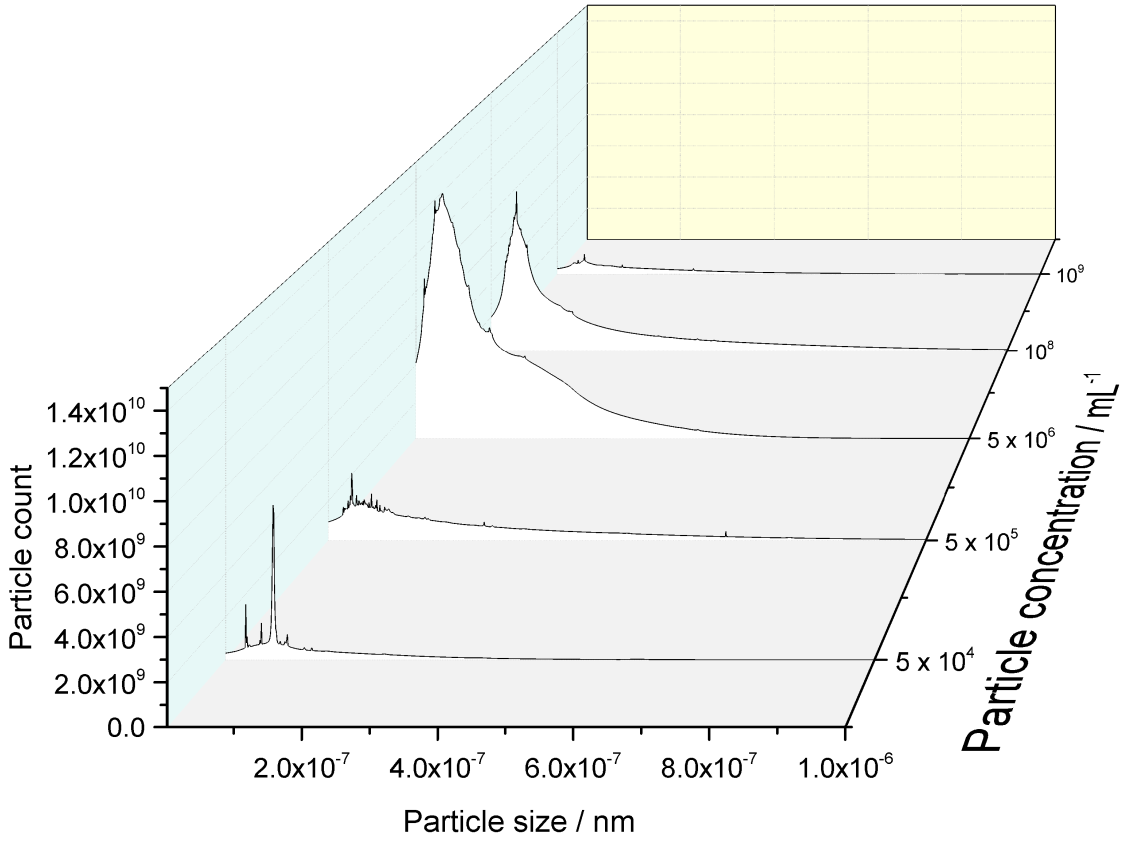

(a) Plot showing representative size distributions for 30 nm particles at all measured concentrations.

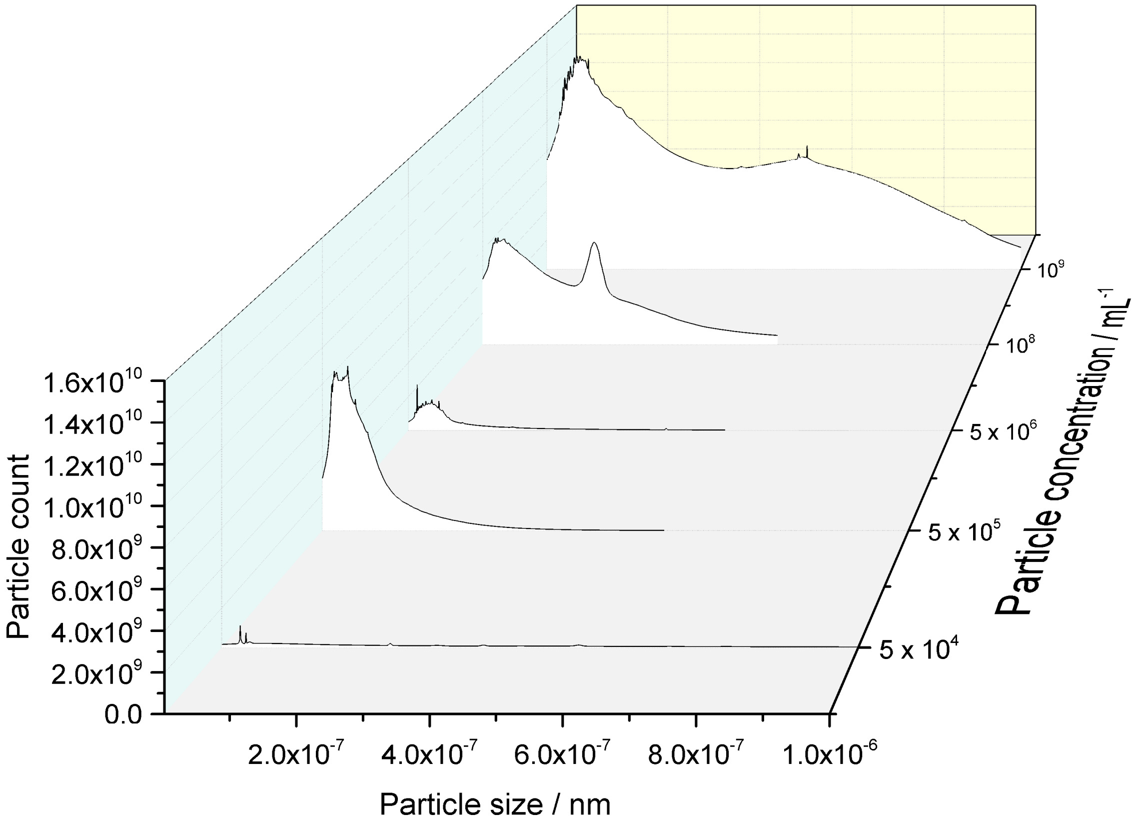

(b) Plot showing representative size distributions for 100 nm particles at all measured concentrations.

Figure 3.7: Representative plots showing the measured size distributions of nominally 30 nm (Figure 3.7a) and 100 nm (Figure 3.7b) particles at all five concentrations tested. Error bars are ommitted for clarity. Complete plots for all tests of all particles are provided in Appendix C.

Concentration	Replicate	10^9 mL^{-1}			10^8 mL^{-1}			5×10^6 mL^{-1}			5×10^5 mL^{-1}			5×10^4 mL^{-1}		
30nm Day 1	1	36	43		40	49	74	33	46	61	33	43	60	66	85	
	2				59	43	78	33	37	42	34	37	42	68	36	
	3				29	77	91	32	35	60	165	44	54	59	81	
	4	90	45					36	51	56	41	64	51	138	122	
	5	77	57		33	36					47	43		82		
Mean Peak		67.7	48.3		40.25	51.25	81	33.5	42.25	54.75	64	46.2	51.75	82.6	81	
30nm Day 2	1	58	38		52	48	24	32	49	98	32	39	73			
	2	45	136	80	51	45	40	36	50		41	51		33		
	3	37	112		50	46	71	20	35	17	42	49		35	33	
	4	52	92		33	30	41	35	39	69	35	60	88	75	57	
	5				30	36	48	38	45	58	41	74		96	93	
Mean peak		48	94.5	80	43.2	41	44.8	32.2	43.6	60.5	38.2	54.6	80.5	59.75	61	
30nm Humic acid	1	51	35	39	36	40	52	42	75	146	55	80	90	93	54	45
	2	55	49	33	40	46	78	69	75	51	73	38	109	33	59	41
	3	212	60	34	32	38	93	56	42	30	47	65	40	36	64	45
	4	64	47	32				63	52	29	55	92	10	60	75	13
	5	142	55	73				40	47	70	118	123	123	53	42	32
Mean peak		104.8	49.2	42.2	36	41.3	74.3	54	58.2	65.2	69.6	79.6	74.4	55	58.8	35.2
100nm Day 1	1	137	139	95	134	103	124	71	166	261	61	71	80			
	2				137	92	120	86	49	122						
	3				138	109	116				118			82	48	132
	4				124	90	165					148	101	91		
	5				81	121	155	64			198	65	77			
Mean peak		137	139	95	122.8	103	136	73.7	107.5	191.5	131.25	79	82.7	82	48	132
100nm Day 2	1	75	111	150	50	98	76				142	71	95			
	2	117	175	73	88	60	105				170	63	86	76	109	
	3	58	70	83	111	78	65	67	132		179	137		112	155	90
	4	54	99	134	191	80	66	93	69		68	97		163	110	
	5	86	109	124	109	65	81	86			102	156	124	145	77	
Mean peak		78	112.8	112.8	109.8	76.2	78.6	82	100.5		132.2	104.8	101.7	124	112.75	90

Table 3.2: Particle size peaks, as localised using the peak detection algorithm built into Origin Pro 2016. The three measurements at each concentration correspond to the three largest peaks detected in those results, given in size order from largest to smallest. All measurements are given in nanometres. When fewer than three modes were detected in a sample, fewer than three are given.

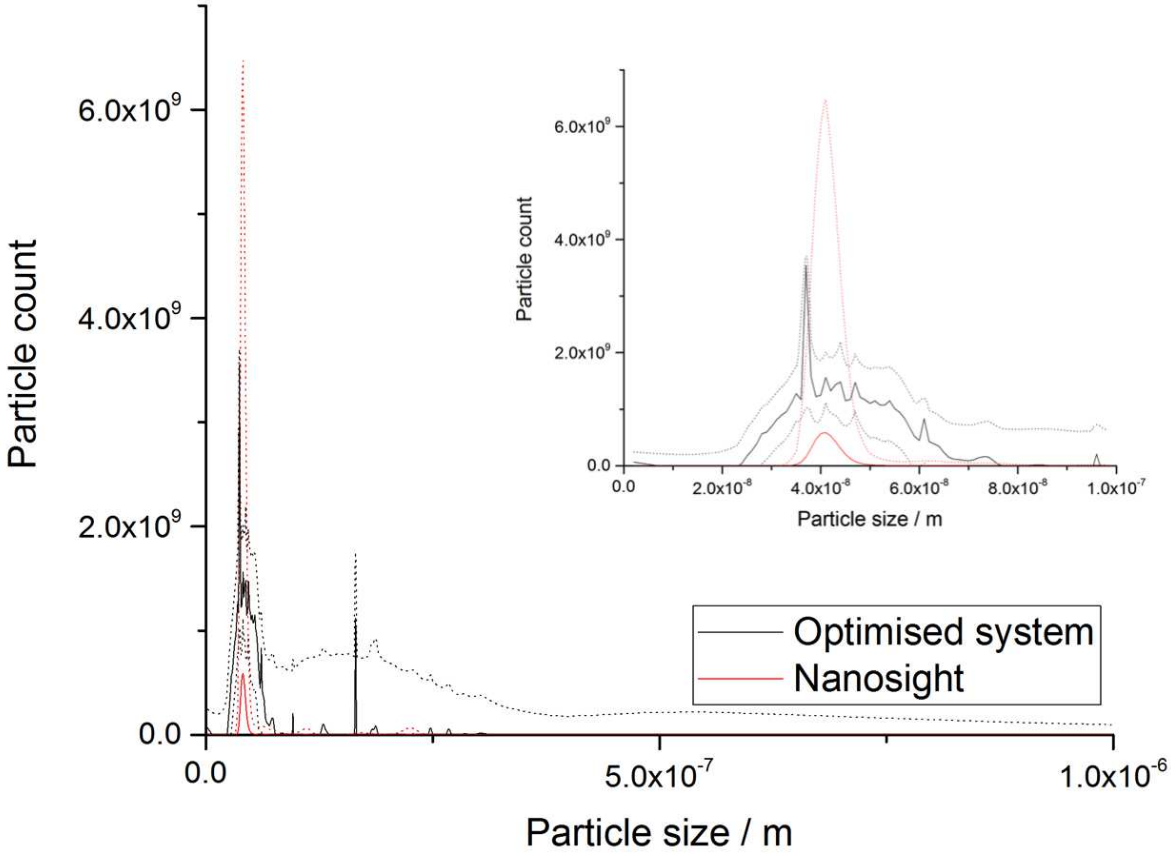

Figure 3.8: Representative size distribution plotted for 30 nm ENPs measured using both the Nanosight instrument at a concentration of 10^8 particles/mL and with the bespoke system at $5{\times}10^5$ particles/mL. The particle counts have been normalised in order to plot them on the same axes. Inset is a close-up of the detected modes. Dotted lines show standard errors.

However, at concentrations of 10^8 mL^{-1}, 30 nm ENPs were reproducibly measurable but 100 nm ENPs were not. This is possibly a result of the higher scattering efficiency of the larger particles – at higher concentrations the out of focus background is much larger, and more efficiently scattering ENPs increase this background. Therefore, at 10^8 mL^{-1}, it is likely that this background interferes with the detection and tracking of 100 nm ENPs while allowing 30 nm ENPs to be measured effectively.

At the highest concentration tested, 10^9 particles/mL, particles were not successfully identified in any case. There are two principal reasons for this. Firstly, because the system has a depth of field that is small compared to the width of the field, in order to sufficiently illuminate the FoV, a considerable depth which is out of focus is also illuminated. This causes a background which may be successfully removed computationally as previously described (see Section 3.2.1.1) at lower concentrations, but as concentrations rise, the difference of intensity between the light scattered by the in-focus particles and the out-of-focus noise becomes too small to accurately recover the particle locations. The other cause of this is the particle localisation. In order to minimise the occurrence of particle-jumping, whereby the particle tracker jumps from following one particle to following another and joining their tracks up, the mosaic particle tracker uses the concept of a ‘particle neighbourhood’, which is set to the same as the maximum jump of a particle between frames. If more than one particle is present in a single neighbourhood, then neither particle is tracked. As the concentration of particles increases, as does the incidence of particles being disregarded as too close to accurately and meaningfully track. This results in a dramatic reduction in the number of particles which are tracked and which contribute to the final particle size distribution.

In all cases, there is a considerable tail on each distribution. This is a statistical artifact generated by the fact that Brownian motion is only being measured in two dimensions. The tacit assumption is that the Brownian motion is equally partitioned between all three dimensions. This is a good approximation over very long observation periods, it becomes less good for shorter durations of a couple of seconds. If a particle is moving more in the unmeasured z-direction during measurement, then this will result in the particle being measured to be larger than it should be and vice versa.

3.3.3 Reproducibility and temporal stability

Measurements of all samples at all concentrations were repeated on at least 2 different dates. Additionally, all samples were measured both before and after a complete strip-down and rebuild of the equipment. In the case of the 30 nm Au ENPs, these were combined, but in the case of the 100 nm Au ENPs these were separate events leading to an extra set of measurements. To demonstrate the repeatability of the technique, results are shown for a single concentration of ENPs, though similar data is available for all concentrations. Only modes were considered, because identification of any larger aggregates present was of no interest – only the reproducibility of measurements of a single population of ENPs is of interest.

Modes were localised using Origin Pro curve fitting tools, which were also used to generate the standard deviations of these localisations. Summary statistics for all ENPs at 5×10^5 mL^{-1} are shown in Table 3.3.

Sample	Mode (nm)	Standard Deviation
30 nm Day 1	41.7	1.6
30 nm Day 2	41.3	1.0
100 nm Day 1	68.8	7.3
100 nm Day 2	81.4	10.1
100 nm Rebuild	65.4	8.2

Table 3.3: Summary of results for all samples at 5×10^5 mL^{-1}, testing for repeatability and temporal stability.

In the case of the measurements of nominally 30 nm particles over time, the measurements are not statistically significantly different at the $P<0.05$ level, so it was concluded that for ENPs of this size, measurements are reproducible and stable over time. Similarly, the measurements of nominally 100 nm ENPs remained stable over time, no individual pairing of measurements exhibiting statistically significant differences at the $p<0.05$ level.

3.3.4 Selectivity

In all the samples spiked with 5 mg/L HA, the ENPs were not successfully detected – in all cases either no particles were successfully tracked above the background, or only the HA particles were successfully tracked and no local maxima in the resultant size distributions corresponded to the ENPs. While particles were successfully detected and tracked at all ENP concentrations, the sizes of these tracked particles corresponded in no cases to the ENPs present; instead, very broad distributions of particles were seen, suggesting that the HA particles were completely eclipsing the ENPs. A representative size-concentration plot, in this case corresponding to a preparation of 10^8 mL^{-1} ENPs spiked with 5 mg/L HA, is shown in Figure 3.9.

Visual examination of the video frames captured from all samples spiked with 5 mg/L HA reveals a very high background. Equally, when configuring the camera to capture the HA-spiked samples, the gain setting needed to be set at about 5 % of the value used for all the other captures in order to prevent the camera from being over-saturated. A pair of representative video frames are shown in Figure 3.10, showing a frame containing 5 mg/L HA spiked into 30 nm 10^8 mL^{-1} ENPs, and a frame containing 5 mg/L HA spiked into DI water.

It is worthy of note that while at the higher ENP concentrations used by Park et al., the HA particles at a concentration of 5 mg/L occur with an HA:ENP ratio of ≈1:1, this ratio slips to ≈1000:1 when the ENPs occur at environmentally relevant concentrations. While it is simple to recover the measurements of ENPs when they constitute 50 % of the sample, it is not so facile to separate them when they constitute only 1 ‰ of the NPs present.

Despite these limitations, three-dimensional histograms were plotted to determine whether it was possible to use the difference in relative scattering efficiencies between gold and HA. A representative histogram is given in Figure 3.11. Clearly, there are no pairs of peaks of significant size which could reasonably correspond to separate signals from the gold and HA.

3.4 Conclusion

The new NTA system and software have been shown to be effective at measuring ENPs at near environmentally relevant concentrations of 5×10^5 particles/mL, up to 3 orders of magnitude

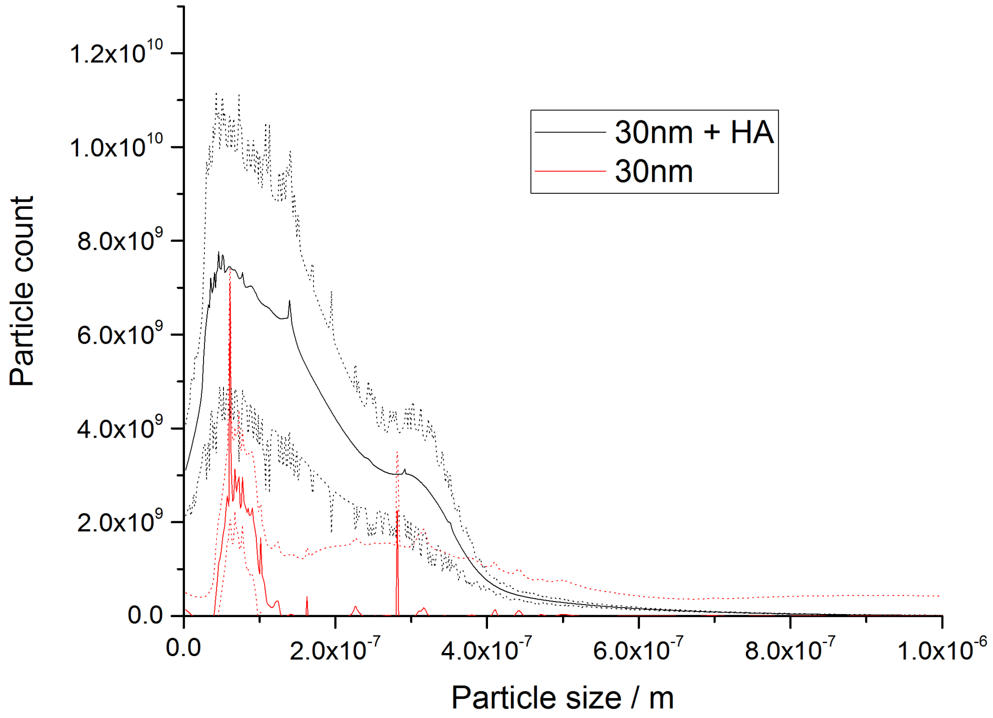

Figure 3.9: Representative size-concentration plot for a sample of 30 nm Au ENPs spiked with 5 mg/L HA. Also plotted is a sample of the same 30 nm ENPs in the absence of HA for comparison. Plots have been normalised so relative particle counts are arbitrary. Dotted lines show standard errors in curves of their respective colours.

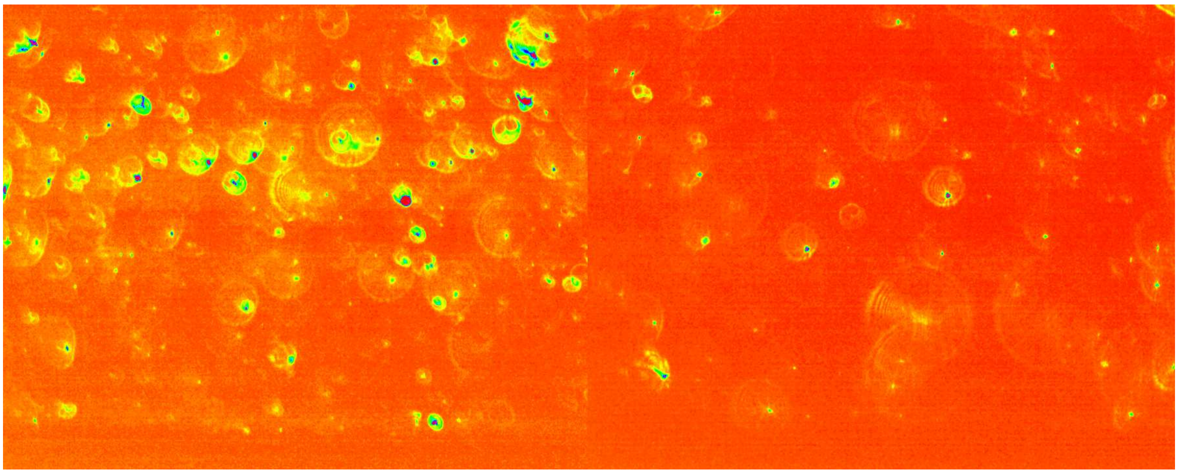

Figure 3.10: Representative video frames containing HA samples. On the left is a sample containing 30 nm Au ENPs with 5 mg.L^{-1} HA spiked in, while on the right is a sample containing no ENPs and 5 mg.L^{-1} HA. False colour has been added to enhance the clarity of the images.

lower concentration than current commercial systems. This has been verified against relevant guidelines in ISO 17025, which has demonstrated that in systems with little interference from other nano-sized objects the measurements taken are both robust and reproducible. However, studies investigating the interference from HA suggest that in the conditions tested, the presence of HA had a deleterious effect upon the resultant measurement. In order for

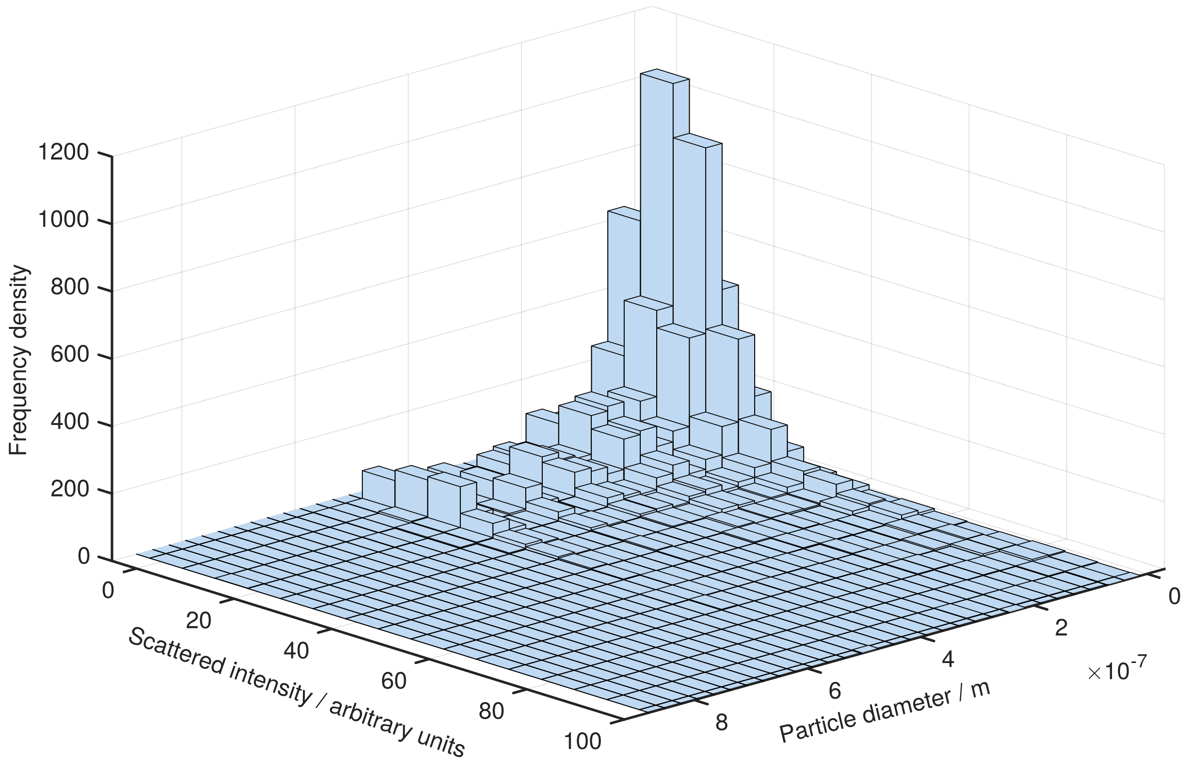

Figure 3.11: Representative plot showing the 30 nm gold particles in the presence of 5 mg/L humic acid. The particle size axis has been reversed in order to clearly show the whole 3-dimensional field. Note that it does not appear possible to differentiate the gold and humic acid when the particle number concentrations at this different.

optical techniques to be more widely useful at these lower concentrations, it is necessary that new and more effective methodologies for removing these organic particles from suspensions without effecting ENPs are developed. Examples of applications that the system is currently unsuitable for include the measurement of ENPs in most natural waters and measurements in artificial media whose ingredients include any significant quantity of natural organic matter.

This work could have a significant impact on a range of fields of science, not least because it renders measurements which were previously slow and expensive cheap and quick. Examples of this include the near real-time monitoring of suspended ENPs for long-term or chronic ecotoxicology assays, drinking water assessment and quality assurance, and nanoparticle behaviour studies at environmentally relevant ENP concentrations. Because the system is completely open, it is also possible to add additional features and apparatus with a minimum of effort. For example, it would be the work of minutes to fit a pair of Helmholtz coils around the sample chamber for the investigation of magnetic effects, magnetic hyperthermia, magnetic self-assembly of nanostructures and more.

Important avenues of study which have been opened up by this development include the measurement and characterisation of nanoparticle kinetics in suspensions at concentrations which were previously inaccessible on short and almost real-time time-scales. Furthermore, with some caveats regarding the organic content of the water, it will be possible carry out chronic exposure ecotoxicological studies while monitoring the ENP content of the water in near real-time.

This new low-concentration capability is demonstrated in Chapter 4, in which it is used to enable a study which would otherwise not have been possible using conventional approaches to NTA.

Chapter 4

NTA analysis of nanoparticle aggregation kinetics at environmentally relevant concentrations

The results in this chapter directly follow on from and build upon the methodologies developed in Chapter 3; the bespoke NTA system described therein is used to carry out an investigation into the aggregation kinetics of ENPs which would have been impossible using commercially-available apparatus. The experimental procedure is the same as a previously-published study which had some unsatisfactory aspects which are addressed here. This also allows many of the concerns raised in Chapter 2 to be addressed.

4.1 Introduction

Studies looking at the behaviour of engineered nanoparticles (ENPs) in suspension in water have been carried out quite intensively, examining a range of conditions, types of water, particle compositions, and particle coatings [31, 43, 100, 102, 119, 137, 318–325]. One of the processes which has been shown to be important in most ENP fate and behaviour studies is aggregation [326]. Broadly, there are two main classifications of aggregation: homoaggregation [327], in which ENPs adhere to other ENPs, and heteroaggregation [328], in which ENPs adhere to other natural nanoparticles (NPs), usually natural organic matter (NOM) [94] in the form of humic and fulvic acids [280], though interactions with clays and iron oxides are also included in this category [326]. Heteroaggregation with much larger NOM particles is sometimes referred to as adsorption, because the particles to which the ENPs adhere may be significantly larger then themselves, but because the norm in ecotoxicological nanoparticle studies is to use ‘heteroaggregation’. Because of the challenges of making robust measurements of ENPs at environmentally relevant concentrations, previous studies have all been carried out at concentrations several orders of magnitude greater than those which have long been predicted (and have recently been measured) in the environment [329].

It has been theorised that ENP aggregation processes at lower (environmentally relevant) concentrations will proceed vastly more slowly, but this has never been robustly demonstrated experimentally. Environmental fate models require a quantitative theory of ENP aggregation behaviour in order to make useful predictions [36], yet the only data on ENP aggregation in common environmental and ecotoxicological media has been taken at concentrations several orders of magnitude higher than those seen in the environment [249] or at undocumented concentrations [330]. This can lead to incorrect predictions of the rate at which ENPs aggregate, sediment, and eventually remove themselves from circulation in natural water systems, and eventually incorrect environmental risk assessments and potential unnecessary serious future risk to both humans and ecosystems. This is because the degree of toxicity of many nanoparticles is linked to their concentration [68]; under-estimated concentrations are therefore a hazard to be avoided.

Using a custom-built optical nanoparticle analysis system (as described in Chapter 3), it was demonstrated that at environmentally relevant concentrations, ENP aggregation doesn’t occur in most test systems at rates similar to those seen in previous studies carried out at higher concentrations.

4.2 Materials and methods

4.2.1 Selection of particles and concentrations

In the study of nanoparticle aggregation in a range of ecotoxicological media and natural waters by Park et al. [249], ENPs of concentration approximately 8×10^8 mL^{-1} were used. This concentration was chosen such that the particles could easily be measured at both the starting concentration and the likely post-aggregation concentration using the Nanosight nanoparticle tracking analysis (NTA) equipment (Nanosight, Salisbury). However, these concentrations are environmentally unrealistic – realistic environmentally-relevant concentrations are in the region of 10^5 mL^{-1} as discussed in Chapters 1 and 3. In order to get a better idea of how the ENPs actually behave in the environment, it is highly desirable to carry out these experiments at, or as close as is possible to, the concentrations predicted and measured in the environment.

Using the custom-built NTA system capable of making measurements of ENPs down to 10^5 mL^{-1} as demonstrated in Section 3.3, this can be accomplished. However, as ENPs aggregate their concentration decreases, so the starting concentration of the study has to be higher than the limit of detection of the equipment. For this reason, a concentration of 5×10^6 mL^{-1} was used. This is more than 2 orders of magnitude lower than the previous study [249], yet leaves sufficient headroom in the detection limit that even significant aggregation or sedimentation should leave a measurable concentration of ENPs in suspension.

As in the study by Park et al., a selection of ENPs with different capping agents with different modes of action were chosen. All particles were gold to prevent any dissolution or chemical interaction if the particle core interfering with the aggregation process or the measurement process. Electrostatically stabilised particles with a negative surface charge in deionised water at pH 7 were chosen, using a citrate capping agent. 30nm nominal particles were obtained form Sigma Aldrich (Southampton, UK). Positively charged particles with an amide-functionalised polyethylene glycol (PEG-NH_2) capping of the same nominal size were obtained from NanoCS (Colorado, USA). The same supplier was used for similarly-sized neutrally-charged sterically-stabilised ENPs with a PEG coating. All ENP sizes were confirmed using transmission electron microscopy (TEM) (JEOL2011, JEOL, Japan). Representative TEM images of all three samples are shown in Figure 4.1.

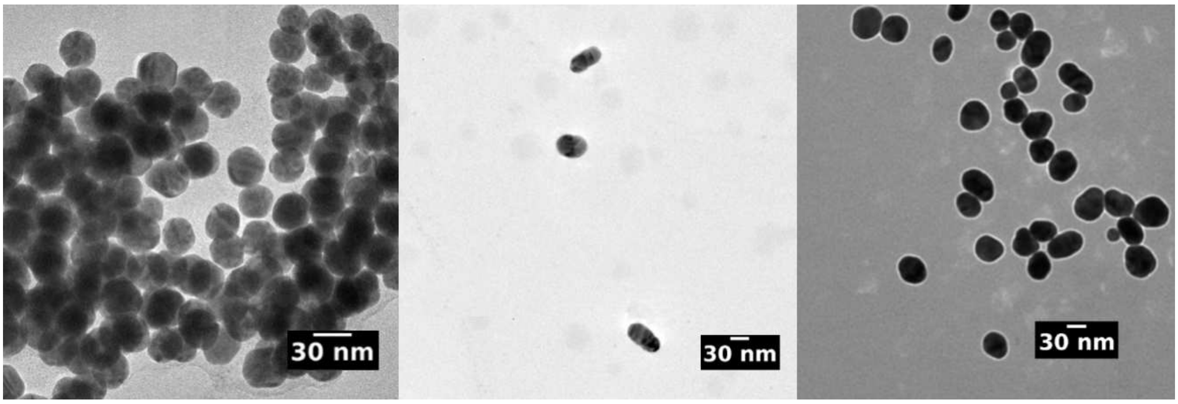

Figure 4.1: Representative TEM images of all three nanoparticle samples used. L-R Au-Citrate, Au-PEG, and Au-PEG-NH_2.

4.2.2 Measurement of nanoparticles at low concentrations

After the initial size measurements using TEM, all other measurements of all ENPs were measured at low concentrations using the custom built NTA apparatus from Chapter 3. This system is capable of measuring highly-scattering (usually metallic) ENPs in liquid suspension at concentrations down to a limit of approximately 10^5 mL^{-1}. Particles were also interrogated for shape, as described in Chapter 5.

4.2.3 Selection of conditions

Park et al. use a selection of natural waters in addition to a number of standard ecotox media when running their experiments. Rather than repeat every single combination of waters tested in the previous experiment, a decision was taken to focus on the more interesting of the conditions reported. In terms of ecotox media, artificial hard water (AHW) [331], artificial pond water (APW) [332], and artificial sea water (ASW) [333] were selected based upon the results of the previous study – ASW and APW gave some of the highest aggregation rates across the board, while AHW resulted in some relatively low aggregation, particularly given the relatively high ionic strength of the medium. DI water was also used as a control.

Unfortunately no natural water samples could be measured at the new low concentrations. This is because of interference in the measurement due to dissolved natural organic matter (NOM). This is discussed in detail in section 3.3.4. While in the study Park et al carried out this was not an issue – at 5 mg/L, humic acid (HA) particles occur broadly in number concentration parity with the ENPs so it is possible to account for them – in the low concentration study the HA particles outnumbered the engineered particles by more than 1000:1, which rendered it impossible to recover the ENPs when performing the analysis without additional sample pre-processing. When interpreting the results, it is worth comparing the results with those given in Figure 4.2 from Park et al. – in the case of citrate-capped particles the ecotox media tested bracket the natural waters perfectly, but for both other types of particles the aggregation in natural waters was always greater than the aggregation in any of the media.

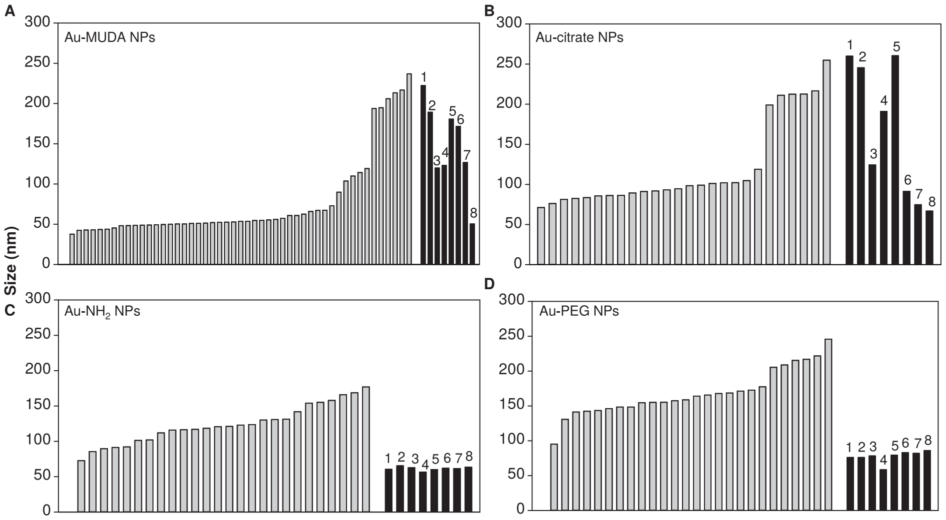

Figure 4.2: Plot showing the aggregation behaviour of four different nanoparticle samples, reproduced from [249]. The grey bars represent unidentified natural waters, while the black bars represent standard ecotoxicology media as follows: 1: APW, 2: M4 media, 3: ASW, 4: Algae growth media, 5: Lemna media, 6: EPA AHW, 7: EPA artificial medium hard water, 8: EPA artificial soft water. The *y*-axis gives mean hydrodynamic diameter as measured using a Nanosight instrument, while the ordering of the *x*-axis and identification of the different natural waters in the chart is ambiguous in the original publication.

4.2.4 Calculation of aggregation kinetics

The rate of aggregation of ENPs in suspension is dependent upon a range of factors. These include temperature T, attachment efficiency α_e (the fraction of collisions between particles which result in aggregation), the concentration of ENPs, [NP], the viscosity of the suspending fluid η, and the cross-sectional area of the ENPs σ. In order to describe the aggregation behaviour of ENPs is suspension we need to use all of these.

The mean free path of an ENP is the mean distance that an ENP travels within a suspension between collisions with other ENPs [334]. This quantity can be calculated from basic kinetic theory using the relation $\lambda = \frac{1}{\sqrt{2}\sigma[\mathrm{NP}]}$ from Chapter 1. In order to convert this into a collision rate, we need the mean velocity the ENPs are travelling at. Again, we can take a result directly from kinetic theory that $\bar{v} = \sqrt{\frac{2k_BT}{6\pi\eta r}}$ [146], where r_h is the sphere-equivalent hydrodynamic radius of the ENPs (assuming them to be perfect spheres). By taking the quotient of these two quantities the mean time elapsed between ENP collisions, Equation (4.1), is obtained.

$$\tau = \frac{\lambda}{\bar{v}} = \frac{1}{2\sigma\,[\mathrm{NP}]}\sqrt{\frac{6\pi\eta r_h}{k_BT}} \tag{4.1}$$

For ENPs at concentrations of $8{\times}10^8$ mL^{-1}, the approximate concentration of 30 nm diameter ENPs used by Park et al., these calculations give a mean free path λ of 0.156 m. By contrast, the mean free path for the same particles at the concentrations of $5{\times}10^6$ mL^{-1} used in this study works out to be some 24.75 m. In both cases, the time-averaged mean velocity comes to $4{\times}10^{-6}$ m.s^{-1} assuming measurements are taken at a temperature of 298 K. This means that for the particles at the higher concentration, the initial mean time between ENP collisions is approximately 10.7 hours, while for the particles at the lower concentration, the mean time between collisions works out to be approximately 1,700 hours.

This means that for the higher concentration particles, over the 48 hour duration of the study, assuming that the increase in particle cross-section through aggregation approximately compensates for a reduction in the concentration of particles through the same process, that the average particle will have collided nearly 5 times. In other words, the average particle has had 5 opportunities to form an aggregate. Conversely, the average particle in the low concentration study had just under 0.03 collisions in the same time frame, and therefore had very little opportunity to aggregate, even in the limiting case that the attachment efficiency is unity. Hence we can make the hypothesis that aggregation in the low concentration samples will proceed at approximately $\frac{1}{160}^{\mathrm{th}}$ of the rate observed at the higher concentration.

At this low aggregation rate, by the end of the study it is unlikely that any aggregates formed would be larger than dimers or trimers. These have a sphere-equivalent hydrodynamic diameter very similar to the original ENPs. A possible further means of determining the aggregation state of the ENPs lies in interrogating their shape. This could be achieved using the method described in Chapter 5. Since all particles started out nominally the same size and nominally spherical, and then any deviation from a spherical particle shape distribution suggests that some aggregation has occurred.

4.2.5 Experimental procedure

As in the study by Park et al., all samples were ultrasonicated prior to being observed over a duration of 48 hours. Nominally, the same time points for these measurements were used, measurements being taken at nominally 0 h, 1 h, 2 h, 4 h, 8 h, 24 h, and 48 h. Because it is challenging to take measurements at exact time points, measurements were made as close as was practically possible to these nominal elapsed times, but the actual times of data capture as recorded in the raw image metadata were used in all the analysis. This is why some samples have slightly different measurement times. pH measurements were taken of each sample coinciding with each measurement of particle size.

All samples were duplicated, and each duplicate was measured three times at each time point. Each measurement involved capturing 45 s of 1280×1024 8-bit video at 60 fps. All the data were collected during a single week to minimise the risk of interference from external sources differing for different samples. Possible examples of such ‘interference’ in this case would principally be sources of low-level background vibration which are commonly found in laboratory environments like vacuum pumps and air conditioning units. Analysis was carried out in parallel on York advanced research computing cluster (YARCC). The software and analysis of this NTA data is described in full in Section 3.2.3.

4.3 Results

The main body of results is summarised in Figure 4.3; enlarged versions of these plots are provided in Appendix D. In all cases except three, the changes in mean ENP size were statistically insignificant at the $p<0.05$ level, 2-way ANOVA. Of the cases in which a statistically significant change in mean particle size was seen, two of these were increases in mean particle size and one was a decrease. The standard deviations of the means are of a similar size to the standard deviations on the data of Park et al., only the published data neglects the variance in each replicate and considers only the variance between replicates. Representative TEM images of each of the three ENP samples are shown in Figure 4.1.

Statistically significant aggregation was seen only in the PEG-capped particles in APW,

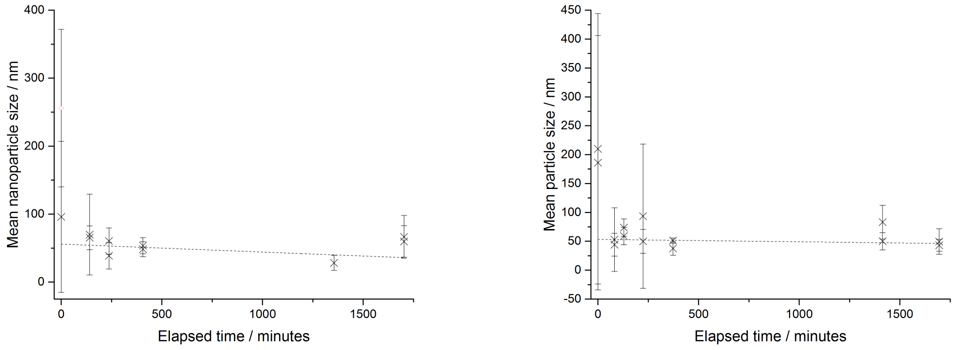

(a) Plot showing the time-evolution of particle size for 30 nm PEG-NH$_2$-coated particles spiked into artificial sea water.

(b) Plot showing the time-evolution of particle size for 30 nm citrate-coated particles spiked into de-ionised water.

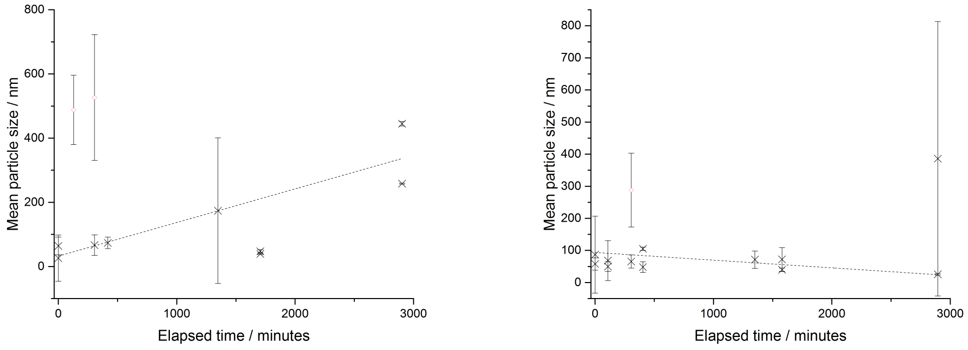

(c) Plot showing the time-evolution of particle size for 30 nm PEG-coated particles spiked into artificial pond water. In this case statistically-significant aggregation at the $p<0.05$ level was seen.

(d) Plot showing the time-evolution of particle size for 30 nm PEG-NH$_2$-coated particles spiked into artificial hard water. This is the single case where an apparent decrease in mean particle size was measured.

Figure 4.3: Representative plots showing the aggregation process as a function of time for a selection of particle-conditions combinations. Figures 4.3a and 4.3b illustrate examples in which no aggregation was detected. Figure 4.3c gives exemplr reslts from a coating-condition combination in which aggregation was observed, and Figure 4.3d illustrates the sole example of an apparent reverse in aggregation. A full set of plots covering all tested combinations of particles and conditions is given in Appendix D.

and in the citrate-capped particles in AHW. The only other statistically significant change in mean ENP size was seen in PEG-NH_2 capped particles in AHW, but this was a decrease in size. It is possible that this was due to the sedimentation of larger ENPs as observed by Park et al. However, at these lower concentrations it was not possible to directly observe this sedimentation if it was indeed present. This is surprising, as the AHW was chosen because of the relative stability of all the particles tested in it compared with the other media as reported by Park et al. In particular, the citrate-capped particles were reported to have aggregated several times more slowly in AHW than in APW or ASW.

The time-resolved pH data are given in Table 4.1. As can be seen, there is very little variation over time between samples except in deoinised water, where in the cases of the electrostatically-stabilised particles the pH drops rapidly during the first four hours, before stabilising. It is possible that this is due to the equilibration of the ions from the capping agents after spiking and ultrasonication, which occurred immediately prior to the first measurement point. It is possible that the reason this drop in pH was not seen in other samples is that the other ions in the ecotoxicology media act as a buffer to prevent a small number of ions from having a large impact upon the overall pH.

Samples were also interrogated for the shapes of particles. As shown in Figure 4.4, many of the samples at the nominal 48 h timepoint exhibited a tri-modal intensity distribution when all particles were treated as an ensemble – a clear evolution from the broadly mono-modal distribution seen at the 0 h timepoint. However, it was not possible to attribute different peaks to different particle shapes, and the existing theory is unable to adequately explain the origins of these peaks. Because the camera gain is uncalibrated, it was not possible to compare the relative intensities of peaks at different timepoints, so the exact evolution over time of the intensity distribution could not be followed. It is likely that the additional peaks suggest some degree of aggregation at a level below that detectable by examining the calculated size distribution. For example, partial dimerisation could cause the formation of an additional pair of peaks which correspond to some rod-like particles with an aspect ratio of 2:1.

4.4 Discussion

These results are closely aligned with the hypothesis – while at 8×10^8 mL^{-1} aggregation proceeded in a forwards direction at a rate sufficient that in all test cases it was readily measurable within the 48 hour timeframe. By comparison, at the more environmentally relevant concentration of 5×10^6 mL^{-1}, after 48 hours only 2 of the 12 combinations of conditions and particles yielded a measurable increase in particle size. Given that the reasons for this are

	ASW			AHW			APW			DI		
Time	Citrate	PEG	PEG-NH_2	Citrate	PEG	PEG-NH_2	Citrate	PEG	PEG-NH_2	Citrate	PEG	PEG-NH_2
0h 1	7.67	7.70	7.80	8.60	8.61	8.63	7.12	7.06	7.14	8.32	7.20	8.01
0h 2	7.69	7.88	7.88	8.42	8.61	8.61	7.13	7.10	7.19	8.30	7.04	7.64
1h 1	7.74	7.90	7.91	8.55	8.64	8.53	6.89	7.11	7.07	6.46	8.18	7.39
1h 2	7.83	7.92	7.93	8.54	8.61	8.61	6.98	7.08	7.09	6.48	7.98	6.97
2h 1	7.79	7.73	7.84	8.40	8.55	8.52	6.92	7.04	6.95	8.00	6.55	7.10
2h 2	7.84	7.87	7.91	8.43	8.57	8.52	6.99	7.09	7.16	7.73	6.36	6.96
4h 1	7.78	7.84	7.88	8.37	8.48	8.40	7.04	7.04	7.01	6.24	7.59	6.60
4h 2	7.82	7.86	7.90	8.35	8.44	8.44	7.03	7.12	6.96	6.23	7.21	6.44
8h 1	7.80	7.88	7.76	8.01	8.14	8.35	7.00	6.91	6.88	6.25	7.14	6.23
8h 2	7.82	7.88	7.87	7.95	8.31	8.32	7.02	6.93	6.78	6.22	6.62	6.12
24h 1	7.60	7.80	7.76	7.85	7.24	8.19	6.89	6.91	7.02	7.55	6.18	6.60
24h 2	7.76	7.85	7.83	7.90	8.24	8.25	6.91	6.90	7.04	7.14	6.17	6.46
48h 1	7.70	7.49	7.81	8.06	8.10	8.17	6.92	7.02	6.92	6.42	6.94	6.44
48h 2	7.80	7.63	7.83	8.14	8.16	8.26	6.94	6.99	6.95	6.34	6.80	6.34

Table 4.1: Table of pH measurements taken of every sample at every time-point. Times are nominal, not actual. Of particular note are the citrate and PEG-NH_2 particles in DI water, for which the pH drops off rapidly during the initial 4 hours.

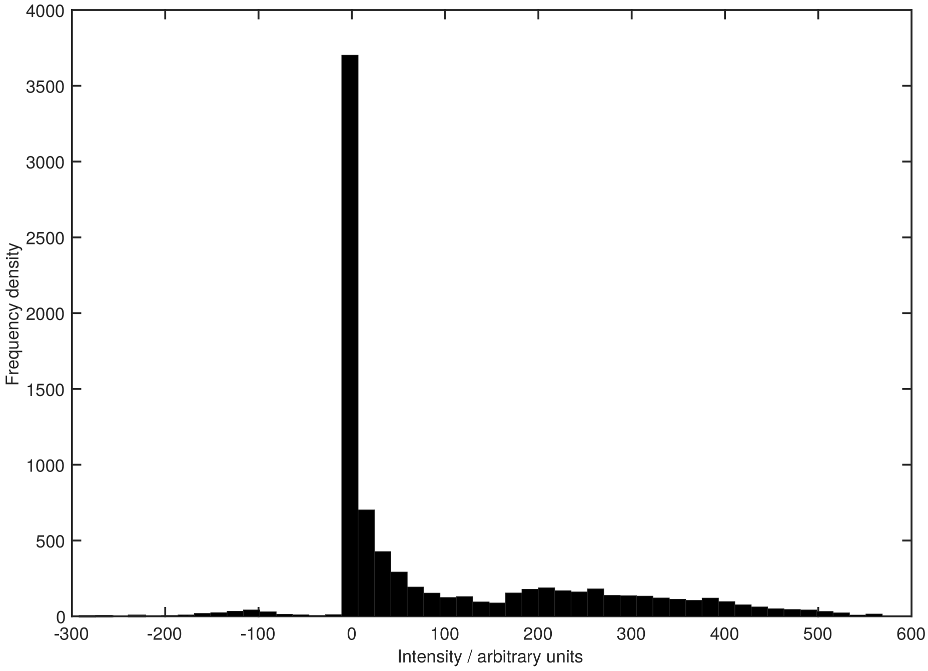

(a) Representative intensity distribution from a sample of PEG-NH_2-coated particles spiked into AHW at time = 0 h. Note how the distribution shape is broadly-speaking mono-modal, but there is already a small shoulder appearing to the right (as dominates the distribution in Figure 4.4b), suggesting that there has already been some activity in the short period between spiking and measurement.

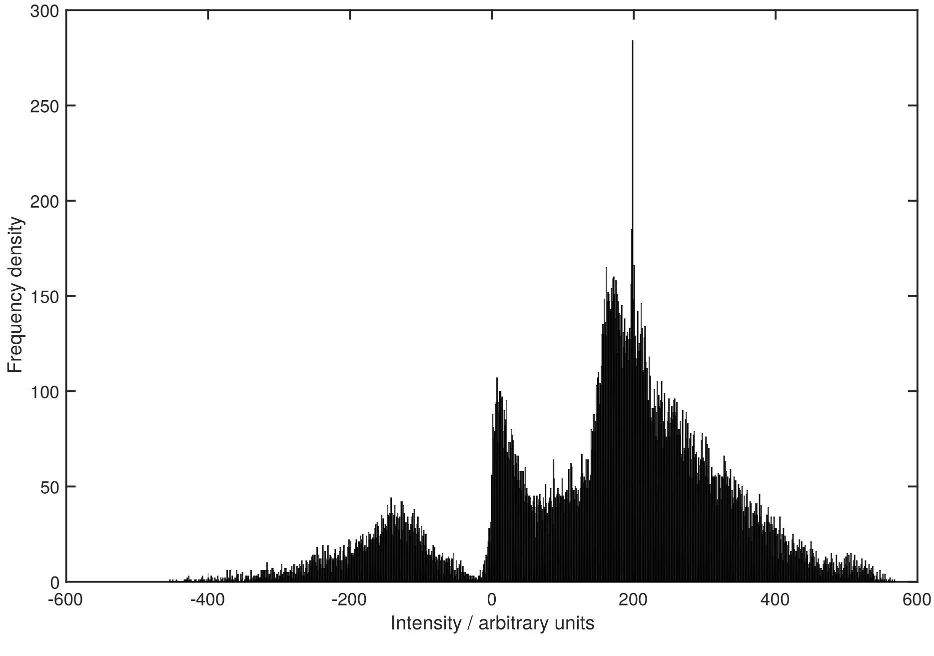

(b) Representative intensity distribution from a sample of PEG-NH_2-coated particles aggregated in AHW for 48 h. Note how the distribution shape is a poor match for any of the theoretical or experimental distributions discussed in Chapter 5.

Figure 4.4: Pair of plots showing the intensity distributions of PEG-NH_2-capped particles spiked into AHW at the first timepoint ($t = 0$ h), and final timepoint ($t = 48$ h). Note that the evolution with time suggests that there is a change in particle shape happening over time. Given that the particles are insoluble, this is probably driven by aggregation at a level too low to be reflected in mean particle sizes. Similar behaviour was seen across all samples to varying degrees.

well-understood, it is reasonable to extrapolate this result to even lower concentrations and infer that when ENPs are released into natural water systems in the quantities they currently are, that homoaggregation behaviour is not a major process affecting their eventual fate. This is in agreement with some experiments which have suggested that heteroaggregation and sedimentation can be dominant processes in the natural environment [335].

The concentrations of HA tested by Park et al. are environmentally accurate, and so while collisions between pairs of ENPs will be very rare, collisions between ENPs and NOM will occur with vastly greater frequency. Therefore, assuming that $\alpha_{e_{\text{NP-NP}}} \approx \alpha_{e_{\text{NP-NOM}}}$ and $\sigma_{\text{NP}} \approx \sigma_{\text{NOM}}$, heteroaggregation of ENPs with NOM will be the vastly dominant process compared to homoaggregation of ENPs, and will still proceed at a measurable rate if at all. Unfortunately, due to hardware limitations, this was not possible to verify. The natural consequence of this is that in natural waters with high NOM content, ENPs will collide frequently, permitting high aggregation rates given large α_e, while in waters largely devoid of NOM, the ENPs will remain unaggregated in suspension for much longer durations than current models may allow for.

The kinetics of ENP aggregation suggest that the aggregation seen in this study should initially occur at approximately $\frac{1}{160}^{\text{th}}$ of the rate observed by Park et al. However, the published dataset doesn't contain sufficient information to extract initial aggregation rates so a direct comparison in this way isn't possible. Taking the approximate gradient of the initial fast aggregation processes from the graphs published by Park et al. (an initial fast aggregation appears to occur up to about 75 nm per hour) and multiplying this by $\frac{1}{160}$ results in an approximate initial homoaggregation rate of ENPs in these experiments of 0.46nm per hour. Making the naïve assumption that the aggregation rate over the 48 hours of the experiment remained constant, this would equate to an increase in mean particle size of 22 nm. However, this data is only presented for MUDA-capped particles, which Park et al. show to aggregate in all the media tested in this experiment at up to about four times the rate of the Au-PEG-NH_2 and Au-PEG particles which were also used in this study. This suggests that a change in particle size of about 5 nm would be expected in these experiments using PEG and PEG-NH_2 coated particles in a 48 h timeframe. Given the uncertainty in the measurements of mean particle size, this 5 nm increase would not usually be statistically significant. This is faster than the kinetic theory suggests, as it would require more than one collision every 1,700 hours to reach this rate of aggregation, but the discrepancy could easily be due to the large uncertainties involved with the estimates taken from the data provided by Park et al.

The evolution of the distribution of scattered light intensities over time strongly suggests that a very low level of aggregation may be occurring, but it was not possible to extract any quantitative data from this approach. The weak dependence of sphere-equivalent hydrodynamic diameter of an aggregate upon the number of constituent particles, as described in Section 1.3.3.2, means that this is a very feasible explanation for the phenomena observed.

4.5 Conclusions

To conclude, this study has demonstrated that ENP homoaggregation is not a dominant process in ENP fate and behaviour in natural waters. This has important consequences for fate and behaviour modelling, and also for any subsequent environmental risk assessment. For example, while most existing environmental fate models used for environmental risk assessment consider homoaggregation to be an important process affecting nanoparticle fate, these results have cast serious doubt on that. In the case of a modelled system which previously relied upon homoaggregation to remove nanoparticles by aggregation and subsequent sedimentation, the eventual modelled concentrations would be very inaccurate, and could lead to significant nanoparticle pollution issues.

For a study duration of 48 hours, aggregation was only observed in two of the 12 particle-condition combinations tested. This confirms the hypothesis from kinetic theory that at environmentally relevant concentrations homoaggregation is no longer significant a contributor to environmental nanoparticle fate. Furthermore, the distribution of single-particle scattered intensities was used to infer the occurrence of a very low level of aggregation below that which was detectable by only considering the Brownian motion of the ENPs. Again, the possibility of this low level of aggregation agrees with the result derived from kinetic theory.

However, previous studies have shown that ENP interactions with NOM play a significant part in ENP fate and behaviour at much higher ENP concentrations, and there is no reason to doubt that NOM still plays an important role in determining ENP speciation, behaviour, and fate at environmentally relevant ENP concentrations and in the natural environment.

An obvious and desirable extension to this work would be the investigation of the precise effects of realistic concentrations of NOM on realistic concentrations of ENPs, though current NTA methodologies are not yet capable of making these measurements robustly and repeatably.

Chapter 5

Determination of nanoparticle shape from NTA data: theory, simulation, and experiment

In this chapter, the uses of the phenomenon of Rayleigh scattering (as described in Section 1.3.4.1) in the measurement of nanoparticles will be considered. Currently, its uses in this field are limited to being able to determine the size of particles [149], and to a limited extent, their composition [228]. Nanoparticle shape is of great relevance for ecotoxicology, and toxicology in general, for reasons which have already been discussed in Section 1.5.1.1. Chronologically, the material presented in this chapter comes immediately after Chapter 2, but is presented here in order to preserve the logical flow of research presented in Chapters 2, 3, and 4. For this reason, the tools described in Chapter 3 were not available at the time this work was carried out, and all the optical scattering data used herein was acquired using the Nanosight system.

5.1 Introduction

The optical measurement of nanoparticle size may be achieved by use of dynamic light scattering (DLS), which is also sometimes referred to as photon correlation spectroscopy (PCS), which leverages the Brownian motion of nanoparticles in a liquid suspending medium in order to infer a distribution of hydrodynamic radii from the autocorrelation decay of the scattered intensity of light, as the particles diffuse away from their initial configuration [202], as described in Section 1.4.3. Using more recent advances, the same result may be achieved using differential dynamic microscopy (DDM) [216] (see Section 1.4.4), or nanoparticle tracking analysis (NTA). In common with DLS, DDM is an ensemble technique that considers a sample in bulk, while NTA uses a microscope to individually track the points of light scattered by particles and can thereby ascribe individual hydrodynamic radii to each particle in its field of view [149].

Differentiation of individual nanoparticles by particle composition using optical means may only be achieved by NTA. Because NTA can attribute an individual hydrodynamic radius to each particle [149], it it possible to calculate the scattering efficiency on a particle-by-particle basis by using the intensity of the particle's scattered light. However, the technique is limited to differentiating between different species of vastly differing refractive indices only, and it is strictly qualitative. It isn't possible to analyse some gold particles and confirm them to be gold, but it is possible to analyse a mixture of gold and latex particles and confirm that there are particles of at least two different compositions present [67, 228].

Given that NTA is apparently the more flexible of the available optical techniques for nanoparticle analysis (see Section 1.4.6), it would appear to be an attractive technique for further development. Current commercially available NTA implementations do not attempt to take into account any non-spherical character of analytes; they assume that all particles are spherical, and will generate sphere-equivalent hydrodynamic radii for particles regardless of their actual shape. The manual for the Nanosight range of NTA instruments goes as far as to state that it isn't possible to derive any shape-related information from the light-scattering data. Herein it is demonstrated that this is not true for single-particle optical tracking, and that nanoparticles can be analysed for shape and size simultaneously using an off-the-shelf NTA setup.

The shape of nanoparticles is a very desirable property to measure for several reasons. As has been previously described and discussed, the behaviour and interactions of engineered nanoparticles in any medium is strongly shape-dependent [336,337], and there are specific traits which have been observed for specific structures including nanorods [9,338], nanoshells [313,339], and nanodiscs [264, 340]. These cited papers cover the full gamut of nanoparticle scenarios including medical applications for drug-delivery and direct therapy, use in self-assembly nanosystems, environmental interactions, and catalytic applications. Optical measurement of this property is particularly desirable because the only current alternative capable of making measurements of nanoparticle shape measurements is TEM. There are a plethora of situations in which TEM is an unsuitable technique for making such measurements, as has already been covered in previous chapters.

It is also salient to consider that one of the major areas which an optical nanoparticle shape measurement paradigm could be applied to is the quality control aspect of nanoparticles at the point of manufacture – currently quality control of non-spherical particles must be carried out off-line using TEM; development of an optical technique capable of carrying out real-time on-line measurements could have a significant effect of lowering the cost and increasing the quality of such non-spherical particles. Another area in which the optical measurement of nanoparticle shape could have a significant impact is the characterisation of exposure of organisms to aqueously-suspended ENPs of different shapes.

5.2 Theory

5.2.1 Polarisation and scattering efficiency

When a particle is moving under the influence of Brownian Motion, it is constantly being buffeted by molecules and particulate matter within the suspending medium. When these impacts hit the particle in question a non-zero distance from its centre of mass (CoM), they impart a torque upon the particle, leading to random rotation [341] in addition to the random translational motion described by Brownian Motion [342]. In a sphere, which is rotationally isotropic, this stochastic rotation has no detectable effect upon the light scattered, and may be ignored. However, for a particle that is rotationally anisotropic (in this chapter we shall consider the special cases of basic oblate and prolate sphereoids – rods and discs), there is a measurable time-resolved effect upon the intensity of scattered light.

The scattering efficiency of a sphere is dependent upon the polarisability α, a scalar quantity which may be calculated using the Lorentz solution, Equation (5.1)

$$\alpha = \frac{3\left(n_a^2 - 1\right)}{4\pi\left(n_a^2 + 2\right)} V = \frac{\left(n_a^2 - 1\right) r_p^3}{n_a^2 + 2} \tag{5.1}$$

where n_a is the complex refractive index, V is the volume of the particle, and r_p is the radius [153].

However, for a rotationally anisotropic sphereoid, the polarisability must be expressed as a tensor property. Qualitatively, taking the example of a nanorod, it will be considerably more polarisable along the length that across the diameter. Consequently, when the illuminating electric field aligns with the principle axis of the nanorod then the nanorod will scatter very strongly, and when the principle axis of the rod is orthogonal to the electric field, it will only scatter weakly. Van de Hulst [156] shows that for such a sphereoid, if orientated such that one of its semi-axes is parallel to the illuminating laser beam, the polarisability tensor becomes diagonalised, and the j^{th} diagonal element may be calculated from Equation (5.2),

$$\underline{E} = \underline{E}_0 - L_j \cdot 4\pi \underline{P} \tag{5.2}$$

where $\underline{E}_0$ is the incident electric field, $\underline{E}$ is the effective electric field, $\underline{P}$ is the polarisation per unit volume, and L_j is a function depending upon the ratios of the three semi-axes to each other.

This can then be used to calculate the L_j by cyclic permutation from Equation (5.3), giving Equations (5.4) and (5.5).

$$L_1 = \int_0^\infty \frac{abc_n \,\mathrm{d}s}{2\left(s+a^2\right)^{\frac{3}{2}}\left(s+b^2\right)^{\frac{1}{2}}\left(s+c_n^2\right)^{\frac{1}{2}}} \tag{5.3}$$

$$L_2 = \int_0^\infty \frac{abc_n \,\mathrm{d}s}{2\left(s+c_n^2\right)^{\frac{3}{2}}\left(s+a^2\right)^{\frac{1}{2}}\left(s+b^2\right)^{\frac{1}{2}}} \tag{5.4}$$

$$L_3 = \int_0^\infty \frac{abc_n \,\mathrm{d}s}{2\left(s+b^2\right)^{\frac{3}{2}}\left(s+c_n^2\right)^{\frac{1}{2}}\left(s+a^2\right)^{\frac{1}{2}}} \tag{5.5}$$

where a, b, and c_n are the three semi-axes, and s is a convenient integration variable.

By contemplating only oblate and prolate sphereoids, only the cases for which $b = c_n$ are considered. In the prolate case, $a > b$, and in the oblate case, the inverse is true. It is possible to solve Integral (5.3) for the two cases respectively, as shown is Equations (5.6) and (5.7),

$$L_{1_{\mathrm{prolate}}} = \frac{1-e_p^2}{e_p^2}\left[-1+\frac{1}{2e_p}\ln\left(\frac{1+e_p}{1-e_p}\right)\right] \tag{5.6}$$

$$L_{1_{\mathrm{oblate}}} = \frac{2-e_p^2}{1-e_p^2}\left[1-\frac{1}{1-e_p}\arctan\left(1-e_p\right)\right] \tag{5.7}$$

where $e_p^2 = 1 - \frac{b^2}{a^2}$ [156].

By substitution for $\underline{P}$ from Equation (5.2) using the relationship $\underline{P}V = \alpha_j \underline{E}_0$, it is possible to calculate α_j using equation (5.8),

$$\alpha_j = \frac{V}{4\pi\left(L_j + \frac{1}{n_a^2-1}\right)} \tag{5.8}$$

where all variables are as previously defined, and α_j is a set of the three diagonal elements of the polarisability. Clearly, either Equation (5.6) or Equation (5.7) could be used to substitute for L_j as appropriate.

Using this relationship, it should be possible to estimate α_j if some experimental means of estimating the L_j and V is found without requiring direct measurement of any polarisation or electric fields.

5.2.2 Intensity distribution shape

Averaged over a long period of time, or over a large number of identical particles, it may be assumed that all possible orientations of the particles occur with identical frequency. Given this assumption, it is necessary to demonstrate whether this may have an observable effect upon the shape of the intensity distribution. In the simplest case, consider a 1-dimensional nano-rod of length l forming an angle θ with the axis of the electric field of a polarised laser source. the polarisation $\underline{P}$ of the rod should vary with θ as $\underline{P} = \underline{E}\alpha l \cos(\theta)$. This is illustrated in Figure 5.1. This only needs to be evaluated for $0 \leq \theta \leq \frac{\pi}{2}$, because all other values of θ produce symmetrical results. Because scattered intensity scales as the square of polarisation and therefore electric field, the scattered intensity scales with $\cos^2(\theta)$.

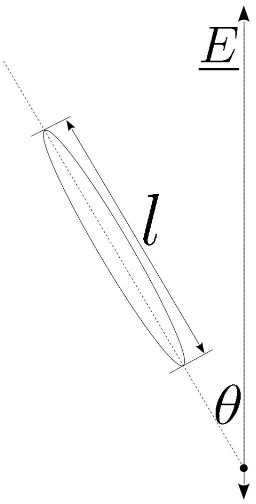

Figure 5.1: Schematic illustrating the origin of the cosine term in the relationship between angle of particle and scattering efficiency.

However, the nanoparticles in question are not simple 1-dimensional entities. If this is generalised to a 2-dimensional nano-rod with semi-major axis l which will still make an identical contribution to the scattering behaviour, and with a semi-minor axis d. Because l and d are perpendicular, when $\theta = 0$, polarisation in the d direction will be zero; indeed simple trigonometry demonstrates the d contribution to the scattered field to scale as $\underline{P} = \underline{E}\alpha d \sin(\theta)$. The total contribution from both possible axes of polarisation to the total scattering intensity pattern is therefore the sum of these, this is given in Equation (5.9),

$$I = \underline{E}^2 \alpha^2 \left[l^2 \cos^2(\theta) + d^2 \sin^2(\theta) \right] \tag{5.9}$$

valid for the region $0 \leq \theta \leq \frac{\pi}{2}$. This gives rise to stationary points at $\theta = 0$ and at $\theta = \frac{\pi}{2}$. This is illustrated in Figure 5.2. In this case, scattering efficiency is a completely arbitrary relative measure of the scattering power of the particle in a given orientation, and can take any value from 0 (no scattering occurring) to 1 (the most efficient scattering observed for the particle in any configuration).

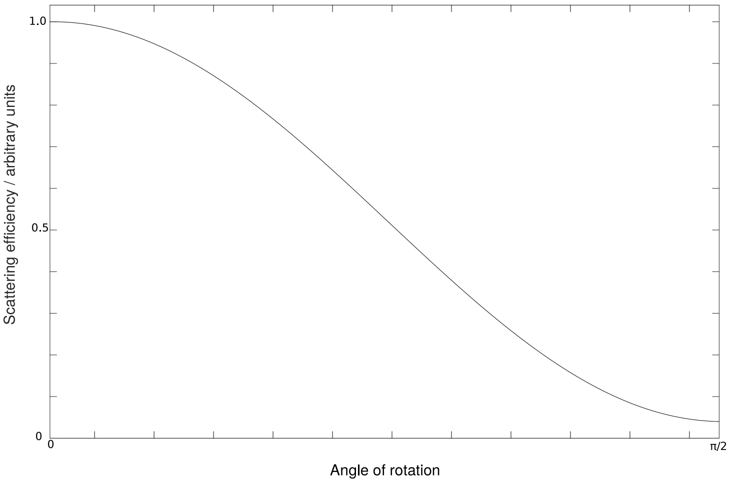

Figure 5.2: Plot showing theoretical scattering efficiency of a 2-dimensional nanorod as a function of angle, for the region $0 \leq \theta \leq \frac{\pi}{2}$. Note the two stationary points at $\theta = 0$ and at $\theta = \frac{\pi}{2}$.

This is of little direct use – at no point in the measurement process is the angle formed between the scatterer and the incident field known. However, since the gradient of the curve is smallest in proximity to its stationary points, it is possible to plot a curve which is distinctive with no assumed knowledge of θ other than the assumption that over a sufficiently long duration, all possible values of θ will have been recorded with approximately equal frequency. Exactly what the minimum duration of observation required in order that this approximation is justified is unclear, and would need to be verified experimentally. If a histogram is plotted from all the different scattered intensities for all values of θ, then there will be maxima at the most frequently-occurring intensities. Such a histogram, made using the simulated data used to plot the graph in Figure 5.2, is shown in Figure 5.3. Because of the gradient profile of the initial distribution from Figure 5.2 (the rate of change of the gradient is smallest near $\theta = 0$ and $\theta = \frac{\pi}{2}$, hence an equal distribution of samples from this background distribution will result in a histogram with two modes at the extrema of intensity), this will be a bimodal distribution with frequency peaks occurring at intensities that correspond to angles of $\theta = 0$ and $\theta = \frac{\pi}{2}$. These two peaks will be of identical heights, and therefore can offer no information on whether the nanoparticle is a rod or a disc; indeed the differentiation makes no sense in a 2-dimensional approximation.

Adding in a third dimension requires a second angle ϕ to be introduced. For a rod, variation of ϕ has no effect upon the polarisation when $\theta = \frac{\pi}{2}$, but does have an effect when $\theta = 0$. This means that, should both vary completely randomly, then the scattering efficiency

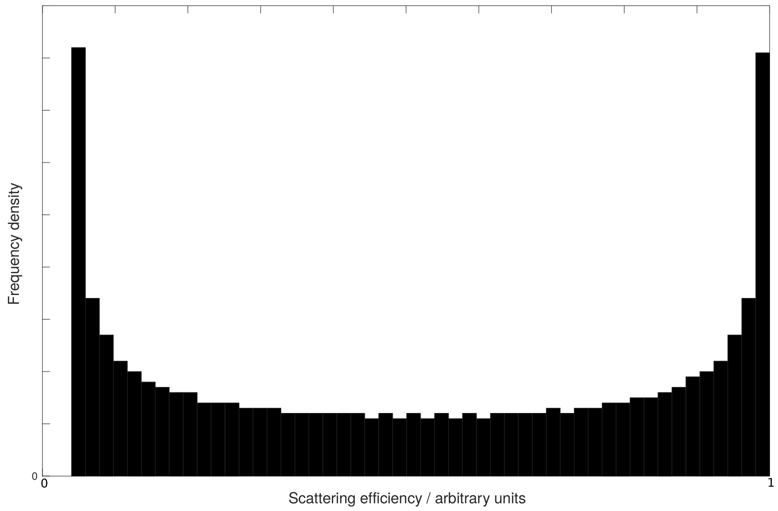

Figure 5.3: Plot showing theoretical histogram for a 2-dimensional rod, plotted using the same data used to plot the graph shown in Figure 5.2.

corresponding to the 2-dimensional case of $\theta = \frac{\pi}{2}$ should occur with double the frequency of the efficiency seen at $\theta = 0$ in the final scattering histogram. The converse is true for a disc. In this case, the variation of ϕ has no effect when $\theta = 0$, but does have one at $\theta = \frac{\pi}{2}$, which leads to the scattering behaviour seen at $\theta = 0$ occurring with twice the frequency of $\theta = \frac{\pi}{2}$. The result of this is that for a rod, with the shortest semi-axis repeated, there are twice as many low-scattering configurations as highly-scattering configurations. This means that the low-intensity peak in the resultant histogram will have approximately double the height of the high-intensity peak. The converse is true for discs, which repeat their longer semi-axis, and will therefore have a larger high-intensity peak in the intensity histogram. Theoretical distributions showing this are given in Figure 5.4.

Thereby it should be possible to use the shape of the measured intensity distribution to determine whether the particle is spherical by the presence of one or more intensity peaks, and furthermore classify non-spherical particles as either rods or discs.

5.2.3 Calculation of nanoparticle dimensions

If we proceed from Equation (5.2) by substituting $\underline{P}$ in terms of L and using the relationship $I = \frac{c}{8\pi} \left|\underline{E}\right|^2$, the scattered intensity may be written as

$$I = \frac{c}{8\pi} \left| \underline{E}_0 \left(1 - \frac{L_j}{L_j + \frac{1}{m^2-1}} \right) \right|^2 \tag{5.10}$$

This can be rearranged to express L_j as a function of I and $\underline{E}_0$. Then choosing L_j and L_{j+1} and taking their ratio allows $\underline{E}_0$ to be eliminated (since $\underline{E}_0$ remains the same for all

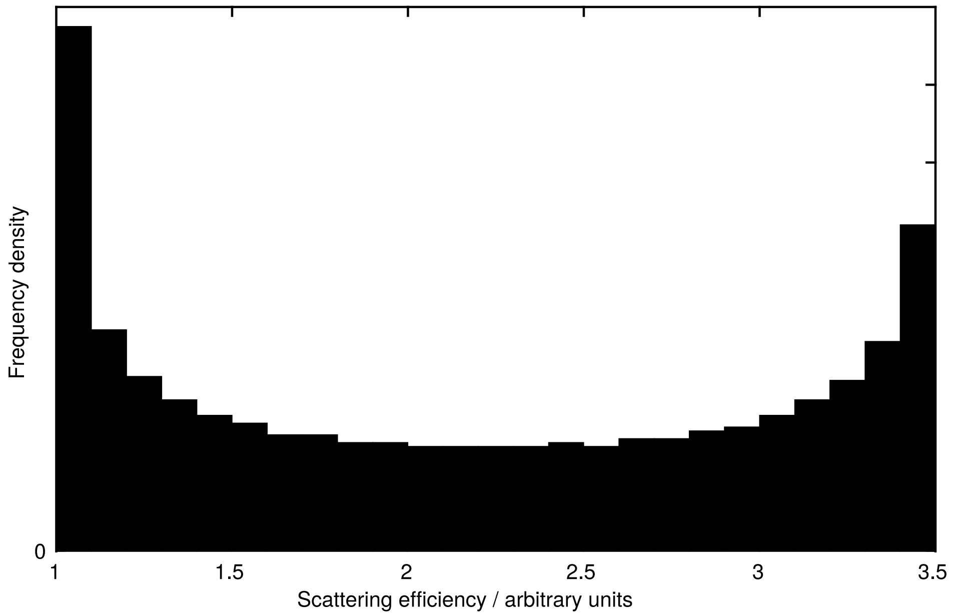

(a) Histogram showing the theoretical scattering efficiency distribution of a rod-shaped particle. Note that the scattering peak at lower efficiency is approximately twice as far above the baseline (in the centre of the distribution) as the peak at higher efficiency.

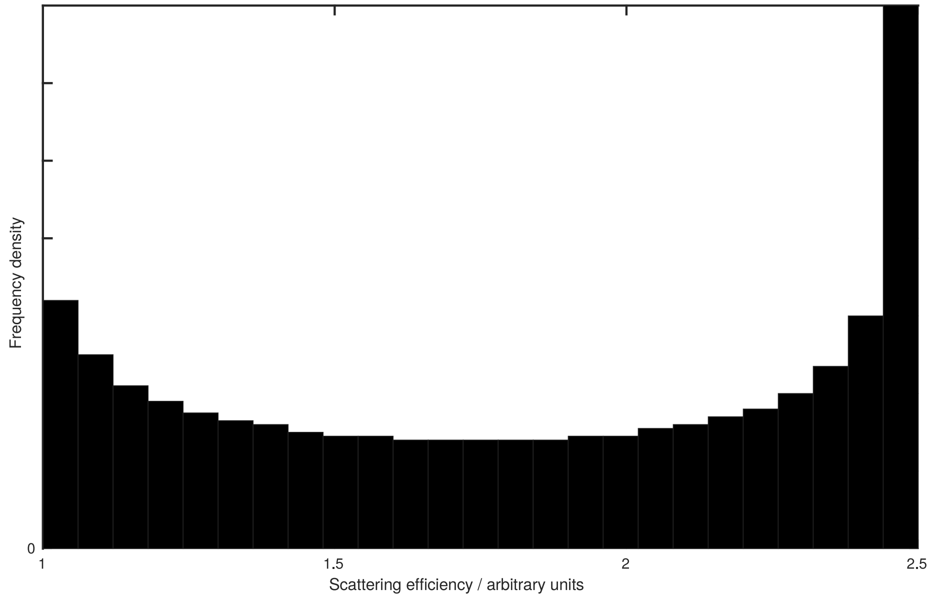

(b) Histogram showing the theoretical scattering efficiency distribution of a disc-shaped particle. Note that the scattering peak at higher efficiency is approximately twice as far above the baseline (in the centre of the distribution) as the peak at lower efficiency.

Figure 5.4: Theoretical histograms showing the scattering efficiency for a rod-shaped particle (5.4a) and a disc-shaped particle (5.4b). These are three-dimensional generalisations of the two-dimensional histogram shown in Figure 5.3.

nanoparticle configurations). Thereby it is shown that the ratio of intensities at each intensity which corresponds to an alignment with the incident electric field is directly correlated to the ratio of the squares of the associated L.

It is then possible to express the ratio of the L_j to each other as a function of m, the I_j, and Ξ, where $\Xi = 2\sqrt{\frac{2\pi}{c}}$, as shown in Equation (5.11).

$$\frac{L_{j+1}}{L_j} = \frac{\left(\pm\left(m^2-1\right) - \Xi I_{j+1}^{\frac{1}{2}}\right) I_j^{\frac{1}{2}}}{\left(\pm\left(m^2-1\right) - \Xi I_j^{\frac{1}{2}}\right) I_{j+1}^{\frac{1}{2}}} \tag{5.11}$$

Because we are only considering cases when α is a diagonalised tensor, and α is only diagonalised when $\underline{E}$ is aligned with a semi-axis of the particle, these I_j must therefore correspond to the intensities of the intensity peaks calculated in Section 5.2.2. They may be experimentally found, or predicted numerically using the stationary points of the scattering efficiency as a function of particle orientation.

Because $\Xi I^{\frac{1}{2}}$ is always small compared to $m^2 - 1$ (in the extreme case that I corresponds to the entire intensity of the incident laser beam, $\Xi I^{\frac{1}{2}}$ will still be $\approx$1% of the magnitude of m^2-1 for a highly-scattering metal), the $\left(m^2-1\right) - \Xi I_j$ terms will always very nearly cancel for any m, leaving Equation (5.12).

$$\frac{L_{j+1}}{L_j} = \sqrt{\frac{I_j}{I_{j+1}}} \tag{5.12}$$

All that remains is to relate these parameters to the dimensions of the particles, which can be done using the measured sphere-equivalent hydrodynamic diameter from the same NTA data. By rearranging Equation 5.8 for L and substituting, bearing in mind the two approximations $\Sigma L_j = 1$ and $L_1 : L_2 : L_3 = \frac{1}{a} : \frac{1}{b} : \frac{1}{c_n}$ [156], it is possible to derive an aspect ratio for the particles. Use of the sphere-equivalent hydrodynamic radius calculated from the measured diffusion coefficient then makes it a simple task to calculate the numerical values for the semi-axes. This makes the assumption that the 'sphere-equivalent' hydrodynamic diameter returned by the Nanosight instrument is indeed equally applicable to all shapes of particle; this is strictly incorrect, as the diffusion coefficients from which these diameters are calculated will vary with shape as well as sphere-equivalent size. A correction for this has been calculated for discs [343], and is given by

$$D_h = \frac{8D_p\left(1-\Phi^2\right)^{\frac{3}{2}}}{-\left(2\Phi^2-3\right)\arcsin\left(\sqrt{1-\Phi^2}\right) + \left(1-2\Phi^2\right)\arctan\left(\frac{\sqrt{1-\Phi^2}}{\Phi}\right)} \tag{5.13}$$

where all variables are as previously defined, D_p is the circular diameter, and Φ is the ratio between D_p and the thickness of the disc. However, applying this correction requires foreknowledge of several of the variables which are supposed to be being calculated (the thickness and circular diameter of the discs), so it is not possible to meaningfully use this. The same goes for the equivalent corrections for particles of other shapes. This is worth bearing in mind as a source of uncertainty in the final calculated shape and size.

Because for the linearly-deformed sphereoids this theory is capable of describing, one of the semi-axes will always be repeated, it is possible to derive expressions for L_1 and L_2 in terms of the two remaining unique semi-axes, a and b, given by Equations (5.14) and (5.15).

$$L_1 = \frac{1}{\left(1 + \frac{2a}{b}\right)} \tag{5.14}$$

$$L_2 = \frac{1}{\left(\frac{b}{a} + 1\right)} \tag{5.15}$$

By substituting the geometric relationship between r_h, a, and b (given by $a = \frac{3r^2 - b^2}{2b}$) in order to eliminate a before taking the ratio of Equations (5.14) and (5.15) in order to express the relationship in terms of the ratio of $L_1 : L_2$ (which is known) results in Equation (5.16).

$$b = \pm \frac{\sqrt{3} r_h}{\sqrt{2\frac{L_2}{L_1} + 1}} \tag{5.16}$$

It then follows that:

$$a = \frac{3r_h^2 - b^2}{2b} \tag{5.17}$$

for rods and:

$$a = \sqrt{b^2 + 3r_h^2} - b \tag{5.18}$$

for discs (accounting for a different repeated axis). These results may be applied directly to the ratio of L_1 and L_2 (calculated using Equation (5.12)) and the NTA measurement of r_h in order to calculate estimates the dimensions of the semi-axes of the particles. Obviously a negative value for b makes no physical sense, so the negative solution may always be neglected.

5.3 Numerical simulation

5.3.1 Motivation

A potential issue identified in the analytic theory is the dependence upon treating all the particles as simple dipoles; the same assumptions used in Rayleigh scattering. As has already been discussed in Section 1.3.4.1, the accepted limits within which the Rayleigh model is valid are not generally agreed upon; however the particles used (described below) when illuminated with 400 nm radiation fall outside most proposed cutoff criteria. A numerical model such as this allowed for verification that the dipole-based theory was adequate for this circumstance. In order to confirm whether this analytic theory did indeed describe the behaviour of the particles in a theoretical environment free from experimental interferences, numerical simulations of a selection of nanorods and nanodiscs were carried out using the COMSOL Multiphysics® [344] finite element wave optics package.

5.3.2 Simulation configuration

Models were constructed using the approximation of Rakić et al [345] for the relevant optical properties of gold and silver. Particles modelled were a nanodisc with thickness 10 nm and radius 70 nm, and a nanorod of length 64 nm and diameter 5 nm; these reflect some of the particles used for the experimental confirmation in Section 5.4. In order to make use of the symmetry of the systems, concentric spheres were used; the inner of which was filled with virtual water, and the outer being a ‘perfectly matched layer’ to create a ‘soft’ boundary to the modelled domain causing no reflections and allowing far-field measurements to be taken without modelling a much larger volume, as described in the COMSOL manual. The nanoparticle was suspended at the centre of these spheres. A uniform plane-polarised background electric field was created, and then the far-field scattering patterns were calculated for different angles between the nanoparticle and axis of illumination. A diagram showing the setup for a silver nanodisc is shown in Figure 5.5. The colour scale is completely arbitrary.

When observing the light scattered by a population of suspended nanoparticles through an optical microscope, light is effectively being gathered from a small solid angle of each nanoparticle. Ideally, this solid angle will be centered upon a point perpendicular to the illuminating radiation. However, on a real physical system such as the Nanosight NTA, this is not necessarily the case – it is known that the illumination in the Nanosight is at a slightly oblique angle, and much of the optics are proprietary. In order to sidestep this issue, simulations were run for two limiting cases. The first is the ideal case of measurements only being taken from a single point, perfectly perpendicular to the illumination. This is the equivalent to using a lens which only accepts light that’s perfectly collimated. The other limiting case is that of measurements being taken from every possible angle. This corresponds to a lens of infinite radius focussing all the light that falls upon it, regardless of the angle it should make with the surface of the lens. Clearly neither is perfectly representative of the real situation which falls between these two limits. It is salient to note that because when considering each extreme, it was still possible to localise the two peaks of the requisite bimodal

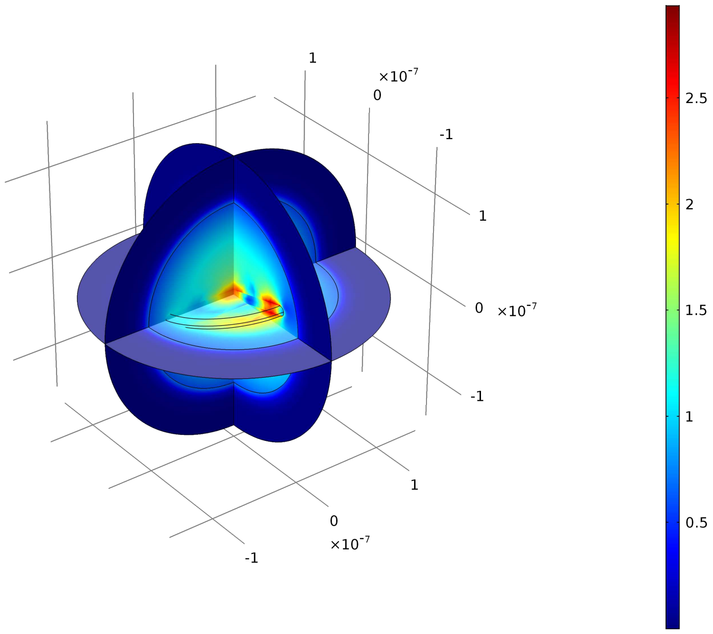

Figure 5.5: Diagram showing the COMSOL setup, with concentric spheres surrounding the nanoparticle, in this case a nanodisc. The outer spherical shell is the 'perfectly matched layer'. The nanodisc is shown rotated at an angle of about $\frac{\pi}{8}$ for clarity; in simulations the particle was rotated between angles of 0 and $\frac{\pi}{2}$.

distribution, the exact solid angle from which light is collected is largely inconsequential for the ability to measure the nanoparticle shape.

These two limits can be better visualised by considering the three-dimensional scattering pattern at a single angle of illumination. The greatest scattered intensity is always perpendicular to the illumination, and the scattering pattern becomes much weaker at scattering angles approaching 0 and π. This is illustrated in Figure 5.6, showing the illuminating beam propagating in the positive y-direction. As in Figure 5.5, the colour scale is completely arbitrary.

5.3.3 Simulated results

In the first case, where light was gathered only from a single point, the results agree perfectly with the analytical prediction in Section 5.2.2 for all nanoparticle configurations tested. This is no surprise, as the two make exactly the same approximation. The numerically calculated graph for a nanodisc is shown in Figure 5.7a (red data).

For the case of a nanoparticle observed from all possible angles, the results are slightly less straightforward. This method is significantly more computationally complex, and typically took weeks rather than days to compute for each shape. For this reason, only one example for a rod and one for a disc were calculated. In these cases, the result was less clear. Figure 5.7a gives the example calculated for the same nano-disc as considered in Figures 5.5 and 5.6. As

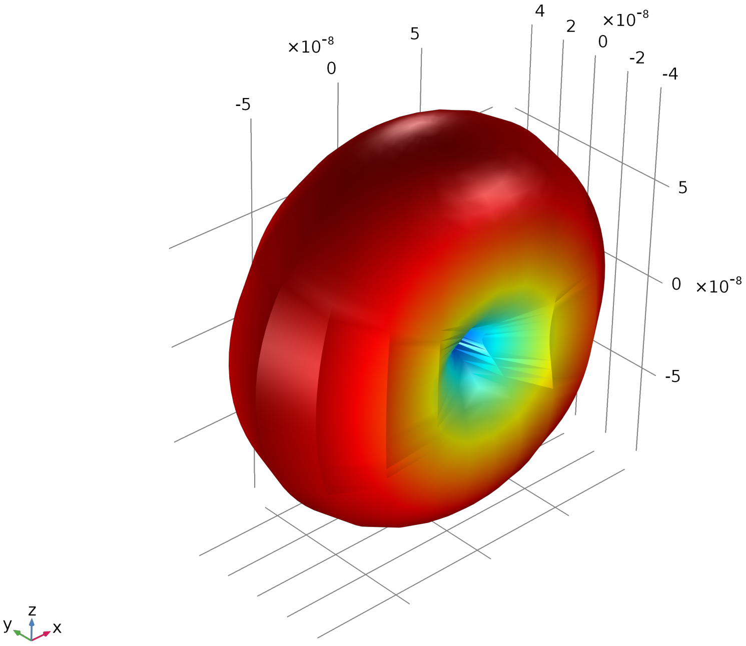

Figure 5.6: 3-dimensional scattering pattern from a nanodisc, illuminating beam propagating in the positive y-direction.

can be seen, there is a significant tail on the distribution. This is generated mainly from the scattering at angles either close to $\theta = 0$ or $\theta = \pi$. Some of this tail would be captured by a real microscope, but not all. Furthermore, the numerical model assumes equal sensitivity to light at all possible intensities (that may be represented using a 64-bit float). A real camera has some finite limit on intensity resolution at both high and low intensities, a characteristic that will further curtail the measurement of this tail in real systems. Quantisation is also evident in the higher-intensity region. These individual peaks each correspond to a single angle between the nanoparticle and the incident radiation. Calculating a greater number of angular slices would fill in these gaps at the expense of a large amount of computer time.

As a result of the level of agreement between the analytic theory and the numerically simulated results, it is reasonable to conclude that while the particles do not meet either of the proposed criteria for the applicability of Rayleigh scattering discussed in Section 1.3.4.1, the Rayleigh dipole approximation is a sufficiently good approximation in these circumstances.

5.4 Experimental confirmation

5.4.1 Materials and methods

An experimental confirmation of these theoretical results was carried out using some NTA equipment (Nanosight LM14), using similar particles to those which were simulated, and a laser of wavelength 532 nm (green). The Nanosight NTA software can output an ‘all tracks’

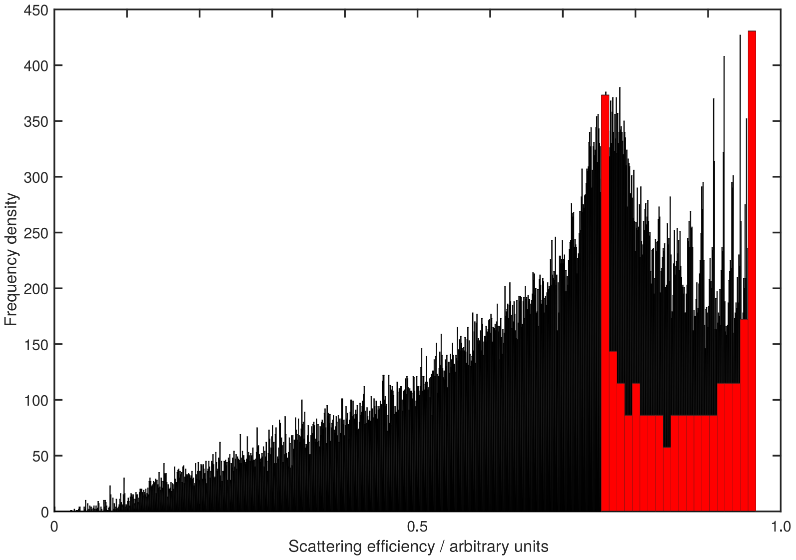

(a) Simulated scattering behaviour for a nanodisc using the all-angles approximation (black) and simulated scattering behaviour for a nanodisc using the single-angle approximation (red). The respective heights of the peaks inprecise due to the limited angular resolution used. This compares to the analytic plot shown in Figure 5.3. Note the high-intensity peak in the multi-angle approximation is quantised by the angular resolution of the scan; at higher angular resolutions it would become a continuous (and higher) peak.

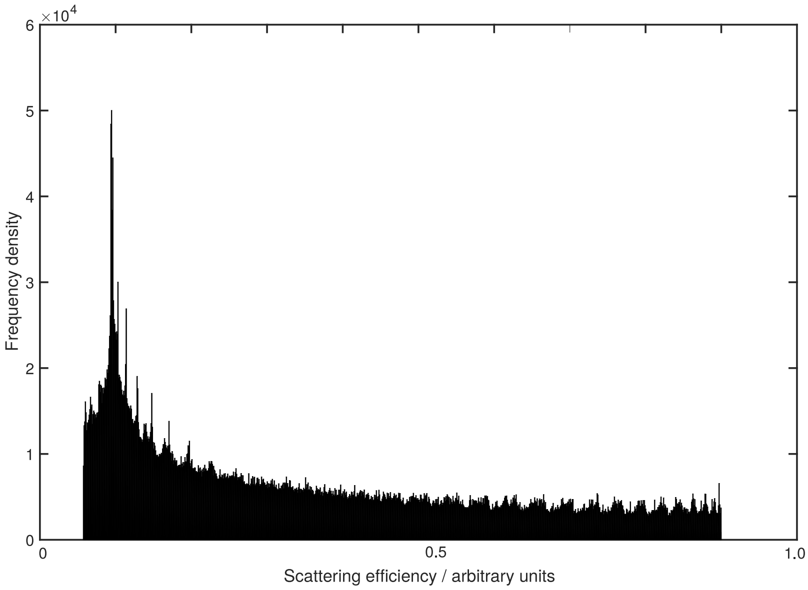

(b) Simulated scattering behaviour for a nanorod using the all-angles approximation. While the high-intensity peak is not immediately obvious, it can be seen that the frequency of the peaklets increases at higher scattering efficiencies; a simulation with better angular resolution would generate an actual peak here.

Figure 5.7: Simulated intensity distributions for a gold nanorod (5.7a) and a silver nanodosc (5.7b).

file, which contains (among other things) a complete list of the intensity of every particle detected in every frame. This allows either all particles to be treated as an ensemble or the variation of individual particles' intensity over time to be investigated. Both of these approaches are detailed below.

ENPs of four different shapes were obtained (Nanopartz, Colorado). Two were gold nano-rods of different sizes and aspect ratios, and the other two were silver platelets. Ideally all the ENPs would have been gold, but no gold platelets or discs are currently commercially available. The ENPs had different stabilising agents, but these should have no effect upon the light-scattering behaviour of the core material. The particles used are described in Table 5.1. All nanoparticle samples were analysed upon receipt using transmission electron microscopy (TEM). Determination of nanodisc thickness relied upon the occasional stack of particles not laid flat on the TEM grid. For example, the Ag1050 rods only had 44 measurements of particle thickness b made, contrasting the 450 measurements of the diameter a. Representative TEM images of the non-spherical ENPs are shown in Figure 5.14. Further analysis was undertaken using NTA, recording video files for 90 s at 25 frames per second.

5.4.2 Experimental results

Firstly, it was confirmed that the recorded intensity of scattered light from the nanoparticles does indeed vary over time. Tracking a single nanorod over a duration of 4 seconds at 25 frames per second yielded a variation of intensity with time as shown in Figure 5.8. The nanorods used for this were the gold, nominally 62 nm length and 6 nm radius (Nanopartz, Colorado). They are described more fully in Table 5.1 as the 'Au900' particles.

If a histogram is plotted of the raw intensity data, a rod-shaped nanoparticle will produce a bimodal distribution, with the two modes corresponding as previously described to the two semi-axes. A spherical particle, however, will merely produce a skewed gaussian distribution. Conversely, platelets will produce a signal that is nearly indiscernible from that of a sphere, unless the logarithms of the intensities are taken prior to histogram binning. Once these logarithms have been taken, then we once again receive a bimodal distribution for platelets, and a skewed gaussian for spheres. Rods will also produce a skewed gaussian. It is not entirely clear why this is necessary, though it is likely to be related to a combination of some non-linearity of the camera sensor and proprietary intensity-determination algorithms in the Nanosight software. Graphs demonstrating this effect are given in Figure 5.9 for rods, and Figure 5.10 for discs. It is worth noting that the Nanosight NTA output files by default contain the logarithmic intensity data, not the raw intensity data.

In agreement with the theory, in all cases discs produced the larger of the two peaks at

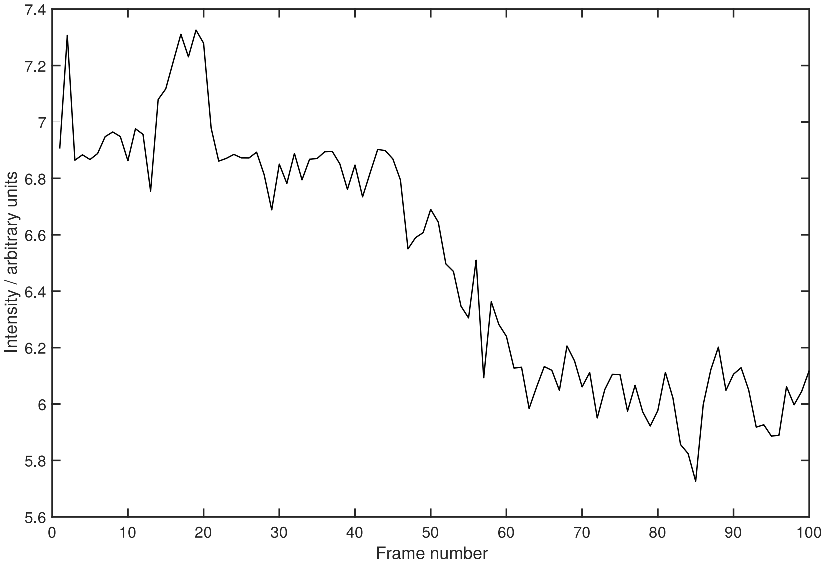

Figure 5.8: Plot showing the measured intensity of light scattered by a single rod-shaped particle over the tracked duration of 100 frames or 4 seconds.

higher intensity, while the rods produced a larger peak at lower intensity. Representative histograms from both the discs samples are given in Figure 5.11, and representative histograms for both the rods samples are given in Figure 5.12.

When considering individual particles, for all non-spherical shape classes it was possible to correctly attribute the particles a shape class from their single-particle intensity distributions about 80 % of the time. Exemplar single-particle intensity distributions are given in Figure 5.13. Because the Nanosight NTA is only capable of tracking individual particles for a maximum of 100 frames, this places a hard upper-limit on the number of datapoints which may be attributed to a single particle. It is of note that while only 80% of individual particles were 'correctly' ascribed a shape, this is not dissimilar to the percentage of nanoparticles in these samples that the TEM analysis revealed to not belong to the background distribution of nanoparticles. This suggests another possible application of this technique in nanoparticle manufacture as a quick and cheap in-situ or flow-through form of quality assurance. Given that across all samples the single-particle measurements gave the nominal shape of the sample approximately 80% of the time, while the TEM measurements suggest that approximately 85% of the particles are of the nominal shape, it is therefore reasonable to place a lower bound on the accuracy of the single-particle technique by suggesting that at least 5% of particles are incorrectly ascribed a shape. Similarly, an upper bound for the mis-attribution rate can be established by calculating that in the worst-case scenario, the 20% of particles NTA measured as belonging to a population of a different shape from the nominal one were in face all from the nominal shape, and all the non-nominally-shaped particles were identified as belonging to the

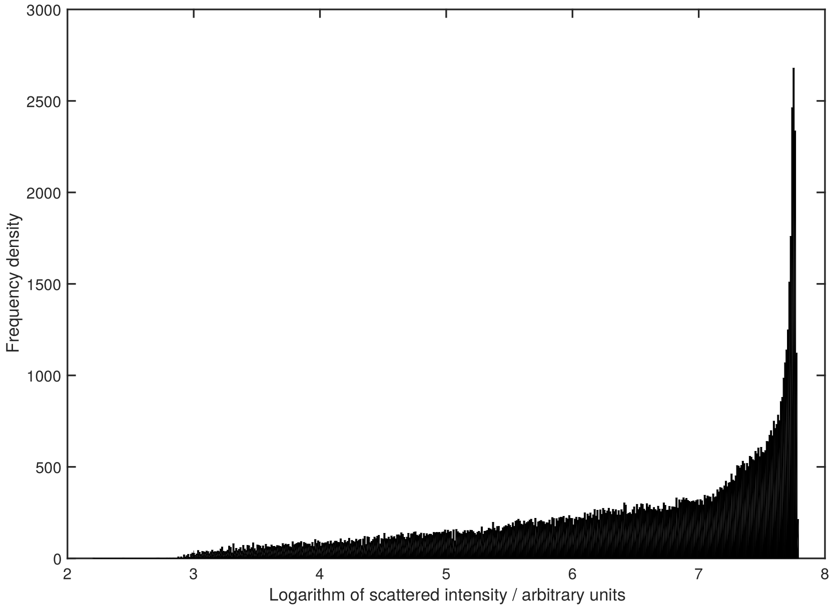

(a) Histogram showing the logarithmic distribution output from the Nanosight software by default for some representative nanorods. Note that there is only a single mode visible.

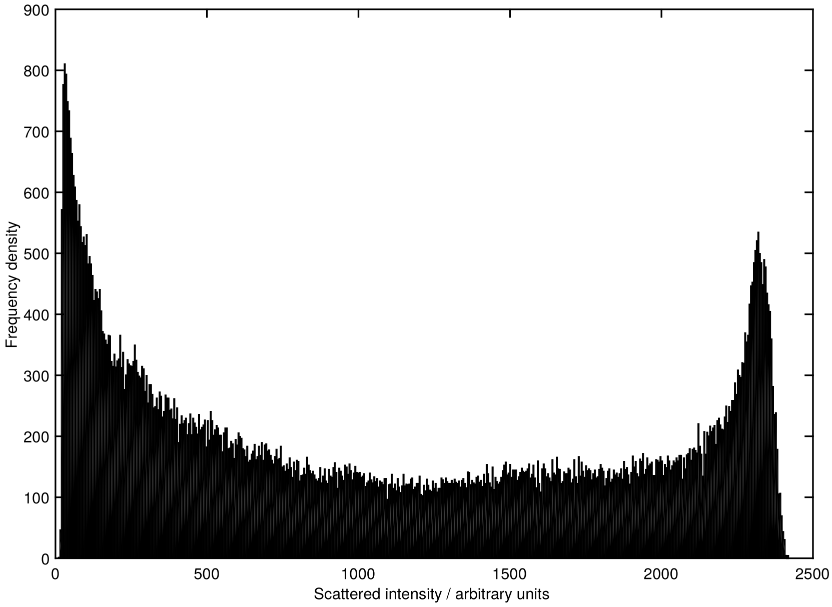

(b) Histogram plotted using the same data as Figure 5.9a, only having been exponentiated prior to histogram binning. Note that it is now easily possible to discern the bimodal distribution which the theory suggests should be present.

Figure 5.9: Experimental intensity histograms for a representative sample of nanorods. Figure 5.9a shows a plot of the raw (logarithmic) data output from the Nanosight software, while Figure 5.9b gives the exponentiated data, making it possible to discern the two modes necessary for size measurement.

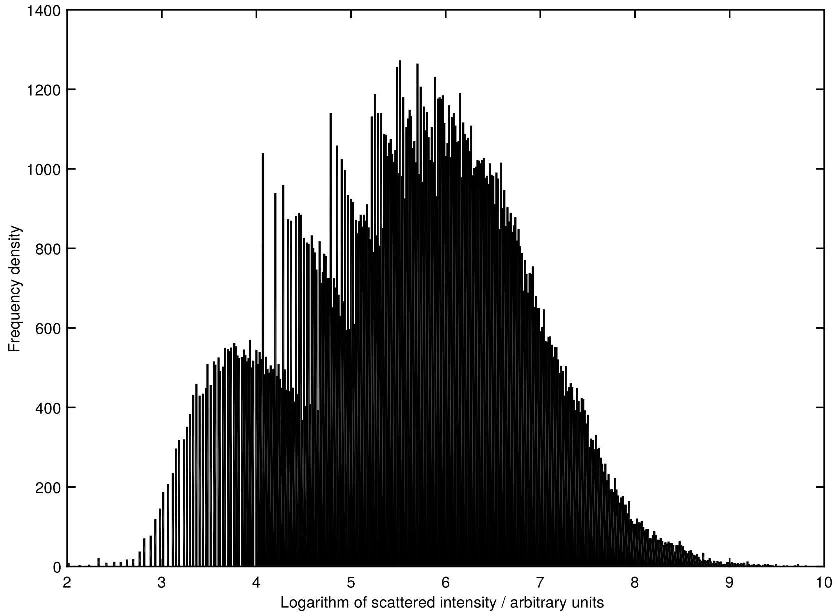

(a) Histogram showing the logarithmic distribution output from the Nanosight software by default for some representative nanodiscs. Note that there there are two modes visible, with the smaller mode occurring at lower intensity, as predicted.

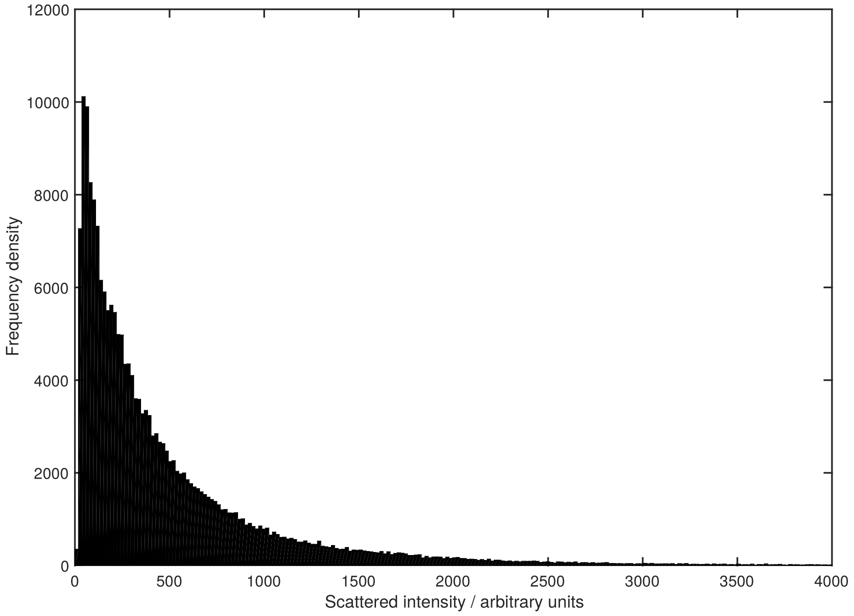

(b) Histogram plotted using the same data as Figure 5.10a, only having been exponentiated prior to histogram binning. Note that it is now no longer possible to measure more than a single peak, and as such the shape of the particles can no longer be determined.

Figure 5.10: Experimental intensity histograms for a representative sample of nanodiscs. Figure 5.10a shows a plot of the raw (logarithmic) data output from the Nanosight software, while Figure 5.10b gives the exponentiated data. Twin modes are only visible in the former, meaning that for shape determination, this is the form which should be used to measure the peak locations.

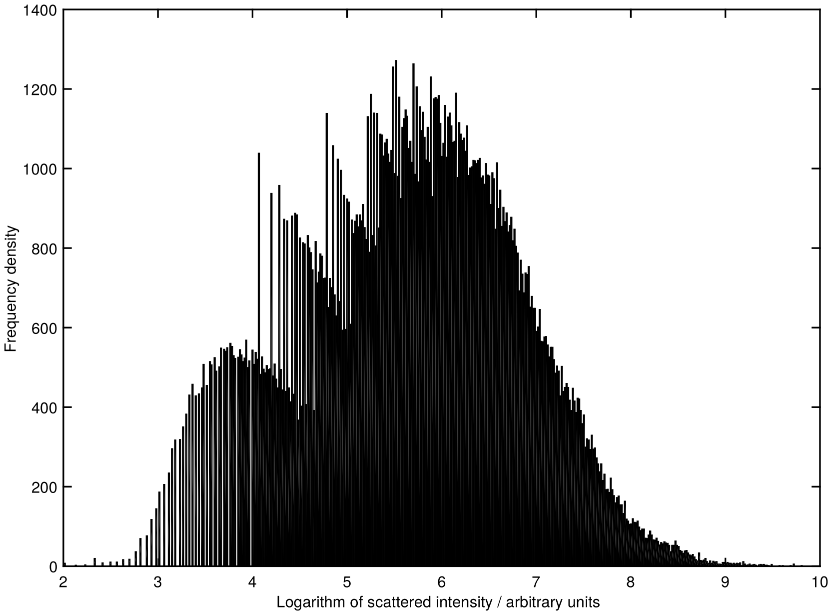

(a) Histogram showing the intensity distribution for a representative sample of the 'Ag550' sample of nanodiscs.

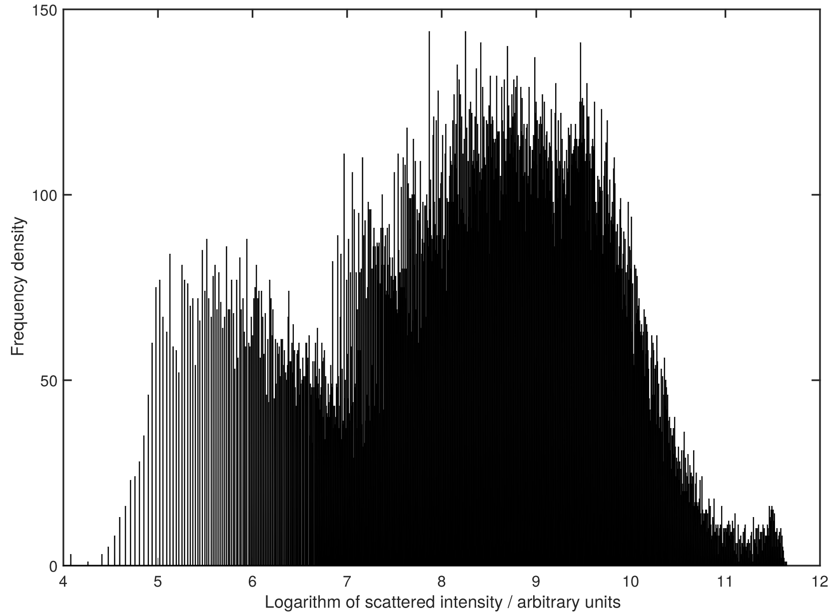

(b) Histogram showing the intensity distribution for a representative sample of the 'Ag1050' sample of nanodiscs.

Figure 5.11: Experimental intensity histograms for representative samples of both 'Ag550' (Figure 5.11a) and 'Ag1050' (Figure 5.11b) nanodiscs. Note that in both cases, bimodal distributions are received for which the smaller peak occurs at a lower scattered intensity consistent with the prediction for nanodiscs.

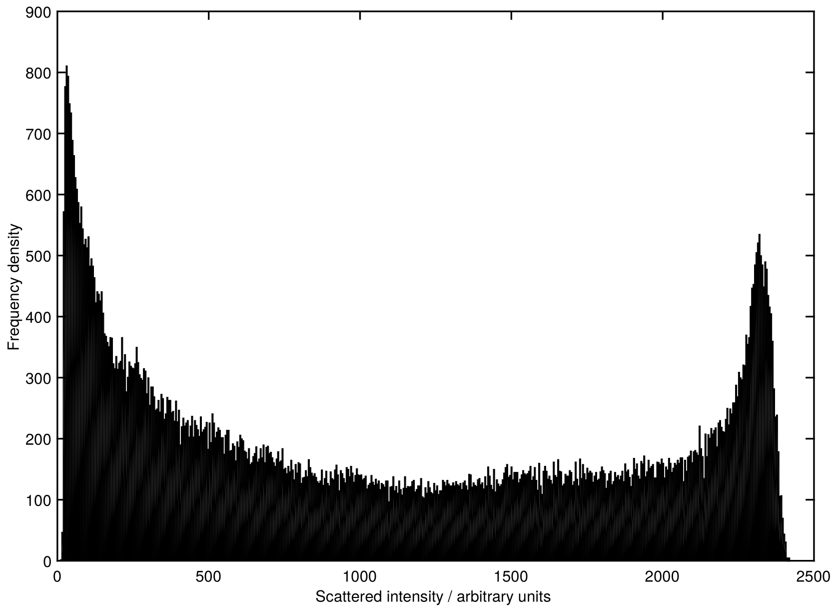

(a) Histogram showing the intensity distribution for a representative sample of the 'Au900' sample of nanorods.

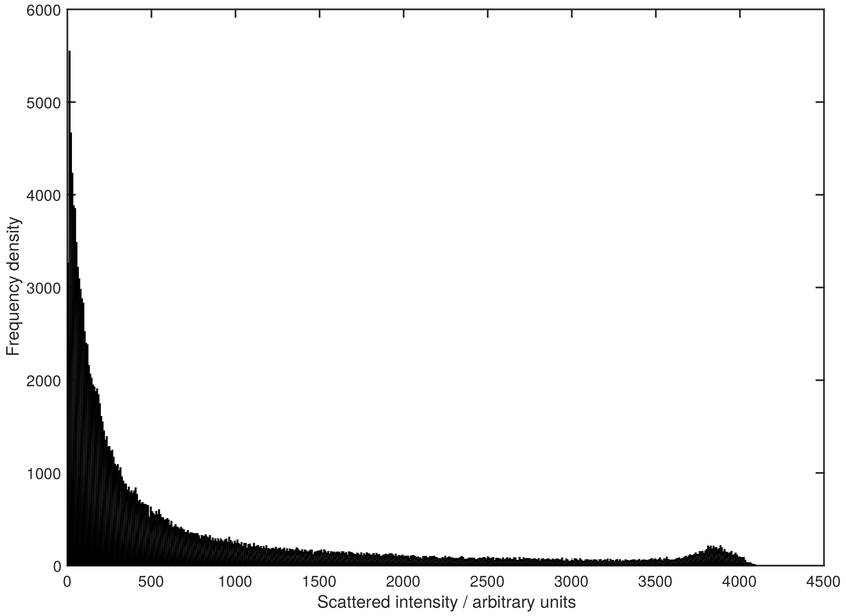

(b) Histogram showing the intensity distribution for a representative sample of the 'Au750' sample of nanorods.

Figure 5.12: Experimental intensity histograms for representative samples of both 'Au900' (Figure 5.12a) and 'Au750' (Figure 5.12b) nanorods. Note that in both cases, bimodal distributions are received for which the smaller peak occurs at a higher scattered intensity consistent with the prediction for nanorods.

nominal distribution. In this case, all 15% of non-nominal particles would be mis-measured, as would a further 20% of the nominal particles. This places an upper bound on the rate of mis-attribution at 35%. This is an unrealistically high number, but without being certain to measure the same particle with both NTA and TEM, it is challenging to assert with any robustness that it is any lower.

When analysing the data for all particles in a sample as a single population, it was possible in all cases to determine whether the particles were rod-like, disc-like, or roughly spherical. However, the determination of the degree of eccentricity was not always predicted quite as efficiently; while all eccentricities were predicted within an order of magnitude of the nominal value, some of the predictions varied greatly in accuracy when compared to the TEM measurements. The results are summarised in Figure 5.1.

Particle	**Au750 rod**	**Au900 rod**	**Ag550 disc**	**Ag1050 rod**
Nominal a	53 nm	62 nm	50 nm	140 nm
Nominal b	10 nm	12 nm	10 nm	10 nm
Nominal aspect ratio	3.5:1	5.1:1	5:1	14:1
TEM a	(42±9) nm	(80±18) nm	(100±20) nm	(150±70) nm
TEM b	(13±5) nm	(22±10) nm	(24±6) nm	(17±6) nm
TEM aspect ratio	3.3:1	3.7:1	4.1:1	9:1
NTA a	70.6 nm	64.2 nm	30.6 nm	73.1 nm
NTA b	4.9 nm	11.5 nm	14.6 nm	31.1 nm
NTA aspect ratio	14.4:1	5.6:1	2.1:1	2.4:1
Error in a	68.9 %	21.2 %	68.1 %	53.0 %
Error in b	61.1 %	8.7 %	38.9 %	80.8 %
Error in aspect ratio	336.4 %	51.4 %	48.8 %	41.7 %

Table 5.1: Experimental results comparing nominal sizes, TEM values, and NTA values. Errors in NTA values are calculated relative to TEM values rather than nominal values.

Representative intensity distributions from which these results were derived are shown for rods, discs, and spheres respectively in Figures 5.15a, 5.15b, and 5.15c. Note that the distribution for the sphere has a small shoulderlet on the left, reminiscent of the disc's distribution; likewise, if it were exponentiated, it also exhibits a small flick where it would be expected for a rod. This suggests that the spherical particles aren't perfectly spherical, which is to be expected for a real-world non-idealised sample of particles.

5.5 Sources of error

There are several sources of error, some of which can be significant in certain circumstances. The majority of these can be grouped together into a single category; those which give rise to additional fluctuation in the intensity, but which aren't due to the non-spherical nature of the particles. These sources of intensity spectrum distortion include the following. Firstly, there is a quantisation error associated with particles whose scattered light saturates pixels on

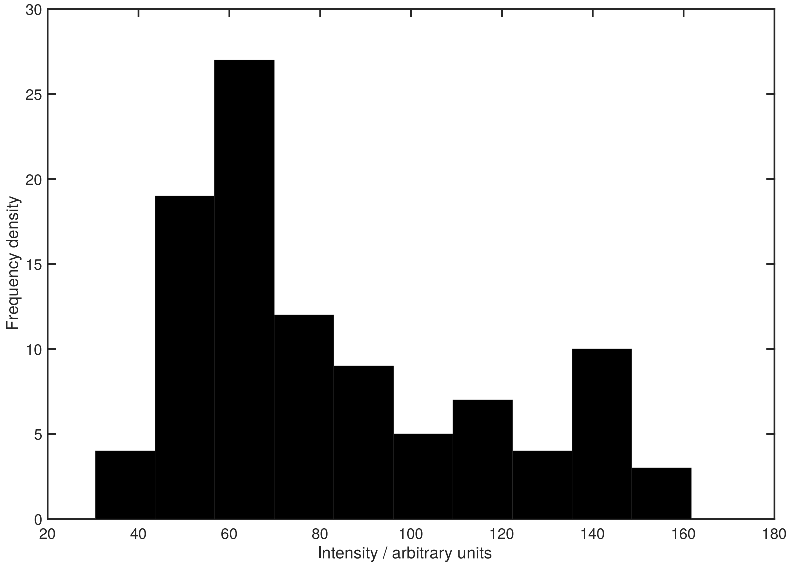

(a) Representative single-particle intensity histogram; in this case from the 'Au900' sample of rods. While the intensity profile clearly identifies this particle as a rod, because of the small number of datapoints the peak localisation is very poor. Correspondingly, the estimate of particle dimensions was largely meaningless.

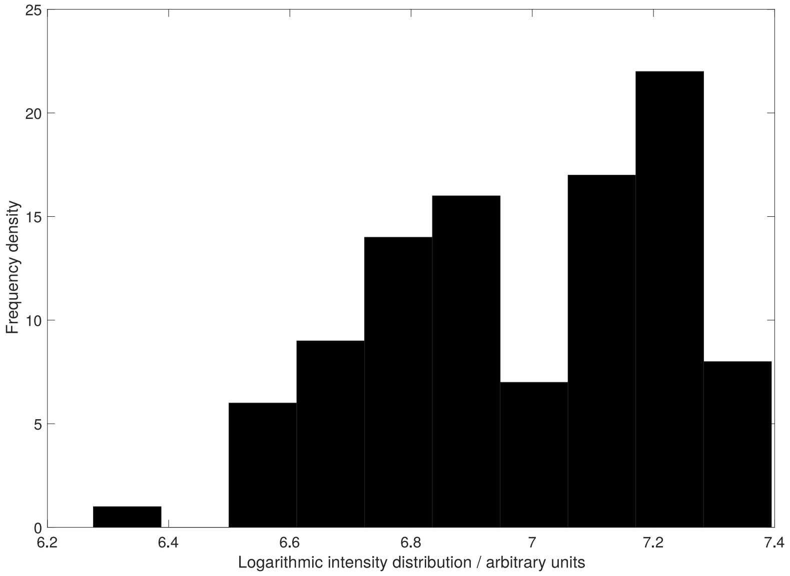

(b) Representative single-particle intensity histogram; in this case from the 'Ag550' sample of discs. While the intensity profile clearly identifies this particle as a disc, because of the small number of datapoints the peak localisation is very poor. Correspondingly, the estimate of particle dimensions was largely meaningless.

Figure 5.13: Representative single-particle intensity profiles for a rod (5.13a) and for a disc (5.13b). Note that the small number of datapoints available (100) results in very poor peak localisation and therefore very poor dimension resolution.

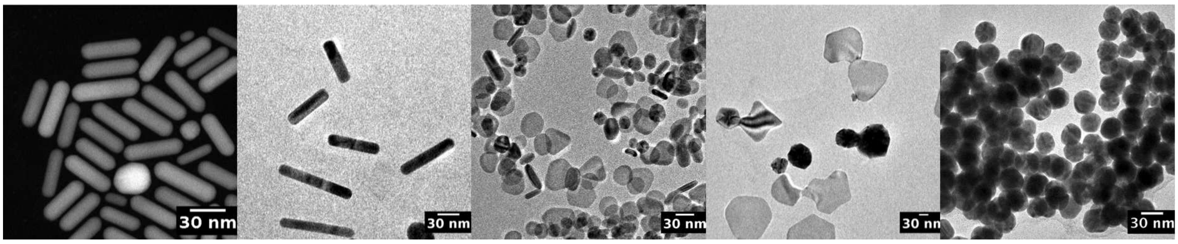

Figure 5.14: Representative TEM images of the ENPs used. L-R, Au750, Au900, Ag550, Ag1050, reference nano-spheres. All bright-field images from JEOL 2011, dark-field image from JEOL 2200FS.

the camera. This has the effect that, even with gaussian fitting, the intensity of the particle in a given frame may be significantly underestimated. Secondly, in a more concentrated sample containing many particles, the background light level will become increased. This background light level will necessarily compress the range of available measureable intensities, leading to both systematically incorrect measurements of intensity, and increased quantisation error (noting that an 8-bit camera can only digitise 256 different shades, a background of 20, and headroom of the same to avoid saturation can lead to a 16 % decrease in the ability to resolve differing intensities). It must also be considered that these calculations have always assumed no multiple scattering is taking place; in any real-life sample multiple scattering will be present, and this could further increase the peak intensity measured.

The laser in the Nanosight appears to be a single-mode gaussian first order (00) laser, and as such, the intensity cross-section when viewed from above isn't uniform, it's more intense in the middle. Thereby, a particle which starts being tracked in the centre of the beam and then moves to the edge (where the flux is lower) will have an intensity profile that isn't representative of the particle.

It is also important to remember that particles that are nominally spherical may not necessarily be either perfectly spherical, or uniform. It is of note that the intensity distributions from the spherical particles exhibit a small high-intensity peak in the raw intensity profile, and also a small low-intensity peak in the logarithmic intensity profile, suggesting that the sample contains a small quantity of slightly rod-like particles and a small quantity of slightly disc-like particles. Establishing a significance threshold for these peaks is an important step in adapting the technique for automated analytical use.

Interestingly, it appears that the sphere-equivalent hydrodynamic radii $\bar{r}_h$ being reported by the nanosight are not necessarily accurate for eccentric sphereoids – in one case only was the measured $\bar{r}_h$ similar to that expected given the TEM measurements of semi-axes. For the remaining rods, the reported value was nearly 3 times larger than expected, while for all the discs, $\bar{r}_h$ was reported to be less than half than expected. This arises because the diffusion

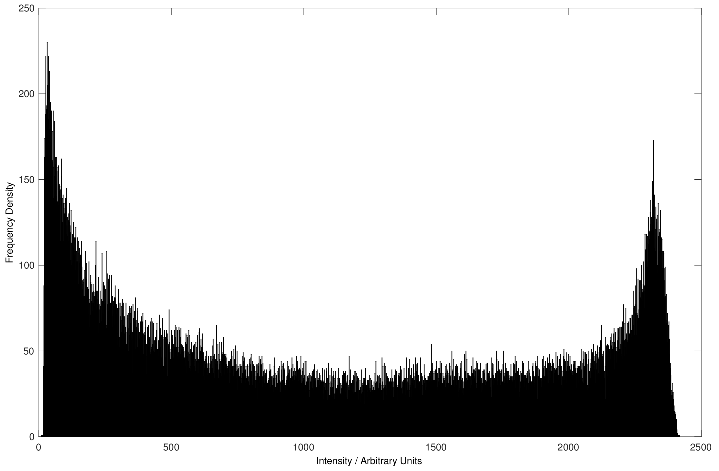

(a) Typical bimodal intensity distribution received from some nanorods.

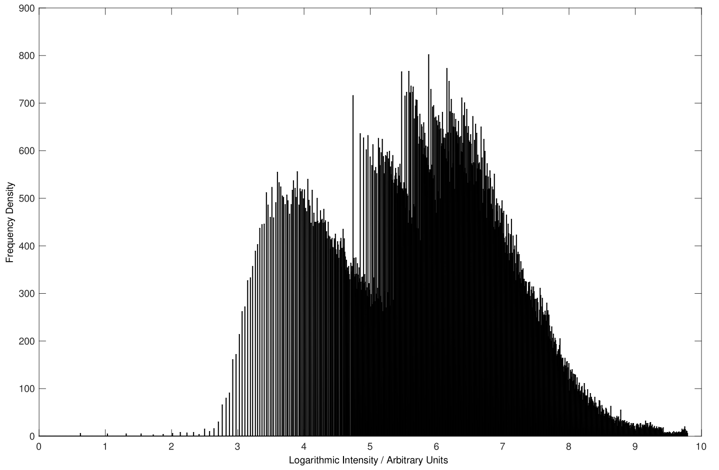

(b) Typical bimodal intensity distribution received from some nanodiscs.

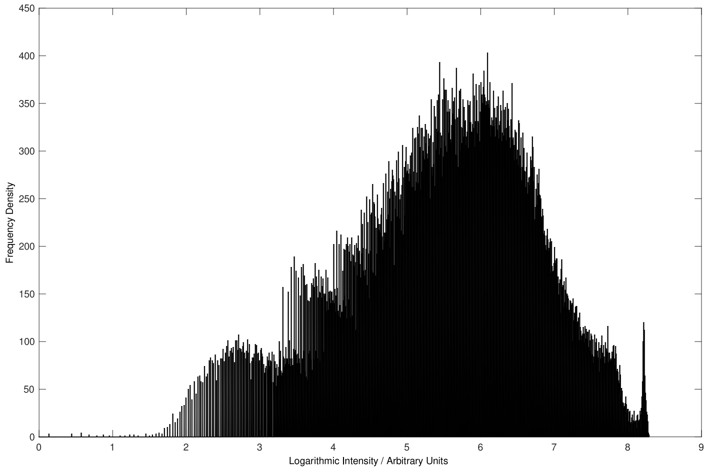

(c) Typical monomodal intensity distribution received from some nanospheres.

Figure 5.15: Typical many-particle intensity distributions for the three different shape classes of particle investigated: rods 5.15a, discs 5.15b, and spheres 5.15c. In all these cases, all the particles in the sample were treated as a single homogeneous population.

behaviour of non-spherical objects differs from that of a sphere, as drag forces don't scale linearly with surface area or volume [343]. The results would have been far more representative of the particles tested had the values of $\bar{r}_h$ been better determined, though this is not possible without additional knowledge of the shape and size of the particle in the first instance, as already discussed.

In this chapter, only analysis of the bulk of a sample of eccentric nano-sphereoids – taking data for all the particles and aggregating it into a single distribution – has been hugely successful. While this is very good for the statistical robustness of the method, it doesn't allow for particle-by-particle shape measurements. In the case of a polymorphic sample, this method will merely yield a multimodal intensity distribution which defies separation into individual populations of particles. There are two possible solutions to this.

Firstly, the most thorough solution is to consider the intensity distribution for each particle individually, ascribe each individual particle an aspect ratio, and then output an aspect ratio distribution. The major hitch in this approach is the lack of data – in order to satisfy the central limit theorem for a bimodal distribution, more than 50 datapoints would be needed for every particle, even assuming there to be no outliers. By comparison, a very clean sample of homogeneous rods were tracked in the Nanosight, and found to be tracked for, on average, 17.3 frames ($\approx \frac{7}{10}$ of a second). It is possible to do some crude analysis by only considering rare particles that are tracked for longer, and this approach has yielded considerable success 80 % of particles were correctly identified as rods or discs, though the degree of eccentricity reported was highly inaccurate. The obvious mitigation of this would involve the use of an optical trap or optical tweezer [338, 346–348], in which the trap operates at a sufficiently different wavelength from the illumination laser that any signal scattered from the trapping laser could be effectively filtered from the signal. This would allow particles to be loosely held in place, such that their intensity distributions could be built up over much longer periods of time. This is not possible on the commercially available Nanosight platform, though would be entirely possible on other non-proprietary apparatus.

These results only account for sphereoids which have been distorted along a single semi-axis; two of the semi-axes of all our test samples were the same. The mathematics becomes slightly more complex in the case of a truly general sphereoid in which all three semi-axes are free to vary independently, and the theory suggests that there are insufficient fitting parameters to be able to achieve such accuracy. Matters are further complicated by the lack of commercially available nanosphereoids of arbitrary semi-axis length.

5.6 Conclusion

In conclusion, herein is presented here a novel concept for the determination of shapes of ENPs, complete with the mathematical framework and experimental procedure, and with experimental confirmation of the technique. While the errors currently associated with the method are reasonably large, it is reliably and reproducibly possible to differentiate between 5 different particle populations of different morphologies while using effectively no computational power over and above that already used by the Nanosight system to determine the size distribution of a sample of nanoparticles.

The method described here could readily be adapted using a flow-through system for the real-time monitoring of nanoparticle shape. An example of where this could be useful might be at a manufacturing plant, where quality control could be dramatically improved and streamlined by a more rapid and low-cost means of characterising the shapes of the particles being produced. This could have the effect of increasing the quality of available particles while reducing their costs.

These results only account for sphereoids which have been distorted along a single semi-axis; two of the semi-axes of all our test samples were the same. The mathematics becomes slightly more complex in the case of a truly general sphereoid in which all three semi-axes are free to vary independently, and the theory suggests that there are insufficient fitting parameters to be able to achieve such accuracy. Matters are further complicated by the lack of commercially available nanosphereoids of arbitrary semi-axis length.

This technique is further utilised in Chapter 4.

Chapter 6

Conclusions

6.1 General conclusions

To conclude, progress of significant moment has been made in the area of optical nanoparticle tracking and measurement. This progress is manifest in several ways. Firstly, as presented in Chapter 2, existing commercial technology was leveraged in order to arrive at two important new results. These were that the previously-reported reversibility of nanoparticle aggregation in lab conditions could be replicated in environmentally relevant conditions. This is highly significant and has important repercussions for the development of environmental fate and behaviour models, and all manner of environmental risk assessment activities. The other important result obtained using the commercial equipment concerns the preservation of water samples containing suspended nanoparticles. It was shown that regardless of the means of freezing, the freeze-thaw process had a significant deleterious effect upon the suspended particles, such that any measurements taken post-thaw were completely unrepresentative of the contents of the sample as measured before freezing. This means that any use of freezing as a sample preservation technique for aqueous suspensions of nanoparticles is likely to interfere completely with the sample. While it is further likely that a similar effect is present to varying degrees in other suspending media, this was not tested and so no firm conclusion in that regard may be made.

One of the major drawbacks which was highlighted as a result of this work was the unrealistically high particle concentrations necessary in order to facilitate optical measurement via NTA. While significant aggregation and disaggregation events were seen at the concentrations used, these are not necessarily representative of nanoparticle conditions at environmentally relevant concentrations in natural surface waters, and it would be unwise to assume that these results are perfectly representative of the real situation. This discrepancy between laboratory-based study and the real environmental conditions was one of the key motivations behind the follow-up work presented in Chapter 3.

A key limitation to existing approaches to single-particle tracking and analysis is the relatively high concentrations of particles necessary to facilitate a measurement – the requisite concentrations are of no use for many applications, including the measurement and study of nanoparticles in the environment and related lab-based experimentation. By analysis of existing commercial nanoparticle tracking apparatus in order to determine the roots of this concentration limitation, a bespoke optimised system was constructed using almost entirely off-the-shelf hardware and open-source software. This improved system, as described in Chapter 3, proved capable of measuring the particle sizes at concentrations approximately three orders of magnitude lower than those attained by the commercial alternative in its default configuration. The new system was then validated using guidelines based upon ISO17025 standards for reproducibility, stability, and resistance to interference. It was found that the system proved itself capable in the tests of reproducibility and stability, repeatedly correctly identifying particles at a range of concentrations ranging from those covered by commercial NTA apparatus down to those given by several environmental predictions. However, the results of the interference assessment suggested that it was vulnerable to interference from natural organic matter at environmentally relevant concentrations. The consequence of this is that while the system has been demonstrated to be suitable for idealised systems and natural systems containing little or no natural organic matter, it is not appropriate for use measuring particles suspended in samples containing any significant quantity of organics. This could be alleviated using some filtration techniques, at the cost of the possibility of losing an unknown quantity of the target particles in the filter as well.

This new capability for making optical measurements of suspended nanoparticles at significantly lower concentrations was leveraged in order to study the kinetics of nanoparticle homoaggregation at concentrations that were previously unattainable by optical means, as presented in Chapter 4. When modelling the environmental fate of engineered nanoparticles, homoaggregation is one of the dominant physical processes which is usually included. However, this understanding of aggregation rates is usually grounded in experimental results from unrealistically high concentrations. Because particles can only adhere to each other when they collide, with the lower collision rates characteristic of lower concentrations, the aggregation rate should be correspondingly slower. This study repeated a subset of some previous experiments investigating the aggregation behaviour of engineered nanoparticles in a range of ecotoxicology media. It was found that in all combinations of nanoparticles and ecotoxicology media excluding two, the rate of aggregation was sufficiently low that the examination of the measured size distributions suggested that absolutely no aggregation had taken place. Examination of the single-particle intensity distributions in the manner described in Chapter 5 suggested that the particle morphology had changed subtly during the experimental period, which gave strong evidence that the nanoparticle shape had changed, though the intensity distributions that were measured didn't fit directly within the limits of current theory. Therefore it was concluded that a low level of aggregation had occurred, but at a sufficiently low level that the effect of this aggregation upon the size distribution was not visible.

The final significant result, as presented in Chapter 5, is the ability to use sub-diffraction-limit light scattering data of a type that may be obtained readily using either existing commercial light-scattering platforms in order to determine the shapes of the particles being imaged. This was accomplished by considering the variation of scattered intensity by single particles as they rotate in suspension, and it allows the determination of the shape as a sphere, or a linearly deformed sphere (either a disc-like sphereoid or a rod-like sphereoid). This scattering data may then be interrogated in several ways. All the particles can be treated together as an ensemble if they belong to a single population, and using this relatively large quantity of data an accurate measurement of the particle shape may be achieved. This data may also be analysed by splitting particles into sub-populations by size; each of these sub-populations may then be analysed for shape as separate ensembles. Finally, the light-scattering behaviour may be analysed on a single-particle basis. Because a single particle will only have been tracked for a limited number of video frames before it is either lost by the tracking algorithm or diffuses out of the field of view, this doesn't allow for an accurate determination of the shape of the nanoparticle, only a rough classification as either a rod, sphere, or disc.

6.2 Proposals for further work

The work contained herein has the potential to facilitate a great deal more research in related topics. A few suggestions of the more interesting directions this could be taken in the future are outlined below.

6.2.1 Optical trapping

One of the key limitations that exists both in the bespoke nanoparticle tracking apparatus described here and in commercial solutions is that a single particle cannot be tracked for a very large number of frames, thereby limiting the quantity of data that can be extracted about individual particles – in most cases it is necessary to consider a very great number of particles and average across the population to build up a good picture of the contents of even a monodisperse suspension. This is the case both for measurement of nanoparticle size and for the measurement of nanoparticle shape. For example, the Nanosight commercial NTA software is technically incapable of tracking particles for in excess of 100 frames (which at the default 25 frames per second equates to 4 seconds), and the bespoke NTA apparatus described in Chapter 3 is similarly only capable of tracking particles for a similar duration, this time limited by the rate of convection of the suspending medium.

However, should a particle be trapped in such a way that it was free to diffuse within a known potential field, like those that may be implemented using optical trapping apparatus suitable for nanoparticle trapping [346, 347, 349–352], then it should be possible to gather far more detailed information about single particles without the need to consider them as a small part of a population. Recent progress in optical trapping of nanoparticles has developed tools which would allow nanoparticles to be trapped within the field of view of an NTA setup. Given the open nature of the particle tracking equipment described here, this would be a relatively simple step to incorporate, though would require significant modification to the software to account for the additional non-diffusive forces present.

6.2.2 Magnetic hyperthermia

A property of nanoparticles which was not considered fully in any of the investigations in this thesis other than as a cause for convection is the heating of nanoparticles, particularly using magnetic particles in an oscillating magnetic field. This has many uses, and one of the most important of these which is currently being actively investigated is in the treatment of cancer [353–355]. Magnetic nanoparticles are injected at the site of a tumour, and an oscillating magnetic field is used to heat the particles until they start destroying the cancer cells [356, 357]; too cool and they will have no effect, too hot and they'll damage surrounding tissue. It is nearly impossible to measure the temperatures of the nanoparticles in situ from outside of the body, so the strength of the magnetic interaction with the nanoparticles must be very precisely known, though this is also a highly challenging thing to determine experimentally.

To add an additional layer of complexity, the particles which are most commonly used in such trials are iron [17]. These form a layer of iron oxide on the surface. Iron oxide has a smaller magnetic moment than unoxidised iron, and so the thicker the oxide layer, the less strongly the particle will couple to a magnetic field and the smaller the heating effect will be for a given field strength and treatment duration. As the particles age, the thickness of this oxide layer will increase; while this isn't an issue on a timescale of hours, it is a problem when the particles may be fabricated several weeks or months prior to therapeutic use – the ability to select optimal treatment parameters are dependent upon knowledge of the exact magnetic response of the nanoparticles.

Because diffusion rate of particles in suspension is highly sensitive to local liquid temperature, it should be possible to utilise the Stokes-Einstein relation in reverse, using the known size of particles to deduce the local temperature given the known relationship between the viscosity of water and its temperature. Using the open particle tracking apparatus described in Chapter 3, it would be a relatively simple matter to install a set of Helmholtz coils to generate a uniform oscillating magnetic field within the sample chamber, before using the measured diffusion coefficients to deduce the degree of heating caused by a known magnetic field. This could allow for quick and cheap assessment of the magnetic behaviour of the nanoparticles immediately prior to injection, allowing the magnetic responses of the particles to be precisely known at the point of introduction to the body, which has the potential to improve treatment effectiveness and safety, leading to more positive patient outcomes.

6.3 Also attached

Attached as appendices is some additional supporting information. This includes a summary I was asked to write for SETAC's 'Globe' publication reviewing a session I proposed and chaired at the SETAC Nantes conference in 2016. Also attached are full instructions for the utilisation of the software that was developed to facilitate much of the experimental work and for the more general use of officially unsupported hardware interfaces with Matlab, as are required for the correct functioning of this software.

Appendix A

Calculating the mean hydrodynamic diameter of aggregates

Throughout this section, it is assumed that the mean hydrodynamic radius of a particle, $\bar{r_h}$, can be approximated to the arithmetic mean of the hydrodynamic radii of it's possible elevations, $\bar{r}_{1\ldots k}$, such that the effective hydrodynamic radius, given by Equation (A.1), may be calculated. This is only an approximation, as the actual cross-sectional area will vary sinusoidally with rotation rather than linearly.

$$\bar{r_h} = \frac{1}{k}\sum_{n=1}^{k} \bar{r}_n \tag{A.1}$$

For a nanoparticle monomer, the hydrodynamic diameter is simply twice the radius to a good approximation. However, a dimer is slightly more complex. There is only one possible formation of a dimer. In this formation, there are two possible principal elevations - one in which the particle is end-on, and appears (ignoring turbulence) to have a hydrodynamic radius the same as a single particle, and the other two identical elevations, each with two particles side-by-side, whose effective hydrodynamic radius, $\bar{r}_2$, is given by $\sqrt{2}r$. Any elevations in between will be accounted for by the average of the three. This average, $\bar{r}$ is given by Equation (A.2).

$$\bar{r_h} = \frac{r\left(2\sqrt{2}+1\right)}{3} \tag{A.2}$$

In a three-particle system, there is more than one possible trimer structure. Either three particles in a linear format, or three particles in a flat, 2-dimensional triangle. In the linear arrangement, there is the additional degree of freedom in that the angle formed by the three particles is free to vary between straightness (angle of π right round until it has become precisely equivalent to the triangular trimer at an angle of $\frac{2\pi}{3}$. In this treatment of the trimer, it is assumed that when the angle increases above $\frac{\pi}{2}$ that the surface properties of the particles are such that either the particles rapidly adhere, transforming into the triangular trimer, or that the repulsion of the particles is such that the angle cannot increase any further. For a linear trimer with an angle of π, the particle can be treated exactly as the dimer was, such that one face (again, neglecting the effects of turbulence) can be treated as a single particle. Thence, $\bar{r}_1 = r$, where r is the radius of a single particle, and $\bar{r_h}_2 = \bar{r}_3 = \sqrt{3}r$. Therefore, the value of $\bar{r}$ may be calculated using Equation (A.1), and is found to be Equation (A.3).

$$\bar{r} = \frac{r\left(2\sqrt{3}+1\right)}{3} \tag{A.3}$$

However, the linear trimer can also flex within our model up to an angle of $\frac{\pi}{2}$. If we assume that the trimer exists in the whole range of possible angles with an equal possibility, then it is possible to calculate the value of $\bar{r}$ at both extremes, and take the mean to achieve the mean $\bar{r}$. At the extreme of $\frac{\pi}{2}$, the particle presents two elevations that resemble the dimer, and one that resembles the other linear trimer, such that these two results may be combined into Equation (A.4) for the angular trimer.

$$\bar{r} = \frac{r\left(2\sqrt{2}+\sqrt{3}\right)}{3} \tag{A.4}$$

The triangular trimer presents something more of a challenge. Again, it may be effectively modelled using three different elevations. The first of these is simply a top view looking down onto the plane of the triangle, $\bar{r}_1$, and this presents three particles, none of them blocking any of the others, and so the result for a linear trimer can be reused. From one of the side elevations,$\bar{r}_2$, it appears as a dimer, so again that result can be recycled. However, in order to get a fair representation of the mean radius, is is necessary to consider the plane mutually perpendicular to the two already known $\bar{r}_3$, in which one particle is partially blocking the others. It can be shown via a lot of geometry that Equation (A.5) describes this elevation. For simplicity's sake, this may be approximated to $\bar{r}_3 \approx 2.66r^2$.

$$\bar{r}_3 = \pi r^2 \left[-1 - 2\arccos\left(\sqrt{3}-1\right) - \frac{1}{2\pi}\right] \tag{A.5}$$

Obviously, using the long form of $\bar{r}_3$ has very little benefit over and above its approximation in this context, so henceforth, the exact form (as shown in Equation (A.5)) will not be used.

Using Equation (A.1), it is possible to derive an approximate expression for $\bar{r}$, as shown in Equation (A.6).

$$\bar{r} = \frac{r}{3}\left(\sqrt{\frac{\pi + 2.66}{\pi}} + \sqrt{2} + \sqrt{3}\right) \tag{A.6}$$

For four particles, it is trivial to show using results already derived that for a simple linear arrangement, $\bar{r} = \frac{5}{3}r$, and that a planar triangle with a singly attached trailing particle can be described by Equation (A.7). Similarly, it is possible to calculate the value for a planar square to be as given in Equation (A.8).

$$\bar{r} = \frac{r}{3}\left(2 + \sqrt{2} + \sqrt{\frac{2\pi + 2.66}{\pi}}\right) \tag{A.7}$$

$$\bar{r} = \frac{r}{3}\left(2\sqrt{2} + 2\right) \tag{A.8}$$

The non-trivial calculation for the nanoparticle tetramer is that of the tetrahedral formation. From above, it may be modelled as a solid triangle with precisely $1\frac{1}{2}$ full cirlces, calculated in Equation (A.9). From another elevation, it behaves like the partially masked elevation of the triangular trimer, only with a third particle which has been doubly masked to approximately the same degree. Therefore, the reaults from Equation (A.5) can be used to arrive at Equation (A.11). Similarly, the third elevation can be derived to be given by Equation (A.10).

$$\begin{aligned}
\bar{r}_1 &= r\sqrt{\frac{\sqrt{3} + \frac{3}{2}\pi}{\pi}} && \text{(A.9)}\\
\bar{r}_2 &= r\sqrt{\frac{2\pi + 2.18}{\pi}} && \text{(A.10)}\\
\bar{r}_3 &= r\sqrt{\frac{\pi + 2.66 + 2.18}{\pi}} && \text{(A.11)}
\end{aligned}$$

Using these results from Equations (A.9),(A.10), and (A.11), it is possible to arrive at Equation (A.12) for the final particle.

$$\bar{r} = \frac{r}{3\sqrt{\pi}}\left(\sqrt{2\pi + 2.18} + \sqrt{\sqrt{3} + \frac{3}{2}\pi} + \sqrt{\pi + 2.66 + 2.18}\right) \tag{A.12}$$

Exactly the same techniques can be used to derive equations for larger numbers of particles. In this report, only aggregates of up to 5 particles have been considered, because above that, there quickly becomes an unmanageably large family of possible structures. However, the results considered thus far may be used to gain an idea of the trend in aggregate size as a function of number of constituent particles. Because of the large number of 5-particle aggregates possible, an exhaustive consideration of these is not included here.

In the calculation of the average hydrodynamic radius of n-particle aggregates, it was assumed that each possible aggregate exists with the same probability. This is evidently not going to be the case in the real world - some structures may be energetically unfavourable, others may be very stable, while yet others won't persist long because their shape is favourable for the binding of additional particles to create yet larger compound particles. A more thorough study of factors influencing this would be required for this to be taken into account.

It is also important to note that all the effective hydrodynamic radii calculated here are still only approximations, which completely fail to account for any kind of turbulence effects causing increased drag and therefore an increase in measured hydrodynamic radius vs that calculated, and any effects in which a loosely-bound aggregate may be deformed by applied force as opposed to being accelerated by it, again creating a potential disparity between the calculated hydrodynamic radius and that which would be measured.

Appendix B

DLVO Theory

It should be noted that this is not an exhaustive or rigorous derivation of DLVO theory, but is merely a quick rundown of its origins and means of derivation. For a rigorous derivation, see [127].

Using the full version of the Debye-Hückel Equation (Equation (B.1)), where e is the electronic charge, γ is the the concentration of the binary electrolyte, n_1 and n_2 are the concentrations on anions and cations per molecule of electrolyte, k is the Boltzmann constant, and T is the absolute temperature, it is possible to arrive at a more general and widely applicable expression, as given in (B.1).

$$\Delta\psi = \frac{a}{2}\left(e^{n_1 b\psi} - e^{-n_2 b\psi}\right)\begin{cases} a = \frac{8\pi}{D} e n_1 z_1 \gamma = \frac{8\pi}{D} e n_2 r_2 \gamma = \frac{8\pi}{D} ec \\ b = \frac{e}{kT} \\ c = n_1 z_1 \gamma = n_2 z_2 \gamma \end{cases} \tag{B.1}$$

For a pair of flat idealised infinite plates (rather than spherical particles) it can then be shown that the interaction of the particles, $P(h)$ per unit area is as given in Equation (B.2), where E_1 and E_2 are the values of the electric field at the surface of the plates, h is the distance between the plates. All other variables are as previously defined.

$$P(h) = \frac{D}{8\pi}\left[E_2^2 - E_1^2\right] = \frac{D}{8\pi}\frac{a}{b}\left(C_1 - C_2\right) = ckT\left[\frac{\left(e^{n_1 b\psi_1} - 1\right)}{z_1} + \frac{\left(e^{n_2 b\psi_1} - 1\right)}{z_2}\right] \tag{B.2}$$

This gives us an implicit dependence on h, since C is in fact an implicit function of h. C and h are related by the integral equation, Equation (B.3). This is derived by integrating Equation (B.1).

$$\frac{1}{2}h = \sqrt{\frac{b}{a}} \int_{\psi_1}^{\psi_0} \frac{\mathrm{d}\psi}{\sqrt{\frac{e^{n_1 b\psi}}{z_1} + \frac{e^{-n_2 b\psi}}{z_2} - C_1}} \tag{B.3}$$

By assuming that ψ_0 is non-zero, it is possible to simplify Equations (B.2) and (B.3) in the forms given by Equations (B.4) and (B.5) respectively.

$$P = p\left[\frac{e^{x_1\eta_1} - 1}{z_1} + \frac{e^{-x_2\eta_1} - 1}{z_2}\right] \tag{B.4}$$

$$\frac{x'h}{2} = \int_{\eta_1}^{\infty} \frac{\mathrm{d}\eta}{\sqrt{\frac{e^{x_1\eta}}{z_1} + \frac{e - x_2\eta}{z_2} - \frac{e^{x_1\eta_1}}{z_1} - \frac{e^{-x_2\eta_1}}{z_2}}} \tag{B.5}$$

In the case of a symmetrical electrolyte (that is, one which produces an equal number of primary and auxilliary ions), Equation (B.4) may be simplified to Equation (B.6), where P_0 is another constant.

$$P = 2p\left(z_1 + z_2\right)\eta_0^2 e^{-xh} = P_0 e^{-xh} \tag{B.6}$$

In the case of an asymmetric electrolyte, η_0 is accessible via equation (B.7), in which $\beta = \frac{z_1}{z_2}$. In the case of the symmetric electrolyte, this cancels significantly, since $\beta = 1$.

$$\ln\left(z_1\eta_0\right) = F\left(\beta\right) = \int_0^1 \left[\frac{\sqrt{\frac{1+\beta}{2}}}{\sqrt{e^t + \frac{e^{-\beta t}}{\beta} - 1 - \frac{1}{\beta}}} - \frac{1}{t}\right]\mathrm{d}t + \int_1^{\infty} \frac{\sqrt{\frac{1+\beta}{2}}\mathrm{d}t}{\sqrt{e^t + \frac{e^{-\beta t}}{\beta} - 1 - \frac{1}{\beta}}} \tag{B.7}$$

For such a symmetric electrolyte, the integration substitutions (B.8) may be used, to transform the integral into the form of Equation (B.9) using accepted methods of manipulation of elliptical integrals of the second kind (of which this is one).

$$\begin{cases} u = \frac{1}{k\cosh\left(\frac{z\eta}{2}\right)} \\ k = \frac{1}{\cosh\left(\frac{z\eta_1}{2}\right)} \end{cases} \tag{B.8}$$

$$\begin{aligned} \tfrac{x'h}{2} &= \int_{\eta_1}^{\infty} \tfrac{z\mathrm{d}\eta}{\sqrt{2(\cosh(z\eta) - \cosh(z\eta_1))}} \\ &= \int_{\eta_1}^{\infty} \tfrac{z\mathrm{d}\eta}{2\sqrt{\cosh^2\left(\frac{z\eta}{2}\right) - \cosh^2\left(\frac{z\eta_1}{2}\right)}} \\ &= k\int_0^1 \tfrac{\mathrm{d}u}{\sqrt{(1-u^2)(1-k^2u^2)}} \end{aligned} \tag{B.9}$$

Then it is possible to rewrite Equation (B.4) in the form of Equation (B.10).

$$P = 4\gamma nkT\left(\frac{1}{k^2} - 1\right) = 4\gamma nkT\cosh^2(\alpha) \tag{B.10}$$

This may then be compared to the van der Waals attraction, Equation (B.11).

$$Q = \frac{A}{6\pi h^3} \tag{B.11}$$

Appendix C

Enlarged graphs from Chapter 3

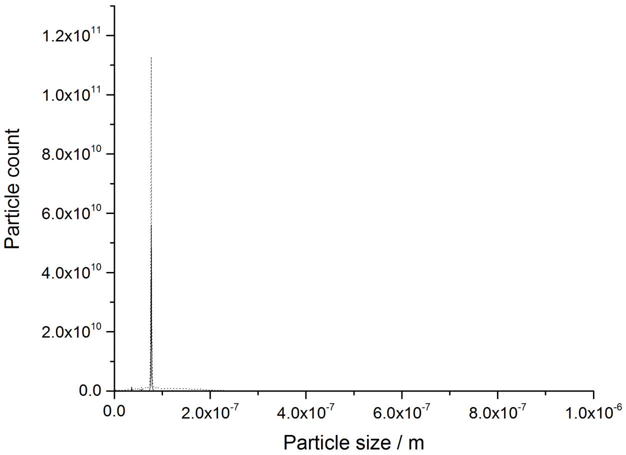

(a) 30 nm particles at concentration of 10^9 particles/mL on first day of measurement.

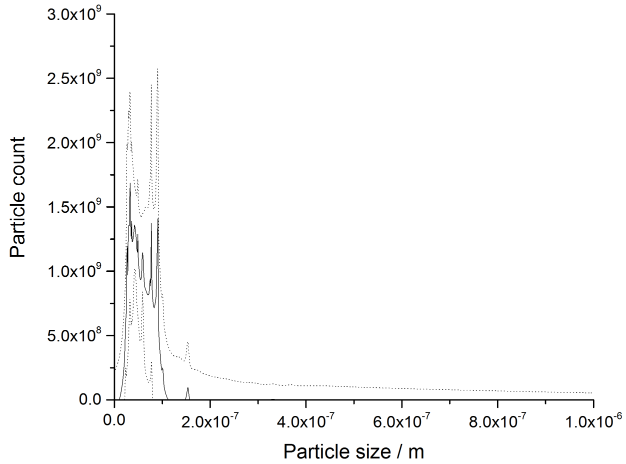

(b) 30 nm particles at concentration of 10^8 particles/mL on first day of measurement.

Figure C.1: 30 nm particles at concentrations of 10^9 particles/mL and 10^{8} particles/mL on the first day of measurement. These are enhanced versions of the plots found in Figure 3.7.

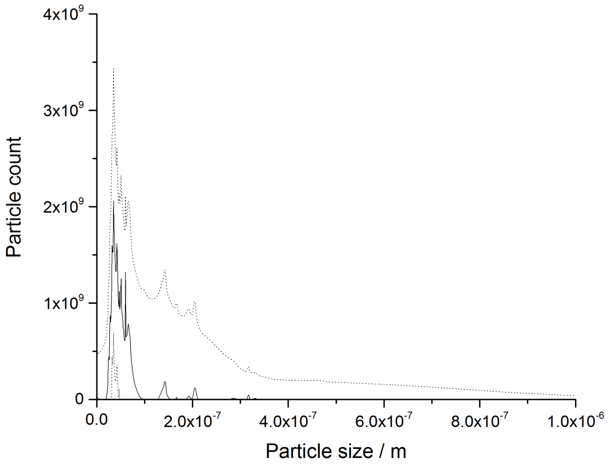

(a) 30 nm particles at concentration of $5{\times}10^6$ particles/mL on first day of measurement.

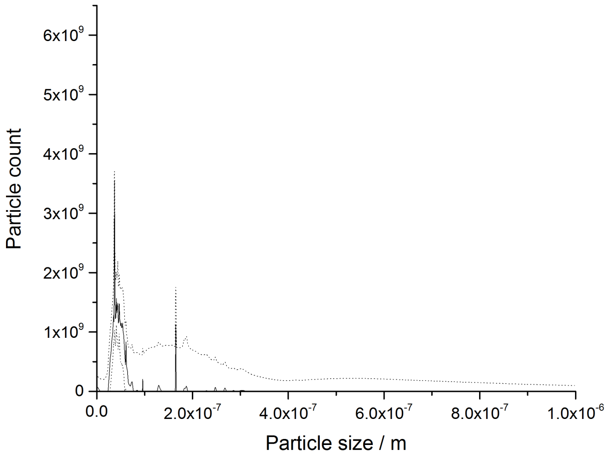

(b) 30 nm particles at concentration of $5{\times}10^5$ particles/mL on first day of measurement.

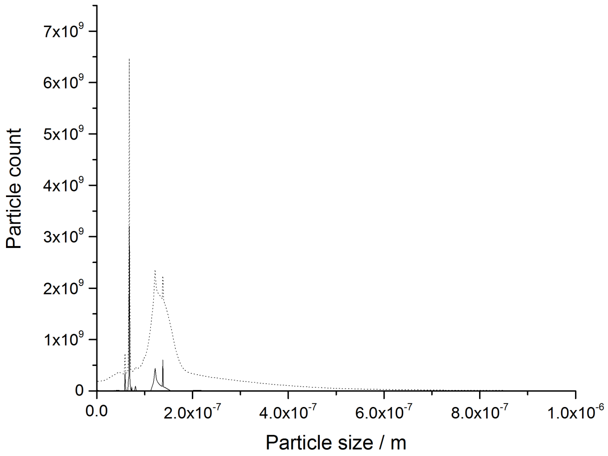

(c) 30 nm particles at concentration of $5{\times}10^4$ particles/mL on first day of measurement.

Figure C.2: 30 nm particles at concentrations of $5{\times}10^6$ particles/mL, $5{\times}10^5$ particles/mL, and $5{\times}10^4$ particles/mL on first day of measurement. These are enhanced versions of the plots found in Figure 3.7.

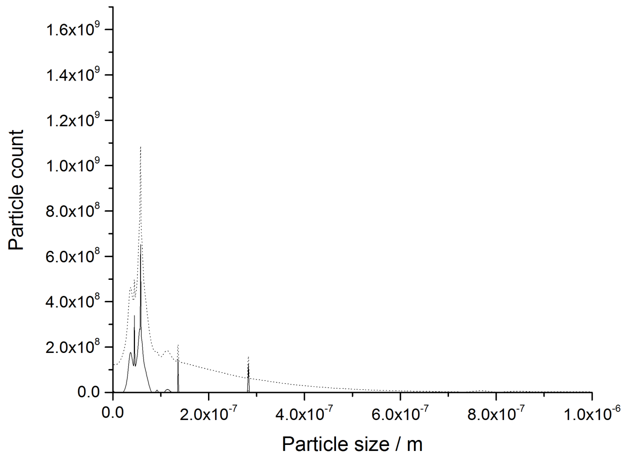

(a) 30 nm particles at concentration of 10^{9} particles/mL on second day of measurement.

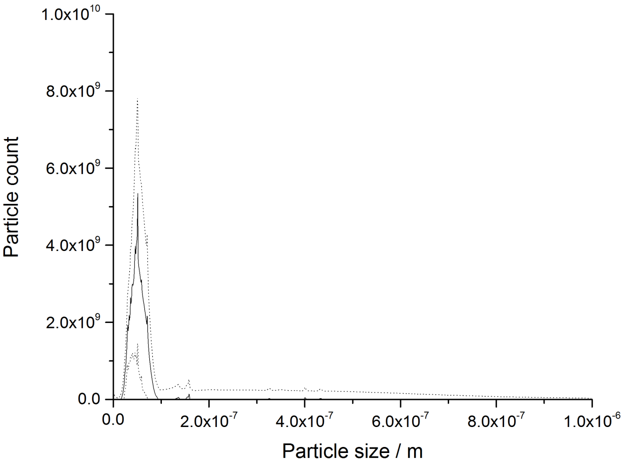

(b) 30 nm particles at concentration of 10^{8} particles/mL on second day of measurement.

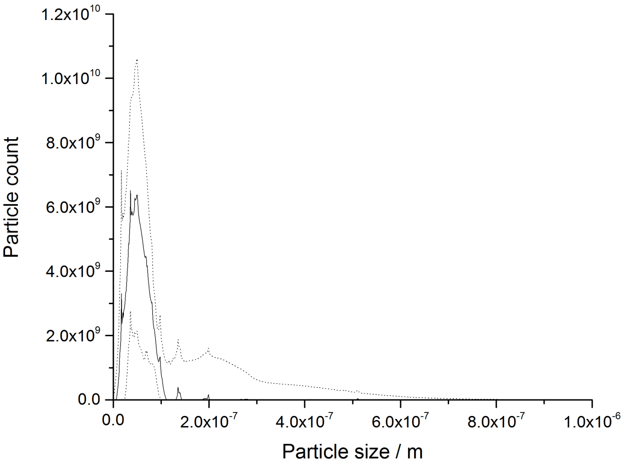

(c) 30 nm particles at concentration of 5×10^{6} particles/mL on second day of measurement.

Figure C.3: 30 nm particles at concentrations of 10^{9} particles/mL, 10 ^{8} particles/mL, and 5×10^{6} particles/mL on the second day of measurement. These are enhanced versions of the plots found in Figure 3.7.

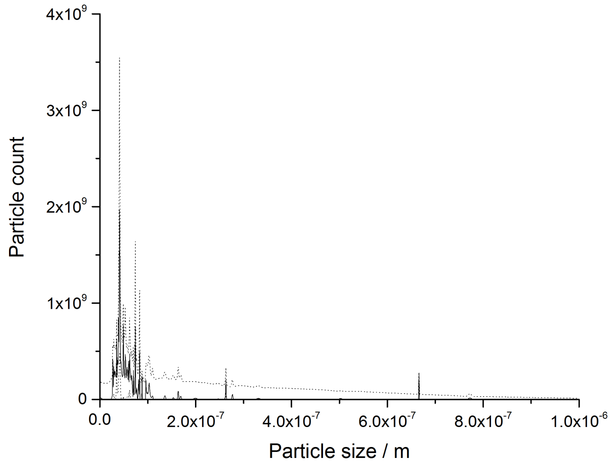

(a) 30 nm particles at concentration of $5{\times}10^5$ particles/mL on second day of measurement.

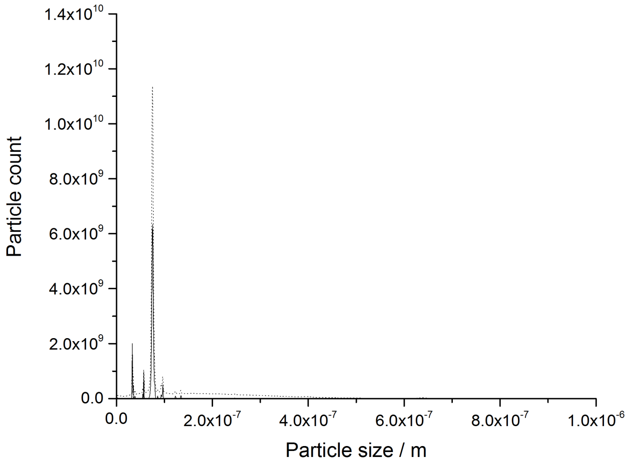

(b) 30 nm particles at concentration of $5{\times}10^4$ particles/mL on second day of measurement.

Figure C.4: 30 nm particles at concentrations of $5{\times}10^5$ particles/mL and $5{\times}10^4$ particles/mL on second day of measurement. These are enhanced versions of the plots found in Figure 3.7.

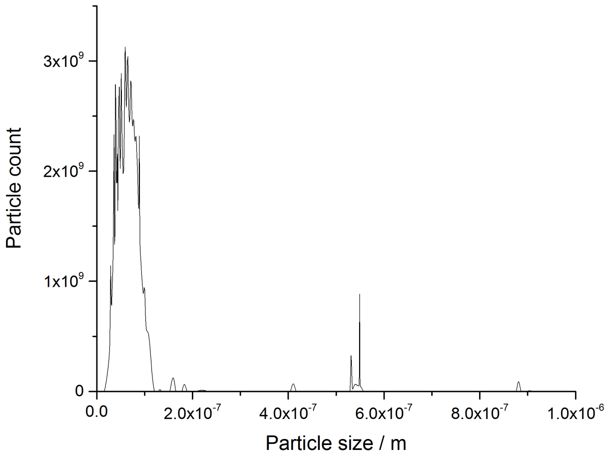

(a) 100 nm particles at concentration of 10^9 particles/mL on first day of measurement.

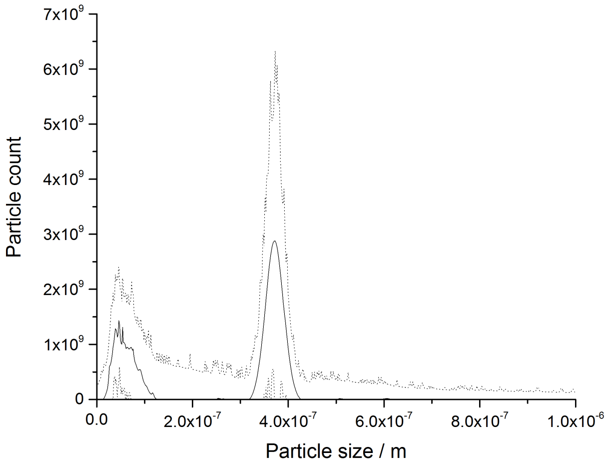

(b) 100 nm particles at concentration of 10^8 particles/mL on first day of measurement.

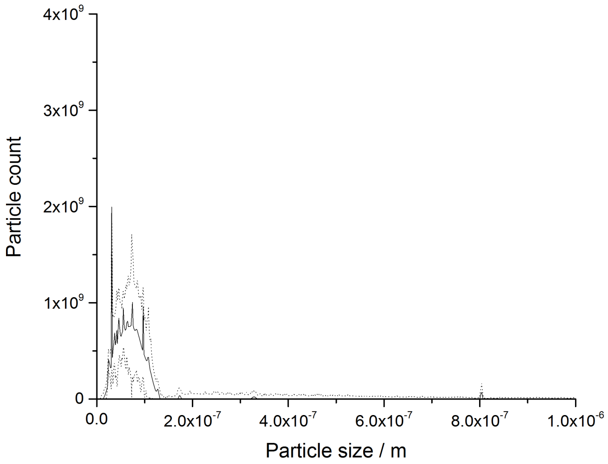

(c) 100 nm particles at concentration of $5{\times}10^6$ particles/mL on first day of measurement.

Figure C.5: 100 nm particles at concentrations of 10^9 particles/mL, 10 ^{8} particles/mL, and $5{\times}10^6$ particles/mL on the first day of measurement. These are enhanced versions of the plots found in Figure 3.7.

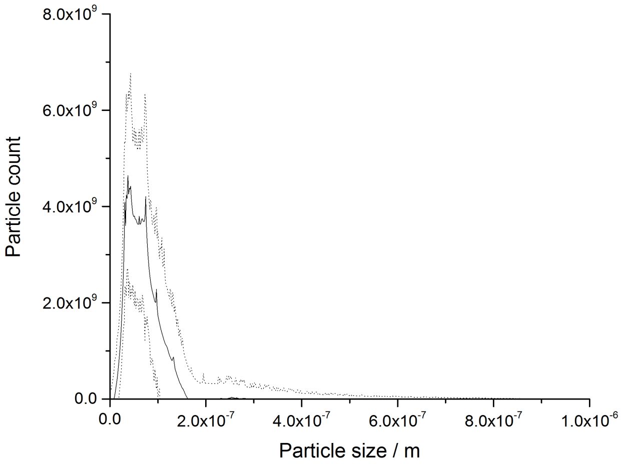

(a) 100 nm particles at concentration of $5{\times}10^5$ particles/mL on first day of measurement.

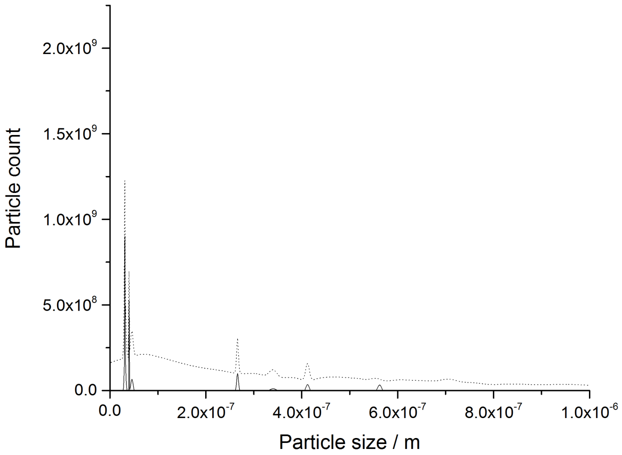

(b) 100 nm particles at concentration of $5{\times}10^4$ particles/mL on first day of measurement.

Figure C.6: 100 nm particles at concentrations of $5{\times}10^5$ particles/mL and $5{\times}10^4$ particles/mL on first day of measurement. These are enhanced versions of the plots found in Figure 3.7.

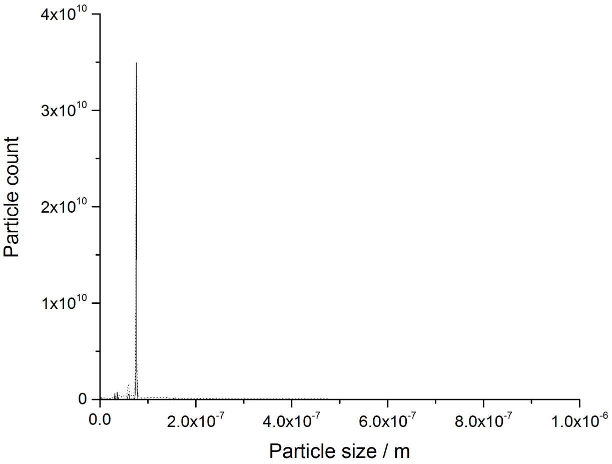

(a) 100 nm particles at concentration of 10^9 particles/mL on second day of measurement.

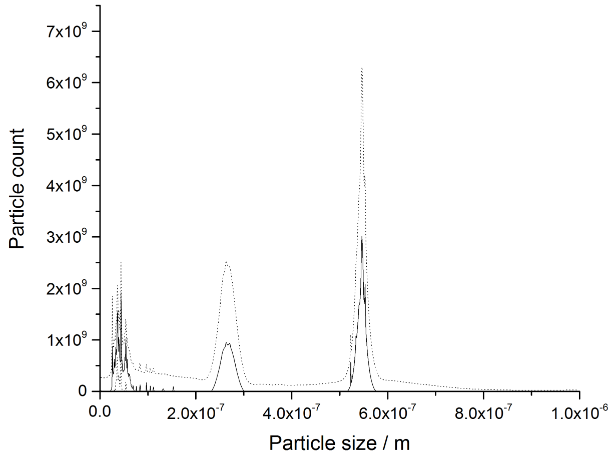

(b) 100 nm particles at concentration of 10^8 particles/mL on second day of measurement.

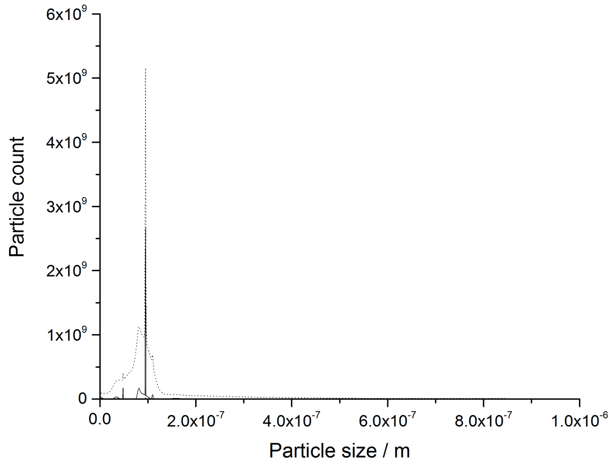

(c) 100 nm particles at concentration of $5{\times}10^6$ particles/mL on second day of measurement.

Figure C.7: 100 nm particles at concentrations of 10^9 particles/mL, 10 ^{8} particles/mL, and $5{\times}10^6$ particles/mL on the second day of measurement. These are enhanced versions of the plots found in Figure 3.7.

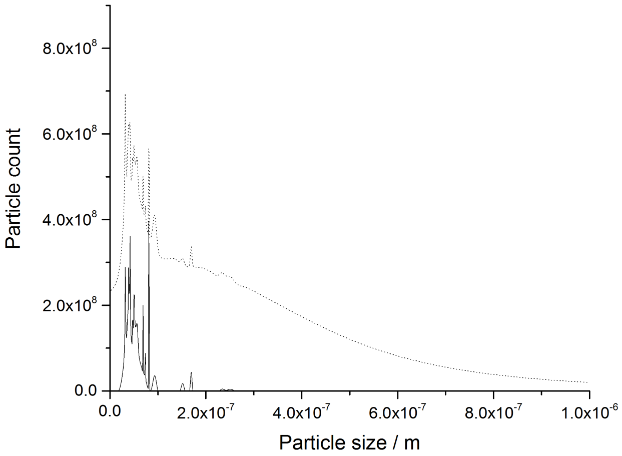

(a) 100 nm particles at concentration of 5×10^5 particles/mL on second day of measurement.

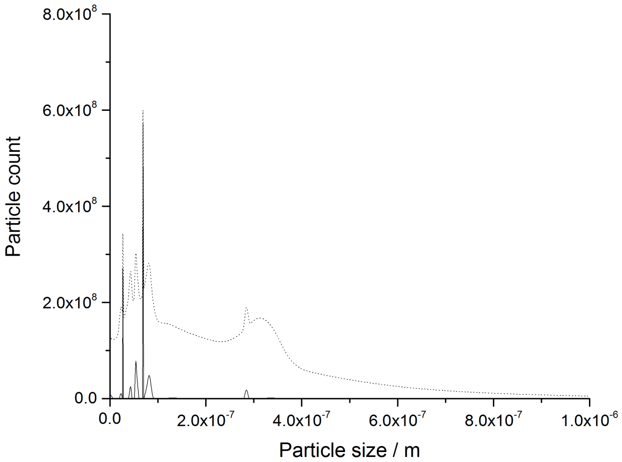

(b) 100 nm particles at concentration of 5×10^4 particles/mL on second day of measurement.

Figure C.8: 100 nm particles at concentrations of 5×10^5 particles/mL and 5×10^4 particles/mL on second day of measurement. These are enhanced versions of the plots found in Figure 3.7.

Appendix D

Enlarged graphs from Chapter 4

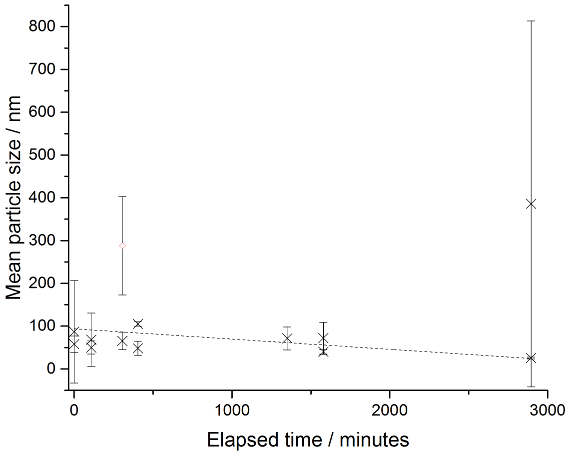

(a) 30 nm PEG-NH_2-capped particles spiked into artificial hard water.

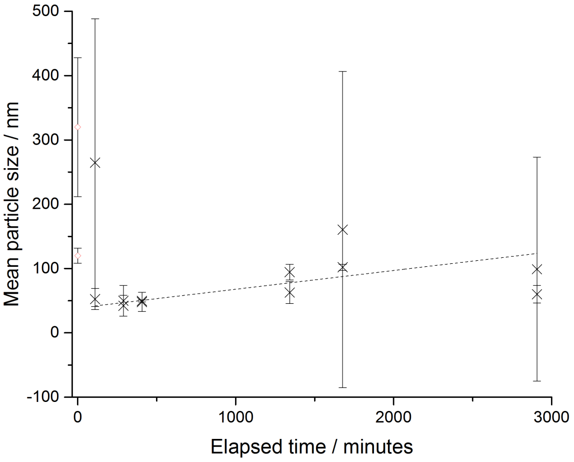

(b) 30 nm citrate-capped particles spiked into artificial hard water.

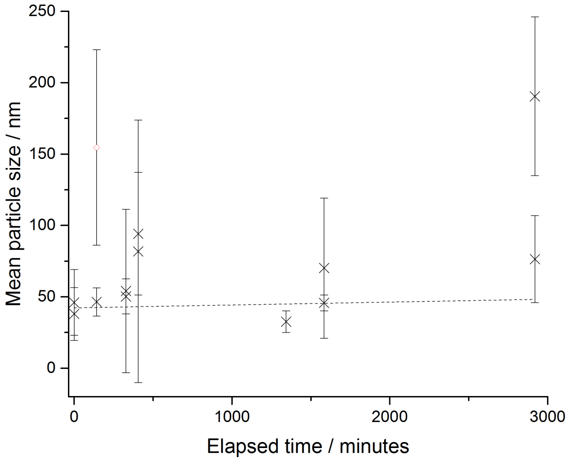

(c) 30 nm PEG-capped particles spiked into artificial hard water.

Figure D.1: 30 nm particles capped with PEG-NH_2, citrate, and PEG, spiked into artificial hard water. These are enlarged versions of plots presented in Figure 4.3

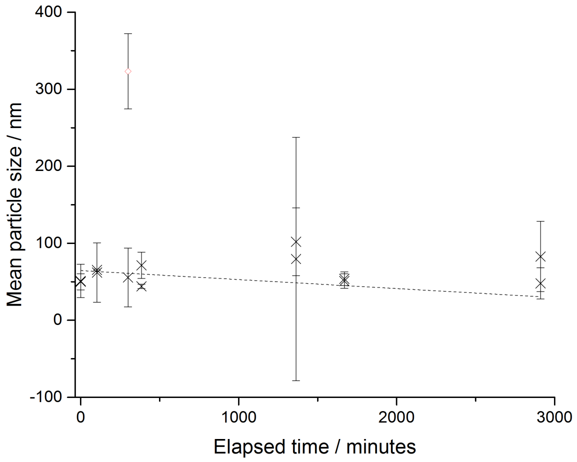

(a) 30 nm PEG-NH$_2$-capped particles spiked into artificial pond water.

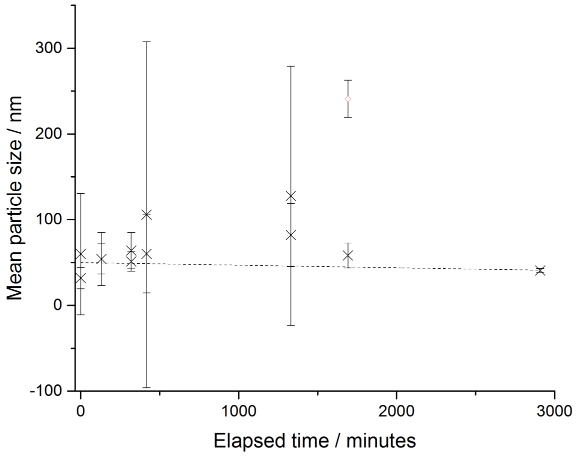

(b) 30 nm citrate-capped particles spiked into artificial pond water.

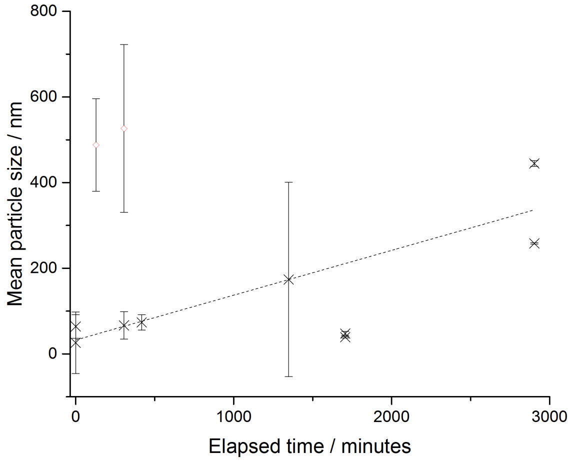

(c) 30 nm PEG-capped particles spiked into artificial pond water.

Figure D.2: 30 nm particles capped with PEG-NH$_2$, citrate, and PEG, spiked into artificial pond water. These are enlarged versions of plots presented in Figure 4.3

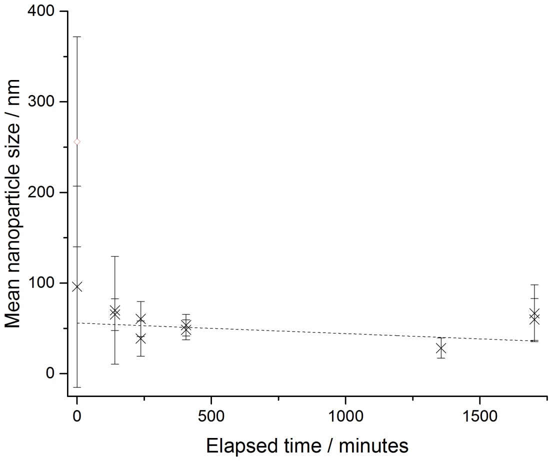

(a) 30 nm PEG-NH$_2$-capped particles spiked into artificial sea water.

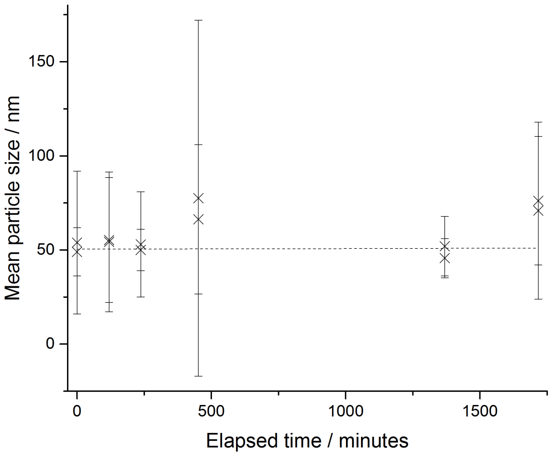

(b) 30 nm citrate-capped particles spiked into artificial sea water.

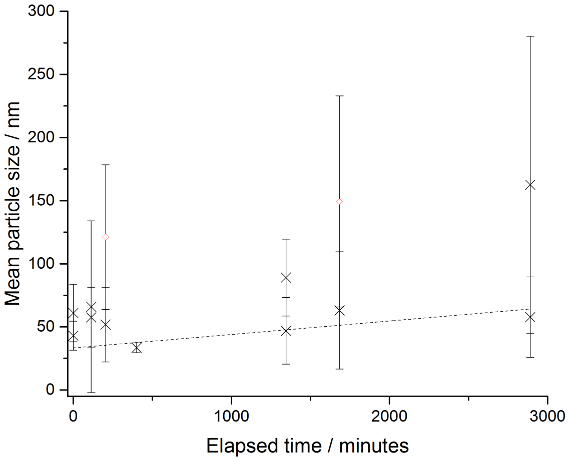

(c) 30 nm PEG-capped particles spiked into artificial sea water.

Figure D.3: 30 nm particles capped with PEG-NH$_2$, citrate, and PEG, spiked into artificial sea water. These are enlarged versions of plots presented in Figure 4.3

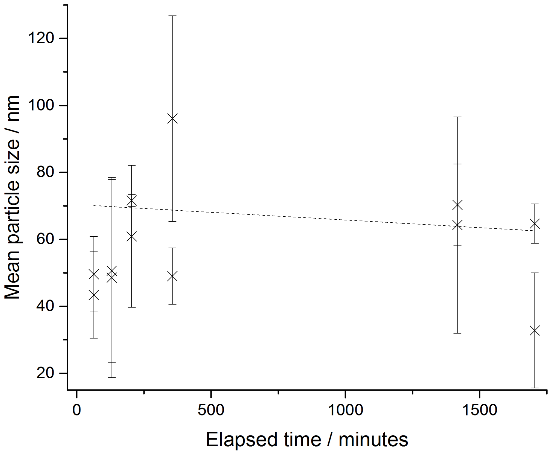

(a) 30 nm PEG-NH_2-capped particles spiked into dionised water.

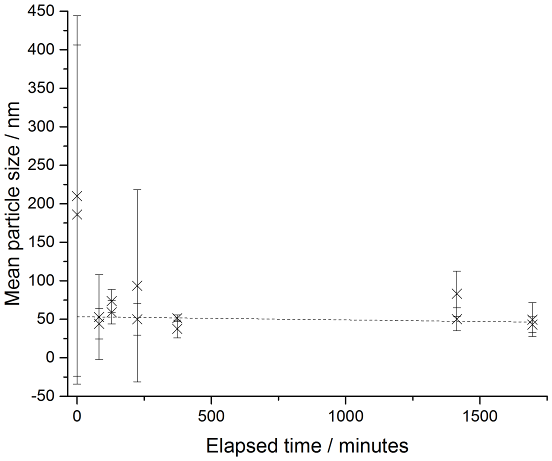

(b) 30 nm citrate-capped particles spiked into deionised water.

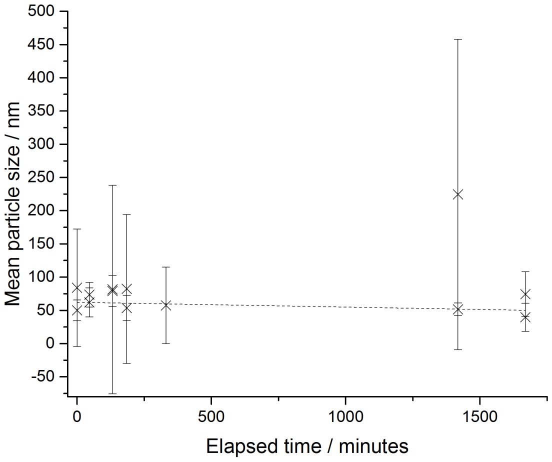

(c) 30 nm PEG-capped particles spiked into deionised water.

Figure D.4: 30 nm particles capped with PEG-NH_2, citrate, and PEG, spiked into deionised water. These are enlarged versions of plots presented in Figure 4.3

Appendix E

SETAC Globe - Pushing Nanoparticle Studies To the Limit: Working at Environmentally Relevant Concentrations and in Complex Matrices

Samuel R Thompson, University of York, Patrick Bauerlein, KWR Watercycle Research, Lars Michael Skjolding, Denmark Technical University, and Ralf Kaegi, Swiss Federal Institute of Aquatic Science and Technology (EAWAG)

Environmental nanoparticle studies, while becoming increasingly commonplace, are difficult to perform at low enough concentrations, and challenging to perform in sufficiently complex matrices, in order to represent real-world conditions. However, new tools, techniques and methodologies are being developed that allow studies to more closely approach true environmental relevance. Literature has recently been published demonstrating incremental improvements in detection limits using techniques such as single particle inductively coupled plasma mass spectrometry (spICP-MS), particularly showing improvements in differentiating particles against complex backgrounds. This session built upon that foundation by discussing not only some of the more recent developments in the field but also applications of wide-ranging techniques, from X-ray nanotomography and nanoparticle tracking, thermo-optical analysis and spICP-MS. These were reported to have been applied in a broad selection of contexts, including laboratory-based proof-of-concept experiments through fully integrated field studies.

Seventeen platform presentations were delivered in three two-hour segments. The first segment addressed recent developments in instrumentation with most of the talks focusing upon developments of variants of single particle ICP-MS, including variously modified systems to include capabilities such as time-of-flight (TOF) and fast acquisition speed technique (FAST) apparatus. While the majority of engineered nanoparticle studies tend to have an emphasis in natural waters, one presenter discussed the development of spICP-MS for making measurements of particles in soil matrices. Another presentation was on the development of X-ray micro- and nano-tomography as a tool for probing nanoparticleorganism interactions. One presentation addressed the application of thermo-optical analysis for differentiating carbon nanotubes (CNTs) from other sources of carbon, particularly when used as a structural material. The final talk in the first segment detailed the development of nanoparticle tracking analysis (NTA) to allow it to function not only at environmentally relevant concentrations but also to determine nanoparticle shape at the same time as size.

The second segment took a closer look at the applications of these new technologies in the laboratory and in the field. Two presenters spoke about the successful detection and measurement of engineered nanoparticles in natural river water, one site in the Netherlands and another site in France. A further update was provided on the environmentally relevant bioaccumulation of nanosilver in fish using the experimental lakes system in Ontario, Canada. Researchers found significant bioaccumulation of silver even at higher trophic levels. Attention was given to the leaching of nanoparticles into the environment, both from more conventional sources like sewage treatment plants (STPs) and landfill sites, but also from recently identified sources such as nanoparticle impregnated textiles and the effects of various detergents have upon the leaching process of these materials. The majority of studies in this segment focused on inorganic nanoparticles.

The final segment of platform presentations examined the behavior and measurement of nanoparticles in artificial media. These presentations included effects-based studies interested in the metabolomics of fullerene interactions with mussels, assessments of nanoparticle stability over time in marine waters and freshwaters, and an in-depth study of the hetero- and homo-aggregation of engineered nanoparticles and naturally occurring organic matter, revealing that natural aggregation processes are almost entirely driven by hetero-aggregation. The session ended with a final talk detailing the assessment of detection limits of isolopically labeled quantum dots (QDs) in a range of complex media and demonstration of detection to the low nanograms per litre, paving the way for future studies involving QDs.

The session had good attendance, with an estimated audience of more than 200 at several of the presentations. Some of the most important points discussed include:

- Several of the more established nanoparticle analysis systems are now sufficiently advanced that they can be used to monitor engineered nanoparticles in situ in natural water and soil systems at environmentally relevant concentrations.

- There are still many nanoparticle analysis techniques under development. This should yield the widespread ability in coming years to make measurements of nanoparticles of types and in matrices which are currently not viable.

- Further work is necessary to improve the detection and measurement of organic nanoparticles in environmentally relevant samples. This should focus on the specific properties that differentiate the engineered particles from the natural analogues.

- Despite the substantial progress that has been made in the analytical development, the next step requires harmonization, standardization and validation of the experimental methods currently in use.

- The speed of analysis is in need of further refinement in order to allow for more real-time monitoring.

Author' s contact information: `samuel.thompson@york.ac.uk`

Appendix F

Software installation and use

F.1 system requirements

Operating system Windows 7+, OSX 10.9 Mavericks+, Linux kernel 3.11+. Earlier systems may work but are untested.

Software Matlab R2014b or more recent. Graphical elements may lay themselves out non-optimally on some platform/version combinations.

RAM 16GB RAM per minute of video analysed (in a single video file. There is no limit to the total length of video analysable in smaller chunks). This is also approximately correct for video capture. RAM use is very intensive, and error-correcting (ECC) RAM is highly recommended.

Processor Any amd64 (x86-64) processor. Either and AMD FX- series or Intel Xeon recommended for data analysis.

In addition to this, for video capture the following additional requirements must be met:

Operating system Linux only is directly supported. If IDS releases their SDK for OSX, OSX will also be automatically supported. Video may be captured using any software on another platform provided it can output archival (uncompressed) AVI video files.

Hard drive Sufficiently fast storage device. Capture to a slower hard drive is possible, but is *very* slow. SSD or RAID array capable of sustained sequential writes of >350MiB/s highly recommended.

Interface Suitable interface (USB3/GigE) for compatible camera.

Camera Compatible camera (IDS/Thorlabs).

Compiler GNU Compiler Collection (GCC) 4.8+. Compilation is possible using Clang/LLVM instead, but is not covered here.

F.2 Installation and use

The software is provided as a collection of code files rather than a compiled Matlab Runtime to enable the end user to modify it freely. This means that installation and configuration is slightly more complex. Some of the files are not my own; these all have the appropriate 3rd-party license in their comments. All files without an explicit license are covered by a GPLv3 license.

Most of the matlab files are in a single folder. The two of these that are of most direct use are `GUI.m` and `yarccscript.m`. Running GUI.m will run the program in graphical mode from within the Matlab desktop workspace. This is good for troubleshooting, but only allows a single instance of the program to be run. This is the only supported way of running the software under Windows. yarccscript.m is a modified non-graphical non-interactive version of the program, written specifically for use on computing clusters based on Sun grid engine (SGE), though should in theory run on any correctly-configured computer running Linux or OSX. Both files rely upon the same back-end files and execute an identical analysis.

Also provided is a shell script, particle_tracker.sh. This is a very simple script which allows the particle tracker to be started independently of the Matlab desktop environment on Linux and OSX. The script assumes that your installation of Matlab is in the default location, and will need editing for the correct version of Matlab. After inserting the correct Matlab version number, create a soft link to the script file in `/usr/local/bin`, or some other location in your default `$PATH`. Thereafter, the interface may be called by running 'particle_tracker' directly from the terminal. Users of OSX should note that the long path to the Matlab executable is necessary despite the default Matlab installer creating a symlink in `/usr/bin`. If the system default symlink is used, only one instance of the interface may be run at a time, which in many circumstances can be a frustration. OSX users should also note that OSX will not load the Matlab desktop if the particle tracker is already running.

The GUI contains three sections. Generally speaking, the left-hand section is for data capture, the central section is for data analysis, and the right-hand section is for data visualisation and export. The different controls are described below:

F.2.1 Data capture

Data capture is carried out using c++ mex files for the hardware interface. This is only supported under Linux. More detail is given in the appropriate appendix.

Camera Selection This is currently unused. Support for multiple cameras may use this at a later date.

Gain this is the camera gain setting.

Gain boost some supported cameras have a gainboost setting for additional hardware gain. This will enable it if available.

Exposure This modifies the exosure. Occasionally, setting the maximum possible exposure will cause a camera issue and it will reset back to minimum exposure. Exposure in interdependent upon framerate and area of interest.

ROI Most supported cameras allow for a higher framerate for smaller regions of interest. This allows it to be set. This functionality is occasionally temperamental, and should not be used when the camera is in monochrome mode.

Capture in... This allows the camera to be set in either colour or monochrome mode. Monochrome mode currently just takes the blue channel from the camera. This may be modified to make it more flexible in later versions.

Snapshot Take a high-quality image using the current settings. This is saved in the current working directory (usually the directory the code is stored in).

I'm using an SSD Because a decent SSD is capable of writing video as fast as it is captured, selecting this option bypasses the lengthy file-writing stage of the capture process. Only use on and SSD with the scheduler set to NOOP (no optimisation), and which is capable of sustaining sequential writes sufficient for the camera and framerate in use. When using this option, the capture will be a stack of uncompressed and sequentially-named .tif images. When not using this option, files will be stored as a single archival (uncompressed) AVI video file. Unfortunately AVI output is not possible in real time.

Live Begins a live preview in the preview window. This is a low-quality preview captured at about 1 frame per second. Some cameras don't support the functions used, in which case it does nothing. On cameras which support it, and capture parameter may be modified live.

Stop This stops any live preview.

Update Preview This will update the contents of the preview window according to the current settings. It is always a good idea to click this even after changing a parameter which has apparently already updated the preview - sometimes the driver will only send a partial update the first time.

Capture This institutes a capture of a video. This writes a custom c++ file with the correct capture settings in, compiles it against the current Matlab libraries, and then executes the capture function as a matlab executables file. For more details on this, see the relevant appendix. No progress bar is displayed, but progress may be tracked using a resource utilisation monitor. It is possible to skip the compilation stage by disabling a switch that's hidden in a codefile. Because this can cause capture to fail catastrophically and even cause kernel panics if the mex binary uses CPU features from a different machine, this is hidden. Compilation typically takes <1 second, and should in nearly all cases be left on.

Select framerate Used to select the framerate of the capture. These are only approximate framerates - the software will try to set the closest possible match, usually within <0.1 frames per second, but the program will write the exact framerate into the output file. Setting a framerate higher than supported will result in the highest available framerate being used.

Select capture duration This is used to select the duration to capture for. Setting a capture duration that will run you out of RAM will cause the capture to fail, and will leave you at the mercy of your kernel's OOM killer.

Enter save path here Enter the path to save your captured data here, or click the button to the right to get a save-as dialog. Always save each capture into a different folder, otherwise some ancillary files will be overwritten by subsequent captures.

F.2.2 Data analysis

Data analysis is available on all platforms supported by Matlab. Analysis of files captured using different software/equipment is possible. Options are described below.

Scrubber This allows you to scrub through your file in the preview window and check analysis parameters.

Disc filter This needs to be enabled with the adjacent checkbox. It works on the assumption that all particles will be disc-like entities in the video, and will use a filter to remove non disc-like objects. The slider alters how strongly this selection is applied.

Compress This needs to be enabled using the adjacent checkbox. This compresses the dynamic range of the input video and thereby enhances the contrast by expanding the brightest fraction of the dynamic range to fill the whole dynamic range, thus expunging the darkest parts of the images. The slider controls the threshold for this.

Blur This needs to be enabled using the adjacent checkbox. This applies a basic gaussian blur to the image. This may be useful for removing speckle noise. The amount of blur is controlled using the slider.

Screen Gain This needs to be enabled using the adjacent checkbox. This just changes the overall gain of the image. It may be useful for images which were under-exposed.

Global size parameter This is the minimum distance between particles in order for the software to determine them to be two different particles rather than just parts of the same particle. This should be set to be greater than or equal to the max step length parameter to avoid the tracker oscillating between two particles.

Cutoff The software assigns each possible particle a probability of being a particle. This alters the cutoff probability. This should be adjusted until only objects that look like particles are identified as such in the preview window.

Percentile threshold This has no effect, and will probably be removed in later revisions of software.

Restore This restores analysis parameters saved using the export function.

Input selection This allows selection of files for analysis. Select either the relevant AVI video file, or for a .tif stack, choose the `params.ids` file associated with the relevant .tif stack.

Minimum steps per track This is the smallest number of jumps a single particle must be tracked for before it is added to the list of particles outputted in the result. Remember that a particle detected in n frames will have been tracked for $n-1$ jumps.

Minimum % standard error This discriminates particles on the distribution of step lengths. Particles whose step-length distribution gives the estimate for the sphere-equivalent hydrodynamic diameter an uncertainty greater than this are discarded. It should generally be set to be large, and used carefully.

Analysis type This is used to select whether all of the selected file or just a fraction should be analysed. Partial analysis is currently only available for AVI videos; analysis will fail for .tif stacks. If n frames are requested for analysis, this will always be the first n frames.

Pixel size This should be set to the change in displacement in metres of a particle moving by a single pixel. This will need to be calculated using the pixel pitch of the camera and the magnification of the optical system. Reading this from the camera is not supported, this will be removed in later versions.

Suspension medium This is used to input the properties of the suspending medium. The system has built-in values for the properties of pure water so only needs a temperature. All other media need their viscosity at the recorded temperature to be input in pascal-seconds.

Minimum expected particle size This is the minimum particle size expected - any particles measured to be smaller than this will be ignored. This is useful to weed out sub-nanometre noise, and should not be used to weed out inconvenient results!

Max step length This is the maximum number of pixels that a particle may jump between frames before it is classified as a new particle. This should be the same or smaller than the global size parameter to prevent oscillation between particles.

Evaluate shape This is experimental and should not be used authoritatively. It requires the refractive index of the particle material, if known. Currently very inaccurate and unreliable.

Drift correction This option examines the mean trajectory of all detected particles and where drift is detected, will remove it. This is useful for correcting for the effects of convection, but care should be taken when only a few particles are detected in each frame, as this could skew the analysis result.

Export gaussian This tool can be useful for further analysis of video data using differential dynamic microscopy (DDM). This creates a new AVI video from the detected particles, replacing each particle with a normalised gaussian.

Enter save path here Enter the path to save the processed gaussian export to. Not necessary for normal analyses, which will export the analysis results to the original data directory.

Export config This exports the current analysis parameters to a config file. This can be very useful for analysis using compute clusters - analysis parameters may be set using this tool, and then the exported config file may be sent to the cluster with the data for remote analysis.

Process! This starts a local processing job. A progress bar is displayed for each of the three stages - pre-processing, particle detection, and trajectory linking. The relative durations of each stage are highly dependent upon the input video and analysis parameters selected. The interface will become unresponsive while analysis is taking place.

F.3 Data visualisation and export

The software only includes some basic visualisation and export tools, other packages are better used to creating graphics for publication.

Enter path here Enter the path the the `output.csv` file generated by the analysis process to visualise.

Histogram binning Select the histogram binning mode. When in histogram mode, this allows the number of bins to be specified. In automatic mode, the software will decide how many bins to plot depending upon the number of datapoints available.

Trimming This can be used to select a maximum and minimum size of particle to consider. This can be useful for removing noise at sizes no particles should be present, or for zooming in on a part of the size range.

Minimum steps per track This allows the minimum steps to be altered at the point of visualisation. Setting a value smaller than the equivalent option used for analysis has no effect.

Peaks to look for This can be used to select the number of peaks to look for. These are listed in the 'peaks found' box below. If more peaks are asked for than are found, then all those found are listed and an error is generated. Peak localisation is by a simple ranked search for local maxima. More advanced algorithms are available in other plotting packages. Peak heights are also calculated, though these are only meaningful or useful in histogram mode. Occasionally, this will fail to find peaks when in smoothed mode and few particles are tracked.

Plot/replot This replots the output with the current plotting settings.

Use distribution smoothing This option can take a few minutes to compute for larger datasets. When plotting a naïve histogram, the uncertainty in each particle's size measurement is neglected, and a particle with a large uncertainty in the estimate of size is given equal significance to one with a small uncertainty. The distribution smoothing option generates a normalised gaussian for every detected particle, whose standard deviation is the same as that associated with that estimate of the particle's size. Thereby it gives a greater weight to more statistically robust measurements of particles.

Export Graph This exports the smoothed data to a CSV file called `output.export.csv`.

Mean size Gives a mean particle size for all particles currently being plotted. Only functions correctly in histogram mode.

Standard error This is the standard error associated with the estimate of the mean particle size. Again, this only functions in histogram mode.

Standard deviation This gives the standard deviation of the size distribution when in histogram mode.

Particle count Gives the number of particles currently included in the distribution. Only gives a sane result when in histogram mode.

Save and capture again Reinitialises the camera for subsequent capture without reloading software.

Save and exit Closes software.

F.4 Software availability

Owing to the large number of lines of code (>10,000) and the fact that 3 different languages are used, the code is only available digitally.

Appendix G

Integrating a high-speed software framegrabber into Matlab using mex files

G.1 Introduction

It is possible with a lot of tinkering to persuade matlab to work with a uEye camera under linux, with the aid of some C++ coding, the API provided by the uEye drivers, some mex files, and the OpenCV C library for computer vision. This manual is divided up into sections. It assumes a rudimentary knowledge of linux, C++, and matlab.

This manual starts by going through the proceedure to obtain still images, and then extends the technique to capturing strings of images, and then videos. It it *not* a comprehensive manual of the uEye API, not does it aspire to be. Rather, it aims to help the reader overcome the steep learning curve of the new uEye API user and get them to the stage at which the complete reference manual makes a bit more sense than it did to me the first time I saw it.

This should work with all USB (2&3) uEye cameras, and probably GigE-based, though I can't test this (I think the GigE cameras may have a slightly different initialisation routine). 'uEye cameras' includes all such branded cameras sold by IDS, and all rebranded cameras, such as those sold in the DCU range by Thorlabs.

G.2 Mex files

Mex files are a means of integrating code in C, C++, or Fortran into a matlab project. Under linux, matlab detects the g++ compiler (part of the GCC compiler collection) automatically, and should be able to use it automatically. If you use windows, seriously consider switching operating systems, or you're letting yourself in for a world of pain. I think there are free Microsoft C++ Redistributable packages, but I have never used them. There are no uEye drivers for OSX, though you could probably port them from the linux versions if you were that way inclined (I'm not). Under OSX mex still works, and will automatically detect either g++ or CLang compilers. You can manually select between different available compilers by running `mex -setup` from the matlab command prompt. CLang usually can optimise code slightly better, but since we won't be optimising at all, it is of remarkably little consequence which we use. It is worthy of note that g++ has a larger user community, so troubleshooting will tend to be easier.

A mex file in C++ (which is what this manual deals with) has several important things that need to be included with it. These are:

-The correct mex header file

-The correct gateway function

-Pointers to the matlab variables

-A self-termination

G.2.1 Mex header file

The mex header file should be included in all mex functions. This may be done in the normal way, by adding `#include <mex.h>` to the preamble. If your matlab installation has been done properly, and the compiler is correctly configured, then g++ should be able to find the correct file automatically. If the header file isn't automatically found, then if you ask nicely I might be able to write you a script that fixes it for you.

The mex header file does several things:

-It defines several C++ types that don't appear in normal C++. These include things like `mxArray`, which allow C++ to correctly read matlab arrays right from the memory address matlab stores them at using pointers, rather than copying the variables across, thus saving on both the memory burden and the computational time.

-It introduces functions that can convert between matlab types and C++ types (for example, if you pass an array from matlab to C++, you use some C++ libraries that require an input array to be a C++ array, you need to have a means of converting the array to be readable to the external library. It also allows for conversion the other way.

G.2.2 Gateway function

Normal C++ programs require a `main` function, which returns an integer `1` upon successful completion. Matlab has no capacity for a mex function to return any data in the ordinary way, and because a `main` function always has to return an integer, your mex code cannot contain a `main` function. Instead, it needs a 'gateway function', which must always be called 'mexFunction', and must always return nothing, ie `void mexFunction()`. This mexFunction needs to have precisely 4 arguments, which takes us on to the next section...

G.2.3 Pointers to matlab variables

Of the 4 arguments that mexFunction takes, two are pointers to matlab variables, and the other two enumrate them - the 4 arguments are paired as follows:

-`nrhs`, which is the number of variables on the right hand side of the matlab equation. For example, if the line of code calling a mex function called `myFunc` was `out1,out2 = myFunc(inArray, var1, var2);`, then `nrhs` would be the integer '3'.

-`nlhs` is the corresponding number of variables on the left hand side of the calling function, so in the case of the above example, this would be the integer '2'.

-`prhs[]` is a pointer to the right hand side of the matlab function. For example, `prhs[0]` would contain the input variable `inArray` from the example, `prhs[1]` would point to `var1` and so on.

-`plhs[]` is exactly the same, only it points to the left hand side, so `plhs[0]` would return a pointer to `out1`.

Therefore, the line declaring the gateway function must *always* be as follows:

```
void mexFunction(int nlhs,mxArray *plhs[],int nrhs,const
    mxArray *prhs[])
```

It is important to note that these two pointers don't behave like an ordinary C++ pointer - it isn't possible to de-reference them normally. Let's look at it with the aid of an example: say we were calling a function `a = myFunc(b);` from matlab. Then `prhs[0]` would be a matlab pointer to `b` in matlab. If `b` was of type `double` in order to access the value associated with `b` from C++, we would use a function from mex.h, `mxGetScalar`, as follows:

```
double b = mxGetScalar(prhs[0]);
```

`b` could then be used in exactly the same manner that one would use the double `b` in matlab.

Similarly, assigning return functions isn't as simple as it could be. While it should be possible to assign a variable to provide the value of `plhs[n]` perfectly trivially, it actually requires that a new pointer be declared. For example, using again the simplest case of double type variables and `a = myFunc(b);`

```
double *a = mxGetPr(plhs[0]);
```

then `a` may be used as a normal C++ variable, and when the mexFunction terminates, the value of `a` will be transferred back into matlab as the output.

for more complex systems, the same may be repeated with `plhs[1], plhs[2]....plhs[n]`, and the same with `prhs[1]` etc....

It is also possible to assign arrays to these output pointers by using the function `mxCreateDoubleMatrix()`, documentation available from mathworks.

G.2.4 Self-termination

Because mexFunction doesn't return anything upon successful execution, your mexFunction must be self-terminating - it doesn't just come to the end of the block of code associated with mexFunction and terminate gracefully - it can behave erratically. It is best to make sure that there's always a `return;` at the end of the block. It will fail to compile if there's anything between the `return` and the semicolon - a function that returns `void` cannot return a value!

mex functions can be compiled from within matlab using the command

```
mex myFunc.cpp
```

`myFunc.cpp` must be in the active matlab directory. Thereafter, it can be called in the `argsin = myFunc(argsout);` syntax of any other matlab function.

G.2.5 Mex with other libraries

While you can write as much mex code as you want at this point, later on you'll find that while your code compiles, it will likely ask for a shared object file that it looks like it already has. This is because a given version of matlab is designed to run with a specific version of GCC, and if a more recent version of GCC is used during compilation, the library that matlab installs for itself is incompatible with the compiler.

This is easily remedied:

open a terminal window and login as root (run `sudo -i`). then run

```
find / | grep NAME_OF_LIBRARY_MATLAB_WANTS
```

you'll find that there's a library (`.so`) file with that name should be installed in `/usr/lib/` (unless you've been playing with your GCC installation), and also in your matlab install folder. `cd` to the matlab version, and change its name to add a `.old` extension on the end of it. Then create a symlink to the other version of it (run `ln -s PATH_TO_GCC_LIBRARY NAME_OF_SYMLINK`) The name of the symlink should obviously be the same as the file it replaces. Repeat this for as many shared objects as matlab wants.

Next time you compile and run the code, matlab should follow the symlink and your code should execute successfully with the correct library.

G.3 uEye API

The uEye API can be simply added to a mex file. There are two components that the uEye API requires in order to work. The first of these is just another header file, that on a normal installation of uEYE can be included by using:

```
#include <ueye.h>
```

The header file contains mappings and definitions for user-readable parameters (`IS_WAIT` is far more user-friendly than `0x1F33FA1B`), and declares some new and useful types and structs. You should never need to worry about the header file though.

However, it also needs to be compiled against a shared object. Shared objects in linux are pre-compiled binaries, which have the file extension `.so` and always start with the filestub `lib`. Once again, a standard uEye installation should allow g++ to find the shared object automatically. If you're not using linux, this isn't the case, but you still need to compile against the same object. I have no idea how this works, but you could try passing the same arguments to the compiler and see what happens...

In order to pass this library to the compiler to compile against, we need to compile against `libueye_api.so`. This may be accomplished using the compilation command:

```
mex myFunc.cpp -lueye_api
```

The uEye API contains a wide range of functions. This rudimentary manual will contain only the required information to allow the user to capture still frames rather than active video

- it should help the user gain an understanding of some of the more counter-intuitive nicities of the API.

The code given here will *not* work alone - there are missing gaps that require another API to fill - that's why OpenCV is included in this tutorial. This section is purely looking at communicationg with a uEye camera.

Firstly, we need to tell the uEye drivers which camera to connect to. This is more complex (translation: I havn't a clue) with multiple camera environments. If there is only one camera, that camera (unless you tell it to behave otherwise) will always be assigned the handle '1'. Before we can communicate with the camera, we need to explicitly tell the API which camera to talk to, and we do this with the line:

```
HIDS hCam = 1;
```

This uses the type `HIDS`, which is included in `ueye.h`. The name `hCam` is purely arbitrary, but is used in the uEye manual, so I'll use it here for consistency. Once you've declared your camera handle, you then need to initialise the camera, using:

```
int initcamera = is_Init_Camera(&hCam,NULL);
```

This is a good example to use to introduce the syntax of a great many uEye functions. `is_Init_Camera()` can be called without an output argument (in the example, `initcamera`), but things start going badly if that command fails. All (or nearly all) uEye functions will return an integer. This integer will contain a value that reflects the outcome: `0` means it executed successfully, and other numbers up to `206` reflect different failures. A full table of these may be found in the manual, or by trawling through ueye.h. One way of using these diagnostic numbers could involve:

```
if (initcamera != IS_SUCCESS){
    //some function if the initialisation fails
}
```

The library allows you to query the error associated with the number, so `!=IS_SUCCESS` could be replaced by `!=0`, though using the mapped names makes the code far more readable in retrospect. You also need to declare a few other things:

```
SENSORINFO = sensor_info;
CAMINFO = camera_info;
```

Again, this uses non-standard types that are included in the header files (really, they're just structs filled with enums, but you don't have to worry about that).

These variables may be populated using the following couple of lines of code, passing them as references.

```
int camerainfo = is_GetCameraInfo(hCam,&camera_info);
int sensorinfo = is_GetSensorInfo(hCam,&sensor_info);
```

These commands will have populated `sensor_info` and `camera_info`. This step allows us to then pull out the maximum sensor size:

```
int pXPos = (sensor_info.nMaxWidth);
int pXPos = (sensor_info.nMaxHeight);
```

We'll need to pass these later on to the actual capture stage.

We also need to set the colour mode, which will depend upon the camera you're using. In my case, my camera can support up to RGB24, so that's what I'm going to set:

```
int colormode = is_Set_ColorMode(hCam,IS_SET_CM_RGB24);
```

Similarly, `IS_SET_CM_RGB24` corresponds to a number you could look up and use instead, but this is a far more common-sense means of doing it.

Now we're ready to claim some memory off the heap and load it onto the stack for us to capture data into. This has several steps: declaring `NULL` pointers, allocating the memory to the camera, and then telling the camera it can record data to those pointers:

```
char* m_pcImageMemory;
int m_lMemoryId;
int rit = is_AllocImageMem(hCam,pXPos,pYPos,24,&
   m_pcImageMemory,&m_lMemoryId);
int rat = is_SetImageMem(hCam,m_pcImageMemory,m_lMemoryId);
```

Those lines should be self-explanatory - it's more or less standard C++ syntax. When allocating memory, you need to allocate sufficient for the X and Y size of the image, the bit-depth (in this case, 24), and it needs references to allocate to the stack.

Before actually capturing any data, there are several other things it's recommended you set. I've put some code below you may copy, changing the common sense declared values. However, be careful - you *must* declare them in this way - the functions don't like being given floats or integers as arguments, they just want pointers or references, even if the variables aren't changed by the function.

```
//set colour correction factor
double strength_factor = 1.0;
int colorcorrection = is_SetColorCorrection(hCam,
   IS_CCOR_ENABLE,&strength_factor);
//set white-balance correction
double pval = 1;
int whiteb = is_SetAutoParameter(hCam,
   IS_SET_ENABLE_AUTO_WHITEBALANCE,&pval,0);
//set gain parameter
double gval = 1;
int gains = is_SetAutoParameter(hCam,IS_SET_ENABLE_AUTO_GAIN
   ,&gval,0);
```

There are a few final things that need setting before we can capture anything. I'll be honest and admit I haven't an earthly what they do or why they're necessary, but I do know that it doesn't work without them:

```
int dummy;
char *pMem,*pLast;
```

Finally, we can capture some image data!

```
int sho = is_FreezeVideo(hCam,IS_WAIT);
```

This leaves some raw image data stored in `m_pcImageMemory`. If one simply tries to write this to a file, you'll end up with a meaningless string of hex, with odd unicode characters in it. Good luck trying to find anything that can open it (I only found one program out of a multitude that could even tell me that much about it). Clearly we need another piece of software that can deal with just such a raw image stream, but that's for the next section...

To conclude, we need to release the camera so another piece of software (or another call of the same function) can call it. If this was a manual for a stand-alone C++ code that exited once it had executed, this wouldn't be necessary, but because we're looking at using mex, when a mex file opens the camera, camera ownership actually gets passed higher up the process tree and it gets given to matlab. If you forget to close the camera, then you'll need to restart matlab in order to open it again! This includes if the program fails halfway through. This is a good use case for many conditional statements to catch the case of `if(/*a variable*/ != IS_SUCCESS){}`, allowing you to then close the camera and manually return, allowing the camera to be called multiple times successively from a single matlab instance.

```
int en = is_ExitCamera(hCam);
```

And now you should be able to capture image data using the uEye API!

**Important addendum - using this technique for stand-alone programming, all is fine and dandy - once the program has captured an image, saved it, and exited, the memory used will be freed. However, this is not the case if calling it as a mex file from matlab - in this case, memory is only freed upon matlab exiting, unless you free it manually. While you may not miss the odd few megabytes for a frame or two, if you set up something like a slow live-update allowing imaging settings to be changed between every frame (I have) then after a remarkably short period you can find yourself crunching your way through tens of gigabytes of RAM. Adding the following line to the bottom of your code (and before any premature `return` statements) will force your code to release the memory used for video capture before exiting and orphaning it (once your code has exited and left memory allocated to the stack, it's impossible to make matlab release it to the heap again without closing it and re-opening; allowing a different program to access and release the same memory as the original one would be a massive security oversight).

```
int fMem = is_FreeImageMem(hCam,m_pcImageMemory,m_lMemoryId);
```

G.4 OpenCV

In the previous section I said that some kind of go-between program is required to read in the raw image data, and that's where OpenCV comes in. It's a free computer vision toolbox developed mainly be Intel, and it can do quite a few things we need. You'll need to download a tarball and compile it from source, and it has quite a few dependencies that need satisfying as well. Once again, if you're still not on linux, you're completely on your own.

The uEye API does come with the rudimentary ability to create its own image files, but the selection is limited to .jpg, .bmp, and .png. Jpegs and PNGs are compressed and lossy, and often not much use for scientific applications, and it doesn't support windows bitmaps very well under linux, and they're not such a useful file format. Feel free to skip all references to OpenCV, but I'm hoping you'll thank me for making it easy for you!

G.4.1 Installing OpenCV

Dependencies:

GCC 4.4.x+ (which you should have anyway, unless you've gutted your system)

CMake 2.8.7+

Git

GTK+2.x+

Python 2.6+ with NumPy 1.5+

ffmpeg

If your system is Debian-based and uses apt-get to install packages:

```
sudo apt-get install cmake git libgtk2.0-dev pkg-config
   libavcodec-dev libavformat-dev libswscale-dev
```

or if you use aptitude:

```
sudo aptitude install cmake git libgtk2.0-dev pkg-config
   libavcodec-dev libavformat-dev libswscale-dev
```

or if you use something else (portage, yum, zypper, yast, pacman etc) you can probably fend for yourself. Arch users should note that some necessary packages aren't available in the default repositories, and will need to be pulled from the AUR.

I also recommend you install:

```
python-dev python-numpy libtbb2 libtbb-dev libjpeg-dev libpng
   -dev libtiff-dev libjasper-dev libdc1394-22-dev
```

which you can just copy into your package manager of choice.

Now you need the source code, available from sourceforge.net/projects/opencvlibrary . Make sure you get the stable one, the newer ones add no additional useful functionality unless you need advanced object recognition and 3D rendering (we don't).

Fire up a terminal, and `cd` to the directory you expanded the tarball to (or if you don't know how to extract a tarball, go to your downloads folder, and run `tar -xvf FILENAME.tar` and then cd into the new folder), and run:

```
mkdir release && cd release && cmake -D CMAKE_BUILD_TYPE=
   RELEASE -D CMAKE_INSTALL_PREFIX=/usr/local ..
```

This should take a minute or so to execute. Then type `make -j8`, where the 8 would run 8 parallel threads. The fastest compile times are achieved if you choose a number of threads that corresponds to the number of physical cores on your machine. This may take upwards of half an hour even on a relatively fast machine, and will probably use several gigabytes of RAM. Once this has completed, follow it up with `sudo make install`. This will install OpenCV on your machine. If at any point you decide to uninstall OpenCV, navigate back to this directory and run `sudo make uninstall`, and it'll do a complete removal of it (because you compiled it yourself, your package manager probably doesn't know about it, so using a package manager to remove it won't work).

G.4.2 Including OpenCV in a C++ file

It's remarkably non-trivial to include the library in your code. Firstly, you need to include quite a lot more stuff for it to work. You need to add the following to your preamble:

```
#include <stdlib.h>
#include <stdio.h>
#include <opencv2/core/core.hpp>
#include <cv.h>
#include <highgui.h>
```

and you'll also want to change your namespace to `cv` (for the uninitiated, add `using namespace cv;` to the bottom of your preamble). If you've followed this tutorial so far, you won't have used anything that will be affected by this. If you've played the loose cannon, and at compile you get an error along the lines of `TYPE does not exist in this namespace`, then add `std::` in front of the offending declaration.

Right at the top of your mexFunction, you'll want to create a matrix to store your snapshots in, using a type from namespace CV:

```
Mat frame(CAPTURE_HEIGHT,CAPTURE_WIDTH,CV_8UC3);
```

Because it's a computer vision library, it assumes every object in a matrix is an image, and so the third argument it takes tells it you're after a Mat with 8 bits per channel, and 3 channels. note the non-standard syntax it takes - `frame` is the name of the `Mat`, but it's called like a function!

Now we don't need to do anything else until our camera has captured the image data:

```
IplImage* tmpImg = cvCreateImage(cvSize(pXPos,pYPos),
   IPL_DEPTH_8U,3);
tmpImg->imageData = m_pcImageMemory;
frame = cv::cvarrToMat(tmpImg);
```

If you care about what this code does, then feel free to look it up! I think the `cv::` is unnecessary, but there's no harm in leaving it in. Now you have either the choice of saving the image, or displaying it. Unfortunately, there's not any facility I've found yet to pass an image back to matlab directly (please let me know if you find one), so I'd prefer to save it to disk, but I'll cover both here. Firstly, saving the file to disk:

```
imwrite("image.jpg",frame);
```

Here, `image.jpg` is the name of the file to be written to the same directory as the program is running from (which will be your matlab active folder when calling the file from there). You can choose from several popular image formats, though jpeg and tiff are probably the most useful. It is trivial to read image files back into matlab - if you don't know how, then I'd probably go as far as to say that this tutorial probably isn't for you. (hint: `imread(‘filename’);`)

Alternatively:

```
imshow("Image",frame);
waitKey(0);
```

This opens a window called `Image`, and displays `frame` in it. The wait command means that the program pauses until the window is closed, preventing the program from exiting and purging the memory while it's still being displayed (while this wouldn't be an issue in something like java, which implements garbage collection, C++ leaves memory [mis]management to the user).

G.4.3 Compiling using OpenCV

If you take the time to read the official OpenCV documentation, they tell you to use a compiler that they provide template files for already, but that's not feasible (while it is possible to use a compiler outside of matlab to compile mex files, it's a bigger world of pain than trying to use Windows 8) if we're restricting ourselves to matlab. Compiling mex files outside of matlab is covered under 'Advanced Features' at the bottom of this tutorial.

You need to add some more compiler arguments in matlab after `mex FILENAME.cpp -lueye_api`, or more specifically:

```
-I/usr/local/include/opencv -I/usr/local/include/opencv2 -L/
   usr/local/lib/ -g -lopencv_calib3d -lopencv_contrib -
   lopencv_core -lopencv_features2d -lopencv_flann -
   lopencv_highgui -lopencv_imgproc -lopencv_legacy -
   lopencv_ml -lopencv_objdetect -lopencv_photo -lopencv_ts
```

It's a bit of a joke, and a massive faff to type out every time. I recommend you make yourself an m-file in matlab such that all you have to change to compile different mex files is the filename. Alternatively, if your code is to be used on different platforms, it might make sense to write the compile commands into your wider matlab codebase so they compile every time you run the matlab function (it has a minimal time overhead unless you have many very complex mex files), as it means that your files will always work (if the machine has the correct libraries installed).

G.5 Video Capture

Capturing video using the camera is slightly more complex - the simplest way is to save a string of image files, and then stitch them back into a video in Matlab - that's the method that will be covered here.

Proceed as before, by setting the camera handle and initialising the camera. However, since we want to be able to control video capture from the computer, the next thing we need to do is set the camera triggering. Capture of a video frame wants to be arbitrated by the computer, so we want something like:

```
if (is_SetExternalTrigger(hCam,IS_GET_EXTERNALTRIGGER) !=
    IS_SET_TRIGGER_SOFTWARE){
     int nTrig = is_SetExternalTrigger(hCam,
        IS_SET_TRIGGER_SOFTWARE);
}
```

Which queries the current triggering settings, and then changes them if necessary.

If you are using a USB3 camera, your interface should be fast enough to transfer images as fast as the camera can capture them; in this case you'll benefit most from setting the pixel clock as high as it goes. If you have a slower camera, then you may want to play with the pixel clock settings for your specific application. In general, the higher the pixel clock, the higher the framerate you can capture, but the higher the likelihood you'll drop some frames. The pixel clock can easily be set to its maximum as follows:

```
UINT nRange[3];
ZeroMemory(nRange,sizeof(nRange));
int nClock = is_PixelClock(hCam,IS_PIXELCLOCK_CMD_GET_RANGE,(
    void*)nRange,sizeof(nRange));
UINT nMax = nRange[1];
int nClockSet = is_PixelClock(hCam,IS_PIXELCLOCK_CMD_SET,(
    void*)&nMax,sizeof(nMax));
```

This method will get the camera to return a 3-element array containing `[0]`:Minimum clock setting, `[1]`:Maximum clock setting, and `[2]`:Minimum increment for clock setting. Obviously, in this example, the clock is just set to the highest returned value.

The length of video recorded will be determined by the framerate, and the number of frames. Both of these should be passed from matlab in the usual way, via `prhs[]`. It will henceforth be assumed that `frame_count` and `NewFPS` correspond to these two values. Everything else that was initialised for the single frame capture (other than the memory allocation) should be run here.

*

Now we need to set the framerate. The uEye camera can very rarely set the exact framerate that you specify, so it is also important for scientific purposes to know the exact rate at which the camera is running. The following code will do the trick:

```
double ActualFPS;
INT frameset = is_SetFrameRate(hCam,NewFPS,&ActualFPS);
```

So we make a new variable to hold the actual framerate the camera has been set to run at, and then pass is to the frame-rate setting function as a reference to be populated by the camera. It will probably be sensible to pass this back to matlab for further processing of the video data.

Note that if you attempt to set a framerate that's above the maximum supported, you will not receive an error, the camera will just respond by setting it as high as possible given the other contraints (exposure and pixel clock).

*

Now we need to allocate memory. If your computer is short on RAM, then you need to be careful - this method is the simplest, but does mean that you need sufficient RAM to hold the entire video sequence in - with a colour camera with a large field of view, each frame may take upwards of 5MB. I'll break the necessary code into chunks:

```
char *pFrameBuffer[frame_count];
INT pFrame[frame_count];
is_ClearSequence(hCam);
```

First we declare an array of chars, one char per frame to be captured. We also declare an accompanying array of memory IDs, of type int. Then we tell the camera to clear any previous sequence it may have been holding.

```
for (int i = 0;i < frame_count;i++){
```

```
    int nAlloc = is_AllocImageMem(hCam,pXPos,pYPos,24,&
      pFrameBuffer[i],&pFrame[i]);
    int nSeq = is_AddToSequence(hCam,pFrameBuffer[i],pFrame[i
      ]);
    pFrame[i] = i + 1;
}
```

Then we iterate over the number of frames we want in our sequence, each time allocating some memory to successive chars, and also adding new IDs into our identifiers. Then we add them to the sequence of memory addresses to be recognised by the camera. Please note, this isn't the fastest way of doing this - it can take several seconds to allocate sufficient memory for a large video capture, and so this method isn't suited to applications where it is critical that video capture should commence as soon as possible.

It is noteable that this approach can use a large amount of memory, and due to the rate at which data needs to be written for higher-frame-rate capture, it is advisable not to run on swap - this can cause a buffer over-run (where the buffer in the camera that holds images until such a time as the computer is ready to receive them runs out of memory to hold frames in and will start dropping them). It might be helpful to do a back-of-the-envelope calculation of bits per channel x number of channels x number of pixels x number of frames to work out a sensible maximum number of frames that your hardware can safely capture, and thereby code in a hard limit. If you're a lot better at C++ than me, you could even dynamically calculate the maximum number of frames based on the amount of currently available memory.

*

Next, we tell the camera to start capturing in free-run mode:

```
int nCap = is_CaptureVideo(hCam,IS_WAIT);
```

...and initialise the image queue for the images to end up in:

```
int nInit = is_InitImageQueue(hCam,0);
char *pBuffer = NULL;
INT nMemID = 0;
```

Now we go about writing the captured images to memory as the camera sends them to the computer:

```
int k = 0;
while (k < frame_count){
    int nBuffer = is_WaitForNextImage(hCam,1000,&pBuffer,&
       nMemID);
    k++;
}
```

You could do this with a `for` loop instead if you wish - the difference is minimal (I think). It is obvious that the program waits for the camera to send an image, puts it in the correct buffer, and then advances to the next buffer to write to.

*

Thus far, we have a load of raw image data stored in RAM, and this needs writing to disk somehow. We'll save it as a stack of .tif files - they're uncompressed, so very little information will be lost. Once again, we'll make use of OpenCV, only this time we'll need to put the image-writer into a loop as follows:

```
k=0;
while (k < frame_count){
    IplImage* tmpImg = cvCreateImage(cvSize(pXPos,pYPos),
       IPL_DEPTH_8U,3);
    tmpImg->imageData = pFrameBuffer[k];
    frame = cv::cvarrToMat(tmpImg);
//convert k to a string so images may be labelled
    std::ostringstream strs;
    strs << k;
    std::string str = strs.str();//str is the name of the new
        string
//append this to a filestub
    std::string stub = "image";
    std::string extension = ".tif";
    std::string filename = stub + str + extension;
//write actual file
    imwrite(filename,frame);
```

```
    k++;
}
```

As you should be able to see, this iterates through the memory addresses of progressive frames, and for each one writes a .tif file called `image` followed by the frame number. Obviously you can change this for your own purposes with your own filestub. OpenCV supports many different image formats; it autodetects the file extension, so you just need to change that. I put some comments in this snippet, to make sure it was obvious which bits of code do what. In order for this to work, we also need to include `string` and `string.h` in our preamble.

Now we just need to clear all the memory we used. This doesn't appear to be as simple as it would be nice if it was:

```

is_ClearSequence(hCam);
is_UnlockSeqBuf(hCam,nMemID,pBuffer);
int nSeq2 = is_ClearSequence(hCam);
k=0;
while (k < frame_count){
    int fMem = is_FreeImageMem(hCam,pFrameBuffer[k],pFrame[k
        ]);
    k++;
}
int fMem2 = is_FreeImageMem(hCam,(char*)&pFrameBuffer,*pFrame
    );
```

Without going into detail about what all this gubbins does, it doesn't seem to properly clear the memory - it remains under the control of matlab and isn't released back again to the wider system. However, it is available for future mexFunction calls - if you run the same capture proceedure twice, the second time it won't appear to use any additional memory. The reasons for this aren't altogether clear, though. Could be some incompatibilities between the uEye API and matlab's implementation of memory management with mex.

*

Now you just need to convert your stack of .tif images into a video file. We'll do this in Matlab. We'll assume your mexfile has been compiled and is now available as a matlab function. Something like the following should do the trick:

```
%call whatever your mexfunction is...
frame_rate = mexFunction(args[]);
%initialise a new video
vid = VideoWriter('filename.avi');
vid.FrameRate = frame_rate;
vid.Quality = 100;
%open it
open(vid);
for i = 0 : frames-1
    %read your image files
    img = imread(strcat('image',num2str(i),'.tif'));
    %add them to your video file
    writeVideo(vid,img);
    %and delete the original image file
    delete(strcat('image',num2str(i),'.tif'));
end
```

`frames` is referring to the number of frames captured. This code will also delete all your intermediate image files. Your remaining file will be an uncompressed .avi video file in your matlab active directory.

There you have it!

G.6 Advanced Features

G.6.1 Higher Framerates

It is possible to achieve higher framerates with many uEye cameras if a smaller area is imaged. Certainly for our camera (UI-324 series) the following is true.

In general, the rate at which the camera can capture data is restricted by several things: the rate of data connection to the computer; the rate at chich the camera can read out lines of image; the number of lines in the image. It turns out that for the USB3.0 connection we're using, capturing 24-bit colour images, the bottleneck is the rate at which lines of image may be read from the image sensor. This has an important effect: the highest framerates achievable by the camera can be achieved while maintaining the full width of the sensor (1280 pix), but only reading out 4 lines. In this way, we have managed to far surpass the 229fps limit that the camera is specified to. However, a word of caution: running the camera at very high framerates does cause the camera to generate a fair amount of heat, and pushing it past the specification framerate for an expended period of time is not something I could at all recommend unless you've installed some custom cooling mechanics (in which case, you'd probably have done better to have purchased a far more expensive camera in the first place).

G.6.2 Area of interest (AOI)

In order to set a reduced area of interest (AOI), you need 4 parameters. Firstly, you need an x-y pair describing the corner of your area of interest. The uEye reads this from the top-right corner of the image. Then you need a second x-y pair giving the x-dimension (width) and y-dimension (height) you want your AOI to have. These are stored in a special C++ struct defined by `uEye.h`, called `IS_RECT`. You would initialise and populate your `IS_RECT` as follows:

```
IS_RECT myNewAOI;
myNewAOI.s32X = YOUR_X_CO-ORDINATE;
myNewAOI.s32Y = YOUR_Y_CO-ORDINATE;
myNewAOI.s32Width = YOUR_X_DIMENSION;
myNewAOI.s32Height = YOUR_Y_DIMENSION;
```

All 4 parameters are of type int. It is important to note that different cameras have different requirements on the parameters: ours has a minimum of 4 and increment of 2 for the height, and a minimum of 16 and an increment of 4 for the width. Co-ordinates of the corner have increments of 2 over the entire field of view. It is simple in matlab (or anything else) to validate these conditions. Below is some sample matlab code for validating (and correcting) the width:

```
%make sure it's a multiple of 4
if rem(width,4) ~= 0
    while rem(width,4) ~= 0
        width = width + 1;
    end
end
%and make sure it's larger than the minimum
if width < 16
    width = 16;
```

```
end
```

This is then passed to the camera using the command:

```
is_AOI(hCam,IS_AOI_IMAGE_SET_AOI,(void*)&myNewAOI,sizeof(
    myNewAOI));
```

As usual, this will return an int corresponding to a return type specified in the full manual. It is important to remember that with a reduced AOI, memory pointers must be adjusted to point to a smaller area of memory, and that the conversion from DIB to .tif also needs the dimensions of the image re-specifying.

G.6.3 Multiple AOIs

This feature is useless to us, so I haven't tried implementing it, but the documentation for this is actually rather good, so given what you'll have learned from this tutorial you should be able to work it out for yourself! In essence, all AOIs must share at least one co-ordinate and one dimension with at least one other AOI, so such a feature is not useful for things like adaptive feature-tracking (only recording small parts of the FOV corresponding to multiple independently-moving objects eg following multiple faces).

G.6.4 Ring Buffering

I said earlier that there was a limit on the number of frames that could be captured in a single file. This isn't strictly true, but breaking that limit does require the use of more complex C++. In the 2011 standard for C++, the idea of native multi-threading was introduced. There is plenty of good documentation for this feature available online, but basic ring-buffering requires 2 threads, and proper robust ring-buffering requires 3. The process goes as follows:

1. Allocate a short sequence of buffers as described in the section on video capture.

2. Initialise capture into this sequence

3. Start a second thread that looks for buffers which have been filled with an image, writes that image to a file, and then re-initialised the buffer so it can be written into again.

4. When the original thread (the one writing images into the buffers) gets to the last buffer in the sequence, rather than terminating, it needs to loop back to the first buffer, which has hopefully been emptied by now.

This is quite simple to achieve, but the obvious issue with this is the 'hopefully emptied by now' part - if the images are being captured much faster than they can be written to disk, then some errors are going to start occurring whereby frames are overwritten in memory before they can be written to disk. This is why a third thread is really needed. This third thread needs to monitor the relative rates of frame processing of the original 2 threads, and, if necessary, dynamically insert more buffers into the sequence to allow for any file-lag. This evidently requires the passing of variables between concurrent threads, which is *not* something C++ is particularly good at (that's why concurrent languages like Erlang exist). If you don't have a computer science degree, probably just go out and buy more RAM.

Alternatively, you could buy an SSD, turn off the OS default queue optimisation (under linux, usually CFQ), and set it to noop (no optimisation), and try and ensure that no system processes that are likely to cause disk IO saturation will run. For a USB3 camera, this is probably a safe bet - a modern SSD can write much faster than USB3 can transfer data, so a buffer over-run is unlikely.

G.6.5 Compiling multi-threaded mex files

There are only certain kinds of argument that mex will allow you to pass to the compiler, and it turns out that if you want to multi-thread, the necessary arguments cannot be passed (at least in R2013a), and either matlab will throw an error that it doesn't know what to do with the argument, or the compiler will throw an error saying it doesn't have valid parameters. Luckily there is a workaround.

Firstly, work out which libraries and arguments are disagreeing with matlab. The errors that were being thrown should give you a hint about this. By whatever means necessary, eliminate these from your code temporarily (commenting out both the inclusion and use of the offending components). Then attempt to compile the code in matlab, using `mex -v` for verbose mode. This should give you a lot of confusing text output to the matlab command prompt. Ignore most of it.

The last few lines of bumf will include two lines starting with `g++.......` These are the raw commands that matlab is actually sending to the compiler. Copy these out and drop them in an empty text file. Save the file with an arbirtary name, and the extension '.sh'. Modify the commands to include the compiler arguments that were offending matlab before. Then go back into matlab, and replace your `mex .......` with:

```
! sh FILENAME.sh;
```

This will run your shell script to compile your mexfile rather than the dumbed-down matlab version, and will allow you to compile far more complex things, including GUIs using gtk or Qt (matlab doesn't like them). Because you copied the arguments from matlab, it will compile it into a .mexa64 library that exports mexFunction, and matlab can immediately use as if matlab had compiled it itself. The beauty of this approach is it means you can compile mexFunctions on computers that don't have matlab installed - all you need are the right header files and shared libraries, which are simple enough to copy across.

This technique can be applied to many other situations in which it is easier to write a shell script to do something than script matlab to do the same. This can include things involving network directories, anything involving copying or deleting large numbers of files (shell scripts support a far better variety of wildcards), useful functions like `scp`, `dd`, etc. Any line of matlab code prefixed by an exclamation mark '`!`' will be sent to the default root terminal (matlab in linux always runs as root). Because of this, it is always best to run a script rather than a string of terminal commands - most things are terminal-independent, but there are some things that don't carry well between different shells (xterm, bash, ksh etc). If you write a file and then call it using sh, you can guarantee that it will behave the same on any linux system with all the requisite commands installed.

G.7 Final notes

I hope this saves you a lot of trial and error - had I had such a cribsheet I'd have saved a good several months of incredibly frustrating trial and error. If you appreciate this, then feel free to send donations!

List of abbreviations

Handy list of abbreviations!

AF_4 Asymmetric flow field flow fractionation

CPP C++ (C Plus Plus)

Cryo- Cryogenic

d Diameter

D_f Fractal Dimension

D_h Hydrodynamic Diameter

DDM Differential Dynamic Microscopy

DI De-ionised

water

DLS Dynamic Light Scattering

EM Electron Microscopy

ENM Engineered NanoMaterial

item [ENP] Engineered NanoParticle

FA Fulvic Acid

GUI Graphical User Interface

HA Humic Acid

ICP Inductively-Coupled Plasma

ICP-MS Inductively-Coupled Plasma Mass Spectrometry

IS Ionic Strength

ISO International Standards Organisation

LOD Limit of Detection

MEx Matlab Executables

MS Mass Spectrometry

NOM Natural Organic Matter

NP NanoParticle

NTA Nanoparticle tracking Analysis

PCS Photon Correlation Spectroscopy

r_h Hydrodynamic Radius

SEM Scanning Electron Microscopy

spICP-MS Single-Particle ICP-MS

TEM Transmission Electron Microscopy

1

UV-Vis Ultra-Violet–Visual spectroscopy

UX User eXperience

List of symbols

A van der Waals constant

a First semi-axis of a spheroidal nanoparticle

a_i Relative abundance of measured particles

$A\left(q\right)$ Fitting factor used in differential dynamic microscopy

α Polarisability

α_e Attachment efficiency

α_j j^{th} element of the polarisability tensor

$B\left(q\right)$ Fitting factor used in differential dynamic microscopy

b Second semi-axis of a spheroidal nanoparticle

β Ratio of the valency of the auxilliary ion to the dominating ion in DLVO theory

C_d Fitting constant used in DLVO theory

c Speed of light in a vacuum

c_n Third semi-axis of a spheroidal nanoparticle

D Diffusion coefficient

D_e Dielectric constant

D_f Fractal dimension

D_h Hydrodynamic diameter

D_m Mass diffusion constant

D_p Circular diameter

$D\left(x, y; \Delta t\right)$ Difference image for given time difference Δt.

d Semi-minor axis of nano-rod

δ Infinitesimal change in...

$\underline{E}$ Electric field

$\underline{E}_0$ Incident electric field

e Electronic charge

$\mathbf{e}$ Base of the natural logarithm

e_p Eccentricity of particle

η Viscosity of a fluid

F_D Fourier transform of D

$f_d\left(\beta\right)$ Function of the ‘asymmetry of the electrolyte’ in DLVO theory

γ Electrolyte concentration in DLVO theory

h Separation of infinite parallel plates used in Debye-Hückel theory of dilute colloids

H Smallest separation of curved particle surfaces in Debye-Hückel theory of dilute colloids

h_n Spherical Hankel functions

I Intensity of scattered light

I_0 Intensity of incident light

I_j Scattered intensity moment corresponding to L_j

j_n Spherical bessel functions of the first kind

k Constant used when calculating hydrodynamic radii of nanoarticle aggregates

k_0 Wavenumber of illuminating radiation

k_B Boltzmann constant

$L_{(j)}$ Function depending upon the three-dimensional aspect ratio of a particle

l Semi-major axis of nano-rod

λ Wavelength

λ_f Mean free path

m Relative refractive index

m_p Mass (of a nanoparticle or nanoparticle aggregate)

m_r Reciprocal concentration of the dominating ion in the solution in DLVO theory

μ Nanoparticle permeability

μ_1 Permeability of suspending medium

n_a Refractive index

$n_{\mathbf{col}}$ Mean number of particles in a nanoparticle aggregate

N_d Repulsive force of the curved particle surfaces in Debye-Hückel theory of dilute colloids

$n_{\mathbf{dom}}$ Number of dominating ions per molecule in DLVO theory

$[\mathbf{NP}\ ]Nanoparticlenumberconcentrationinsuspension$

n_p Number concentration of nanoparticles in suspension

$\underline{P}$ Polarisation per unit volume

Φ Ratio between circular diameter and sphereoid thickness

ϕ Scattering angle

ψ Surface potential of nanoparticles in suspension

Q Scattering efficiency

q Scattering vector

r Radius

R Radius of observation

$R(h)$ Repulsion per unit area of parallel plates seperated by distance h.

r_0 Hydrodynamic radius of nanoparticles prior to aggregation

r_h Sphere-equivalent hydrodynamic diameter

$\bar{r}_h$ Mean sphere-equivalent hydrodynamic diameter

r_p Physical radius

ρ Density

s Integration variable used when calculating the scattering efficiency of a spheroidal nanoparticle

σ Collision cross-section for nanoparticles in suspension

$\sigma^2 (\Delta t)$ Sum of squares of all pixels in differential dynamic microscopy

T Absolute temperature

t Time

$t_{\mathbf{tot}}$ Elapsed aggregation time

τ ‘Lag’ used in cross-correlation calculations

τ_i Characteristic time

θ Angle

U Magnitude of primitive vector in frequency space in differential dynamic microscopy

u Total magnitude of vector in frequency space in differential dynamic microscopy

V Volume

$\bar{v}$ Time-averaged mean particle velocity

x_i Reciprocal of the thickness of the ionic ‘atmosphere’ of a nanoparticle in DLVO theory

x_m Substitution factor in Mie scattering theory

Ξ A useful substitution variable for the optical determination of nanoparticle shape

z' Valency of ion with greatest charge in DLVO theory

z_1 Valency of the dominating ion in DLVO theory

z_2 Valency of the auxilliary ion in DLVO theory

Bibliography

[1] Janez POTOČNIK. L 275/38. *Official Journal of the European Union*, (L 275):38–40, 2011.

[2] G.A. Waychunas, B.Gilbert, J.F.Banfield, H.Zhang, Y.S.Jun, and C.S.Kim. Natural nanoparticles structure, properties and reactivity from X-ray studies. *Powder Diffraction*, 24(02):89–93, 2009.

[3] Mikhail G. Shapiro, Jerzy O. Szablowski, Robert Langer, and Alan Jasanoff. Protein nanoparticles engineered to sense kinase activity in MRI. *Journal of the American Chemical Society*, 131(7):2484–2486, 2009.

[4] Sarah Stanley. Biological nanoparticles and their influence on organisms. *Current Opinion in Biotechnology*, 28:69–74, 2014.

[5] Yongzhong Wang, Leming Sun, Sijia Yi, Yujian Huang, Scott C. Lenaghan, and Mingjun Zhang. Naturally occurring nanoparticles from arthrobotrys oligospora as a potential immunostimulatory and antitumor agent. *Advanced Functional Materials*, 23(17):2175–2184, 2013.

[6] Li Zhu, Jing Zhang, Shifang Ren, and Yinlong Guo. Facile and fast enrichment of phosphopeptides prior to matrix-assisted laser desorption/ionization time-of-flight mass spectrometric analysis using natural nanoparticle-bentonite. *International Journal of Mass Spectrometry*, 343-344:23–27, 2013.

[7] Thomas B. Brill. Why objects appear as they do. *Journal of Chemical Education*, 57(4):259, 1980.

[8] D J Barber and I C Freestone. an Investigation of the Origin of the Color of the Lycurgus Cup By Analytical Transmission Electron-Microscopy. *Archaeometry*, 1(32):33–45, 1990.

[9] Bengt Fadeel and Alfonso E. Garcia-Bennett. Better safe than sorry: Understanding the toxicological properties of inorganic nanoparticles manufactured for biomedical applications. *Advanced Drug Delivery Reviews*, 62(3):362–374, 2010.

[10] Tina Masciangioli and Wei-Xian Zhang. Environmental Technologies at the Nanoscale. *Environmental Science & Technology*, 37(5):102A–108A, 2003.

[11] Vicki L Colvin. The potential environmental impact of engineered nanomaterials. *Nature Biotechnology*, 21(10):1166–1170, 2003.

[12] David B. Warheit, Thomas R. Webb, Vicki L. Colvin, Kenneth L. Reed, and Christie M. Sayes. Pulmonary bioassay studies with nanoscale and fine-quartz particles in rats: Toxicity is not dependent upon particle size but on surface characteristics. *Toxicological Sciences*, 95(1):270–280, 2007.

[13] M Methner, L Hodson, A Dames, and C Geraci. Nanoparticle Emission Assessment Technique (NEAT) for the identification and measurement of potential inhalation exposure to engineered nanomaterials–Part B: Results from 12 field studies. *Journal of occupational and environmental hygiene*, 7(3):163–76, mar 2010.

[14] Richard D Handy, Richard Owen, and Eugenia Valsami-Jones. The ecotoxicology of nanoparticles and nanomaterials: current status, knowledge gaps, challenges, and future needs. *Ecotoxicology (London, England)*, 17(5):315–25, jul 2008.

[15] Denise M. Mitrano, Sylvie Motellier, Simon Clavaguera, and Bernd Nowack. Review of nanomaterial aging and transformations through the life cycle of nano-enhanced products. *Environment International*, 77:132–147, 2015.

[16] Karen Van Hoecke, Joris T K Quik, Joanna Mankiewicz-Boczek, Karel A C De Schamphelaere, Andreas Elsaesser, Paul Van der Meeren, Clifford Barnes, George McKerr, C Vyvyan Howard, Dik Van de Meent, Konrad Rydzyński, Kenneth a Dawson, Anna Salvati, Anna Lesniak, Iseult Lynch, Geert Silversmit, Björn De Samber, Laszlo Vincze, and Colin R Janssen. Fate and effects of CeO2 nanoparticles in aquatic ecotoxicity tests. *Environmental science & technology*, 43(12):4537–46, jun 2009.

[17] Sophie Laurent, Silvio Dutz, Urs O Häfeli, and Morteza Mahmoudi. Magnetic fluid hyperthermia: focus on superparamagnetic iron oxide nanoparticles. *Advances in colloid and interface science*, 166(1-2):8–23, aug 2011.

[18] Alan G Howard. On the challenge of quantifying man-made nanoparticles in the aquatic environment. *Journal of environmental monitoring : JEM*, 12(1):135–42, jan 2010.

[19] Troy M. Benn and Paul Westerhoff. Nanoparticle silver released into water from commercially available sock fabrics. *Environmental Science and Technology*, 42(11):4133–4139, 2008.

[20] Nadine S. Taylor, Ruth Merrifield, Tim D. Williams, J. Kevin Chipman, Jamie R. Lead, and Mark R. Viant. Molecular toxicity of cerium oxide nanoparticles to the freshwater alga chlamydomonas reinhardtii is associated with supra-environmental exposure concentrations. *Nanotoxicology*, 5390(2006):1–10, 2015.

[21] Tal Ben-Moshe, Ishai Dror, and Brian Berkowitz. Oxidation of organic pollutants in aqueous solutions by nanosized copper oxide catalysts. *Applied Catalysis B: Environmental*, 85(3-4):207–211, jan 2009.

[22] Maria C. Powell, Martin P A Griffin, and Stephanie Tai. Bottom-up risk regulation? How nanotechnology risk knowledge gaps challenge federal and state environmental agencies. *Environmental Management*, 42(3):426–443, 2008.

[23] Grazyna Bystrzejewska-Piotrowska, Jerzy Golimowski, and Pawel L. Urban. Nanoparticles: Their potential toxicity, waste and environmental management. *Waste Management*, 29(9):2587–2595, 2009.

[24] Kevin L. Dreher. Health and environmental impact of nanotechnology: Toxicological assessment of manufactured nanoparticles. *Toxicological Sciences*, 77(1):3–5, 2004.

[25] Jie Zheng, Yong Ding, Bozhi Tian, Lin Wang Zhong, and Xiaowei Zhuang. Luminescent and raman active silver nanoparticles with polycrystalline structure. *Journal of the American Chemical Society*, 130(32):10472–10473, 2008.

[26] Rodney S. Ruoff, Donald C. Lorents, Bryan Chan, Ripudaman Malhotra, and Shekhar Subramoney. Single Crystal Metals Encapsulated in Carbon Nanoparticles. *Science*, 259(5093):346–348, 1993.

[27] Benjamin Wiley, Thurston Herricks, Yugang Sun, and Younan Xia. Polyol synthesis of silver nanoparticles: Use of chloride and oxygen to promote the formation of single-crystal, truncated cubes and tetrahedrons. *Nano Letters*, 4(9):1733–1739, 2004.

[28] Riccardo Ferrando. Symmetry breaking and morphological instabilities in core-shell metallic nanoparticles. *Journal of physics. Condensed matter : an Institute of Physics journal*, 27(1):013003, 2015.

[29] Karen Tiede, Martin Hassellöv, Eike Breitbarth, Qasim Chaudhry, and Alistair B A Boxall. Considerations for environmental fate and ecotoxicity testing to support environmental risk assessments for engineered nanoparticles. *Journal of Chromatography A*, 1216(3):503–509, 2009.

[30] Catherine C Berry. Progress in functionalization of magnetic nanoparticles for applications in biomedicine. *Journal of Physics D: Applied Physics*, 42(22):224003, nov 2009.

[31] Valeria Garbin, John C Crocker, and Kathleen J Stebe. Nanoparticles at fluid interfaces: exploiting capping ligands to control adsorption, stability and dynamics. *Journal of colloid and interface science*, 387(1):1–11, dec 2012.

[32] Jingfang Zhou, John Ralston, Rossen Sedev, and David A Beattie. Functionalized gold nanoparticles: synthesis, structure and colloid stability. *Journal of colloid and interface science*, 331(2):251–62, mar 2009.

[33] W A Shoults-Wilson, B C Reinsch, O V Tsyusko, P M Bertsch, G V Lowry, and J M Unrine. Effect of silver nanoparticle surface coating on bioaccumulation and reproductive toxicity in earthworms (Eisenia fetida). *Nanotoxicology*, 5(3):432–444, 2011.

[34] Sujung Park, James Woodhall, Guibin Ma, Jonathan Gc Veinot, and Alistair Ba Boxall. Does particle size and surface functionality affect uptake and depuration of gold nanoparticles by aquatic invertebrates? *Environmental Toxicology and Chemistry*, 9999(9999):n/a–n/a, 2014.

[35] Yongdong Jin, Yan Shen, and Shaojun Dong. Electrochemical design of ultrathin platinum-coated gold nanoparticle monolayer films as a novel nanostructured electrocatalyst for oxygen reduction. *Journal of Physical Chemistry B*, 108(24):8142–8147, 2004.

[36] Michael J Mclaughlin. Fate and Risks of Nanomaterials in Aquatic and Terrestrial Environments. *Accounts of chemical research*, 46(3), 2013.

[37] Flemming R Cassee, Erna C van Balen, Charanjeet Singh, David Green, Hans Muijser, Jason Weinstein, and Kevin Dreher. Exposure, health and ecological effects review of engineered nanoscale cerium and cerium oxide associated with its use as a fuel additive. *Critical reviews in toxicology*, 41(3):213–229, 2011.

[38] Andrew C. Johnson and Barry Park. Predicting contamination by the fuel additive cerium oxide engineered nanoparticles within the United Kingdom and the associated risks. *Environmental Toxicology and Chemistry*, 31(11):2582–2587, 2012.

[39] Barry Park, Kenneth Donaldson, Rodger Duffin, Lang Tran, Frank Kelly, Ian Mudway, Jean-Paul Morin, Robert Guest, Peter Jenkinson, Zissis Samaras, Myrsini Giannouli,

Haris Kouridis, and Patricia Martin. Hazard and risk assessment of a nanoparticulate cerium oxide-based diesel fuel additive - a case study. *Inhalation toxicology*, 20(January):547–566, 2008.

[40] Kungang Li, Wen Zhang, Ying Huang, and Yongsheng Chen. Aggregation kinetics of CeO2 nanoparticles in KCl and CaCl2 solutions: measurements and modeling. *Journal of Nanoparticle Research*, 13(12):6483–6491, aug 2011.

[41] Nicole C Mueller and Bernd Nowack. Exposure modeling of engineered nanoparticles in the environment. *Environmental Science & Technology*, 41(0):4447–4453, 2008.

[42] Fadri Gottschalk, Tobias Sonderer, Roland W. Scholz, and Bernd Nowack. Possibilities and limitations of modeling environmental exposure to engineered nanomaterials by probabilistic: Material flow analysis. *Environmental Toxicology and Chemistry*, 29(5):1036–1048, 2010.

[43] M Hassellöv. Occurrence, identification, fate and behavior of engineered nanoparticles and nanoscale pollutants in marine systems. In *ibim.cnr.it*, volume 71, page 3301, 2012.

[44] C Carlson, S M Hussain, a M Schrand, L K Braydich-Stolle, K L Hess, R L Jones, and J J Schlager. Unique cellular interaction of silver nanoparticles: size-dependent generation of reactive oxygen species. *The journal of physical chemistry. B*, 112(43):13608–19, oct 2008.

[45] Hubert Schmidbaur. The fascinating implications of new results in gold chemistry. *Gold Bulletin*, 23(1):11–21, mar 1990.

[46] SL Johnson. Factors influencing stream temperatures in small streams: substrate effects and a shading experiment. *Canadian Journal of Fisheries and Aquatic Science*, 923(July):913–923, 2004.

[47] Andrea Ghermandi, Veronique Vandenberghe, Lorenzo Benedetti, Willy Bauwens, and Peter a. Vanrolleghem. Model-based assessment of shading effect by riparian vegetation on river water quality. *Ecological Engineering*, 35(1):92–104, jan 2009.

[48] Walter Vogel and John Bradley. Transition from five-fold symmetric to twinned FCC gold particles by thermally induced growth. *The Journal of Physical ...*, pages 10853–10859, 1998.

[49] N P Young, M A van Huis, H W Zandbergen, H Xu, and A L Kirkland. Transformations of gold nanoparticles investigated using variable temperature high-resolution transmission electron microscopy. *Ultramicroscopy*, 110(5):506–16, apr 2010.

[50] Michael J Walsh, Kenta Yoshida, Akihide Kuwabara, Mungo L Pay, Pratibha L Gai, and Edward D Boyes. On the structural origin of the catalytic properties of inherently strained ultrasmall decahedral gold nanoparticles. *Nano letters*, 12(4):2027–31, apr 2012.

[51] Amir Zabet-Khosousi, Paul-Emile Trudeau, Yoshinori Suganuma, Al-Amin Dhirani, and Bryan Statt. Metal to Insulator Transition in Films of Molecularly Linked Gold Nanoparticles. *Physical Review Letters*, 96(15):156403, apr 2006.

[52] J Gordon Arbuckle, F William Brownell, David R Case, Wayne T Halbleib, Lawrence J Jensen, Stanley W Landfair, Robert T Lee, Marshall Lee Miller, Karen J Nardi, Austin P Olney, David G Sarvadi, James W Spensley, Daniel M Steinway, and Thomas F P Sullivan. *Environmental Law Handbook, Twelfth Edition.* Government Institutes Inc., Rockville, MD, 12 edition, 1993.

[53] Daniel Bodansky, Jutta Brunée, and Ellen Hey. *The Oxford handbook of environmental law.* Oxford University Press, Oxford, 2007.

[54] Julia Farkas, Hannes Peter, Paul Christian, Julián Alberto Gallego Urrea, Martin Hassellöv, Jani Tuoriniemi, Stefan Gustafsson, Eva Olsson, Ketil Hylland, and Kevin Victor Thomas. Characterization of the effluent from a nanosilver producing washing machine. *Environment international*, 37(6):1057–62, aug 2011.

[55] Arturo A. Keller, William Vosti, Hongtao Wang, and Anastasiya Lazareva. Release of engineered nanomaterials from personal care products throughout their life cycle. *Journal of Nanoparticle Research*, 16(7), 2014.

[56] Marina E. Quadros and Linsey C. Marr. Silver nanoparticles and total aerosols emitted by nanotechnology-related consumer spray products. *Environmental Science and Technology*, 45(24):10713–10719, 2011.

[57] Eric P. Vejerano, Elena C. Leon, Amara L. Holder, and Linsey C. Marr. Characterization of particle emissions and fate of nanomaterials during incineration. *Environmental Science: Nano*, 1(2):133, 2014.

[58] Leonardo Trasande, Philip J. Landrigan, and Clyde Schechter. Public health and economic consequences of methyl mercury toxicity to the developing brain. *Environmental Health Perspectives*, 113(5):590–596, 2005.

[59] Farhana Zahir, Shamim J. Rizwi, Soghra K. Haq, and Rizwan H. Khan. Low dose mercury toxicity and human health. *Environmental Toxicology and Pharmacology*, 20(2):351–360, 2005.

[60] Cynthia C. Gilmour, Georgia S. Riedel, Gerhardt Riedel, Seokjoon Kwon, Richard Landis, Steven S. Brown, Charles A. Menzie, and Upal Ghosh. Activated carbon mitigates mercury and methylmercury bioavailability in contaminated sediments. *Environmental Science and Technology*, 47(22):13001–13010, 2013.

[61] Martin Tsz Ki Tsui and Jacques C. Finlay. Influence of dissolved organic carbon on methylmercury bioavailability across minnesota stream ecosystems. *Environmental Science and Technology*, 45(14):5981–5987, 2011.

[62] Luis Carrasco, Carlos Barata, Emili García-Berthou, Aurelio Tobias, Josep M. Bayona, and Sergi Díez. Patterns of mercury and methylmercury bioaccumulation in fish species downstream of a long-term mercury-contaminated site in the lower Ebro River (NE Spain). *Chemosphere*, 84(11):1642–1649, 2011.

[63] Christoffer Tamm, Joshua Duckworth, Ola Hermanson, and Sandra Ceccatelli. High susceptibility of neural stem cells to methylmercury toxicity: Effects on cell survival and neuronal differentiation. *Journal of Neurochemistry*, 97(1):69–78, 2006.

[64] L K Ball, R Ball, R D Pratt, JC. May, JTC. Sih, RH. Bernier, JA. Frank, TF. Nolan, PA. Simon, RT. Chen, JA. Elliot, B. Schwartz, KR. Mahaffey, RT. Chen, SC. Rastogi, JR. Mullen, AMJN. Blair, B. Clark, HM. Powell, WA. Jamieson, MM. Mason, CC. Cate, J. Baker, NH. Cox, A. Forsyth, M. Goncalo, A. Figueiredo, S. Goncalo, JD. Grabenstein, H. Moller, D. Seal, L. Ficker, P. Wright, V. Andrews, T. Schafer, F. Enders, B. Przybilla, DS. Matheson, TW. Clarkson, EW. Gelfand, HJ. Lowell, S. Burgess, S. Shenoy, M. Peters, TK. Howard, JMH. Axton, J. Rohyans, PD. Walson, GA. Wood, WA. MacDonald, DG. Fagan, JS. Pritchard, TW. Clarkson, MR. Greenwood, R. Pfab, H. Muckter, G. Roider, T. Zilker, L. Magos, AW. Brown, S. Sparrow, E. Bailey, RT. Snowden, WR. Skipp, J. Zhang, TW. Clarkson, M. Harada, F. Bakir, SF. Damlugi, L. Amin-Zaki, PW. Davidson, GJ. Myers, C. Cox, P. Grandjean, P. Weihe, RF. White, G. Stajich, CJ. Clements, LK. Ball, and R. Ball. An assessment of thimerosal use in childhood vaccines. *Pediatrics*, 107(5):1147–54, 2001.

[65] Gerald T. Ankley, George P Daston, Sigmund J Degitz, Nancy D Denslow, Robert A Hoke, Sean W Kennedy, Ann W Miracle, Edward J Perkins, Jason Snape, Donald E Tillitt, Charles R Tyler, and Donald Versteeg. Toxicogenomics in regulatory ecotoxicology. *Environmental science & technology*, 40(13):4055–4065, 2006.

[66] Richard Judson, Ann Richard, David J Dix, Keith Houck, Matthew Martin, Robert Kavlock, Vicki Dellarco, Tala Henry, Todd Holderman, Philip Sayre, Shirlee Tan, Thomas Carpenter, and Edwin Smith. The Toxicity Data Landscape for Environmental Chemicals. *Environmental Health Perspectives*, 117(5):685, 2009.

[67] Robert I MacCuspie, Kim Rogers, Manomita Patra, Zhiyong Suo, Andrew J Allen, Matthew N Martin, and Vincent a Hackley. Challenges for physical characterization of silver nanoparticles under pristine and environmentally relevant conditions. *Journal of environmental monitoring : JEM*, 13(5):1212–26, may 2011.

[68] Marie-Noele Croteau, Agnieszka D Dybowska, Samuel N Luoma, Superb K Misra, and Eugenia Valsami-Jones. Isotopically modified silver nanoparticles to assess nanosilver bioavailability and toxicity at environmentally relevant exposures. *Environmental Chemistry*, 11:247–256, 2014.

[69] Nina Dragicevic and Howard I Maibach. *Percutaneous Penetration Enhancers Chemical Methods in Penetration Enhancement Modifi cation of the Stratum Corneum*. 2016.

[70] Su Hui Tan and Xian Jun Loh. *Nanoparticle safety in cosmetics*, volume 2016-Janua. The Royal Society of Chemistry, 2016.

[71] Pratim Biswas and Chang-Yu Wu. Nanoparticles and the Environment. *Journal of the Air & Waste Management Association*, 55(6):708–746, jun 2005.

[72] J. Ferin, G. Oberdörster, and D. P. Penney. Pulmonary retention of ultrafine and fine particles in rats. *American journal of respiratory cell and molecular biology*, 6(5):535–542, 1992.

[73] Villem Aruoja, Henri-Charles Dubourguier, Kaja Kasemets, and Anne Kahru. Toxicity of nanoparticles of CuO, ZnO and TiO2 to microalgae Pseudokirchneriella subcapitata. *The Science of the total environment*, 407(4):1461–8, feb 2009.

[74] Joseph N. Mwangi, Ning Wang, Andrew Ritts, James L. Kunz, Christopher G. Ingersoll, Hao Li, and Baolin Deng. Toxicity of silicon carbide nanowires to sediment-dwelling invertebrates in water or sediment exposures. *Environmental Toxicology and Chemistry*, 30(4):981–987, 2011.

[75] Catherine M. Goodman, Catherine D. McCusker, Tuna Yilmaz, and Vincent M. Rotello. Toxicity of gold nanoparticles functionalized with cationic and anionic side chains. *Bioconjugate Chemistry*, 15(4):897–900, 2004.

[76] S. M. Hussain, K. L. Hess, J. M. Gearhart, K. T. Geiss, and J. J. Schlager. In vitro toxicity of nanoparticles in BRL 3A rat liver cells. *Toxicology in Vitro*, 19(7):975–983, 2005.

[77] Joseph N. Mwangi. *Aquatic toxicity of one-dimensional carbon nanomaterials.* PhD thesis, 2010.

[78] Yong Soon Kim, Jin Sik Kim, Hyun Sun Cho, Dae Sik Rha, Jae Min Kim, Jung Duck Park, Byung Sun Choi, Ruth Lim, Hee Kyung Chang, Yong Hyun Chung, Il Hoon Kwon, Jayoung Jeong, Beom Seok Han, and Il Je Yu. Twenty-eight-day oral toxicity, genotoxicity, and gender-related tissue distribution of silver nanoparticles in Sprague-Dawley rats. *Inhalation toxicology*, 20(6):575–583, 2008.

[79] Renata de Lima, Amedea B. Seabra, and Nelson Durán. Silver nanoparticles: A brief review of cytotoxicity and genotoxicity of chemically and biogenically synthesized nanoparticles. *Journal of Applied Toxicology*, 32(11):867–879, 2012.

[80] Jiangxin Wang, Xiaoshan Zhu, Xuezhi Zhang, Zheng Zhao, Huan Liu, Rajani George, Jeanne Wilson-Rawls, Yung Chang, and Yongsheng Chen. Disruption of zebrafish (Danio rerio) reproduction upon chronic exposure to TiO2 nanoparticles. *Chemosphere*, 83(4):461–467, 2011.

[81] Yi-Ge Zhou, Neil V. Rees, and Richard G. Compton. The Electrochemical Detection and Characterization of Silver Nanoparticles in Aqueous Solution. *Angewandte Chemie International Edition*, 50(18):4219–4221, 2011.

[82] Adam Pluskota, Eva Horzowski, Olaf Bossinger, and Anna Von Mikecz. In Caenorhabditis elegans nanoparticle-bio-interactions become transparent: Silica-nanoparticles induce reproductive senescence. *PLoS ONE*, 4(8), 2009.

[83] R Elghanian, James J Storhoff, Rober C Mucic, Robert L Letsinger, and Chad A Mirkin. Selective Colorimetric Detection of Polynucleotides Based on the Distance-Dependent Optical Properties of Gold Nanoparticles. *Science*, 277(5329):1078–1081, 1997.

[84] Rongchao Jin, Guosheng Wu, Zhi Li, Chad A. Mirkin, and George C. Schatz. What controls the melting properties of DNA-linked gold nanoparticle assemblies? *Journal of the American Chemical Society*, 122(19):4640–4650, 2000.

[85] Ludwig K Limbach, Yuchun Li, Robert N Grass, Tobias J Brunner, Marcel a Hintermann, Martin Muller, Detlef Gunther, and Wendelin J Stark. Oxide nanoparticle uptake in human lung fibroblasts: effects of particle size, agglomeration, and diffusion at low concentrations. *Environmental science & technology*, 39(23):9370–6, dec 2005.

[86] Bernd Nowack, Mohamed Baalousha, Nikolaus Bornhöft, Qasim Chaudhry, Geert Cornelis, Jane Cotterill, Andreas Gondikas, Martin Hassellöv, Jamie Lead, Denise M Mitrano, Frank von der Kammer, and Tim Wontner-Smith. Progress towards the validation of modeled environmental concentrations of engineered nanomaterials by analytical measurements. *Environ. Sci.: Nano*, 2:421–428, 2015.

[87] Elizabeth A Casman and Jeremy M Gernand. Seeing the trees for the forest. *Nature Nanotechnology*, 11(5):405–407, 2016.

[88] Laura Paesano, Alessio Perotti, Annamaria Buschini, Cecilia Carubbi, Marta Marmiroli, Elena Maestri, Salvatore Iannotta, and Nelson Marmiroli. Markers for toxicity to HepG2 exposed to cadmium sulphide quantum dots; damage to mitochondria. *Toxicology*, 374:18–28, 2016.

[89] Pedro M. Costa and Bengt Fadeel. Emerging systems biology approaches in nanotoxicology: Towards a mechanism-based understanding of nanomaterial hazard and risk. *Toxicology and Applied Pharmacology*, 299:101–111, 2016.

[90] Natàlia Garcia-Reyero and Edward J. Perkins. Systems biology: Leading the revolution in ecotoxicology. *Environmental Toxicology and Chemistry*, 30(2):265–273, 2011.

[91] Shana J Sturla, Alan R Boobis, Rex E Fitzgerald, Julia Hoeng, Robert J Kavlock, Kristin Schirmer, Maurice Whelan, Martin F Wilks, and Manuel C Peitsch. Systems Toxicology: From Basic Research to Risk Assessment. *Chem.Res.Toxicol.*, 2014.

[92] Jie Zhang, Liangpo Liu, Xiaofei Wang, Qingyu Huang, Meiping Tian, and Heqing Shen. Low-Level Environmental Phthalate Exposure Associates with Urine Metabolome Alteration in a Chinese Male Cohort. *Environmental Science & Technology*, page acs.est.6b00034, 2016.

[93] Sara Diegoli, Adriana L. Manciulea, Shakiela Begum, Ian P. Jones, Jamie R. Lead, and Jon A. Preece. Interaction between manufactured gold nanoparticles and naturally occurring organic macromolecules. *Science of the Total Environment*, 402(1):51–61, 2008.

[94] Martin Scheringer, Antoine Thill, and Konrad Hungerbu. Heteroaggregation of Titanium Dioxide Nanoparticles with Model Natural Colloids under Environmentally Relevant Conditions. *Environmental Science & Technology*, 48(18):10690–8, 2014.

[95] Boris Meisterjahn, Elisabeth Neubauer, Frank Von der Kammer, Dieter Hennecke, and Thilo Hofmann. Asymmetrical Flow-Field-Flow Fractionation coupled with inductively coupled plasma mass spectrometry for the analysis of gold nanoparticles in the presence of natural nanoparticles. *Journal of chromatography. A*, 1372C:204–211, 2014.

[96] Nicole Sani-Kast, Martin Scheringer, Danielle Slomberg, Jérôme Labille, Antonia Praetorius, Patrick Ollivier, and Konrad Hungerbühler. Addressing the complexity of water chemistry in environmental fate modeling for engineered nanoparticles. *Science of The Total Environment*, 535:150–159, 2015.

[97] Thomas K Darlington, Arianne M Neigh, Matthew T Spencer, Oanh T Nguyen, and Steven J Oldenburg. Nanoparticle characteristics affecting environmental fate and transport through soil. *Environmental toxicology and chemistry / SETAC*, 28(6):1191–9, jun 2009.

[98] Garrison Sposito, C S LeVesque, Joseph P LeClaire, and A C Chang. Trace Metal Chemistry in Arid-Zone Field Soils Amended with Sewage Sludge: III. Effect of Time on the Extraction of Trace Metals. *Soil science society of america*, 47:898–902, 1983.

[99] Kerstin Nylund, Lillemor Asplund, Bo Jansson, Per Jonsson, Kerstin Litzén, and Ulla Sellström. Analysis of some polyhalogenated organic pollutants in sediment and sewage sludge. *Chemosphere*, 24(12):1721–1730, 1992.

[100] Andrew C Johnson, Michael J Bowes, Alison Crossley, Helen P Jarvie, Kerstin Jurkschat, Monika D Jürgens, Alan J Lawlor, Barry Park, Phillip Rowland, David Spurgeon, Claus Svendsen, Ian P Thompson, Robert J Barnes, Richard J Williams, and Nan Xu. An assessment of the fate, behaviour and environmental risk associated with sunscreen TiO nanoparticles in UK field scenarios. *The Science of the total environment*, 409(13):2503–10, jun 2011.

[101] Z M Migaszewski and A Gałuszka. The characteristics, occurrence, and geochemical behavior of rare earth elements in the environment: A review. *Critical Reviews in Environmental Science and Technology*, 45(5):429–471, 2015.

[102] Xuyang Liu, Gexin Chen, and Chunming Su. Effects of material properties on sedimentation and aggregation of titanium dioxide nanoparticles of anatase and rutile in the aqueous phase. *Journal of colloid and interface science*, 363(1):84–91, nov 2011.

[103] D. M. Mitrano, J. F. Ranville, a. Bednar, K. Kazor, a. S. Hering, and C. P. Higgins. Tracking dissolution of silver nanoparticles at environmentally relevant concentrations in laboratory, natural, and processed waters using single particle ICP-MS (spICP-MS). *Environmental Science: Nano*, 1(3):248, 2014.

[104] GC Na and N Rajagopalan. Use of non-ionic cloud point modifiers to minimize nanoparticle aggregation during sterilization. *European Patent 0 601 619 A2*, 1993.

[105] Eun Chul Cho, Qiang Zhang, and Younan Xia. The Effect of Sedimentation and Diffusion on Cellular Uptake of Gold Nanoparticles. *Nature Nanotechnology*, 6(6):385–391, 2011.

[106] Dionne Dickson, Guangliang Liu, Chenzhong Li, Georgio Tachiev, and Yong Cai. Dispersion and stability of bare hematite nanoparticles: Effect of dispersion tools, nanoparticle concentration, humic acid and ionic strength. *Science of the Total Environment*, 419:170–177, 2012.

[107] Joris T K Quik, Martien Cohen Stuart, Marja Wouterse, Willie Peijnenburg, A. Jan Hendriks, and Dik van de Meent. Natural colloids are the dominant factor in the sedimentation of nanoparticles. *Environmental Toxicology and Chemistry*, 31(5):1019–1022, 2012.

[108] Steven E Mylon, Kai Loon Chen, and Menachem Elimelech. Influence of natural organic matter and ionic composition on the kinetics and structure of hematite colloid aggregation: implications to iron depletion in estuaries. *Langmuir : the ACS journal of surfaces and colloids*, 20(21):9000–6, oct 2004.

[109] T. Graham. Liquid Diffusion Applied to Analysis. *Philosophical Transactions of the Royal Society of London*, 151(0):183–224, 1861.

[110] Ira N Levine. *Physical Chemistry*. McGraw-Hill, Brooklyn, New York, 1 edition, 1978.

[111] Alberto Tiraferri, Kai Loon Chen, Rajandrea Sethi, and Menachem Elimelech. Reduced aggregation and sedimentation of zero-valent iron nanoparticles in the presence of guar gum. *Journal of colloid and interface science*, 324(1-2):71–9, aug 2008.

[112] Zouhir E Allouni, Mihaela R Cimpan, Paul J Høl, Tore Skodvin, and Nils R Gjerdet. Agglomeration and sedimentation of TiO2 nanoparticles in cell culture medium. *Colloids and surfaces. B, Biointerfaces*, 68(1):83–7, jan 2009.

[113] Nia C Bell, Caterina Minelli, Jordan Tompkins, Molly M Stevens, and Alexander G Shard. Emerging techniques for submicrometer particle sizing applied to Stöber silica. *Langmuir : the ACS journal of surfaces and colloids*, 28(29):10860–72, jul 2012.

[114] Agnieszka Dudkiewicz, Stephan Wagner, Angela Lehner, Qasim Chaudhry, Stéphane Pietravalle, Karen Tiede, Alistair B A Boxall, Guenter Allmaier, Dirk Tiede, Ringo Grombe, Frank von der Kammer, Thilo Hofmann, and Kristian Mølhave. A uniform measurement expression for cross method comparison of nanoparticle aggregate size distributions. *The Analyst*, 140:5257–5267, 2015.

[115] Wei Jiang, D Brynn Hibbert, Grainne Moran, Jan Herrmann, Asa K Jamting, and Victoria a Coleman. Characterisation of gold agglomerates: size distribution, shape and optical properties. *RSC Advances*, 3(20):7367–7374, 2013.

[116] Sonia Ramirez-Garcia, Lan Chen, Michael a Morris, and Kenneth a Dawson. A new methodology for studying nanoparticle interactions in biological systems: dispersing titania in biocompatible media using chemical stabilisers. *Nanoscale*, 3(11):4617–24, nov 2011.

[117] Heather E Pace, Nicola J Rogers, Chad Jarolimek, Victoria a Coleman, Evan P Gray, Christopher P Higgins, and James F Ranville. Single particle inductively coupled plasma-mass spectrometry: a performance evaluation and method comparison in the determination of nanoparticle size. *Environmental science & technology*, 46(22):12272–80, nov 2012.

[118] Ignacio Moreno-Garrido, Sara Pérez, and Julián Blasco. Toxicity of silver and gold nanoparticles on marine microalgae. *Marine environmental research*, 111:60–73, 2015.

[119] Denise M. Mitrano, Yadira Arroyo Rojas Dasilva, and Bernd Nowack. Effect of Variations of Washing Solution Chemistry on Nanomaterial Physicochemical Changes in the Laundry Cycle. *Environmental Science and Technology*, 49(16):9665–9673, 2015.

[120] Yongbo Dan, Weilan Zhang, Runmiao Xue, Xingmao Ma, Chady Stephan, and Honglan Shi. Characterization of gold nanoparticle uptake by tomato plants using enzymatic extraction followed by single-particle inductively coupled plasma-mass spectrometry analysis. *Environmental science & technology*, 49(5):3007–3014, 2015.

[121] Nashwa El-Gendy and Cory Berkland. Combination chemotherapeutic dry powder aerosols via controlled nanoparticle agglomeration. *Pharmaceutical research*, 26(7):1752–63, jul 2009.

[122] E J E Stuart, N V Rees, J T Cullen, and R G Compton. Direct electrochemical detection and sizing of silver nanoparticles in seawater media. *Nanoscale*, 5(1):174–7, jan 2013.

[123] Susan A. Cumberland and Jamie R. Lead. Particle size distributions of silver nanoparticles at environmentally relevant conditions. *Journal of Chromatography A*, 1216(52):9099–9105, 2009.

[124] Gilbert W Castellan. *Physical Chemistry.* Addison-Wesley, Tokyo, Japan, 1 edition, 1964.

[125] Philip J Bromberg. *Physical Chemistry.* Allyn and Bacon, Boston, US, 2 edition, 1980.

[126] Gordon M Barrow. *Physical Chemistry.* McGraw-Hill, Singapore, 1 edition, 1988.

[127] B Derjaguin and L Landau. Theory of the stability of strongly charged lyophobic sols and of the adhesion of strongly charged particles in solutions of electrolytes. *Progress in Surface Science*, 605(1927):30–59, 1941.

[128] E J W Verwey and J T G Overbeek. Theory of the Stability of Lyophobic Colloids. *Journal of Colloid Science*, 10(2):224–225, 1955.

[129] H Schulze. Antimontrisulfid in wässeriger Lösung. *Journal für Praktische Chemie*, 27(1):320–332, 1883.

[130] W B Hardy. A preliminary investigation of the conditions which determine the stability of irreversible hydrosols. *Proceedings of the Royal Society of London*, 66(424-433):110–125, 1899.

[131] M Smoluchowski. Three lectures on diffusion, Brownian movement and coagulation of colloidal particles. *Physikalische Zeitschrift*, 17:585–599, 1916.

[132] Guozhong Cao. *Nanostructures & Nanomaterials: Synthesis, Properties & Applications.* Imperial College Press, London, UK, 2004.

[133] Elizabeth Allen, Paul Smith, and Jim Henshaw. A Review of Particle Agglomeration. Technical report, US Department of Energy, 2001.

[134] Christina Cruickshank Miller. The Stokes-Einstein Law for Diffusion in Solution. *Mathematical and Physical Character*, 106(740):724–749, 1924.

[135] G E Uhlenbeck and L S Ornstein. On the theory of the Brownian motion. *Physical Review*, 36:823–841, 1930.

[136] D Grasso, K Subramaniam, and M Butkus. A review of non-DLVO interactions in environmental colloidal systems. *Reviews in Environmental science and biotechnology*, pages 17–38, 2002.

[137] Amro M El Badawy, Kirk G Scheckel, Makram Suidan, and Thabet Tolaymat. The impact of stabilization mechanism on the aggregation kinetics of silver nanoparticles. *The Science of the total environment*, 429:325–31, jul 2012.

[138] Max L. Eggersdorfer, Dirk Kadau, Hans J. Herrmann, and Sotiris E. Pratsinis. Aggregate morphology evolution by sintering: Number and diameter of primary particles. *Journal of Aerosol Science*, 46:7–19, 2012.

[139] T. A. Witten and L. M. Sander. Diffusion-limited aggregation. *Physical Review B*, 27(9):5686–5697, 1983.

[140] R. C. Ball, D. A. Weitz, T. A. Witten, and F. Leyvraz. Universal kinetics in reaction-limited aggregation. *Physical Review Letters*, 58(3):274–277, 1987.

[141] T A Witten and Leonard M. Sander. Diffusion-limited aggregation, A kinetic critical phenomenon. *Physical Review Letters*, 47(19):1400–1403, 1981.

[142] M. Y. Lin, H. M. Lindsay, D. A. Weitz, R. C. Ball, R. Klein, and P. Meakin. Universal reaction-limited colloid aggregation. *Physical Review A*, 41(4):2005–2020, 1990.

[143] Paul Meakin and Fereydoon Family. Structure and dynamics of reaction-limited aggregation. *Physical Review A*, 36(11):5498–5501, 1987.

[144] Di He, Mark W Bligh, and T David Waite. Effects of Aggregate Structure on the Dissolution Kinetics of Citrate- Stabilized Silver Nanoparticles. *Environmental Science and Technology*, 47:9148–9156, 2013.

[145] James Clerk Maxwell. Illustrations of the Dynamical Theory of Gases. Part I . On the Motions and Collisions of Perfectly Elastic Spheres. *Philosophical Magazine Series 4*, 19(124):19–32, 1860.

[146] Bruce J Berne and Robert Pecora. *Dynamic Light Scattering.* John Wiley & Sons Inc, 1976.

[147] H Saveyn, B De Baets, O Thas, P Hole, J Smith, and P Van der Meeren. Accurate particle size distribution determination by nanoparticle tracking analysis based on 2-D Brownian dynamics simulation. *Journal of colloid and interface science*, 352(2):593–600, dec 2010.

[148] Gerald Oster. The scattering of light and its applications to chemistry. *Chemical reviews*, 1948.

[149] Andrew Malloy and Bob Carr. NanoParticle Tracking Analysis - The Halo System. *Particle & Particle Systems Characterization*, 23(2):197–204, aug 2006.

[150] Guifu Zhang, J. Vivekanandan, and Edward a. Brandes. A Method for Estimating Rain Rate and Drop Size Distribution from Polarimetric Radar Measurements. *IEEE Transactions on Geoscience and Remote Sensing*, 39(4):830–841, 2001.

[151] JL Keddie, Paul Meredith, RAL Jones, and AM Donald. Film formation of acrylic latices with varying concentrations of non-film-forming latex particles. *Langmuir*, 7463(8):3793–3801, 1996.

[152] A L Friedberg, R B Fischer, and F A Petersenr. Effect of Size and Shape of Titanium Oxide Crystals on Spectrophotometric Properties of Titanium-Bearing Porcelain Enamels*. *Journal of the American Ceramic Society*, 31(9):246–253, 1948.

[153] Milton Kerker. *The scattering of light and other electromagnetic radiation.* Academic Press Inc, New York and London, 1969.

[154] A. J. Cox, Alan J. DeWeerd, and Jennifer Linden. An experiment to measure Mie and Rayleigh total scattering cross sections. *American Journal of Physics*, 70(6):620, 2002.

[155] Lord Rayleigh. On the electromagnetic theory of light. *Philosophical Magazine Series 5*, 12(12:73):81–101, 1881.

[156] H. C. van de Hulst. *Light Scattering by Small Particles.* Dover Publications, New York, 2 edition, 1957.

[157] H. Seiler. Secondary electron emission in the scanning electron microscope. *Journal of Applied Physics*, 54(11), 1983.

[158] FEI. http://fei.com/products/sem/, 2017.

[159] P Luo, I Morrison, A Dudkiewicz, K Tiede, E Boyes, P O'Toole, S Park, and Alistair B A Boxall. Visualization and characterization of engineered nanoparticles in com-

plex environmental and food matrices using atmospheric scanning electron microscopy. *Journal of microscopy*, 250(1):32–41, apr 2013.

[160] Francisco Laborda, Eduardo Bolea, Gemma Cepriá, María T. Gómez, María S. Jiménez, Josefina Pérez-Arantegui, and Juan R. Castillo. Detection, characterization and quantification of inorganic engineered nanomaterials: A review of techniques and methodological approaches for the analysis of complex samples. *Analytica Chimica Acta*, 904:10–32, 2016.

[161] Agnieszka Dudkiewicz, Karen Tiede, Katrin Loeschner, Louise Helene Soegaard Jensen, Eric Jensen, Rafal Wierzbicki, Alistair B A Boxall, and Kristian Molhave. Characterization of nanomaterials in food by electron microscopy. *TrAC - Trends in Analytical Chemistry*, 30(1):28–43, 2011.

[162] Paul Y. Kim, Alexander E. Ribbe, Thomas P. Russell, and David A. Hoagland. Visualizing the Dynamics of Nanoparticles in Liquids by Scanning Electron Microscopy. *ACS Nano*, 10(6):6257–6264, 2016.

[163] A Prasad, J R Lead, and M Baalousha. Science of the Total Environment An electron microscopy based method for the detection and quantification of nanomaterial number concentration in environmentally relevant media. *Science of the Total Environment*, 537:479–486, 2015.

[164] JEOL. http://www.jeol.co.jp/en/products/list_tem.html, 2017.

[165] Albert V. Crewe. Scanning transmission electron microscopy. *Journal of Microscopy*, 100(3):247–259, 1974.

[166] R R Schröder, B Barton, H Rose, and G Benner. Contrast Enhancement by Anamorphotic Phase Plates in an Aberration Corrected TEM. *Microscopy and Microanalysis*, 13(S03):136–137, 2007.

[167] Juan Liu, Zhiwei Wang, Anxu Sheng, Feng Liu, Fuyu Qin, and Zhong Lin Wang. In Situ Observation of Hematite Nanoparticle Aggregates Using Liquid Cell Transmission Electron Microscopy. *Environmental Science & Technology*, page acs.est.5b06305, 2016.

[168] Lynn M. DiMemmo, A. Cameron Varano, Jonathan Haulenbeek, Yanping Liang, Kaya Patel, Madeline J. Dukes, Songyan Zheng, Mario Hubert, Steven P. Piccoli, and Deborah F. Kelly. Real-time observation of protein aggregates in pharmaceutical formulations using liquid cell electron microscopy. *Lab Chip*, 17:315–322, 2017.

[169] Won Chul Lee, Byung Hyo Kim, Sun Choi, Shoji Takeuchi, and Jungwon Park. Liquid Cell Electron Microscopy of Nanoparticle Self-Assembly Driven by Solvent Drying. *The Journal of Physical Chemistry Letters*, pages 647–654, 2017.

[170] P L Gai, E D Boyes, S Helveg, P L Hansen, S Giorgio, and C R Henry. Atomic-resolution environmental transmission electron microscopy for probing gas-solid reactions in heterogeneous catalysis. *MRS Bulletin*, 32(12):1044–1050, 2007.

[171] Pratibha L. Gai and Edward D. Boyes. Advances in atomic resolution in situ environmental transmission electron microscopy and la aberration corrected in situ electron microscopy. *Microscopy Research and Technique*, 72(3):153–164, 2009.

[172] Tsutomu Nomizu, Satoshi Kaneco, Tomokazu Tanaka, Tsuyoshi Yamamoto, and Hiroshi Kawaguchi. Determination of Femto-gram Amounts of Zinc and Lead in Individual Airborne Particles by Inductively Coupled Plasma Mass Spectrometry with Direct Air-Sample Introduction. *Analytical Sciences*, 9(6):843–846, 1993.

[173] Ariel R. Donovan, Craig D. Adams, Yinfa Ma, Chady Stephan, Todd Eichholz, and Honglan Shi. Single particle ICP-MS characterization of titanium dioxide, silver, and gold nanoparticles during drinking water treatment. *Chemosphere*, 144:148–153, 2016.

[174] D. M. Mitrano, J. F. Ranville, A. Bednar, K. Kazor, A. S. Hering, and C. P. Higgins. Tracking dissolution of silver nanoparticles at environmentally relevant concentrations in laboratory, natural, and processed waters using single particle ICP-MS (spICP-MS). *Environmental Science: Nano*, 1(3):248, 2014.

[175] G. A. Jenner, H. P. Longerich, S. E. Jackson, and B. J. Fryer. ICP-MS - A powerful tool for high-precision trace-element analysis in Earth sciences: Evidence from analysis of selected U.S.G.S. reference samples. *Chemical Geology*, 83(1-2):133–148, 1990.

[176] Antonia Praetorius, Alexander Gundlach-Graham, Eli Goldberg, Willi Fabienke, Jana Navratilova, Andreas Gondikas, Ralf Kaegi, Detlef Günther, Thilo Hofmann, and Frank von der Kammer. Single-particle multi-element fingerprinting (spMEF) using inductively-coupled plasma time-of-flight mass spectrometry (ICP-TOFMS) to identify engineered nanoparticles against the elevated natural background in soils. *Environ. Sci.: Nano*, 2017.

[177] Denise Mitrano, James F Ranville, and Chady Stephan. Quantitative Evaluation of Nanoparticle Dissolution Kinetics using Single Particle ICP-MS : A Case Study with Silver Nanoparticles. Technical report, Perkin Elmer, 2014.

[178] Sungyun Lee, Xiangyu Bi, Robert B Reed, James F Ranville, Pierre Herckes, and Paul Westerhoff. Nanoparticle Size Detection Limits by Single Particle ICP-MS for 40 Elements. *Environmental Science & Technology*, 48(17):10291–10300, 2014.

[179] Denise Mitrano, James F Ranville, and Kenneth Neubauer. Coupling Flow Field Flow Fractionation to ICP-MS for the Detection and Characterization of Silver Nanoparticles. Technical report, Perkin Elmer, 2012.

[180] D Mitrano, J Ranville, K Neubauer, and R Thomas. Field-flow-fractionation coupled with ICP-MS for the analysis of engineered nanoparticles in environmental samples. *Spectroscopy (United States)*, 27(9):1–7, 2012.

[181] Denise M. Mitrano, Angela Barber, Anthony Bednar, Paul Westerhoff, Christopher P. Higgins, and James F. Ranville. Silver nanoparticle characterization using single particle ICP-MS (SP-ICP-MS) and asymmetrical flow field flow fractionation ICP-MS (AF4-ICP-MS). *Journal of Analytical Atomic Spectrometry*, 27(7):1131, 2012.

[182] Lieve Balcaen, Eduardo Bolea-Fernandez, Martín Resano, and Frank Vanhaecke. Inductively coupled plasma - Tandem mass spectrometry (ICP-MS/MS): A powerful and universal tool for the interference-free determination of (ultra)trace elements - A tutorial review. *Analytica Chimica Acta*, 894(November):7–19, 2015.

[183] Alexander Gundlach-Graham, Marcel Burger, Steffen Allner, Gunnar Schwarz, Hao A. O. Wang, Luzia Gyr, Daniel Grolimund, Bodo Hattendorf, and Detlef Günther. High-Speed, High-Resolution, Multielemental Laser Ablation-Inductively Coupled Plasma-Time-of-Flight Mass Spectrometry Imaging: Part I. Instrumentation and Two-Dimensional Imaging of Geological Samples. *Analytical Chemistry*, 87(16):8250–8258, 2015.

[184] Marcel Burger, Alexander Gundlach-Graham, Steffen Allner, Gunnar Schwarz, Hao A O Wang, Luzia Gyr, Simon Burgener, Bodo Hattendorf, Daniel Grolimund, and Detlef Günther. High-Speed, High-Resolution, Multielemental LA-ICP-TOFMS Imaging: Part II. Critical Evaluation of Quantitative Three-Dimensional Imaging of Major, Minor, and Trace Elements in Geological Samples. *Analytical Chemistry*, 87(16):8259–8267, 2015.

[185] Olga Borovinskaya, Maryam Aghaei, Luca Flamigni, Bodo Hattendorf, Martin Tanner, Annemie Bogaerts, and Detlef Gunther. Diffusion- and velocity-driven spatial separation of analytes from single droplets entering an ICP off-axis. *Journal of Analytical Atomic Spectrometry*, 29(2):262–271, 2014.

[186] Olga Borovinskaya, Sabrina Gschwind, Bodo Hattendorf, Martin Tanner, and Detlef Günther. Simultaneous mass quantification of nanoparticles of different composition in a mixture by microdroplet generator-ICPTOFMS. *Analytical Chemistry*, 86(16):8142–8148, 2014.

[187] Karen Tiede, Alistair B. a. Boxall, Dirk Tiede, Steven P. Tear, Helen David, and John Lewis. A robust size-characterisation methodology for studying nanoparticle behaviour in real' environmental samples, using hydrodynamic chromatography coupled to ICP-MS. *Journal of Analytical Atomic Spectrometry*, 24(7):964, 2009.

[188] Karen Tiede, Alistair B. a. Boxall, Xinmei Wang, David Gore, Dirk Tiede, Malcolm Baxter, Helen David, Steven P. Tear, and John Lewis. Application of hydrodynamic chromatography-ICP-MS to investigate the fate of silver nanoparticles in activated sludge. *Journal of Analytical Atomic Spectrometry*, 25(7):1149, 2010.

[189] Michael H. Smith, Antoinette B. South, Jeffrey C. Gaulding, and L. Andrew Lyon. Monitoring the erosion of hydrolytically-degradable nanogels via multiangle light scattering coupled to asymmetrical flow field-flow fractionation. *Analytical Chemistry*, 82(2):523–530, 2010.

[190] Wolfgang Haller. Virus isolation with glass of controlled pore size: MS2 bacteriophage and kilham virus. *Virology*, 33:740–743, 1967.

[191] Hamish Small. Hydrodynamic chromatography: a trchnique for size analysis of colloidal particles. *Journal of colloid and interface science*, 48(1):147–161, 1974.

[192] Rodney J Noel, Karen M Gooding, Fred E Regnier, Dean M Ball, Clyde Orr, and M E Mullins. Capillary hydrodynamic chromatography. *Journal of chromatography*, 166:373–382, 1978.

[193] Emil Chmela, Robert Tijssen, Marko T. Blom, Han J G E Gardeniers, and Albert Van den Berg. A chip system for size separation of macromolecules and particles by hydrodynamic chromatography. *Analytical Chemistry*, 74(14):3470–3475, 2002.

[194] Marko T. Blom, Emil Chmela, R. Edwin Oosterbroek, Rob Tijssen, and Albert Van Den Berg. On-Chip Hydrodynamic Chromatography Separation and Detection of Nanoparticles and Biomolecules. *Analytical Chemistry*, 75(24):6761–6768, 2003.

[195] A. W J Brough, D. E. Hillman, and R. W. Perry. Capillary hydrodynamic chromatography –an investigation into operational characteristics. *Journal of Chromatography A*, 208(2):175–182, 1981.

[196] Evan P. Gray, Thomas A. Bruton, Christopher P. Higgins, Rolf U. Halden, Paul Westerhoff, and James F. Ranville. Analysis of gold nanoparticle mixtures: a comparison of hydrodynamic chromatography (HDC) and asymmetrical flow field-flow fractionation (AF4) coupled to ICP-MS. *Journal of Analytical Atomic Spectrometry*, 27(9):1532, 2012.

[197] Cesar A. Silebi and Anthony J. McHugh. An analysis of flow separation in hydrodynamic chromatography of polymer latexes. *AIChE Journal*, 24(2):204–212, 1978.

[198] G. Stegeman, R. Oostervink, J. C. Kraak, H. Poppe, and K. K. Unger. Hydrodynamic chromatography of macromolecules on small spherical non-porous silica particles. *Journal of Chromatography A*, 506(C):547–561, 1990.

[199] B.R. Ware and W.H. Flygare. The simultaneous measurement of the electrophoretic mobility and diffusion coefficient in bovine serum albumin solutions by light scattering. *Chemical Physics Letters*, 12(1):81–85, 1971.

[200] B R Ware. Electrophoretic Light Scattering Study. *Advances in colloid and interface science*, 4:1–44, 1974.

[201] Toshio Takagi. Electrophoretic Light Scattering. *Electrophoresis*, 14:1255–1256, 1993.

[202] Bruce J Berne and Robert Pecora. *Dynamic Light Scattering: Applications of Photon Correlation Spectroscopy.* Springer, 1 edition, 1985.

[203] R Bracewell. Pentagram notation for cross-correlation. In *The fourier transform and its applications*, page 46. 1965.

[204] Stephen W Provencher. Inverse Problems in Polymer Characterization: Direct Analysis of Polydispersity with Photon Correlation Spectroscopy. *Die Makromolekulare Chemie*, 180(1):201–209, 1979.

[205] S W Provencher. A constrained regularization method for inverting data represented by linear algebraic or integral equations, 1982.

[206] Stephen W. Provencher. CONTIN: A general purpose constrained regularization program for inverting noisy linear algebraic and integral equations., 1982.

[207] Stephen W. Provencher. A constrained regularization method for inverting data represented by linear algebraic or integral equations. *Computer Physics Communications*, 27(3):213–227, 1982.

[208] Gary Bryant and John C Thomas. Improved Particle Size Distribution Measurements Using Multiangle Dynamic Light Scattering. *Langmuir*, 11(7):2480–2485, 1995.

[209] Philip J Wyatt. Submicrometer Particle Sizing by Multiangle Light Scattering following Fractionation. *Journal of Colloid and Interface Science*, 197(1):9–20, 1998.

[210] D.J. Pine, D.a. Weitz, J.X. Zhu, and E. Herbolzheimer. Diffusing-wave spectroscopy: dynamic light scattering in the multiple scattering limit. *Journal de Physique*, 51(18):2101–2127, 1990.

[211] Navid B Saleh, Lisa D Pfefferle, and Menachem Elimelech. Aggregation kinetics of multiwalled carbon nanotubes in aquatic systems: measurements and environmental implications. *Environmental science & technology*, 42(21):7963–9, nov 2008.

[212] Khanh An Huynh and Kai Loon Chen. Aggregation kinetics of citrate and polyvinylpyrrolidone coated silver nanoparticles in monovalent and divalent electrolyte solutions. *Environmental science & technology*, 45(13):5564–71, jul 2011.

[213] Kai Loon Chen and Menachem Elimelech. Aggregation and deposition kinetics of fullerene (C60) nanoparticles. *Langmuir : the ACS journal of surfaces and colloids*, 22(26):10994–1001, dec 2006.

[214] Xuan Li, John J. Lenhart, and Harold W. Walker. Dissolution-accompanied aggregation kinetics of silver nanoparticles. *Langmuir*, 26(22):16690–16698, 2010.

[215] Vincent A. Martinez, Rut Besseling, Ottavio A. Croze, Julien Tailleur, Mathias Reufer, Jana Schwarz-Linek, Laurence G. Wilson, Martin A. Bees, and Wilson C K Poon. Differential dynamic microscopy: A high-throughput method for characterizing the motility of microorganisms. *Biophysical Journal*, 103(8):1637–1647, 2012.

[216] Roberto Cerbino and Veronique Trappe. Differential Dynamic Microscopy: Probing Wave Vector Dependent Dynamics with a Microscope. *Physical Review Letters*, 100(18):188102, may 2008.

[217] Fabio Giavazzi, Doriano Brogioli, Veronique Trappe, Tommaso Bellini, and Roberto Cerbino. Scattering information obtained by optical microscopy: Differential dynamic microscopy and beyond. *Physical Review E - Statistical, Nonlinear, and Soft Matter Physics*, 80:1–15, 2009.

[218] L. G. Wilson, V. A. Martinez, J. Schwarz-Linek, J. Tailleur, G. Bryant, P. N. Pusey, and W. C. K. Poon. Differential Dynamic Microscopy of Bacterial Motility. *Physical Review Letters*, 106(1):018101, jan 2011.

[219] F. Ferri, A. D'Angelo, M. Lee, A. Lotti, M. C. Pigazzini, K. Singh, and R. Cerbino. Kinetics of colloidal fractal aggregation by differential dynamic microscopy. *European Physical Journal: Special Topics*, 199:139–148, 2011.

[220] Peter J. Lu, Fabio Giavazzi, Thomas E. Angelini, Emanuela Zaccarelli, Frank Jargstorff, Andrew B. Schofield, James N. Wilking, Mark B. Romanowsky, David A. Weitz, and Roberto Cerbino. Characterizing concentrated, multiply scattering, and actively driven fluorescent systems with confocal differential dynamic microscopy. *Physical Review Letters*, 108(May):1–5, 2012.

[221] Alexandra V Bayles, Todd Squires, and Matthew E Helgeson. Dark-field differential dynamic microscopy. *Soft Matter*, 12:2440–2452, 2016.

[222] R Colin, R Zhang, and LG Wilson. Fast, high-throughput measurement of collective behaviour in a bacterial population. *Journal of The Royal Society Interface*, (July), 2014.

[223] David Germain, Mathieu Leocmach, and Thomas Gibaud. Differential dynamic microscopy to characterize Brownian motion and bacteria motility. *American Journal of Physics*, 84(3):202–210, 2016.

[224] Andrew Wittmeier, Andrew Leeth Holterhoff, Joel Johnson, and John G. Gibbs. Rotational Analysis of Spherical, Optically Anisotropic Janus Particles by Dynamic Microscopy. *Langmuir*, 31(38):10402–10410, 2015.

[225] Mohammad S. Safari, Maria A. Vorontsova, Ryan Poling-Skutvik, Peter G. Vekilov, and Jacinta C. Conrad. Differential dynamic microscopy of weakly scattering and polydisperse protein-rich clusters. *Physical Review E - Statistical, Nonlinear, and Soft Matter Physics*, 92(4):1–12, 2015.

[226] Nanosight LTD. Nanosight - Frequently Asked Questions. pages 0–3, 2013.

[227] Andrew Malloy and Bob Carr. Nanoparticle tracking analysisthe Halo system. *Particle & Particle Systems Characterization*, 23(April):197–204, 2006.

[228] Bob Carr and Matthew Wright. *Nanoparticle Tracking Analysis: A review of Applications and Usage 2010-2012*, volume 44. 2012.

[229] Bradley Anderson, Mohammed H Rashid, Chandi Carter, Gary Pasternack, Chythanya Rajanna, Tamara Revazishvili, Timothy Dean, Andre Senecal, and Alexander Sulakvelidze. Enumeration of bacteriophage particles: Comparative analysis of the traditional plaque assay and real-time QPCR- and nanosight-based assays. *Bacteriophage*, 1(2):86–93, jan 2011.

[230] John H Seinfeld and Spyros N Pandis. *Atmospheric chemistry and physics: from air pollution to climate change*. John Wiley {&} Sons Inc, Hoboken, New Jersey, 2006.

[231] James Holland. Noise sources of NTA. *MPhys Dissertation*, 2013.

[232] Vasco Filipe, Andrea Hawe, and Wim Jiskoot. Critical evaluation of Nanoparticle Tracking Analysis (NTA) by NanoSight for the measurement of nanoparticles and protein aggregates. *Pharmaceutical research*, 27(5):796–810, may 2010.

[233] Nanosight. *Third Party Papers citing Nanosight or NTA data split by application*. Nanosight, 2013.

[234] Julian A. Gallego-Urrea, Jani Tuoriniemi, and Martin Hassellöv. Applications of particle-tracking analysis to the determination of size distributions and concentrations of nanoparticles in environmental, biological and food samples. *TrAC Trends in Analytical Chemistry*, 30(3):473–483, mar 2011.

[235] Nanosight. Nanosight frequently asked questions (FAQ).

[236] Irène Schwyzer, Ralf Kaegi, Laura Sigg, Rita Smajda, Arnaud Magrez, and Bernd Nowack. Long-term colloidal stability of 10 carbon nanotube types in the absence/presence of humic acid and calcium. *Environmental pollution (Barking, Essex : 1987)*, 169:64–73, oct 2012.

[237] Iker Montes-Burgos, Dorota Walczyk, Patrick Hole, Jonathan Smith, Iseult Lynch, and Kenneth Dawson. Characterisation of nanoparticle size and state prior to nanotoxicological studies. *Journal of Nanoparticle Research*, 12(1):47–53, oct 2010.

[238] H Saveyn, B De Baets, O Thas, P Hole, J Smith, and P der Meeren. Accurate particle size distribution determination by nanoparticle tracking analysis based on {2-D} Brownian dynamics simulation. *J. Colloid Interface Sci.*, 352:593–600, 2010.

[239] Wei Lv, Cong-Hui You, Sida Wu, Baohua Li, Zhen-Ping Zhu, Maozhang Wang, Quan-Hong Yang, and Feiyu Kang. pH-Mediated fine-tuning of optical properties of graphene oxide membranes. *Carbon*, 50(9):3233–3239, aug 2012.

[240] Trishikhi Raychoudhury, Nathalie Tufenkji, and Subhasis Ghoshal. Aggregation and deposition kinetics of carboxymethyl cellulose-modified zero-valent iron nanoparticles in porous media. *Water Research*, 46(6):1735–1744, 2012.

[241] Scott Lambert, Chris J Sinclair, Emma L Bradley, and Alistair A B A Boxall. Effects of environmental conditions on latex degradation in aquatic systems. *Sci. Total Environ.*, 447:225–234, 2013.

[242] Rebecca a Dragovic, Christopher Gardiner, Alexandra S Brooks, Dionne S Tannetta, David J P Ferguson, Patrick Hole, Bob Carr, Christopher W G Redman, Adrian L Harris, Peter J Dobson, Paul Harrison, and Ian L Sargent. Sizing and phenotyping of cellular vesicles using Nanoparticle Tracking Analysis. *Nanomedicine : nanotechnology, biology, and medicine*, 7(6):780–8, dec 2011.

[243] Shangfeng Du, Kevin Kendall, Panteha Toloueinia, Yasamin Mehrabadi, Gaurav Gupta, and Jill Newton. Aggregation and adhesion of gold nanoparticles in phosphate buffered saline. *Journal of Nanoparticle Research*, 14(3):758, feb 2012.

[244] Kevin Kendall and Maria R. Kosseva. Nanoparticle aggregation influenced by magnetic fields. *Colloids and Surfaces A: Physicochemical and Engineering Aspects*, 286(1-3):112–116, sep 2006.

[245] Cheska Gillespie, Peter Halling, and Darren Edwards. Monitoring of particle growth at a low concentration of a poorly water soluble drug using the NanoSight LM20. *Colloids and Surfaces A: Physicochemical and Engineering Aspects*, 384(1-3):233–239, jul 2011.

[246] Vasco Filipe, Robert Poole, Marika Kutscher, Katrien Forier, Kevin Braeckmans, and Wim Jiskoot. Fluorescence single particle tracking for the characterization of submicron protein aggregates in biological fluids and complex formulations. *Pharmaceutical research*, 28(5):1112–20, may 2011.

[247] Iker Montes-Burgos, Dorota Walczyk, Patrick Hole, Jonathan Smith, Iseult Lynch, and Kenneth Dawson. Characterisation of nanoparticle size and state prior to nanotoxicological studies. *J. Nanopart. Res.*, 12:47–53, 2009.

[248] Robert I MacCuspie, Kim Rogers, Manomita Patra, Zhiyong Suo, Andrew J Allen, Matthew N Martin, and Vincent A Hackley. Challenges for physical characterization of silver nanoparticles under pristine and environmentally relevant conditions. *J. Environ. Monit.*, 13:1212–1226, 2011.

[249] Sujung Park, James Woodhall, Guibin Ma, Jonathan G C Veinot, Malcolm S Cresser, and Alistair B A Boxall. Regulatory ecotoxicity testing of engineered nanoparticles: are the results relevant to the natural environment? *Nanotoxicology*, (February):1–10, jul 2013.

[250] Zhuang Wang, Jingwen Chen, Xuehua Li, Jianping Shao, and Willie J G M Peijnenburg. Aquatic toxicity of nanosilver colloids to different trophic organisms: contributions of particles and free silver ion. *Environmental toxicology and chemistry / SETAC*, 31(10):2408–13, oct 2012.

[251] Tsz Yan Ling, Zhili Zuo, and David Y H Pui. Detection and Identification: Instrumentation and Calibration for Air/Liquid/Surface-borne Nanoscale Particles. *Journal of Physics: Conference Series*, 429, 2006.

[252] Scott Lambert, Chris J Sinclair, Emma L Bradley, and Alistair B A Boxall. Effects of environmental conditions on latex degradation in aquatic systems. *The Science of the total environment*, 447:225–34, mar 2013.

[253] Maria del Prado Domercq. *Environmental behaviour of Bi2O3 nanoparticles: a green energy study case*. PhD thesis, University College Dublin, 2014.

[254] Sujung Park, James Woodhall, Guibin Ma, Jonathan G C Veinot, Malcolm S Cresser, and Alistair B A Boxall. Regulatory ecotoxicity testing of engineered nanoparticles: are the results relevant to the natural environment? *Nanotoxicology*, Early Onli:1–10, 2013.

[255] Glen Cowan. *Statistical data analysis*. Oxford University Press, Oxford, UK, 1998.

[256] Aliasger K Salem, Peter C Searson, and Kam W Leong. Multifunctional nanorods for gene delivery. *Nature materials*, 2(October):668–671, 2003.

[257] Ken Donaldson, Robert Aitken, Lang Tran, Vicki Stone, Rodger Duffin, Gavin Forrest, and Andrew Alexander. Carbon nanotubes: A review of their properties in relation to pulmonary toxicology and workplace safety. *Toxicological Sciences*, 92(1):5–22, 2006.

[258] A Poland Craig, Duffin Rodger, Kinloch Ian, Maynard Andrew, A H Wallace William, Seaton Anthony, Stone Vicki, Brown Simon, Macnee William, and Donaldson Ken. Carbon nanotubes introduced into the abdominal cavity of mice show asbestos-like pathogenicity in a pilot study. *Nature nanotechnology*, 3(7):423–428, 2008.

[259] Ken Donaldson, Fiona A Murphy, Rodger Duffin, and Craig A Poland. Asbestos, carbon nanotubes and the pleural mesothelium: a review of the hypothesis regarding the role

of long fibre retention in the parietal pleura, inflammation and mesothelioma. *Particle and fibre toxicology*, 7:5, 2010.

[260] Megan J Osmond-McLeod, Craig A Poland, Fiona Murphy, Lynne Waddington, Howard Morris, Stephen C Hawkins, Steve Clark, Rob Aitken, Maxine J McCall, and Ken Donaldson. Durability and inflammogenic impact of carbon nanotubes compared with asbestos fibres. *Particle and fibre toxicology*, 8:15, 2011.

[261] Ken Donaldson, Craig A. Poland, Fiona A. Murphy, Marion MacFarlane, Tatyana Chernova, and Anja Schinwald. Pulmonary toxicity of carbon nanotubes and asbestos - Similarities and differences. *Advanced Drug Delivery Reviews*, 65(15):2078–2086, 2013.

[262] E E McConnell. A science-based paradigm for the classification of synthetic vitreous fibers. *Regulatory toxicology and pharmacology : RTP*, 32(1):14–21, 2000.

[263] Brooke T Mossman, L. Gee, and J. Bernard. Asbestos Related Disease. *The New England Journal of Medicine*, 320(26):1730, 1989.

[264] Matthew D. Ooms, Yogesh Jeyaram, and David Sinton. Wavelength-selective plasmonics for enhanced cultivation of microalgae. *Applied Physics Letters*, 106(6), 2015.

[265] JM Beman, KR Arrigo, and PA Matson. Agricultural runoff fuels large phytoplankton blooms in vulnerable areas of the ocean. *Nature*, 434(7030):211–214, 2005.

[266] R. Agarwal, V. Singh, P. Jurney, L. Shi, S. V. Sreenivasan, and K. Roy. Mammalian cells preferentially internalize hydrogel nanodiscs over nanorods and use shape-specific uptake mechanisms. *Proceedings of the National Academy of Sciences*, 110(43):17247–17252, 2013.

[267] Eun Chul Cho, Qiang Zhang, and Younan Xia. The effect of sedimentation and diffusion on cellular uptake of gold nanoparticles. *Nature nanotechnology*, 6(6):385–91, jun 2011.

[268] Fanyao Qu, R. H. Oliveira, and P. C. Morais. Effects of nanocrystal shape on the surface charge density of ionic colloidal nanoparticles. *Journal of Magnetism and Magnetic Materials*, 272-276(III):1668–1669, 2004.

[269] Glenn A. Waychunas, Christopher S. Kim, and Jillian F. Banfield. Nanoparticulate iron oxide minerals in soils and sediments: Unique properties and contaminant scavenging mechanisms. *Journal of Nanoparticle Research*, 7(4-5):409–433, 2005.

[270] Kyoungweon Park, Hilmar Koerner, and Richard A. Vaia. Depletion-induced shape and size selection of gold nanoparticles. *Nano Letters*, 10(4):1433–1439, 2010.

[271] Vivek Sharma, Kyoungweon Park, and Mohan Srinivasarao. Shape separation of gold nanorods using centrifugation. *Proceedings of the National Academy of Sciences of the United States of America*, 106(13):4981–5, 2009.

[272] B B Mandelbrot. Stochastic models for the Earth's relief, the shape and the fractal dimension of the coastlines, and the number-area rule for islands. *Proceedings of the National Academy of Sciences of the United States of America*, 72(10):3825–8, 1975.

[273] B H Kaye. Specification of the Ruggedness and/or Texture of a Fine Particle Profile by its Fractal Dimension. *Powder Technology*, 21:1–16, 1978.

[274] A G Flook. The use of dilation logic on the quantimet to achieve fractal dimension characterisation of textured and structured profiles. *Powder Technology*, 21:295 – 298, 1978.

[275] Jean C. Sung, Danielle J. Padilla, Lucila Garcia-Contreras, Jarod L. Verberkmoes, David Durbin, Charles A. Peloquin, Katharina J. Elbert, Anthony J. Hickey, and David A. Edwards. Formulation and pharmacokinetics of self-assembled rifampicin nanoparticle systems for pulmonary delivery. *Pharmaceutical Research*, 26(8):1847–1855, 2009.

[276] Fadri Gottschalk, Tobias Sonderer, Roland W Scholz, and Bernd Nowack. Modeled environmental concentrations of engineered nanomaterials (TiO(2), ZnO, Ag, CNT, Fullerenes) for different regions. *Environmental science & technology*, 43(24):9216–22, 2009.

[277] AC Templeton and FP Zamborini. Controlled and reversible formation of nanoparticle aggregates and films using Cu2+-carboxylate chemistry. *Langmuir*, 16:6682–6688, 2000.

[278] Fangfang Wang, Shuzhen Liu, Mingxia Lin, Xing Chen, Shiru Lin, Xiazhen Du, He Li, Hongbin Ye, Bin Qiu, Zhenyu Lin, Longhua Guo, and Guonan Chen. Colorimetric detection of microcystin-LR based on disassembly of orient-aggregated gold nanoparticle dimers. *Biosensors and Bioelectronics*, 68:475–480, 2015.

[279] Suprit Deol, Nisala Weerasuriya, and Young-Seok Shon. Stability, cytotoxicity and cell uptake of water-soluble dendronconjugated gold nanoparticles with 3, 12 and 17 nm cores. *J. Mater. Chem. B*, 3(29):6071–6080, 2015.

[280] Mohammed Baalousha. Aggregation and disaggregation of iron oxide nanoparticles: Influence of particle concentration, pH and natural organic matter. *Science of the Total Environment*, 407(6):2093–2101, 2009.

[281] P. Christian, F. Von Der Kammer, M. Baalousha, and Th Hofmann. Nanoparticles: Structure, properties, preparation and behaviour in environmental media. *Ecotoxicology*, 17(5):326–343, 2008.

[282] Katherine A Dunphy Guzman, Michael P Finnegan, and Jillian F Banfield. Influence of surface potential on aggregation and transport of titania nanoparticles. *Environmental science & technology*, 40(24):7688–93, dec 2006.

[283] Luis M. Tupas, Brian N. Popp, and David M. Karl. Dissolved organic carbon in oligotrophic waters: experiments on sample preservation, storage and analysis. *Marine Chemistry*, 45(3):207–216, 1994.

[284] D A Morrison. Transformation in Escherichia-Coli - Cryogenic Preservation of Competent Cells. *Journal of Bacteriology*, 132(1):349–351, 1977.

[285] C. Krembs, H. Eicken, K. Junge, and J. W. Deming. High concentrations of exopolymeric substances in Arctic winter sea ice: Implications for the polar ocean carbon cycle and cryoprotection of diatoms. *Deep-Sea Research Part I: Oceanographic Research Papers*, 49(12):2163–2181, 2002.

[286] Carol E. Smith and Henry G. Schwartzberg. Ice Crystal Size Changes During Ripening in Freeze Concentration. *Biotechnology Progress*, 1(2):111–120, 1985.

[287] W. L J Hinrichs, F. A. Manceñido, N. N. Sanders, K. Braeckmans, S. C. De Smedt, J. Demeester, and H. W. Frijlink. The choice of a suitable oligosaccharide to prevent aggregation of PEGylated nanoparticles during freeze thawing and freeze drying. *International Journal of Pharmaceutics*, 311(1-2):237–244, 2006.

[288] Julián A. Gallego-Urrea, Jani Tuoriniemi, Tobias Pallander, and Martin Hassellöv. Measurements of nanoparticle number concentrations and size distributions in contrasting aquatic environments using nanoparticle tracking analysis. *Environmental Chemistry*, 7(1):67, 2010.

[289] Rebecca a French, Astrid R Jacobson, Bojeong Kim, Sara L Isley, R Lee Penn, and Philippe C Baveye. Influence of ionic strength, pH, and cation valence on aggregation kinetics of titanium dioxide nanoparticles. *Environmental science & technology*, 43(5):1354–9, mar 2009.

[290] Xuyang Liu, Mahmoud Wazne, Christos Christodoulatos, and Kristin L Jasinkiewicz. Aggregation and deposition behavior of boron nanoparticles in porous media. *Journal of colloid and interface science*, 330(1):90–6, feb 2009.

[291] Geoffrey Fryer. *The Freshwater Crustacea of Yorkshire.* Yorkshire Naturalists Union, Leeds Philosophical & Literary Society, 1993.

[292] Kai Loon Chen, Steven E Mylon, and Menachem Elimelech. Aggregation kinetics of cerium oxide nanoparticles in monovalent and divalent electrolytes. *Environmental Science and Technology*, 40(5):1516–1523, 2006.

[293] Yimin Xuan, Qiang Li, and Weifeng Hu. Aggregation structure and thermal conductivity of nanofluids. *AIChE Journal*, 49(4):1038–1043, apr 2003.

[294] Fadri Gottschalk, Tianyin Sun, and Bernd Nowack. Environmental concentrations of engineered nanomaterials: Review of modeling and analytical studies. *Environmental Pollution*, 181:287–300, 2013.

[295] Wan Seob Cho, Minjung Cho, Jinyoung Jeong, Mina Choi, Hea Young Cho, Beom Seok Han, Sheen Hee Kim, Hyoung Ook Kim, Yong Taik Lim, Bong Hyun Chung, and Jayoung Jeong. Acute toxicity and pharmacokinetics of 13nm-sized PEG-coated gold nanoparticles. *Toxicology and Applied Pharmacology*, 236(1):16–24, 2009.

[296] Jinyuan Chen, Xia Dong, Jing Zhao, and Guping Tang. In vivo acute toxicity of titanium dioxide nanoparticles to mice after intraperitioneal injection. *Journal of Applied Toxicology*, 29(4):330–337, 2009.

[297] K. Doiron, E. Pelletier, and K. Lemarchand. Impact of polymer-coated silver nanoparticles on marine microbial communities: A microcosm study. *Aquatic Toxicology*, 124-125:22–27, 2012.

[298] Min Kyeong Yeo and Dong Ha Nam. Influence of different types of nanomaterials on their bioaccumulation in a paddy microcosm: A comparison of TiO2 nanoparticles and nanotubes. *Environmental Pollution*, 178:166–172, 2013.

[299] Pierre Emmanuel Buffet, Marion Richard, Fanny Caupos, Aurore Vergnoux, Hanane Perrein-Ettajani, Andrea Luna-Acosta, Farida Akcha, Jean Claude Amiard, Claude Amiard-Triquet, Marielle Guibbolini, Christine Risso-De Faverney, Helene Thomas-Guyon, Paul Reip, Agnieska Dybowska, Deborah Berhanu, Eugenia Valsami-Jones, and Catherine Mouneyrac. A mesocosm study of fate and effects of CuO nanoparticles on endobenthic species (Scrobicularia plana, Hediste diversicolor). *Environmental Science and Technology*, 47(3):1620–1628, 2013.

[300] Pierre Emmanuel Buffet, Aurore Zalouk-Vergnoux, Amélie Châtel, Brigitte Berthet, Isabelle Métais, Hanane Perrein-Ettajani, Laurence Poirier, Andrea Luna-Acosta, Hélène

Thomas-Guyon, Christine Risso-de Faverney, Marielle Guibbolini, Douglas Gilliland, Eugenia Valsami-Jones, and Catherine Mouneyrac. A marine mesocosm study on the environmental fate of silver nanoparticles and toxicity effects on two endobenthic species: The ragworm Hediste diversicolor and the bivalve mollusc Scrobicularia plana. *Science of the Total Environment*, 470-471:1151–1159, 2014.

[301] Fan Wu, Bryan J. Harper, and Stacey L. Harper. Differential dissolution and toxicity of surface functionalized silver nanoparticles in small-scale microcosms: impacts of community complexity. *Environ. Sci.: Nano*, 4:359–372, 2017.

[302] Kwangjae Cho, Xu Wang, Shuming Nie, Zhuo Chen, and Dong M. Shin. Therapeutic nanoparticles for drug delivery in cancer. *Clinical Cancer Research*, 14(5):1310–1316, 2008.

[303] S.U.S. Choi and J.A. Eastman. Enhancing thermal conductivity of fluids with nanoparticles. *ASME International Mechanical Engineering Congress and Exposition*, 66(January 1995):99–105, 1995.

[304] K. D. Hermanson. Dielectrophoretic Assembly of Electrically Functional Microwires from Nanoparticle Suspensions. *Science*, 294(5544):1082–1086, 2001.

[305] Huaqing Xie, Jinchang Wang, Tonggeng Xi, Yan Liu, Fei Ai, and Qingren Wu. Thermal conductivity enhancement of suspensions containing nanosized alumina particles. *Journal of Applied Physics*, 91(7):4568–4572, 2002.

[306] Christof M. Niemeyer. Biotechnology Meets Materials Science. *Angewandte Chemie (International ed. in English)*, 40(22):4128–4158, 2001.

[307] Wassim Abdelwahed, Ghania Degobert, Serge Stainmesse, and Hatem Fessi. Freeze-drying of nanoparticles: Formulation, process and storage considerations. *Advanced Drug Delivery Reviews*, 58(15):1688–1713, 2006.

[308] Jonghwi Lee and Yu Cheng. Critical freezing rate in freeze drying nanocrystal dispersions. *Journal of Controlled Release*, 111(1-2):185–192, 2006.

[309] Richard Hogg. Bridging flocculation by polymers. *KONA Powder and Particle Journal*, 30(30):3–14, 2012.

[310] Abhilash Sasidharan, Jim E. Riviere, and Nancy A. Monteiro-Riviere. Gold and silver nanoparticle interactions with human proteins: impact and implications in biocorona formation. *J. Mater. Chem. B*, 3(10):2075–2082, 2015.

[311] Denis Pristinski and Thomas Q Chastek. A versatile, low-cost approach to dynamic light scattering. *Measurement Science and Technology*, 20(4):045705, 2009.

[312] Bob Carr and Andrew Malloy. Nanosight user manual, 2006.

[313] Molly M. Miller and Anne A. Lazarides. Sensitivity of Metal Nanoparticle Surface Plasmon Resonance to the Dielectric Environment. *The Journal of Physical Chemistry B*, 109(46):21556–21565, 2005.

[314] Susie Eustis and Mostafa a El-Sayed. Why gold nanoparticles are more precious than pretty gold: noble metal surface plasmon resonance and its enhancement of the radiative and nonradiative properties of nanocrystals of different shapes. *Chemical Society reviews*, 35(3):209–217, 2006.

[315] I F Sbalzarini and P Koumoutsakos. Feature point tracking and trajectory analysis for video imaging in cell biology. *Journal of structural biology*, 151(2):182–95, aug 2005.

[316] Julián A Gallego-Urrea, Jani Tuoriniemi, and Martin Hasselöv. Applications of particle-tracking analysis to the determination of size distributions and concentrations of nano particles in environmental, biological, and food samples. *Trends in analytical chemistry*, 30(3):473–483, 2011.

[317] International Standard Organization. ISO/IEC 17025 General requirements for the competence of testing and calibration laboratories. *International Standard*, 2005:1–36, 2005.

[318] Frank von der Kammer, P Lee Ferguson, Patricia a Holden, Armand Masion, Kim R Rogers, Stephen J Klaine, Albert a Koelmans, Nina Horne, and Jason M Unrine. Analysis of engineered nanomaterials in complex matrices (environment and biota): general considerations and conceptual case studies. *Environmental toxicology and chemistry / SETAC*, 31(1):32–49, jan 2012.

[319] Sherrie Elzey and Vicki H. Grassian. Agglomeration, isolation and dissolution of commercially manufactured silver nanoparticles in aqueous environments. *Journal of Nanoparticle Research*, 12(5):1945–1958, oct 2009.

[320] Adamo R Petosa, Deb P Jaisi, Ivan R Quevedo, Menachem Elimelech, and Nathalie Tufenkji. Aggregation and deposition of engineered nanomaterials in aquatic environments: role of physicochemical interactions. *Environmental science & technology*, 44(17):6532–49, sep 2010.

[321] Rute F Domingos, Nathalie Tufenkji, and Kevin I Wilkinson. Aggregation of titanium dioxide nanoparticles: role of a fulvic acid. *Environmental science & technology*, 43(5):1282–6, mar 2009.

[322] Beng Joo Reginald Thio, Dongxu Zhou, and Arturo a Keller. Influence of natural organic matter on the aggregation and deposition of titanium dioxide nanoparticles. *Journal of hazardous materials*, 189(1-2):556–63, may 2011.

[323] Xuyang Liu, Mahmoud Wazne, Yun Han, Christos Christodoulatos, and Kristin L Jasinkiewicz. Effects of natural organic matter on aggregation kinetics of boron nanoparticles in monovalent and divalent electrolytes. *Journal of colloid and interface science*, 348(1):101–7, aug 2010.

[324] Benjamin Gilbert, Reyn K Ono, Kristen a Ching, and Christopher S Kim. The effects of nanoparticle aggregation processes on aggregate structure and metal uptake. *Journal of colloid and interface science*, 339(2):285–95, nov 2009.

[325] Arturo a Keller, Hongtao Wang, Dongxu Zhou, Hunter S Lenihan, Gary Cherr, Bradley J Cardinale, Robert Miller, and Zhaoxia Ji. Stability and aggregation of metal oxide nanoparticles in natural aqueous matrices. *Environmental science & technology*, 44(6):1962–7, mar 2010.

[326] Ernest M. Hotze, Tanapon Phenrat, and Gregory V. Lowry. Nanoparticle Aggregation: Challenges to Understanding Transport and Reactivity in the Environment. *Journal of Environment Quality*, 39(6):1909, 2010.

[327] George Metreveli, Allan Philippe, and Gabriele E. Schaumann. Disaggregation of silver nanoparticle homoaggregates in a river water matrix. *Science of the Total Environment*, 535:35–44, 2015.

[328] Peter D. Yates, George V. Franks, Simon Biggs, and Graeme J. Jameson. Heteroaggregation with nanoparticles: Effect of particle size ratio on optimum particle dose. *Colloids and Surfaces A: Physicochemical and Engineering Aspects*, 255(1-3):85–90, 2005.

[329] Antonia Praetorius, Martin Scheringer, and Konrad Hungerbühler. Development of environmental fate models for engineered nanoparticles–a case study of TiO2 nanoparticles in the Rhine River. *Environmental science & technology*, 46(12):6705–13, 2012.

[330] Mila Tejamaya, Isabella Römer, Ruth C. Merrifield, and Jamie R. Lead. Stability of citrate, PVP, and PEG coated silver nanoparticles in ecotoxicology media. *Environmental Science and Technology*, 46(13):7011–7017, 2012.

[331] USEPA. Methods for Measuring the Acute Toxicity of Effluents and Receiving Waters to Freshwater and Marine Organisms. Technical Report October, 2002.

[332] Caroline Naylor, Lorraine Maltby, and Peter Calow. Scope for growth in Gammarus pulex, a freshwater benthic detritivore. In M Munawar, G Dixon, C I Mayfield, T Reynoldson, and M H Sadar, editors, *Environmental Bioassay Techniques and their Application: Proceedings of the 1st International Conference held in Lancaster, England, 11–14 July 1988*, pages 517–523. Springer Netherlands, 1989.

[333] D R Kester, I W Duedall, D N Connors, and R M Pytkowicz. Preparation of Artificial Seawater. *Limnology and Oceanography*, 12(1):176–179, 1967.

[334] E. Cunningham. On the Velocity of Steady Fall of Spherical Particles through Fluid Medium. *Proceedings of the Royal Society of London. Series A, containing papers of a mathematical and physical character*, 83(563):357–365, 1910.

[335] Ilona Velzeboer, Joris T K Quik, Dik van de Meent, and Albert A. Koelmans. Rapid settling of nanoparticles due to heteroaggregation with suspended sediment. *Environmental Toxicology and Chemistry*, 33(8):1766–1773, 2014.

[336] Clément Levard, E. Matt Hotze, Gregory V. Lowry, and Gordon E. Brown. Environmental transformations of silver nanoparticles: Impact on stability and toxicity. *Environmental Science and Technology*, 46(13):6900–6914, 2012.

[337] Qian Chen, Hoduk Cho, Karthish Manthiram, Mark Yoshida, Xingchen Ye, and A. Paul Alivisatos. Interaction Potentials of Anisotropic Nanocrystals from the Trajectory Sampling of Particle Motion using in Situ Liquid Phase Transmission Electron Microscopy. *ACS Central Science*, 1(1):150323114811004, 2015.

[338] Ting Yu, Fook-Chiong Cheong, and Chorng-Haur Sow. The manipulation and assembly of CuO nanorods with line optical tweezers. *Nanotechnology*, 15(12):1732–1736, 2004.

[339] Faruq Mohammad, Gopalan Balaji, Andrew Weber, Rao M Uppu, and Challa S S R Kumar. Influence of Gold Nanoshell on Hyperthermia of Super Paramagnetic Iron Oxide Nanoparticles (SPIONs). *The journal of physical chemistry. C, Nanomaterials and interfaces*, 114(45):19194–19201, jan 2010.

[340] Human Cypa, Aleksandra Z Kijac, Ying Li, Stephen G Sligar, and Chad M Rienstra. Articles Magic-Angle Spinning Solid-State NMR Spectroscopy of Nanodisc-Embedded. *Biochemistry*, 46:13696–13703, 2007.

[341] James a Hutchison, Hiroshi Uji-I, Ania Deres, Tom Vosch, Susana Rocha, Sibylle Müller, Andreas a Bastian, Jörg Enderlein, Hassan Nourouzi, Chen Li, Andreas Herrmann, Klaus Müllen, Frans De Schryver, and Johan Hofkens. A surface-bound molecule that undergoes optically biased Brownian rotation. *Nature nanotechnology*, 9(2):131–6, 2014.

[342] Albert Einstein. Investigations on the theory of the Brownian Movement. *Annalen der Physik*, 17:549, 1905.

[343] Julián Alberto Gallego-Urrea, Julia Hammes, Geert Cornelis, and Martin Hassellöv. Multimethod 3D characterization of natural plate-like nanoparticles: Shape effects on equivalent size measurements. *Journal of Nanoparticle Research*, 16(5), 2014.

[344] COMSOL AB Stockholm Sweden. COMSOL Multiphysics® v. 5.2a., 2017.

[345] A D Rakic, A B Djurisic, J M Elazar, and M L Majewski. Optical properties of metallic films for vertical-cavity optoelectronic devices. *Applied optics*, 37(22):5271–5283, 1998.

[346] Mathieu L Juan, Maurizio Righini, and Romain Quidant. Plasmon nano-optical tweezers. *Nature Photonics*, 5(June), 2011.

[347] M. Dienerowitz, M. Mazilu, and K. Dholakia. Optical manipulation of nanoparticles: a review. *Journal of Nanophotonics*, 2(September):1–32, 2008.

[348] Allen H J Yang, Sean D Moore, Bradley S Schmidt, Matthew Klug, Michal Lipson, and David Erickson. Optical manipulation of nanoparticles and biomolecules in sub-wavelength slot waveguides. *Nature*, 457(7225):71–75, 2009.

[349] Mu-ying Wu, Dong-xiong Ling, Lin Ling, William Li, and Yong-qing Li. Stable optical trapping and sensitive characterization of nanostructures using standing-wave Raman tweezers. *Scientific Reports*, 7(January):42930, 2017.

[350] Mingrui Yuan, Lin Cheng, Pengfei Cao, Xu Li, Xiaodong He, and Xiaoping Zhang. Optical Manipulation of Dielectric Nanoparticles with Au Micro-racetrack Resonator by Constructive Interference of Surface Plasmon Waves. *Plasmonics*, 2017.

[351] Perry Schein, Dakota O'Dell, and David Erickson. Orthogonal Nanoparticle Size, Polydispersity, and Stability Characterization with Near-Field Optical Trapping and Light Scattering. *ACS Photonics*, page acsphotonics.6b00628, 2016.

[352] E B Aranas, P Z G Fonseca, Barker P F, and T S Monteiro. Thermometry of levitated nanoparticles in a hybrid electro-optical trap. *Journal of Optics*, 19:1–12, 2017.

[353] Jelena Kolosnjaj-Tabi and Claire Wilhelm. Magnetic nanoparticles in cancer therapy: how can thermal approaches help? *Nanomedicine*, 12:nnm–2017–0014, 2017.

[354] Vanessa Zamora-Mora, Mar Fernández-Gutiérrez, Álvaro González-Gómez, Beatriz Sanz, Julio San Román, Gerardo F. Goya, Rebeca Hernández, and Carmen Mijangos. Chitosan nanoparticles for combined drug delivery and magnetic hyperthermia: From preparation to in vitro studies. *Carbohydrate Polymers*, 157:361–370, 2017.

[355] Qi Ding, Dongfang Liu, Dawei Guo, Fang Yang, Xingyun Pang, Renchao Che, Naizhen Zhou, Jun Xie, Jianfei Sun, Zhihai Huang, and Ning Gu. Shape-controlled fabrication of magnetite silver hybrid nanoparticles with high performance magnetic hyperthermia. *Biomaterials*, 124:35–46, 2017.

[356] Dong Hyun Kim, Kyoung Nam Kim, Kwang Mahn Kim, and Yong Keun Lee. Targeting to carcinoma cells with chitosan- and starch-coated magnetic nanoparticles for magnetic hyperthermia. *Journal of Biomedical Materials Research - Part A*, 88(1):1–11, 2009.

[357] Q.A. Pankhurst, J. Connolly, and S.K. Jones. Applications of magnetic nanoparticles in biomedicine. *Journal of Physics D: Applied Physics*, 167, 2003.